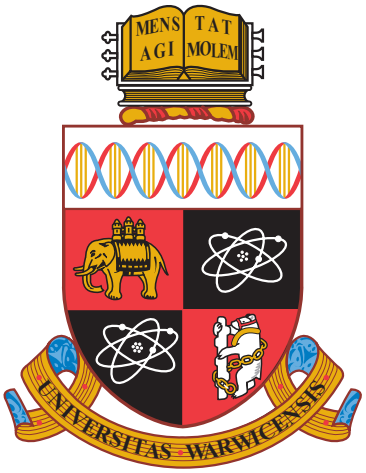

Homonuclear Correlation in Solid-State NMR: Developing Experiments for Half-Integer Quadrupolar Nuclei

by

Nathan Simon Barrow

Thesis

Submitted to the University of Warwick

in fulfilment of the requirements

for the degree of

Doctor of Philosophy

Department of Physics

December MMIX

THE UNIVERSITY OF WARWICK

CONTENTS

LIST OF TABLES

LIST OF FIGURES

DECLARATIONS

The work contained herein is wholly my own, with the exception of results obtained in collaboration with others. These collaborative results are indicated in the text along with the nature and extent of my individual contribution.

Figures 6-7 and 7-15 have previously been published [32].

This thesis has not been submitted for a degree at another university.

This *θέσις* was typed in TEXnicCenter and typeset by LaTeX 2_ε. Diagrams and spectra were processed in Illustrator CS2. References were stored using EndNote X2.

ABSTRACT

The objective was to develop solid-state nuclear magnetic resonance (NMR) homonuclear correlation experiments for half-integer quadrupolar nuclei so as to study atomic proximities and connectivities in disordered materials. Nearby nuclear spins are coupled through space via their magnetic dipole moments. Dipolar broadening is removed by magic angle spinning (MAS) for isolated spin pairs. However, the noncommutation of the electric quadrupolar interaction with the dipolar interaction means that the latter will not be removed by MAS. This interplay between the dipolar and quadrupolar interactions, combined with the effects of multiple noncommutating homonuclear dipolar couplings, was investigated by observing spin-echo dephasing curves as well as magnetisation transfer in 2D spin diffusion experiments. Polycrystalline lithium diborate samples were synthesised to act as model compounds. The preparation of samples with differing ^{11}B isotopic abundances enabled a comparison of samples with either predominantly isolated spin-pairs or multiple coupled nuclei.

Spin diffusion experiments probed ^{11}B–^{11}B correlation at three magnetic field strengths, 80% and 25% ^{11}B isotopic abundances, MAS rates from 4427 Hz to 7602 Hz and under DOR. Enhanced magnetisation transfer was observed for the higher ^{11}B isotopic abundance and at slower spinning speeds. The latter dependence was reproduced by four-spin computer simulations. Second-order quadrupolar broadened spin diffusion cross-peaks under MAS had a mixed positive and negative appearance for the 80% ^{11}B sample. A similar effect was previously observed for four dipolar-coupled $I = 1/2$ nuclei.

Spin-echo dephasing curves were recorded for 5%, 25% and 100% ^{11}B isotopic abundances and MAS rates of 5 kHz to 20 kHz. Depletion of ^{11}B isotopic abundance prolonged the coherence dephasing time because of a reduction of noncommuting homonuclear dipolar couplings. Faster dephasing was observed for the smaller $C_{\mathrm{Q}} = 0.51$ MHz site; four-spin computer simulations showed this is consistent with the reintroduction of the dipolar coupling being most efficient when the MAS rate and first-order quadrupolar interaction are of the same magnitude. Speeding-up the MAS rate prolonged the dephasing time for the $C_{\mathrm{Q}} = 2.56$ MHz site but not for the $C_{\mathrm{Q}} = 0.51$ MHz site because of an interplay between the quadrupolar and multiple dipolar interactions. Through-bond J-couplings between ^{11}B nuclei were not detected, setting an upper bound of $^{2}J_{\mathrm{BB}}$ <3 Hz in polycrystalline lithium diborate.

ABBREVIATIONS

ACRONYMS

2DAC	2-Dimensional Anisotropy Correlated
3Q	Triple Quantum
6Q	Six Quantum
COSY	Correlation Spectroscopy
CP	Cross Polarisation
CS	Chemical Shift
CSA	Chemical Shift Anisotropy
DAS	Dynamic Angle Spinning
DFS	Double Frequency Sweep
DFT	Density Functional Theory
DOR	Double Rotation
DQ	Double Quantum
DQHDR	Double Quantum Homonuclear Dipolar Recoupling
EDX	Energy-Dispersive X-ray Spectroscopy
EFG	Electric Field Gradient
EM	Electromagnetic
EMF	Electromotive Force
FAM	Fast Amplitude Modulation
FASTER	Fast Spinning Gives Transfer Enhancement at Rotary Resonance
FID	Free Induction Decay
H-HSQC	Homonuclear-Heteronuclear Single-Quantum Correlation
HMQC	Heteronuclear Multiple-Quantum Correlation
HS	Hyperbolic Secant
INADEQUATE	Incredible Natural Abundance Double Quantum Transfer Experiment

INEPT	Insensitive Nuclei Enhanced by Polarisation Transfer
MAS	Magic Angle Spinning
MQ	Multiple Quantum
MQMAS	Multiple Quantum MAS
NMR	Nuclear Magnetic Resonance
NOE	Nuclear Overhauser Effect
NOESY	Nuclear Overhauser Effect Spectroscopy
NQR	Nuclear Quadrupole Resonance
PDSD	Proton Drive Spin Diffusion
ppm	Parts Per Million
QCPMG	Quadrupolar Carr–Purcell–Meiboom–Gill
RAPT	Rotor-Assisted Population Transfer
RF	Radio Frequency
RIACT	Rotation-Induced Adiabatic Coherence Transfer
rpm	Revolutions Per Minute
SATSE	Saturation Spin Echo
SEM	Scanning Electron Microscopy
SQ	Single Quantum
STMAS	Satellite Transition MAS
SW	Spectral Width
TPPI	Time Proportional Phase Increment
XRD	X-Ray Diffraction
ZCW	Zaremba–Conroy–Wolfsberg

SYMBOLS

Numbers, units[1] and elemental names are in roman type. Physical constants and variables are in *italic* type.

$A_{\ell,m}$	Spatial Irreducible Spherical Tensor of Rank ℓ and Order m
B_0	Magnetic Field Strength in T
B_{RF}	Peak Magnetic Field Strength of Oscillating EM Wave in T
b_{jk}	Dipolar Coupling Constant in $\mathrm{rad\,s^{-1}}$
C_{Q}	Quadrupolar Coupling Constant in Hz
D^{ℓ}	Wigner D-matrix of Rank ℓ
$\hat{\mathscr{H}}$	Hamiltonian Operator in $\mathrm{rad\,s^{-1}}$
$\hat{\mathbf{I}}$	Nuclear Spin Operator in J s
$\hat{I}_x$, $\hat{I}_y$, $\hat{I}_z$	Cartesian Components of $\hat{\mathbf{I}}$—Angular Momentum Operators
${}^{n}J$	Nuclear Spin-Spin Coupling through n Bonds in Hz

[1] Abbreviated following the *Système international d'unités* guidelines

P_ℓ	Legendre Polynomial of Rank ℓ
T_1	Longitudinal (Spin-Lattice) Relaxation Time in s
T_2	Intrinsic Transverse Relaxation Time in s
T_2^*	Total Transverse Magnetisation Dephasing Time in s
$T_2^{'}$	Interaction Based Contribution to Dephasing Time in s
$\hat{T}_{\ell,m}$	Spin Irreducible Spherical Tensor Operator of Rank ℓ and Order m
$\mathbf{V}$	Electric Field Gradient in $\mathrm{V\,m^{-2}}$
$Y_{\ell m}^*$	Spherical Harmonic
γ	Gyromagnetic Ratio in $\mathrm{rad\,s^{-1}\,T^{-1}}$
$\Delta\delta_{\mathrm{iso}}$	Isotropic Chemical Shift Difference in Hz
η_{Q}	Quadrupolar Asymmetry Factor
$\boldsymbol{\mu}$	Nuclear Magnetic Dipole Moment in $\mathrm{J\,T^{-1}}$
ν_0	Larmor Precession Frequency in Hz
ν_{nut}	Nutation Frequency in Hz
ν_{r}	MAS Rate in Hz
ν_{RF}	Irradiating Radio Wave Frequency in Hz
$\hat{\boldsymbol{\rho}}$	Density Matrix Operator
τ	Time Duration between Pulses in s
ψ	Spin Wavefunction
ω_0	Larmor Precession Frequency in $\mathrm{rad\,s^{-1}}$
ω_{nut}	Nutation Frequency in $\mathrm{rad\,s^{-1}}$
ω_{Q}	Quadrupolar Coupling Constant in $\mathrm{rad\,s^{-1}}$
ω_{r}	MAS Rate in $\mathrm{rad\,s^{-1}}$
ω_{RF}	Irradiating Radio Wave Frequency in $\mathrm{rad\,s^{-1}}$

CHAPTER 1

Historical Context and Overview

Old spectroscopists never die,
they just become decoherent

1.1 The Development of NMR

1.1.1 Early Days

Nuclear magnetic resonance (NMR) has now been flourishing for two-thirds of a century, but is a field that has come from centuries of scientific development. Esteemed fellows such as Pieter Zeeman (Nobel Prize, 1902) and Sir Joseph Larmor (knighted 100 years ago in 1909) worked on magnetism, charge and radiation long before intrinsic angular momentum was hypothesized or even the proton was discovered.

In the 1920s significant progress was made toward the discovery of nuclear magnetic resonance (NMR). Otto Stern (Nobel Prize, 1943) and Walter Gerlach found quantised angular momentum of molecular beams and measured the electron magnetic moment. George Uhlenbeck and Samuel Goudsmit introduced the concept of a spinning electron with a quantised angular momentum of $\hbar/2$, together with a magnetic dipole arising from this spin. Wolfgang Pauli (Nobel Prize, 1945) developed a framework of electron spin and quantum me-

chanics as well as suggesting that some nuclei may possess spin (along with a parallel magnetic moment).

Otto Stern found this nuclear spin in 1933, by using his molecular beam technique to measure the magnetic moment of the proton. Isidor Rabi (Nobel Prize, 1944) is credited with being the first person to observe nuclear magnetic resonance. He added to Stern's technique a loop of wire, capable of generating an RF field over the atomic beam. When tuned to the Larmor frequency of the nuclei Rabi registered an absorption on his atomic-beam detector indicating the spins were flipping. By knowing the magnetic field strength and the frequency of the irradiation the magnetic moment of the nuclei in question can be calculated [257]. Rabi made another important discovery, the small electric quadrupole moment on the deuteron. A fuller historical perspective of these fundamental events, as well as further technical details, are retold by Rigden [263].

Technological advances in radio made during World War II allowed Felix Bloch and Edward Purcell (both shared the Nobel Prize, 1952) to invent a simpler method of magnetic resonance. With a sample placed in a strong homogeneous magnetic field, tuned radio waves were applied and the electromagnetic induction caused by nuclear reorientation was detected by a suitably wound coil of wire around the sample.

Towards the end of 1945, Purcell, Torrey and Pound obtained their first positive results from protons in paraffin [255]. Bloch, Hansen and Packard found their results in water, a few weeks later [38]. Their groups were separate and it was not immediately clear they had observed the same phenomenon, Purcell naming the effect "resonance absorption by nuclear magnetic moments" and Bloch "nuclear induction." Bloch's fascinating and detailed historical account can be found in his Nobel lecture [39]. Pound provides a similar recount, from the other camp [253]. A 157-page comprehensive account, including 1099 references, on the development of NMR can be found in the first article of the *Encyclopedia of Nuclear Magnetic Resonance* [35].

In the late 1940s and 1950s, when the techniques were unified under the moniker of nuclear magnetic resonance, much of the theoretical groundwork was prepared; interactions were discovered, NMR experiments for chemical characterisation were developed and commercial companies were incorporated. The

stage was set for the revolutionary discoveries that made NMR spectroscopy the technique that we know today.

1.1.2 Modern Era

Andrew and Lowe took the first steps into the modern era, around 1958, by introducing *magic angle spinning* (MAS) [14, 15, 194]. Rotating the sample at a certain angle (54.74°) to the static magnetic field removed the dipolar broadening and enhanced resolution (see §2.4). This paved the way for solids to be as accessible to NMR as liquids. The basic idea of suspending and spinning a rotor using compressed air is central to solid-state NMR today.

Around this time, Lowe and Norberg were the first to Fourier transform the resulting NMR signal after an RF pulse [195]. However, it was Ernst (Nobel Prize, 1991) and Anderson that provided a full treatment of the Fourier transform method (§3.6) and realised the dramatic implications for sensitivity enhancement this entailed [98, 99].

Pulsed NMR took another leap forward with Haeberlen and Waugh's treatment on coherent averaging effects [122]. This seminal paper demonstrated RF could be used to remove specific interactions and sowed the seeds of phase cycling. Double-resonance techniques allowed previously unconnected spins to interact via RF irradiation [129]. Pines, Gibby and Waugh used this interaction to great effect when they cross-polarised (CP) an isotopically rare nuclear species (^{13}C) using the magnetisation of abundant spins (^{1}H) [249, 250]. During the 1970s, the combination of CP with MAS by Schaefer, Stejskal and Buchdahl [274] introduced the modern era, with pulsed NMR under MAS being favoured over continuous-wave static experiments [102]. A factor of ∼1000 improvement in signal gained by FT-CPMAS has undoubtably changed the world of organic chemistry, amongst other fields, forever. Despite their importance, heteronuclear experiments play only a secondary role in this thesis.

Homonuclear correlation experiments can arguably trace their beginnings back to one of the first 2D NMR experiments invented; a three-pulse sequence by Jeener et al. that is popularly known in the solution-state NMR world as NOESY [151]. The sequence marked the birth of exchange spectroscopy and

detail about this experiment is forthcoming in §3.7.

Two-dimensional experiments of the time had a complex problem regarding the shape of the peaks, which reduced the resolution of the spectrum. The precise cause and solution is covered in §3.6 thanks to the pioneering work of States, Haberkorn and Ruben [287] as well as Marion and Wüthrich [211] in the early 1980s. Shortly after these developments pure-absorption-mode exchange spectra began to appear, heralding the new age of quantitative exchange spectroscopy [158].

Also at this time pulse sequence development gained maturity, aided by the groundbreaking paper of Sørensen et al. that introduced product-operator formalism to describe experiments [284]. Another seminal work, this time by Bodenhausen, Kogler and Ernst, gave the different pulse sequences a unified picture by describing them graphically according to their coherence-transfer pathways [43]. This key concept is described in §3.2, as all NMR experiments in this thesis are presented in this manner.

1.1.3 High Resolution Spectra of Half-Integer Quadrupolar Nuclei

It was noted that recording a spectrum where the spectral width was equal to the magic-angle spinning speed gave a lineshape devoid of sidebands and thus mimicked spinning infinitely fast [209]. Whilst this gave very narrow and featureless lineshapes for spin $I = 1/2$ nuclei[1], half-integer quadrupolar nuclei suffered from second-order quadrupolar broadening—an effect explained in §2.10.1. This broadening significantly decreased the spectral resolution, starting the quest for high-resolution NMR of half-integer quadrupolar nuclei.

Ganapathy, Schramm and Oldfield provided theory, simulation and experimental data on the effects of this broadened lineshape when the rotor was spun at different angles to the "magic" one [112]. Their variable angle spinning (VAS) approach reintroduced the first-order dipolar broadening MAS sought to remove, but in certain cases the resolution was improved. Lefebvre et al. continued this study, noting an angle (43.5°) at which all lineshapes had the

[1] Spin and the quantum number, I, are explained in §2.1.

same width regardless of the quadrupolar asymmetry[2] [185].

A breakthrough occurred in 1988 when Llor and Virlet realised there are complementary angles in the first- and second-order broadening mechanisms. They reasoned that if the rotor was spun at one angle for a certain time, then rapidly switched to its complementary angle for another time, they would obtain an isotropic spectrum—free of dipolar and quadrupolar broadening. Thus dynamic angle spinning (DAS) was born [192]. The technical feat was performed in the following years by Alex Pines' group, showing the amazing enhancement of resolution that DAS provided, compared to static, MAS and VAS lineshapes [230, Fig. 11].

At the same time Samoson, Lippmaa and Pines were working on another technique for high-resolution lineshapes that required spinning at two angles simultaneously [269, 270]. The theory of how double-rotation (DOR) averages away the first- and second-order interactions is explained in §2.10.2. The technique produces the same impressive resolution enhancement as DAS, as we shall see in experiments below (e.g. Fig. 2-10). Considering the mechanics of spinning one rotor inside another, it is astounding that the technique is physically possible at all. Any spinning object has a tendency to maintain its orientation unless a torque is exerted upon it. Trying to rotate this spinning object around another axis would therefore require a large torque, continually robbing the outer rotor of its angular momentum. Nevertheless, there is a special condition depending on the inertia and angles of the two rotors that gives a tolerably low torque for a given ratio of spinning speeds [324]. Whilst DOR has enjoyed some success over the past twenty years, simultaneously spinning at two angles still remains technically challenging to perform and the equipment is not commonly available. Perhaps a reason for this is due to another major advancement in the quest for high-resolution NMR of half-integer quadrupolar nuclei.

In 1995, Frydman and Harwood published their landmark paper on multiple-quantum MAS (MQMAS) [106]. Their insight was to realise that the fourth-rank second-order broadening of the quadrupolar lineshape could be *refocussed* in a 2D experiment whilst MAS removes the second-rank portions of the first- and second-order quadrupolar interactions in both dimensions, as ex-

[2] Denoted η_Q as per Eq. (2-42).

plained in §3.8. The experiment is inherently two-dimensional and by taking a certain projection—or shearing—of the 2D spectrum, an isotropic 1D spectrum can be obtained [221]. The mechanically challenging demands of DOR were ousted at the expense of reduced sensitivity in exciting multiple-quantum coherences and the longer experimental times required to acquire a 2D dataset.

Satellite-transition MAS (STMAS) is a similar experiment to MQMAS in that it is a 2D experiment designed to provide an isotropic spectrum of quadrupolar lineshapes [20, 21, 111]. STMAS is more sensitive than MQMAS (by ≈3–7) but depends critically upon the magic angle being accurately set to within 0.003°. Little more shall be said about STMAS in this thesis. Instead, DOR and MQMAS are covered in more detail over the forthcoming chapters as the chosen techniques to achieve high-resolution NMR of half-integer quadrupolar nuclei.

1.2 Thesis Overview and Motivation

A long-standing problem in physics is to characterise and understand the structure of disordered materials. Glasses can have extremely interesting properties and have different macroscopic characteristics (e.g. density) to their crystalline phases. Noncrystalline solids have long been studied with NMR techniques [84], which are suited to probing atomic length scales without requiring long-range order. However, at these shortest length scales oxide glasses and their crystalline phases have similar structures. The crystalline phase corresponding to glasses of interest can therefore be used as a model compound to help develop homonuclear correlation experiments for solid-state NMR—an approach adopted in this thesis.

The introduction to NMR given in Ch. 2 will provide the fundamental physics knowledge for understanding the experiments and conclusions contained herein. Chapter 3 will concentrate on the specific implementation of this physics, introducing techniques and pulse sequences. A review of solid-state NMR correlation experiments for quadrupolar nuclei is then delivered in Ch. 4. Special attention is given to homonuclear dipolar correlation. Then follows Ch. 5 containing the experimental and simulation parameters. Chapter 6

deals with materials science aspects of alkali borates. In these materials the existence of a borate anomaly and presence of superstructural units underlines the motivation of this thesis—to study the local structure of disordered materials. There are experimental details on lithium borate synthesis and select characterisations that help to cement understanding of borates, as well as the important differences between crystalline and disordered materials. Initial NMR results are also presented in Ch. 6, with a focus on the problem of relaxation in crystalline borates. Using the well characterised lithium diborate compound, Ch. 7 then shows NMR observations of spin diffusion between dipolar-coupled nuclei of the same type. This through-space homonuclear correlation is studied in detail, under a variety of conditions. Chapter 8 studies the coherence dephasing of boron in lithium diborate. Interesting differences in dephasing rate are seen as a function of MAS rate and isotopic enrichment. A different kind of homonuclear correlation—through-bond—could in principle be detected by these experiments. The absence of the effects of J-coupling put an upper limit on the strength of this coupling. Backing up the experimental data are extensive simulations, presented in Ch. 9, from which we can pick through the tangled web of nuclear interactions to gain understanding about the spin dynamics involved. Factors affecting spin diffusion can be varied systematically, revealing correlations that would be difficult to uncover in complicated real-world experiments.

By studying spin diffusion and spin-echo dephasing via a combined experimental and simulation approach, a greater understanding of the quadrupolar and dipolar interactions can be achieved. This understanding provides the foundations for the development of future NMR experiments to probe the proximities and connectivities between half-integer quadrupolar nuclei in disordered materials.

CHAPTER 2

Introduction to Solid-State NMR

Spins: One moment they're up, the next they're down!

2.1 Spin and the Density Operator

The angular momentum—or spin[1]—of subatomic particles is a conserved quantity as we observe classically, but in the world of quantum mechanics it is also quantised. This unintuitive fact implies that changes in angular momentum can only come in quanta of $\hbar$. The lowest allowed nonzero spin number is consequently $I = 1/2$, as the difference between *spin up* $(+\hbar/2)$ and *spin down* $(-\hbar/2)$ is $\hbar$. In theory, any half-integer value of I is allowed as the Pauli matrices that represent spin can have half-integer eigenvalues [177]. The exact spin a particular isotope has depends on its nuclear structure, which can be roughly explained by the nuclear shell model [237]. Only nuclei with non-zero spin can be manipulated by NMR. NMR is sensitive to the energy of nuclear spins, which can be affected by various magnetic and electric interactions. The total energy of a spin under these interactions, as the spin moves through time

[1] Like mass and charge, spin is an intrinsic property of the hadrons that constitute atomic nuclei. The term *spin* is used as this property behaves like classical angular momentum.

and space, is described by the nuclear spin Hamiltonian:

$$\hat{\mathscr{H}} = \hat{\mathscr{H}}_{\text{Zeeman}} + \hat{\mathscr{H}}_{\text{Chemical Shift}} + \hat{\mathscr{H}}_{\text{Dipolar}} + \hat{\mathscr{H}}_{J} + \hat{\mathscr{H}}_{\text{Quadrupolar}} + \dots \tag{2-1}$$

where the exact form of the interaction Hamiltonians will be covered below.

The energies and angular momenta are always quantised in units of $\hbar$. Redefining the Hamiltonian to correspond to energies with the dimension of angular frequency (ω, $\mathrm{rad\,s^{-1}}$) allows us to drop a factor of $\hbar$ in subsequent equations for simplicity and readability.

The wavefunction of a spin, ψ, completely describes its quantum mechanical state, e.g. for spin $I = {}^1\!/_2$, a linear superposition of spin-up and spin-down each multiplied by a complex phase. We can define a *density operator* to describe the ensemble average of the entire spin system:

$$\hat{\boldsymbol{\rho}} = \overline{|\psi\rangle\langle\psi|} \tag{2-2}$$

Combining this operator with the time dependent Schrödinger equation:

$$\tfrac{\partial}{\partial t}|\psi(t)\rangle = -\mathrm{i}\hat{\mathscr{H}}|\psi(t)\rangle \tag{2-3}$$

we arrive at the Liouville–von Neumann equation [177, §5.2]:

$$\tfrac{\partial}{\partial t}|\hat{\boldsymbol{\rho}}(t)\rangle = -\mathrm{i}\left[\hat{\mathscr{H}}, \hat{\boldsymbol{\rho}}(t)\right] \tag{2-4}$$

which has a highly relevant solution:

$$|\hat{\boldsymbol{\rho}}(t)\rangle = |\mathrm{e}^{-\mathrm{i}\hat{\mathscr{H}}t}\,\hat{\boldsymbol{\rho}}(0)\,\mathrm{e}^{\mathrm{i}\hat{\mathscr{H}}t}\rangle \tag{2-5}$$

Equation (2-5) says that if we know the initial density operator, $\hat{\boldsymbol{\rho}}(0)$, and the interaction Hamiltonian, $\hat{\mathscr{H}}$, then we can find the density operator at any arbitrary point in the future by inserting the appropriate value of time, t. Further information about propagating density matrices is given elsewhere [134, Ch. 8].

Several visualisations of this abstract density operator have been proposed, the most helpful of which depends on the spin number, I, and the number of coupled spins. A straightforward representation is a vector, which represents the bulk magnetisation of an ensemble of uncoupled spins.

A more powerful portrayal, at the expense of a slight abstraction, is product operator formalism [284]. In this formalism the longitudinal magnetisation

is represented by I_z, and coherent x- and y-magnetisation is represented by I_x and I_y, respectively. These act as vectors too, but in Hilbert space, where the total energy of the system is given by the Hamiltonian [25].

Finally, we can represent the density matrix as an actual matrix [37]. In the Zeeman basis[2] the elements corresponding to longitudinal magnetisation are along the diagonal, whilst off-diagonal elements represent ideas such as coherent x- and y-magnetisation as well as harder to visualise quantum spin phenomena. The density matrix describes the spin system completely, which can then be used directly in Eq. (2-5); a process that is well suited to numerical simulation [133].

2.2 Irreducible Spherical Tensors

Generally, a spin Hamiltonian expressed in irreducible spherical tensor operators can be given as [86, Eq. (59)]:

$$\hat{\mathscr{H}}_\Lambda = \sum_{\ell=0}^{2} C_\ell^\Lambda \sum_{m=-\ell}^{+\ell} (-1)^{\ell-m} A_{\ell,m}^\Lambda \hat{T}_{\ell,-m} \tag{2-6}$$

where A is an irreducible spherical tensor representing the spatial component of a certain interaction, Λ, in the laboratory frame. $\hat{T}$ is an irreducible spherical tensor operator representing the spin part of the Hamiltonian, determined by its rank, ℓ, and order, m. C is an interaction-specific constant.

From the previous section, we know that if we can write down the Hamiltonian we can completely describe the spin dynamics of the system. We also know the spatial tensors of the various possible interactions (see below), which are diagonal in the principal axis system of the interaction. The trick now is to transform the spatial tensor from the principal axis system (A^{P}) to the molecular frame, then to the laboratory frame (A^{L})—additionally via a rotor frame for an MAS experiment—before we can match theory with experiment[3].

The spin tensor operators [46, 47] are not affected by frame transformations, which justifies separation of the space- and spin-components in Eq. (2-6).

[2] A particularly convenient, complete and orthogonal basis set in Hilbert space, see §2.5.
[3] An illustrative graphic showing this frame transformation is available [86, Fig. 8].

2.3 Frame Transformation and Angular Dependencies

Irreducible tensors in spherical coordinates, such as A^{P}, are straightforward to transform under rotations [219]. The task calls for three parameters to specify the rotation and the most useful description is in terms of Euler angles; α, β, γ. The following explication is based upon Rose [264, Ch. IV].

We can create a rotation operator, $\hat{R}(\alpha, \beta, \gamma)$, which is a product of three operators. The rotation operations are successive, with each one defining a new coordinate system and the rightmost operator, $\hat{R}_\alpha$, operating on the tensor first.

$$\hat{R}(\alpha, \beta, \gamma) = \hat{R}_\gamma \hat{R}_\beta \hat{R}_\alpha = \mathrm{e}^{-\mathrm{i}\gamma \hat{I}_{z''}}\ \mathrm{e}^{-\mathrm{i}\beta \hat{I}_{y'}}\ \mathrm{e}^{-\mathrm{i}\alpha \hat{I}_z} \tag{2-7}$$

Explicitly, the steps in Eq. (2-7) are:

(i) A rotation is made about the z-axis through an angle α; the new coordinate axes are x', y', z'.

(ii) A rotation is made about the y'-axis through an angle β; the new coordinate axes are x'', y'', z''.

(iii) A rotation is made about the z''-axis through an angle γ; the new coordinate axes are x''', y''', z'''.

Because of the unitary transformation properties of $\hat{R}$ in general, we can express $\hat{R}_\gamma$ in the coordinate system that results after $\hat{R}_\beta$ has been performed. Similarly we can express $\hat{R}_\beta$ in the coordinate system that results after $\hat{R}_\alpha$ has been performed. The rotation operator then becomes:

$$\hat{R}(\alpha, \beta, \gamma) = \mathrm{e}^{-\mathrm{i}\alpha \hat{I}_z}\ \mathrm{e}^{-\mathrm{i}\beta \hat{I}_y}\ \mathrm{e}^{-\mathrm{i}\gamma \hat{I}_z} \tag{2-8}$$

Equation (2-7) describes[4] a rotation, $\hat{R}$, carried out by three successive Euler rotations; α about z, β about y', then γ about z''. Whereas Eq. (2-8) shows that these rotations may be carried out in the same coordinate system if the order of the rotations is inverted; γ about z, β about y, then α about z.

[4] Graphical descriptions of the Euler angles are readily available [197, Fig. 2.10].

A consistent coordinate system enables us to determine a rotation matrix to describe the operator $\hat{R}$. This matrix is called a Wigner D-matrix and is shown here acting on an arbitrary spherical tensor:

$$\hat{R}(\alpha,\beta,\gamma)A_{\ell m} = \sum_{m'} D^{\ell}_{m'm}(\alpha,\beta,\gamma)A_{\ell m'} \tag{2-9}$$

Now instead of calculating the effect of a rotation operator on a tensor we can simply multiply by a matrix. Interestingly, the Wigner D-matrices are related to spherical harmonics, which may aid visualisation of their effect in three-dimensional space [308].

$$D^{\ell}_{m0}(\alpha,\beta,0) = \sqrt{\frac{4\pi}{2\ell+1}}Y^{*}_{\ell m}(\beta,\alpha) \tag{2-10}$$

For the purposes of frame transformation of interaction tensors in NMR, here is a general example of an ℓ^{th}-rank tensor, going from the principal axis system ($A^{\text{P}}_{\ell m'}$) to the laboratory frame ($A^{\text{L}}_{\ell m}$):

$$A^{\text{L}}_{\ell m} = \sum_{m'=-\ell}^{\ell} D^{\ell}_{m'm}(\alpha_{\text{PL}},\beta_{\text{PL}},\gamma_{\text{PL}})\ A^{\text{P}}_{\ell m'} \tag{2-11}$$

Note that a rotation does not change the rank of a tensor. Similarly, a double frame transformation can be written as:

$$A^{\text{L}}_{\ell n} = \sum_{m=-\ell}^{\ell}\sum_{m'=-\ell}^{\ell} D^{\ell}_{mn}(\alpha_{\text{RL}},\beta_{\text{RL}},\gamma_{\text{RL}})\ D^{\ell}_{m'm}(\alpha_{\text{PR}},\beta_{\text{PR}},\gamma_{\text{PR}})\ A^{\text{P}}_{\ell m'} \tag{2-12}$$

which describes transforming A^{P} to an intermediate "R" frame[5], then on to A^{L}.

The Wigner D-matrices may seem abstract in this form, but they can be reduced to exponentials depending on α and γ that sandwich a Wigner d-matrix that has an angular dependence only on β:

$$D^{\ell}_{m'm}(\alpha,\beta,\gamma) = \mathrm{e}^{-\mathrm{i}m'\alpha}\ d^{\ell}_{m'm}(\beta)\ \mathrm{e}^{-\mathrm{i}m\gamma} \tag{2-13}$$

where some forms of $d^{\ell}_{m'm}(\beta)$ are given in §A.3. In general Wigner matrices can be looked up in a table as their calculation is rather involved [60]. Pleasingly, where NMR is concerned often $m = m' = 0$ (e.g. in Eq. (2-61) below) and the reduced Wigner d-matrices relate to Legendre polynomials like so:

$$d^{\ell}_{00}(\beta) = P_{\ell}(\cos\beta) \tag{2-14}$$

[5] A frame fixed to a spinning rotor, used for the explanation about magic angle spinning.

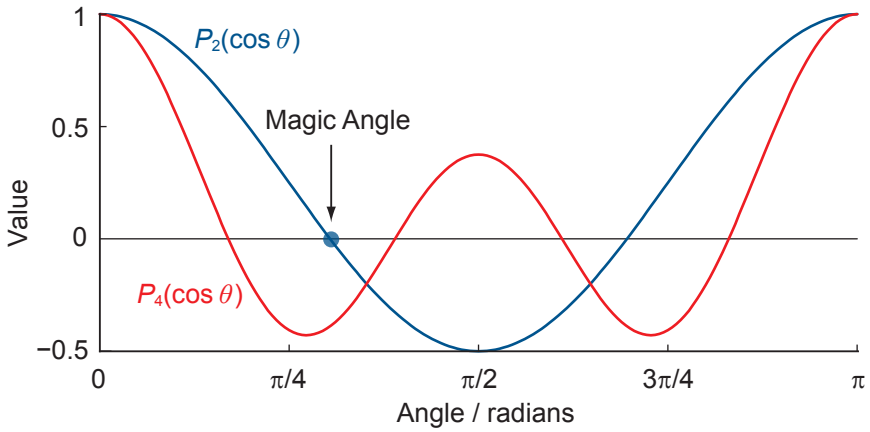

Figure 2-1. Graphical plot of the second (red) and fourth (blue) order Legendre polynomials of $\cos\theta$, which can be found in Eqs. (2-15) and (2-16) respectively. Note the roots of each function never coincide. The magic angle of $\theta = \arctan\sqrt{2} \simeq 54.74°$ is the first root of $P_2(\cos\theta)$. The roots $<90°$ for $P_4(\cos\theta)$ are $\simeq 30.56°$ and $\simeq 70.12°$.

The β-angle in Eq. (2-14) is relevant to NMR as when tranforming from a certain frame (e.g. the rotor or principal axis frames) it describes an angle (referred to generally as θ) between this frame and the z-axis of the laboratory reference frame. The first Legendre polynomial of interest is $P_0(\cos\theta) = 1$. With no angular dependence this represents an isotropic factor that is an important part of the chemical shift as well as the second-order quadrupolar interaction in §2.10. The second-order, $\ell = 2$, Legendre polynomial is:

$$P_2(\cos\theta) = \frac{1}{2}(3\cos^2\theta - 1) \tag{2-15}$$

Finally, the $\ell = 4$ Legendre polynomial is:

$$P_4(\cos\theta) = \frac{1}{8}(35\cos^4\theta - 30\cos^2\theta + 3) \tag{2-16}$$

These latter two Legendre polynomials are plotted in Fig. 2-1, in which is indicated a very special angle in NMR: The magic angle.

2.4 Magic Angle Spinning

Before we get to the magic part, consider a second-rank interaction tensor—in particular, its angular dependencies. For a powder sample[6] there will be

[6] A very large number of small single crystals, or crystallites.

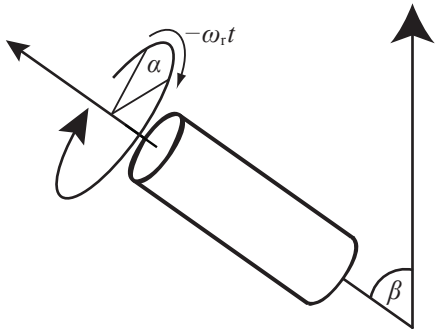

Figure 2-2. Under magic angle spinning (MAS), the solid sample is rotated quickly at a 'magic' angle of $\beta = \arctan\sqrt{2} \simeq 54.74°$ to the static magnetic field. MAS rates can be as quick at 60 kHz (3.6 million rpm). Another Euler angle, α, is perpendicular to β and introduces a time-dependency if the rotor is spinning.

interaction vectors covering all angles. These vectors can be decomposed into components parallel and perpendicular to the rotor axis. Note the rotor itself is tilted relative to the laboratory frame.

To find the energy perturbation in the laboratory frame we must perform the double frame transformation described in Eq. (2-12). For ease of notation we can contract the Eulers angles like so:

$$\alpha_{\mathrm{RL}}, \beta_{\mathrm{RL}}, \gamma_{\mathrm{RL}} = \Omega_{\mathrm{RL}} \tag{2-17}$$

From Eq. (2-12), the D-matrix going from frames P to R to L for a second-rank tensor ($\ell = 2$) is:

$$D^2_{m'n}(\Omega_{\mathrm{PL}}) = \sum_{m=-2}^{2} D^2_{mn}(\Omega_{\mathrm{RL}})\; D^2_{m'm}(\Omega_{\mathrm{PR}}) \tag{2-18}$$

Hence there are five terms to calculate. We focus on the Wigner D-matrix that takes us from the rotor frame to laboratory frame where we make our observations, $D^2_{mn}(\Omega_{\mathrm{RL}})$, and note that we can reduce this term using the relation given in Eq. (2-13):

$$D^2_{mn}(\Omega_{\mathrm{RL}}) = \mathrm{e}^{(-\mathrm{i}m\alpha_{\mathrm{RL}})}\, d^2_{mn}(\beta_{\mathrm{RL}})\, \mathrm{e}^{(-\mathrm{i}n\gamma_{\mathrm{RL}})} \tag{2-19}$$

Physically, the β_{RL} angle is between the rotor frame and the static magnetic field (laboratory frame) and α_{RL} describes an angle perpendicular to the β_{RL} angle—see Fig. 2-2. γ_{RL} is a phase-offset of the α_{RL} angle.

Recall at the start of this section we thought about the interaction vectors being decomposed to have a component perpendicular to the rotor axis.

When the rotor is spun, these vectors rotate along with it and the α angle that describes them becomes time-dependent according to the spinning speed; $\alpha = -\omega_{\mathrm{r}} t$, as shown in Fig. 2-2.

Let us define a rotor period, $t_{\mathrm{r}} = 2\pi/\omega_{\mathrm{r}}$, and average over the time-dependent part of Eq. (2-19):

$$\frac{1}{t_{\mathrm{r}}} \int_0^{2\pi/\omega_{\mathrm{r}}} \mathrm{e}^{(\mathrm{i}m\omega_{\mathrm{r}}t)}\, dt = \begin{cases} \frac{2\pi}{\omega_{\mathrm{r}} t_{\mathrm{r}}} = 1 & m = 0 \\ \frac{\cos(m2\pi)+\mathrm{i}\sin(m2\pi)-1}{\mathrm{i}m\omega_{\mathrm{r}} t_{\mathrm{r}}} = 0 & m = \pm 1, \pm 2, \ldots \end{cases} \tag{2-20}$$

When m, one of the indices in Eq. (2-19), is zero then the time-dependent part equates to unity only after one rotor period has elapsed. This means that only the $D^2_{0n}(\Omega_{\mathrm{RL}})$ terms from Eq. (2-18) survive. When $m = \pm 1, \pm 2, \ldots$ the time-dependent part evaluates to zero after precisely one rotor period. This is part of the magic nature of MAS and can be visualised by imagining the vector components perpendicular to the rotor axis being averaged to zero after one rotor period, so only the components parallel to the rotor axis remain.

Averaging over a complete rotor period, the five terms have been reduced to one:

$$D^2_{m'n}(\Omega_{\mathrm{PL}}) = D^2_{0n}(\Omega_{\mathrm{RL}})\; D^2_{m'0}(\Omega_{\mathrm{PR}}) \tag{2-21}$$

Referring back to Eq. (2-12) we see this term corresponds to A^{L}_{2n}. Under the high-field *secular* approximation, only diagonal terms of the matrix are nonzero, which is equivalent to considering only the A^{L}_{20} term. In this case Eq. (2-21) becomes:

$$D^2_{m'0}(\Omega_{\mathrm{PL}}) = D^2_{00}(\Omega_{\mathrm{RL}})\; D^2_{m'0}(\Omega_{\mathrm{PR}}) \tag{2-22}$$

Now only one angle describes the transformation of the parallel components from R→L. Following the relations described in Eqs. (2-13) and (2-14) the angular dependency of the D^2_{00} term is the $P_2(\cos\theta)$ Legendre polynomial: $\frac{1}{2}(3\cos^2\theta - 1)$. The second magic part is because when the rotor is spun at $\theta = \arctan\sqrt{2}$ then $\frac{1}{2}(3\cos^2\theta - 1) = 0$, thus this final term is also removed.

Magic angle spinning will average any second-rank interaction to zero after one rotor period because of this mechanism. Importantly for this thesis, the dipolar (§2.7) and first-order quadrupolar (§2.9) interactions are second-rank.

2.5 Zeeman Interaction

Having introduced the mathematics of spin, frame transformations and MAS, the physics of the electric and magnetic interactions can now be presented. We start at a fundamental level, with the strong Zeeman interaction.

Consider an angular momentum operator, $\hat{I}_z$, the exact state of which can be specified by two familiar quantum numbers, ℓ and m. Where ℓ can be any half-natural number $(0, 1/2, 1, 3/2, \ldots)$ and m can be any number between $\pm\ell$ in integer steps $(-\ell, -\ell+1, -\ell+2, \ldots, +\ell)$. These can be written in eigenequation form:

$$\hat{I}_z \left|\ell, m\right\rangle = m \left|\ell, m\right\rangle \tag{2-23}$$

such that the eigenvalue of the angular momentum operator along the z-axis is m, called the azimuthal quantum number. For example, if the quantum number of a spin was $I = 3/2$ then the allowed values of m would be $+3/2$, $+1/2$, $-1/2$ and $-3/2$. These represent quantised angular momentum projections on the z-axis.

NMR is conducted in strong[7] static magnetic fields, allowing us to define a z-axis such that $\mathbf{B} = (0, 0, B_0)$. The Zeeman interaction quantises the nuclear spins along this axis, i.e. $\hat{I}_z = m$. The Zeeman Hamiltonian tells us the energy of this interaction:

$$\hat{\mathscr{H}}_\mathrm{Z} = -\gamma B_0 \hat{I}_z \tag{2-24}$$

where γ is the *gyromagnetic ratio* between the nuclear magnetic moment, $\hat{\boldsymbol{\mu}}$, and the spin angular momentum, $\hat{\mathbf{I}}$:

$$\hat{\boldsymbol{\mu}} = \gamma \hat{\mathbf{I}} \tag{2-25}$$

The strength of the Zeeman interaction is indicated by the precession frequency of the magnetic moment of the nucleus in a magnetic field (note the minus sign):

$$\omega_0 = -\gamma B_0 \tag{2-26}$$

The Larmor frequency, ω_0, is in $\mathrm{rad\,s^{-1}}$, the gyromagnetic ratio, γ, is in $\mathrm{rad\,s^{-1}\,T^{-1}}$ and the magnetic field strength, B_0, is in T. The Zeeman interaction lifts the degeneracy[8], by splitting the $2I + 1$ energy levels so they are spaced

[7] Typically five orders of magnitude stronger than the Earth's natural magnetic field.

[8] Without a magnetic field, spin-up and spin-down would have no meaning and their energies would be degenerate.

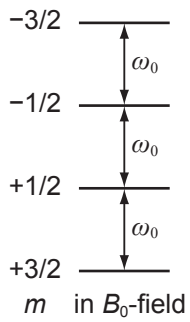

Figure 2-3. An energy level diagram of a spin $I = 3/2$ nucleus in a magnetic field. The otherwise degenerate energy levels split into $2I + 1$ separate levels, spaced ω_0 apart according to Eq. (2-26).

apart by a frequency difference equal to ω_0. For example see Fig. 2-3 for a spin $I = 3/2$ nucleus.

Crucially, each NMR-active isotope has a different Larmor frequency. This important fact allows NMR to discern between different isotopes, which makes the technique valuable for characterisation of materials. The gyromagnetic ratio is very important as it affects both the frequency and the intensity of the resonance [127]. Furthermore, we can define a receptivity of a nuclear species to be:

$$\Gamma = \gamma^3 \times \text{Natural Abundance} \times I(I+1) \tag{2-27}$$

A plot of receptivity against Larmor frequency for naturally-abundant NMR-active isotopes is given in Fig. 2-4, showing the variation of Larmor frequencies.

How strong is the Zeeman interaction? For an ^{11}B nucleus[9] in a magnetic field of 14.1 T, the energy gained by changing from opposing the magnetic field to aligning with it is $\hbar\gamma B_0 = 1.276 \times 10^{-25}$ J. Compare this with the thermal energy available to the room-temperature spin; $k_B T = 4.045 \times 10^{-21}$ J. We find that the energy benefit of magnetically aligning is swamped nearly 32 000 times over by the thermal energy. Therefore, the equilibrium magnetisation is only a tiny fraction of the total magnetisation available to the spins. This small paramagnetic component will be preferentially aligned along the z-axis, the defined direction of B_0. This longitudinal magnetisation is the equilibrium

[9] $\gamma(^{11}\text{B})$ is given in Tab. 5-1.

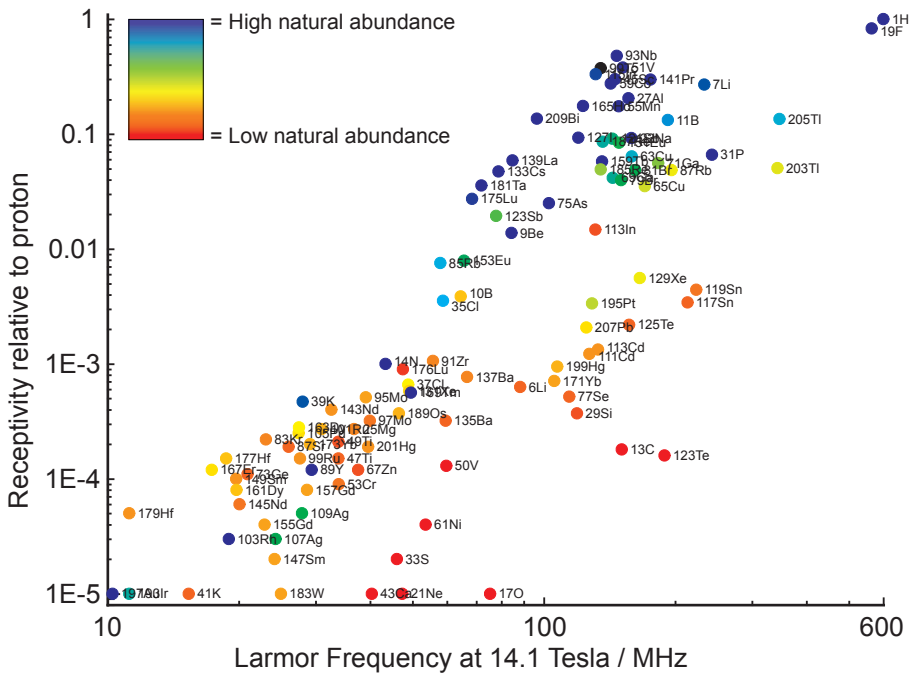

Figure 2-4. A log-log plot of receptivity as a function of Larmor frequency for naturally-abundant NMR-active isotopes.

state of the spins and forms the initial density operator for use in Eq. (2-5) [183]:

$$\hat{\boldsymbol{\rho}}(0) \propto \hat{I}_z \tag{2-28}$$

where for the remainder of this thesis the constant of proportionality is set to one.

This nuclear paramagnetism is very weak. For example, in water the diamagnetism due to the electrons is four orders of magnitude larger than the paramagnetism due to the protons [187]. Observing the nuclear paramagnetism directly would be extremely challenging experimentally, which is why *resonant* techniques are used to manipulate this bulk magnetic moment, giving rise to the name; nuclear magnetic resonance.

Despite the Zeeman interaction being relatively weak as far as interactions go, it is normally the strongest interaction where NMR is concerned and the other interactions can be treated at perturbations.

2.6 Chemical Shift

If the Zeeman interaction was the only mechanism for altering the energy of a nuclear spin in a magnetic field then NMR would not be the major chemical

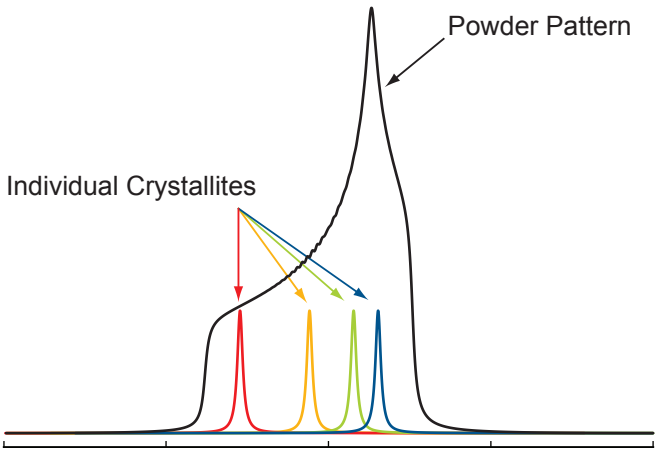

Figure 2-5. A single crystallite has only one Larmor frequency, giving a single sharp spectral line. A powder pattern is the sum, over a sphere, of all these individual crystallites. The exact width and shape depends on the chemical shift anisotropy parameters; Δ and η.

characterisation technique it is today; as each isotope would precess at its own Larmor frequency giving, spectroscopically, just one line per nuclear species.

Charged particles in a magnetic field are subject to a Lorentz force. For bound electrons, this induces a current as electrons circulate within their respective orbitals. This circulating current generates a small magnetic field that adds to, or subtracts from, the large static magnetic field already present at the nucleus. Consequently, the Larmor frequency of the nucleus is shifted slightly depending on the electronic environment that surrounds it—a phenomenon that has changed the world of chemistry forever.

For our purposes it is sufficient to say that the chemical shift allows NMR to clearly discern the difference between, say, a boron atom with three bonds and that of four bonds. The strength of the induced current is proportional to the applied field, B_0, as shown by the interaction Hamiltonian:

$$\hat{\mathscr{H}}_{\mathrm{CS}} = \gamma \hat{\mathbf{I}} \cdot \boldsymbol{\delta} B_0 \tag{2-29}$$

where the second-rank tensor, $\boldsymbol{\delta}$, can be diagonalised by choosing a particular *principal axis system*. In this frame we can define isotropic (δ_{iso}) and anisotropic

(Δ) components of the tensor:

$$\begin{aligned} \delta_{\text{iso}} &= \tfrac{1}{3}(\delta_{xx} + \delta_{yy} + \delta_{zz}) \\ \Delta &= \delta_{zz} - \delta_{\text{iso}} \\ \eta &= \frac{\delta_{yy} - \delta_{xx}}{\Delta} \end{aligned} \tag{2-30}$$

with the principal elements labelled and ordered according to $|\delta_{zz} - \delta_{\text{iso}}| \geq |\delta_{xx} - \delta_{\text{iso}}| \geq |\delta_{yy} - \delta_{\text{iso}}|$. This is the Haeberlen convention [121] and is the same convention used by NMR simulation programs such as SIMPSON and pNMRsim.

The angle between the principal axis system and the static magnetic field provides an orientation dependence[10] on the chemical shift. For a single crystal there is only one frequency so the spectroscopic line remains sharp. In a powdered sample all angles are present, turning the sharp line into an information rich *powder pattern* spectrum, as shown in Fig. 2-5. Duer has further described the interesting theory and application of chemical shifts, that is beyond the scope of this thesis [80, Ch. 3].

2.6.1 Under MAS

Although the static powder pattern contains orientation information, when many spectral lines are close to each other the overlapping lineshapes can hinder analysis of the spectrum. As discussed in §2.4 magic angle spinning can average a second-rank interaction, such as $\boldsymbol{\delta}$, to zero over one rotor period. However, the MAS rate must be much greater than the strength of the interaction for this averaging to result in only a single NMR resonance peak. Commonly in solid-state NMR the spectrum consists of a spectral line at the isotropic frequency and a series of *spinning sidebands* separated by the MAS frequency, ν_{r}, from this line [209]. A concise explanation of these features is given by Edén [85, §6.5.1]. It is noted that these spinning sidebands can be removed by acquiring in a rotor-synchronised fashion.

[10] Given by Eq. (2-15) for the $\eta = 0$ case.

2.7 Dipolar Interaction

The dipolar interaction plays a pivotal role in this thesis as one of the main interactions by which spins can be correlated. (The other important inter-spin interaction being the J-coupling, which is of less relevance to this thesis.) The easily visualised classical analogue is one of two bar magnets held near each other. When one rotates the other also moves to minimise its energy. Calling upon the correspondence principle, we can use the classical energy of interaction between two point magnetic dipoles to form our dipolar interaction Hamiltonian:

$$\hat{\mathscr{H}}_{\mathrm{D}} = -\frac{\mu_0}{4\pi}\frac{\hbar\gamma_I\gamma_S}{r^3}\left(\hat{\mathbf{I}}\cdot\hat{\mathbf{S}} - \frac{3(\hat{\mathbf{I}}\cdot\mathbf{r})(\hat{\mathbf{S}}\cdot\mathbf{r})}{r^2}\right) \tag{2-31}$$

where $\mathbf{r}$ is the internuclear vector and $\hat{\mathbf{I}}$ and $\hat{\mathbf{S}}$ are related to their magnetic moments as given by Eq. (2-25). The scalar factor is called the *dipole-dipole coupling constant*:

$$b_{jk} = -\frac{\mu_0}{4\pi}\frac{\hbar\gamma_I\gamma_S}{r^3} \tag{2-32}$$

from which we can construct the spatial spherical tensor for the dipolar interaction, in its principal axis system:

$$A^{\mathrm{P}}_{20} = \sqrt{6}\, b_{jk} \tag{2-33}$$

Under the secular approximation, this is the only non-zero term. The corresponding spin spherical tensor operator is:

$$\hat{T}_{20} = \frac{1}{\sqrt{6}}(3\hat{I}_z\hat{S}_z - \hat{\mathbf{I}}\cdot\hat{\mathbf{S}}) \tag{2-34}$$

Making the nuclear spin Hamiltonian in the principal axis system:

$$\hat{\mathscr{H}}^{\mathrm{P}}_{\mathrm{D}} = A^{\mathrm{P}}_{20}\hat{T}_{20} = b_{jk}(3\hat{I}_z\hat{S}_z - \hat{\mathbf{I}}\cdot\hat{\mathbf{S}}) \tag{2-35}$$

We note that transforming to the laboratory frame using Eq. (2-11) requires looking up only one Wigner D-matrix:

$$A^{\mathrm{L}}_{20} = A^{\mathrm{P}}_{20}D^2_{00} = A^{\mathrm{P}}_{20}\ \tfrac{1}{2}(3\cos^2\theta - 1) \tag{2-36}$$

where θ is the angle between the two nuclei. As mentioned above, by considering only the A^{L}_{20}, this is the secular approximation—valid for high field strengths

where the dipolar interaction can be considered as a small energy perturbation of the Zeeman interaction.

Digressing to change notation; $\hat{\mathbf{I}} \cdot \hat{\mathbf{S}}$ is defined as $\hat{I}_x\hat{S}_x + \hat{I}_y\hat{S}_y + \hat{I}_z\hat{S}_z$, which makes $\left(3\hat{I}_z\hat{S}_z - \hat{\mathbf{I}}\cdot\hat{\mathbf{S}}\right) = \left(2\hat{I}_z\hat{S}_z - (\hat{I}_x\hat{S}_x + \hat{I}_y\hat{S}_y)\right)$. The angular momentum operators in terms of raising and lowering operators are: $\hat{I}_x = \frac{1}{2}(\hat{I}^+ - \hat{I}^-)$ and $\hat{I}_y = \frac{1}{2\mathrm{i}}(\hat{I}^+ + \hat{I}^-)$. Hence, $(\hat{I}_x\hat{S}_x + \hat{I}_y\hat{S}_y) = \frac{1}{2}(\hat{I}^+\hat{S}^- + \hat{I}^-\hat{S}^+)$.

The full dipolar spin Hamiltonian in the laboratory frame for a static sample is:

$$\hat{\mathscr{H}}_{\mathrm{D}}^{\mathrm{L}} = b_{jk}\,\tfrac{1}{2}(3\cos^2\theta - 1)\left(2\hat{I}_z\hat{S}_z - \tfrac{1}{2}(\hat{I}^+\hat{S}^- + \hat{I}^-\hat{S}^+)\right) \tag{2-37}$$

The $\hat{I}_z\hat{S}_z$ term represents longitudinal magnetisation and since the secular dipolar Hamiltonian must commute with the Zeeman Hamiltonian, the total longitudinal magnetisation must be conserved. But while the total magnetisation remains constant, individual spin pairs can exchange magnetisation via energy-conserving flip-flops. The presence of raising and lowering operators[11] represent the flip-flop exchange of magnetisation as one spin is simultaneously raised ($\hat{I}^+$) as the other is lowered ($\hat{S}^-$). Spin a can exchange with spin b, then b with c and so on. Local imbalances in population may be transported throughout the system and with enough coupled spins this stochastic process gives rise to *spin diffusion* [234].

Spectrally, the dipolar coupling acts to broaden the resonance line. For a powder of isolated pairs of $I = 1/2$ nuclei the resonance line will be distorted to a Pake doublet shape, because of the $(3\cos^2\theta - 1)$ angular dependence [243]. In the more realistic case of a multitude of dipolar coupled spins, the lineshape can resemble a broad Gaussian [297]. The dipolar interaction can therefore reduce the resolution of the spectrum [283, Ch. 3]. One of driving forces behind the development of magic angle spinning was its ability to suppress the dipolar interaction and regain the resolution.

[11] $\hat{I}^+ = \hat{I}_x + \mathrm{i}\hat{I}_y$ and $\hat{I}^- = \hat{I}_x - \mathrm{i}\hat{I}_y$

2.7.1 Under MAS

As shown in §2.4, the Hamiltonian can be described under MAS via a double frame transformation; the result is:

$$\begin{aligned}\hat{\mathscr{H}}_{\mathrm{D}}^{\mathrm{L}} = \sqrt{6}\, b_{jk}\Big[&\tfrac{1}{2}\sin^2(\beta_{\mathrm{PR}})\cos(2\gamma_{\mathrm{PR}} - 2\omega_{\mathrm{r}}t) \\ &-\tfrac{1}{\sqrt{2}}\sin(2\beta_{\mathrm{PR}})\cos(\gamma_{\mathrm{PR}} - \omega_{\mathrm{r}}t)\Big]\hat{T}_{20}\end{aligned} \tag{2-38}$$

The integral of the Hamiltonian over one rotor period is zero, completely removing the dipolar coupling if the magic angle is perfectly set and there are no other interactions [209]. For >3 spins in a non-linear arrangement, MAS does not completely average to zero the homonuclear dipolar couplings and only partial line narrowing is achieved. The dipole-dipole coupling constant, $b_{jk}/2\pi$, can be large (∼kHz) so it is important to spin ($\omega_{\mathrm{r}}/2\pi$) at least several times faster than the interaction strength to fully remove the broadening effects. When the spinning too slow, magnetisation can flip-flop during a rotor period such that the integral is not zero and hence the dipolar coupling remains.

In a state where molecules are free to quickly tumble around in all directions, the direct dipole-dipole interaction between spins is averaged to zero. When spin-spin coupling was surprisingly observed in isotropic liquids it was found to be because of an indirect coupling mechanism involving the bonding electrons between atoms, and was termed J-coupling [123].

2.8 J-Coupling

Electrons are spin $I = 1/2$ particles and as such can interact magnetically with NMR-active nuclei [260]. Imagine two spin-paired electrons ($\cdot \uparrow\downarrow \cdot$) and introduce a nuclear spin. If this nuclear spin is aligned parallel with the closest electron spin the overall energy will be lower ($\uparrow \uparrow\downarrow \cdot$) or *vice versa* higher if aligned antiparallel ($\downarrow \uparrow\downarrow \cdot$). Now introduce another nuclear spin near these electrons. If this second nuclear spin is antiparallel to the first then the overall energy will again be lower ($\uparrow \uparrow\downarrow \downarrow$). Hence, nuclear spins can magnetically interact via electrons to perturb the nuclear spin Hamiltonian. This is the basic mechanism of J-coupling, which operates through bonds rather than through space [187, p. 215].

The full Hamiltonian for the J-coupling between spins I and S is:

$$\hat{\mathscr{H}}_J = 2\pi\hat{\mathbf{I}} \cdot \mathbf{J}_{\mathrm{IS}} \cdot \hat{\mathbf{S}} \tag{2-39}$$

where $\mathbf{J}_{\mathrm{IS}}$ is a second-rank tensor and the only nuclear spin interaction given with units of Hz; which explains the presence of 2π in the above Hamiltonian. Note there is no dependence on induced currents or the Larmor frequency with this interaction, so the J-coupling interaction does not scale with magnetic field strength (as is also the case for the dipolar coupling). In a liquid, $\mathbf{J}_{\mathrm{IS}}$ is averaged to its isotropic form:

$$\hat{\mathscr{H}}_J^{\mathrm{iso}} = 2\pi J_{\mathrm{IS}}\hat{\mathbf{I}} \cdot \hat{\mathbf{S}} = 2\pi J_{\mathrm{IS}}(\hat{I}_x\hat{S}_x + \hat{I}_y\hat{S}_y + \hat{I}_z\hat{S}_z) \tag{2-40}$$

making the isotropic J-coupling a scalar, equal to the average of the diagonal elements of the J-coupling tensor:

$$J_{\mathrm{IS}} = \tfrac{1}{3}(J_{xx} + J_{yy} + J_{zz}) \tag{2-41}$$

The anisotropic part of the full J-coupling tensor has the same form as the dipolar interaction but is usually much smaller, making the two interactions hard to distinguish. The anisotropic J-coupling can be safely ignored in this thesis.

Directly bonded nuclear spins typically give the highest values of J-coupling. However, it is routine to detect J-couplings over two or three bonds, denoted ${}^2J$ and ${}^3J$ respectively. In these cases the values may depend on the structural configuration of the bonds (e.g. the dihedral torsion angle), allowing extra information to be extracted [164, 165].

2.9 First-Order Quadrupolar Interaction

Quadrupolar nuclei are prevalent in NMR; ≈25% of NMR-active nuclei are spin $I = 1/2$ and ≈75% are *quadrupolar*. Hamiltonian theory of the quadrupolar interaction has been extensively covered by Abragam [1, Ch. VI] and Slichter [283, Ch. 10], both making use of irreducible tensor operators. The Hamiltonian approach is not the only method for representing the energy of a nuclear spin under the Zeeman and quadrupolar interactions; it is possible to calculate the energy

exactly using the Liouvillian directly [23]. Nevertheless, the Hamiltonian approach was expanded [80, Ch. 5] to account for high-resolution techniques such as MAS, DOR, DAS and MQMAS. The quadrupolar interaction Hamiltonian has recently been instructively derived from physical principles by Jerschow [155] and the irreducible tensor operators have been used by Sanctuary [271] to helpfully calculate the density matrices for quadrupolar nuclei by solving the Liouville–von Neumann equation [Eq. (2-4)].

The electric charge of a nucleus can be represented by multipole moments ($\ell = 0, 1, 2, 3, \ldots$) which have the same form as s, p, d and f electron orbitals in a hydrogen atom [187]. The first term ($\ell = 0$) corresponds to the electric charge of the nucleus, which is very important for holding the electrons and nuclei together, but not directly important for NMR. All odd terms ($\ell = 1, 3, \ldots$) such as the electric dipolar moment, have to be zero to conserve parity [155]. The next term ($\ell = 2$) is the electric quadrupole moment, which is only present[12] for spins $I > 1/2$. This non-spherical electric charge distribution interacts with the electric field gradient to cause a change in energy of the nuclear spin, which is detectable by NMR[13].

We will first cover the environment of the nucleus—the electric field gradient, eq, then the charge distribution of the nucleus—the electric quadrupole moment, Q.

The quadrupolar interaction is an electric interaction described by a second-rank (3×3) symmetric tensor, $\mathbf{V}$. This tensor comprises nine terms corresponding to the electric field gradient[14] at the nucleus. As with all real and symmetric tensors, this tensor can be diagonalised. The diagonalised form corresponds to the principal axis system. These remaining three terms are conventionally labelled such that $|V_{zz}| \geq |V_{yy}| \geq |V_{xx}|$. Laplace's equation for an electric potential shows us that the quadrupolar tensor is traceless ($V_{xx} + V_{yy} + V_{zz} = 0$) implying that $|V_{zz}| = |V_{xx} + V_{yy}|$. So in fact our nine-term

[12] A consequence explained by the Wigner-Eckart theorem.

[13] As these multipole moments carry a factor proportional to $r_n^\ell / r_e^{\ell+1}$ and the nuclear electric-charge radius is much less than the electron electric-charge radius ($r_n \ll r_e$), the next non-zero multipole term ($\ell = 4$) is very difficult to observe. Nevertheless, the hexadecapole moment has been detected by NMR [305].

[14] $V_{\alpha\beta} = \partial^2 V_{\alpha\beta} / \partial_\alpha \partial_\beta$

tensor can be completely described by two parameters:

$$C_{\mathrm{Q}} = \frac{e^2qQ}{h} = \frac{eQV_{zz}}{h}$$
$$\eta_{\mathrm{Q}} = \frac{V_{xx} - V_{yy}}{V_{zz}} \tag{2-42}$$

These parameters are a magnitude and an asymmetry. Note that $eq = V_{zz}$. The asymmetry, η_{Q}, by this definition, is a number $0 \leq \eta_{\mathrm{Q}} \leq 1$. The *quadrupolar coupling constant*, C_{Q}, is used in NMR as a suitable measure of the magnitude (in Hz) of the electric field gradient at the nucleus. Where e is the electronic charge, q is the gradient of the electric field and Q is the isotope-specific nuclear quadrupolar moment. These moments, which are usually determined with NMR techniques combined with *ab initio* calculation, have been tabulated by Pyykkö in 2001 [256].

The quadrupolar parameters in Eq. (2-42) are important for giving structural and chemical information about the nuclear site. A low quadrupolar coupling constant, C_{Q}, implies the site is spherically symmetric. For perfect cubic symmetry $C_{\mathrm{Q}} = 0$. High quadrupolar coupling constants indicate a more planar arrangement of bonds. If there are more charges in a certain plane than above or below that plane, a large electric field gradient will exist at the nucleus, leading to a high value of C_{Q}. Cylindrically symmetric charge distributions will lead to low values of asymmetry, η_{Q}, whilst highly asymmetric distributions give $\eta_{\mathrm{Q}} \simeq 1$.

An alternative definition of magnitude is more relevant in Ch. 9, and is given here in $\mathrm{rad\,s^{-1}}$:

$$\omega_{\mathrm{Q}} = \frac{2\pi C_{\mathrm{Q}}}{2I(2I-1)} \tag{2-43}$$

which is widely used [155, Eq. (40)][295, Eq. (1.62)] and is equivalent to χ_{Q} in Ref. [92], but can differ by a scalar factor in other sources. Note that for spin $I = 3/2$ nuclei, in Hz, $\omega_{\mathrm{Q}}/2\pi = C_{\mathrm{Q}}/6$, as these terms are used interchangably in Ch. 9.

Now we cover the Hamiltonian for the nuclear electric quadrupolar moment by taking the $\ell = 2$ term in the multipole expansion. The Hamiltonian (in J) in spatial spherical tensor form in the principal axis frame is:

$$\hat{\mathscr{H}}_{\mathrm{Q}}^{\mathrm{P}} = \sum_{m=-2}^{2} (-1)^m \hat{Q}_{2,m}\hat{\varepsilon}_{2,-m} \tag{2-44}$$

where $\hat{Q}_{2,m}$ is a second-rank spatial spherical tensor operator that describes the spatial charge distribution of the nuclear electric quadrupole and $\hat{\varepsilon}_{2,-m}$ does the same for the electronic portion. The follow equations closely follow the approach by Pound [252, cf. Eq. (13)] and Jerschow [155, cf. Eqs. (19)–(38)].

We obtain from the Wigner-Eckart theorem:

$$\begin{aligned}\hat{Q}_{20} &= \alpha\tfrac{1}{2}\left(3I_z^2 - I(I+1)\right)\\ \hat{Q}_{2\pm1} &= \mp\alpha\sqrt{\tfrac{3}{8}}\left(I_zI_\pm + I_\pm I_z\right)\\ \hat{Q}_{2\pm2} &= \alpha\sqrt{\tfrac{3}{8}}\left(I_x \pm \mathrm{i}I_y\right)^2\end{aligned} \tag{2-45}$$

where $\alpha = eQ/I(2I-1)$.

By the definitions in Eq. (2-42) the electronic terms are:

$$\begin{aligned}\hat{\varepsilon}_{20} &= \tfrac{1}{2}eq\\ \hat{\varepsilon}_{2\pm1} &= 0\\ \hat{\varepsilon}_{2\pm2} &= \tfrac{1}{2\sqrt{6}}eq\eta\end{aligned} \tag{2-46}$$

Combining Eqs. (2-44), (2-45) and (2-46) the Hamiltonian is explicitly:

$$\begin{aligned}\hat{\mathscr{H}}_{\mathrm{Q}}^{\mathrm{P}} = {}& \alpha\sqrt{\tfrac{3}{8}}\left(I_x - \mathrm{i}I_y\right)^2 \times \tfrac{1}{2\sqrt{6}}eq\eta_{\mathrm{Q}}\\ &+ \alpha\sqrt{\tfrac{3}{8}}\left(I_zI_- + I_-I_z\right) \times 0\\ &+ \alpha\tfrac{1}{2}\left(3I_z^2 - I(I+1)\right) \times \tfrac{1}{2}eq\\ &- \alpha\sqrt{\tfrac{3}{8}}\left(I_zI_+ + I_+I_z\right) \times 0\\ &+ \alpha\sqrt{\tfrac{3}{8}}\left(I_x + \mathrm{i}I_y\right)^2 \times \tfrac{1}{2\sqrt{6}}eq\eta_{\mathrm{Q}}\end{aligned} \tag{2-47}$$

which, substituting α and multiplying terms, simplifies to:

$$\begin{aligned}\hat{\mathscr{H}}_{\mathrm{Q}}^{\mathrm{P}} = \frac{eQeq}{2I(2I-1)}\Big(&\tfrac{1}{2}\left(3I_z^2 - I(I+1)\right)\\ &+ \tfrac{1}{4}\left(I_x - \mathrm{i}I_y\right)^2\eta_{\mathrm{Q}}\\ &+ \tfrac{1}{4}\left(I_x + \mathrm{i}I_y\right)^2\eta_{\mathrm{Q}}\Big)\end{aligned} \tag{2-48}$$

before finally becoming the familiar[15] quadrupolar Hamiltonian (in J) in the principal axis frame:

$$\hat{\mathscr{H}}_{\mathrm{Q}}^{\mathrm{P}} = \frac{e^2qQ}{4I(2I-1)}\Big(\left(3I_z^2 - I(I+1)\right) + \eta_{\mathrm{Q}}\left(I_x^2 - I_y^2\right)\Big) \tag{2-49}$$

[15] Some texts favour the equivalent notation $\frac{\eta_{\mathrm{Q}}}{2}\left(I_+^2 + I_-^2\right) = \eta_{\mathrm{Q}}\left(I_x^2 - I_y^2\right)$, e.g. Refs. [155, Eq. (38)] and [1, Ch. VI Eq. (24)].

Substituting Eq. (2-42), we can express this Hamiltonian in terms of C_Q in $\mathrm{rad\,s^{-1}}$:

$$\hat{\mathscr{H}}_\mathrm{Q}^\mathrm{P} = \frac{2\pi C_\mathrm{Q}}{4I(2I-1)}\Big(\big(3I_z^2 - I(I+1)\big) + \eta_\mathrm{Q}\left(I_x^2 - I_y^2\right)\Big) \tag{2-50}$$

which translates to spherical tensor form:

$$\hat{\mathscr{H}}_\mathrm{Q}^\mathrm{P} = \frac{2\pi}{2I(2I-1)}\left(A_{20}^\mathrm{P}\hat{T}_{20} + A_{22}^\mathrm{P}\hat{T}_{2-2} + A_{2-2}^\mathrm{P}\hat{T}_{22}\right) \tag{2-51}$$

where the spatial tensors in the principal axis frame are based on Eq. (2-42):

$$\begin{aligned} A_{20}^\mathrm{P} &= \sqrt{\frac{3}{2}}C_\mathrm{Q} \\ A_{22}^\mathrm{P} = A_{2-2}^\mathrm{P} &= \frac{1}{2}\eta_\mathrm{Q}C_\mathrm{Q} \end{aligned} \tag{2-52}$$

and the relevant spin tensor operators from [46, Tab. 1] are reproduced here:

$$\begin{aligned} \hat{T}_{20} &= \frac{1}{\sqrt{6}}\left(3I_z^2 - I(I+1)\right) \\ \hat{T}_{2\pm2} &= \frac{1}{2}I_\pm^2 \end{aligned} \tag{2-53}$$

As our observations are necessarily in the laboratory frame we must calculate the perturbations on the Zeeman splitting caused by the quadrupolar interaction, using the laboratory frame Hamiltonian. To match the approach described above [Eq. (2-6)] for the other interactions, Eq. (2-51) transforms to give:

$$\hat{\mathscr{H}}_\mathrm{Q}^\mathrm{L} = \frac{2\pi}{2I(2I-1)}\left(A_{20}^\mathrm{L}\hat{T}_{20} - A_{21}^\mathrm{L}\hat{T}_{2-1} - A_{2-1}^\mathrm{L}\hat{T}_{21} + A_{22}^\mathrm{L}\hat{T}_{2-2} + A_{2-2}^\mathrm{L}\hat{T}_{22}\right) \tag{2-54}$$

Concentrating on the first spatial tensor initially, we can apply the frame transformation given in Eq. (2-11):

$$A_{20}^\mathrm{L} = A_{20}^\mathrm{P}D_{00}^2 + A_{22}^\mathrm{P}D_{20}^2 + A_{2-2}^\mathrm{P}D_{-20}^2 \tag{2-55}$$

Substituting Eq. (2-52) into Eq. (2-55), the A_{20}^L spatial spherical tensor becomes:

$$A_{20}^\mathrm{L} = C_\mathrm{Q}\left[\sqrt{\frac{3}{2}}D_{00}^2 + \frac{1}{2}\eta_\mathrm{Q}(D_{20}^2 + D_{-20}^2)\right] \tag{2-56}$$

The other spatial tensors in Eq. (2-54) can be found the same way. For a specific case of spin $I = 3/2$ nucleus these spatial tensors can be combined

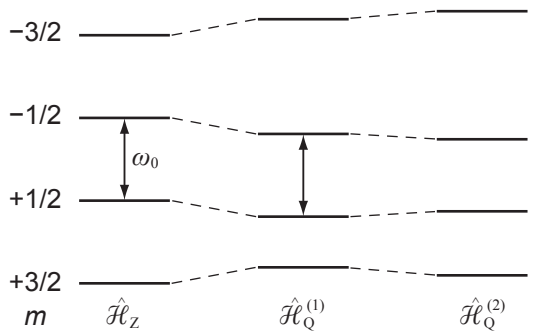

Figure 2-6. An exaggerated energy level diagram showing the effect of adding the quadrupolar interaction to the Zeeman interaction for a spin $I = 3/2$ nucleus. To first order, the central transition is unaffected, as indicated by the arrows. The satellite transitions are shifted by $\pm\omega_Q$, the exact amount is orientation dependent. The second-order quadrupolar interaction moves the $\pm m$ energy levels by equal and opposite amounts. Now the central transition is affected and for a powder with a range of crystallite angles, there is a broadening of the central transition spectral line.

with the relevant spin tensor operators (listed in Appx. A.1) to form the full quadrupolar Hamiltonian:

$$\hat{\mathscr{H}}_Q = \frac{2\pi}{2I(2I-1)}\sqrt{3}\begin{bmatrix} A^L_{20}/\sqrt{2} & A^L_{2-1} & A^L_{2-2} & 0 \\ -A^L_{21} & -A^L_{20}/\sqrt{2} & 0 & A^L_{2-2} \\ A^L_{22} & 0 & -A^L_{20}/\sqrt{2} & -A^L_{2-1} \\ 0 & A^L_{22} & A^L_{21} & A^L_{20}/\sqrt{2} \end{bmatrix} \tag{2-57}$$

When NMR interaction Hamiltonians are displayed in this matrix form they are usually being expressed in the basis set for which the Zeeman Hamiltonian is diagonal. The Zeeman interaction is dominant and we can treat the quadrupolar interaction as a perturbation. The effect these perturbations have on the Zeeman energy levels of a spin $I = 3/2$ nucleus are schematically shown in Fig. 2-6. We can calculate the first order perturbation using time-independent perturbation theory.

$$E^{(1)}_m = \left\langle m \middle| \hat{\mathscr{H}}_Q \middle| m \right\rangle \tag{2-58}$$

The first-order perturbation to the Zeeman energy by the quadrupolar interaction, in practice, involves retaining only the diagonal terms of the Hamiltonian. From Eqs. (2-57) and (2-58) we can see the first-order perturbation of

the $m = \frac{1}{2}$ and $m = -\frac{1}{2}$ levels are equal:

$$\begin{aligned} E^{(1)}_{1/2} &= \left\langle \tfrac{1}{2} \middle| \hat{\mathscr{H}}_{\mathrm{Q}} \middle| \tfrac{1}{2} \right\rangle \\ E^{(1)}_{-1/2} &= \left\langle -\tfrac{1}{2} \middle| \hat{\mathscr{H}}_{\mathrm{Q}} \middle| -\tfrac{1}{2} \right\rangle \\ &= -\frac{2\pi\sqrt{3}}{2I(2I-1)} \frac{A^{\mathrm{L}}_{20}}{\sqrt{2}} \end{aligned} \tag{2-59}$$

The $\left|\pm\frac{1}{2}\right\rangle \leftrightarrow \left|\mp\frac{1}{2}\right\rangle$ transition is called the *central transition* (CT) and as we have just proved, is not affected[16] by the quadrupolar interaction to the first order. Furthermore, from the Wigner D-matrices in Eq. (2-56) we can see there is the familiar angular dependence, D^2_{00}, to this first-order interaction, that will affect the *satellite transitions* (ST), as shown in Fig. 2-6.

2.10 Second-Order Quadrupolar Interaction

Realistically, the quadrupolar interaction can be significantly strong compared to the Zeeman interaction such that the central transition *is* affected. This can be explained by examining the second-order perturbation of the quadrupolar interaction:

$$E^{(2)}_m = \sum_{m \neq n} \frac{\left\langle n \middle| \hat{\mathscr{H}}_{\mathrm{Q}} \middle| m \right\rangle \left\langle m \middle| \hat{\mathscr{H}}_{\mathrm{Q}} \middle| n \right\rangle}{E^{(0)}_n - E^{(0)}_m} \tag{2-60}$$

Visually, the perturbations are shown in Fig. 2-6, where the Zeeman splitting is shown perturbed by the first-order quadrupolar interaction, which is itself perturbed by the second-order quadrupolar interaction described by Eq. (2-60).

It is even possible to calculate a third-order pertubation, but to see the effect experimentally requires a very sensitive experiment to observe the small energy shifts in the satellite transitions [110]. Like the first-order pertubation, there is no third-order perturbation of the central transition [24].

Expanding out Eq. (2-60), we find the second-order quadrupolar Hamiltonian now contains terms proportional to pairs of spatial tensors (e.g. $A_{21}A_{2-1}$) and a factor $\propto \omega^2_{\mathrm{Q}}/\omega_0$. The last factor has an intuitive physical meaning; higher electric field gradients at the nucleus cause quadratically larger energy level shifts whilst higher static magnetic fields linearly reduce such energy level shifts.

[16] Both energy levels shift equally so there is no overall change in frequency.

The consequence of multiplying two spatial tensors together depends on the behaviour of various multiples of second-rank Wigner D-matrices.

We turn to the Clebsch-Gordan series [264, Eq. (4.25)] and note that, unlike in the first order case, the rank changes by multiplying two Wigner D-matrices together. For example:

$$D^2_{01} D^2_{0-1} = -\tfrac{1}{5} D^0_{00} - \tfrac{1}{7} D^2_{00} + \tfrac{12}{35} D^4_{00} \tag{2-61}$$

where the fractional prefactors are multiples of Clebsch-Gordan coefficients, calculated from the Clebsch-Gordan series and looked up in a table.

This means that the second-order quadrupolar energy shift will, in general, depend on three different terms corresponding to zeroth-, second- and fourth-rank Wigner D-matrices. From Eq. (2-14) we know these have different angular dependences corresponding to the P_0, P_2 and P_4 Legendre polynomials of $\cos\theta$. The portion of the second-order quadrupolar interaction containing the P_0 factor represents an isotropic effect—an energy shift that is present regardless of crystallite orientation. The second-rank portion of the second-order quadrupolar interaction will behave like the other second-rank interactions and can be suitably removed by MAS. The fourth-rank portion of the second-order quadrupolar interaction angularly depends on the P_4 Legendre polynomial, which under MAS is only reduced rather than removed. It is this second-order broadening that gives quadrupolar nuclei a distinctive central-transition lineshape compared with those of spin $I = 1/2$ nuclei under MAS.

2.10.1 Under MAS

Whereas other interactions typically have strengths measured in Hz or kHz, the quadrupolar interaction is typically[17] measured in MHz. The broad satellite transition resonances are split up into *spinning sidebands*, as shown in Fig. 2-7.

In practice, we rarely observe the whole half-integer quadrupolar lineshape, concentrating instead on the narrow and more intense central transition. As Eq. (2-59) revealed, this transition is not broadened by the first-order quadrupolar interaction. However, the second-order quadrupolar interaction *does*

[17] Except for highly spherically symmetric sites, see §2.9.

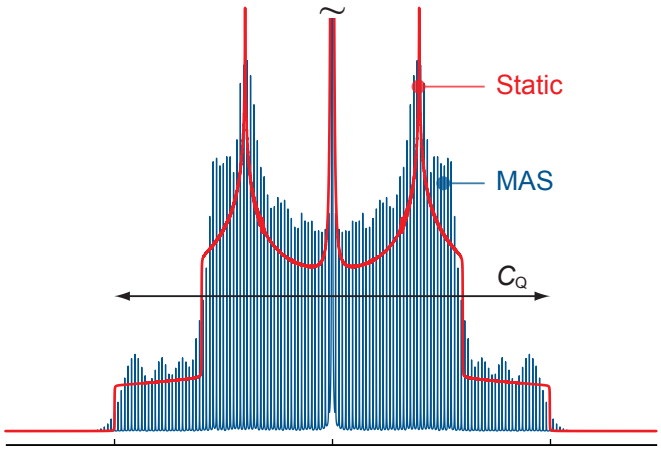

Figure 2-7. Simulation of a first-order quadrupolar interaction, which is much larger than the MAS rate. $I = 3/2$, $C_Q = 2.65\,\text{MHz}$, $\eta_Q = 0.2$, $\nu_0 = 192.5\,\text{MHz}$. Spectra shown are static, scaled ×10, (red) and spinning at $\nu_r = 20\,\text{kHz}$ (blue). The broad features that are split up by MAS are the first-order broadened satellite transitions. The spikes are separated by the MAS rate, $\nu_r = 20\,\text{kHz}$. The central transition is over three-hundred times more intense and has been cropped from the figure. 1000 Hz Lorentzian line broadening has been applied.

affect the central transition. For half-integer quadrupolar nuclei the second-order frequency shift for symmetric coherence order ($|\pm m\rangle \leftrightarrow |\mp m\rangle$) under MAS is given by:

$$\begin{aligned}\omega^{(2)}_{m,-m} = E^{(2)}_m - E^{(2)}_{-m} = 2\frac{(3\omega_Q)^2}{\omega_0}\Big(&A^I_m Q^0 \\ &+ B^I_m Q^2 d^2_{00}(\beta_{RL}) \\ &+ C^I_m Q^4 d^4_{00}(\beta_{RL})\Big)\end{aligned} \tag{2-62}$$

where A, B and C are scalar coefficients and Q^ℓ collects terms of the same rank:

$$\begin{aligned}Q^0 &= 1 + \frac{1}{3}\eta_Q^2 \\ Q^2 &= d^2_{00}(\beta_{PR})\left(1 - \frac{1}{3}\eta_Q^2\right) \\ &\quad - \sqrt{\frac{8}{3}}\eta_Q\, d^2_{20}(\beta_{PR})\cos 2\alpha_{PR} \\ Q^4 &= d^4_{00}(\beta_{PR})\left(1 + \frac{1}{18}\eta_Q^2\right) \\ &\quad + \frac{\sqrt{10}}{3}\eta_Q\, d^4_{20}(\beta_{PR})\cos 2\alpha_{PR} \\ &\quad + \frac{\sqrt{70}}{18}\eta_Q^2\, d^4_{40}(\beta_{PR})\cos 4\alpha_{PR}\end{aligned} \tag{2-63}$$

The definition of ω_Q from Eq. (2-43) has been used, which requires the factor of 3 to be included in Eq. (2-62). The scalar coefficients used in Eq. (2-62)

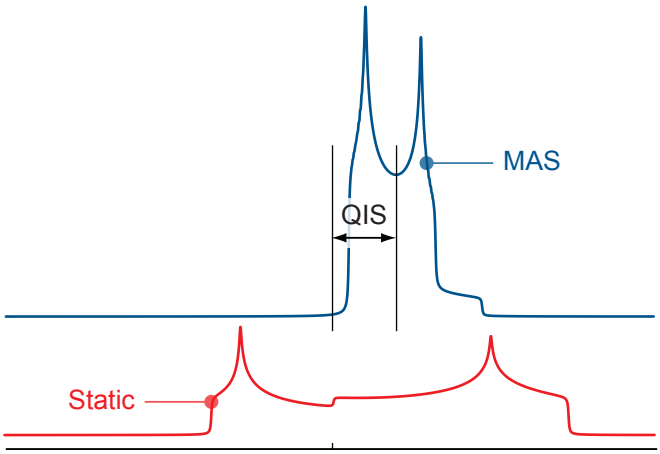

Figure 2-8. Simulation of an NMR powder spectrum, showing the effect magic-angle spinning has on the second-order quadrupolar interaction, restricted to the central transition only. $I = 3/2$, $\eta_Q = 0.2$. Varying η_Q changes the lineshape [197, Fig. 2.14]. For static (red) and spinning at $\nu_r = 20\,\text{kHz}$ (blue). 20 Hz Lorentzian linebroadening has been applied. The centre of gravity of the quadrupolar lineshape is shifted from δ_{iso} by the quadrupolar induced shift (QIS), according to Eq. (2-62).

can be found in Tab. A-1. Scaled[18] coefficients are also given in Refs. [58, Tab. 1] and [197, Tab. 2.4]. α_{PR} and β_{PR} refer to the Euler angles between the principal axis system and the rotor frame, defined in Fig. 2-2.

The isotropic term causes a shift of the central transition—it moves the whole lineshape to the right of the spectrum [167]. Since NMR spectra conventionally have reversed abscissae, the right of the spectra are at lower values of frequency.

The second-rank term angularly depends on the P_2 Legendre polynomial and over a complete MAS rotor period will be averaged to zero, as is the case for each and every second-rank interaction. However, if multiple interactions (e.g. dipolar and quadrupolar) are present simultaneously then MAS will not completely remove their second-rank terms if the interactions do not commute. Removing the second-rank second-order quadrupolar broadening has a large effect on the central transition lineshape—it becomes narrower, improving resolution, and more intense—see Fig. 2-8.

The fourth-rank term angularly depends on the P_4 Legendre polynomial and we can tell from simply looking at Fig. 2-1 that under MAS this term will be reduced but not removed.

[18] The scaling difference is due to differing definitions of ω_Q.

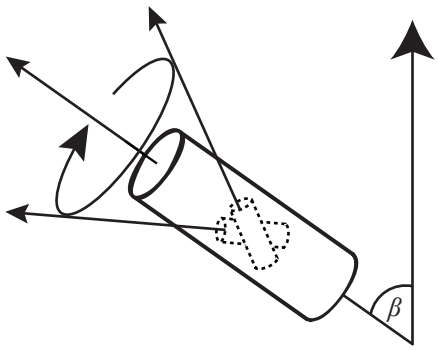

Figure 2-9. Double Rotation (DOR) spins an outer rotor at the P_2 magic angle. Simultaneously an inner rotor spins at an angle of $\simeq 30.56°$ relative to the outer rotor, one of the roots of the fourth order Legendre polynomial of $\cos\theta$. This process can remove second- and fourth-rank interactions simultaneously. An actual schematic of a DOR rotor can be found in Ref. [324, Fig. 2].

Maricq and Waugh noted that the isotropic second-order quadrupolar shift is specific to magic angle spinning in the limit $\omega_r \gg \omega_Q^2/\omega_0$ but not $\omega_r > \omega_0$ [209]. Hence, the shift vanishes in the limit of extremely fast isotropic rotation, which is why large shifts in solution-state NMR of quadrupolar nuclei are not observed. The effect on the spectrum of quadrupolar nuclei under MAS and VAS was reported by Man [207].

2.10.2 Under DOR

From Eq. (2-62) we can see that, to second-order, there are two β_{PR} angular dependencies: $d^2_{00}(\beta_{PR}) = P_2(\cos\beta_{RL})$ and $d^4_{00}(\beta_{PR}) = P_4(\cos\beta_{RL})$. In a similar vein to MAS, (where fast rotation around the root of the P_2 Legendre polynomial averages second-rank interactions to zero) we can expect fast rotation around the root of the P_4 Legendre polynomial to average away fourth-rank interactions. But if we are spinning at a P_4 magic angle then the P_2-dependent interactions will not removed. There is, of course, a direct way to remove both the P_2- and P_4-dependent interactions at once.

Spinning at both angles simultaneously in a double rotation experiment—or DOR for short—is mechanically challenging, but achievable for outer rotor rates of up to 2000 Hz and inner rotor rates up to 8000 Hz [270, 324]. The DOR rotor is schematically shown in Fig. 2-9. The equation for the second-order

perturbation of the quadrupolar interaction under DOR is [142]:

$$\begin{aligned}\omega^{(2)}_{m,-m} = 2\frac{(3\omega_Q)^2}{\omega_0}\Big(&A^I_m Q^0 \\ &+B^I_m Q^2 d^2_{00}(\beta_{R1R2}) d^2_{00}(\beta_{R2L}) \\ &+C^I_m Q^4 d^4_{00}(\beta_{R1R2}) d^4_{00}(\beta_{R2L})\Big)\end{aligned} \tag{2-64}$$

where β_{R2L} is the angle between the outer rotor axis and the laboratory frame and β_{R1R2} is the angle between the inner rotor and the outer rotor. This equation is the same as Eq. (2-62) but instead of one, there are two angular dependency factors because of the two axes of rotation.

To remove both the second- and fourth-rank quadrupolar broadening either $P_2(\cos\beta_{R1R2})$ or $P_2(\cos\beta_{R2L})$ must equal zero whilst simultaneously either $P_4(\cos\beta_{R1R2})$ or $P_4(\cos\beta_{R2L})$ must equal zero too. Typically the outer rotor spins at the P_2 magic angle of $\simeq 54.74^\circ$ and the faster inner rotor spins at the P_4 magic angle of $\simeq 30.56^\circ$ relative to the outer rotor.

With both angular dependencies removed, the second-order broadened lineshape will be narrowed compared to the MAS spectrum. However, we can see from Eq. (2-64) the isotropic term will still shift the spectrum, which is shown in Fig. 2-10. In theory, this isotropic term is the only difference between a DOR spectrum and a first-order only simulation of the central transition. The magnitude of the second-order isotropic shift provides information about the quadrupolar coupling strength and can be separated from the chemical shift by performing an MQDOR experiment [143]. Except where explicitly mentioned, the remainder of this thesis refers to MAS only.

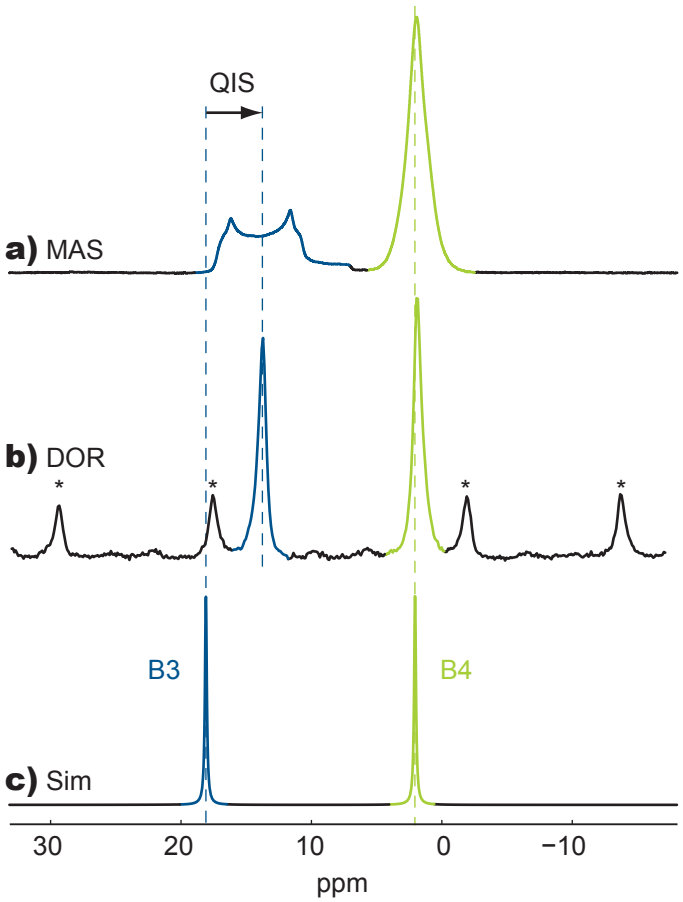

Figure 2-10. Central transition ^{11}B NMR spectra at 14.1 T of two distinct chemical sites—"B3" (blue) and "B4" (green). The B3 site has a considerable C_Q = 2.65 MHz and δ_{iso} = 18 ppm, whilst the B4 has a small C_Q = 0.51 MHz and δ_{iso} = 2 ppm. a) Under MAS the first-order quadrupolar broadening is removed but the reduced second-order interaction shifts and broadens the lineshapes, affecting the larger C_Q site more. b) DOR removes both first- and second-order quadrupolar broadening, making the lineshapes narrower. The second-order isotropic shift remains—note the centre of gravity of all lineshapes under MAS and DOR are equivalent. Spinning sidebands are labelled by asterisks. c) A first-order only simulation of the stated NMR parameters. Broadening is added artificially. Note the centre of gravity of each peak is at the isotropic chemical shift position, as there is no second-order quadrupolar isotropic shift (QIS).

CHAPTER 3

Pulsed Fourier Transform NMR

> The more you know, the more you realise that you know nothing.
>
> Socrates

3.1 Radio-Frequency

The Zeeman interaction section (§2.5) was left stating that the nuclear paramagnetism would be extremely challenging to directly detect, which is why resonant techniques are used. The part of the electromagnetic (EM) spectrum corresponding to typical Larmor frequencies of nuclei range from $\sim 100\,\mathrm{MHz}$ to $\sim 1000\,\mathrm{MHz}$, placing them in the radio part of the spectrum.

A standard NMR probe[1] can be expected to deliver an oscillating EM field with a maximum magnetic contribution of $\sim 1\,\mathrm{mT}$. This field is several orders of magnitude less than the static magnetic field and will generally not interact with the nuclear magnetic moments unless *on-resonance*. Recall the Zeeman Hamiltonian from Eq. (2-24) and add a linearly-polarised oscillating

[1] Ch. 5 discusses NMR hardware.

EM field, considering only the magnetic contribution:

$$\begin{aligned}\hat{\mathscr{H}}^{\mathrm{L}}(t) &= \hat{\mathscr{H}}_{\mathrm{Z}} + \hat{\mathscr{H}}_{\mathrm{RF}} \\ &= -\gamma B_0 \hat{I}_z - \gamma \mathbf{B}_{\mathrm{RF}}(t)\hat{\mathbf{I}} \\ &= \omega_0 \hat{I}_z + 2\omega_{\mathrm{nut}} \cos(\omega_{\mathrm{RF}} t + \phi)\hat{I}_x\end{aligned} \tag{3-1}$$

where the radio waves are defined by; a carrier frequency ω_{RF}, a phase ϕ and an amplitude $\omega_{\mathrm{nut}} = -\gamma B_{\mathrm{RF}}$, with B_{RF} being the maximum magnetic contribution to the radio wave. The time-dependent Hamiltonian in Eq. (3-1) cannot be solved by the Schrödinger equation for all times and we must make an approximation. If the carrier frequency is close to the Larmor frequency ($\omega_{\mathrm{RF}} \approx \omega_0$), as is the case on-resonance, then an approximation can be made by transforming into a frame rotating about the z-axis at ω_{RF}:

$$\hat{\mathscr{H}}^{\mathrm{rot}}_{\mathrm{RF}} = (\omega_0 - \omega_{\mathrm{RF}})\hat{I}_z + \omega_{\mathrm{nut}}(\hat{I}_x \cos\phi + \hat{I}_y \sin\phi) \tag{3-2}$$

In this rotating frame the precessing nuclear magnetic moments are, approximately, stationary and so is the magnetic component of the EM wave. The spins now act under a different effective static magnetic field, B_{RF}, whilst the "original" static magnetic field has only a small effect, proportional to the resonance offset, $(\omega_0 - \omega_{\mathrm{RF}})$.

Without loss of generality, we can apply the oscillating EM field with a certain phase, such that $\phi = 0$ defines the x-axis. Now Eq. (3-2), for $\omega_{\mathrm{RF}} = \omega_0$, becomes:

$$\hat{\mathscr{H}}^{\mathrm{rot}}_{\mathrm{RF}} = -\gamma B_{\mathrm{RF}} \hat{I}_x = \omega_{\mathrm{nut}} \hat{I}_x \tag{3-3}$$

which is analogous to the Zeeman Hamiltonian in Eq. (2-24).

To discover the effect of an on-resonance oscillating EM field we can call upon the solution to the Liouville–von Neumann equation [Eq. (2-5)] and the initial density operator [Eq. (2-28)] to propagate this RF Hamiltonian through time:

$$\hat{\boldsymbol{\rho}}(t) = \mathrm{e}^{-\mathrm{i}\hat{I}_x \omega_{\mathrm{nut}} t}\, \hat{I}_z\, \mathrm{e}^{\mathrm{i}\hat{I}_x \omega_{\mathrm{nut}} t} \tag{3-4}$$

which describes initially longitudinal magnetisation being "rotated" about the x-axis, hence developing a component along the y-axis:

$$\hat{\boldsymbol{\rho}}(t) = \hat{I}_z \cos(\omega_{\mathrm{nut}} t) - \hat{I}_y \sin(\omega_{\mathrm{nut}} t) \tag{3-5}$$

Remember this is happening in a rotating frame of reference. In the laboratory frame a spin, which has angular momentum and is already precessing around the z-axis, is now being "wobbled" down toward a plane perpendicular to the z-axis. The classical term for this behaviour is *nutation* and can be visualised on gyroscopes and planetary bodies.

In this rotating frame, we can see from Eq. (3-5) that depending on the duration that the RF is applied, τ_{RF}, the magnetisation will be tipped through an angle:

$$\theta_{\mathrm{nut}} = \omega_{\mathrm{nut}}\tau_{\mathrm{RF}} \tag{3-6}$$

When $\omega_{\mathrm{nut}}\tau_{\mathrm{RF}} = \pi/2$ we speak of a 90°-pulse, $\omega_{\mathrm{nut}}\tau_{\mathrm{RF}} = \pi$ is a 180°-pulse, and so on.

Using Eq. (3-5), we see the density matrix after an on-resonance 90°-pulse is entirely $-\hat{I}_y$. For an ensemble of spin $I = 1/2$ nuclei, this pulse has produced an equally weighted *coherence* of $\left|-\frac{1}{2}\right\rangle$ and $\left|+\frac{1}{2}\right\rangle$ states. The magnetic moment of each spin now points in a common direction that, as a whole, creates a transverse bulk magnetisation. Now in the absence of resonant RF, each spin will continue to precess around the z-axis as before; but every spin now does so coherently. This rotating magnetic moment induces an EMF (nowadays) in the very coil that applied the RF pulse. This signal is called a *free induction decay* (FID) and the manner of experimental detection is covered below in §3.5.

Not all pulses generate a coherent response from an ensemble of spins. After a 180°-pulse the bulk magnetisation will be aligned along the $-z$-axis and the populations of the $\left|-\frac{1}{2}\right\rangle$ and $\left|+\frac{1}{2}\right\rangle$ states will be inverted [234].

3.1.1 Hard and Soft Pulses

For spins $I > 1/2$ there are more than two energy levels and therefore more possibilities for creating coherences or inverting populations than presented so far. The representation of the spin state, $\hat{\boldsymbol{\rho}}$, can no longer be thought of as a classic vector in a rotating reference frame. The behaviour of half-integer quadrupolar nuclei under RF irradiation, which can be complicated [145], cannot be explored now. However, an immediately relevant fact about quadrupolar nuclei shall be presented.

As shown by the Zeeman-split energy level diagram in Fig. 2-3 the frequency difference between the central transition (CT) energy levels is ω_0, which is the resonant frequency of the applied RF, ω_{RF}. For a double-quantum (DQ) transition the frequency would be $2\omega_0$; affecting the DQ transition with a CT-resonant pulse is surely forbidden. However, during the transformation to the rotating frame in Eq. (3-2) a term was neglected[2] containing a magnetic field oscillating at $2\omega_{\mathrm{RF}}$. As this frequency is far from the Larmor frequency it has a weak effect on the spins and is usually ignored [40]. However, taking the second-order perturbation of the RF interaction on the energy levels split by the first-order quadrupolar interaction, it is revealed that a CT-resonant pulse can affect the forbidden DQ transition [251, Eq. (3)]. Triple-quantum (3Q) and higher coherences can also be created in this manner.

When a pulse is applied to excite all coherences nonselectively it is termed *hard*. These pulses typically have high[3] RF power (B_{RF} amplitude) and are short in duration. For a constant carrier wave frequency, a short-duration high-power pulse generates a broad range of frequencies. These are more efficient at affecting the entire CT lineshape as well as exciting forbidden coherences. The precise behaviour of the spin system depends on the spin (I) of the nucleus and the frequency separation of ω_0 and ω_{RF} [300, §3.3].

Conversely, *soft* pulses with long duration at low RF power have a narrow frequency response. These can be used to selectively excite central or satellite transitions without exciting multiple quantum coherences like DQ or 3Q. Advantageously, this can enable the response of quadrupolar nuclei to be thought of as just a single transition, instead of $(2I+1)$ transitions, allowing the use of a fictitious spin $I = {}^1\!/_2$ operator formalism [301].

Even with a soft pulse, the central transition of half-integer quadrupolar nuclei are still under the influence of the quadrupolar interaction. This is apparent spectrally—the lineshape is broadened by the second-order quadrupolar interaction—and via the nutation rate of the spins under RF irradiation. Depending on the ratio of $\omega_{\mathrm{Q}}/\omega_{\mathrm{nut}}$, the $\hat{I}_z^{2\text{-}3}$ magnetisation[4] nutates at different

[2] Neglected term is $\omega_{\mathrm{nut}}\left(\hat{I}_x\cos(2\omega_{\mathrm{RF}}t+\phi)+\hat{I}_y\sin(2\omega_{\mathrm{RF}}t+\phi)\right)$.

[3] $\omega_{\mathrm{nut}}/2\pi \approx 100\,\mathrm{kHz}$.

[4] For $I = {}^3\!/_2$ the fictitious spin-${}^1\!/_2$ operator $\hat{I}_z^{2\text{-}3} = \begin{bmatrix} 0&0&0&0\\ 0&1&0&0\\ 0&0&1&0\\ 0&0&0&0 \end{bmatrix}$.

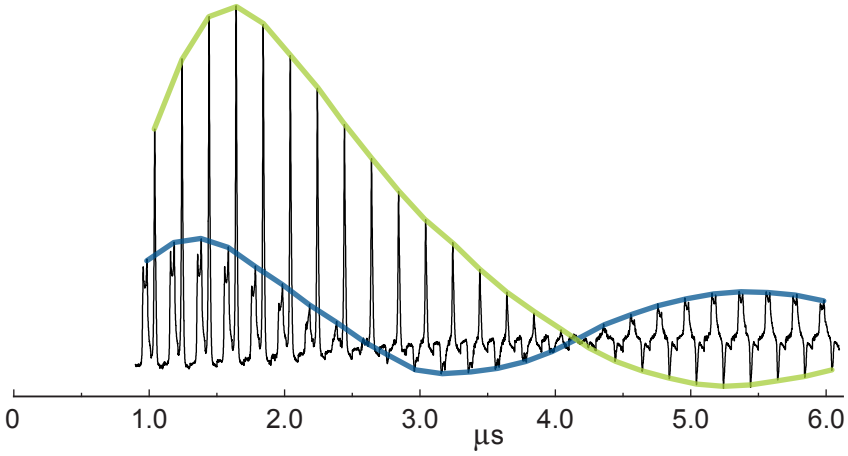

Figure 3-1. The nutation is faster for sites with larger C_Q. This array of ^{11}B spectra shows the effect on lineshape intensity as the pulse length is varied. The site with large C_Q (blue) nutates faster than the site with small C_Q (green). See also theoretical [300, Fig. 9] and experimental [208, Fig. 13] curves.

rates [168]. For vanishing ω_Q (hard pulse limit), the CT nutation rate is that of a spin $I = 1/2$ nucleus. In the (soft pulse) limit $\omega_Q \gg \omega_{nut}$, the CT nutation rate is $(I + \frac{1}{2})$ times faster. This behaviour is shown experimentally in Fig. 3-1. The repercussion of this effect is that small tipping angles (θ_{nut}) must be used to quantitatively compare lineshapes of differing ω_Q [268].

Furthermore, choosing a 180°-pulse length requires the preference of one range of C_Q values over another. Differing nutation rates also explain the difficulty in spin-locking [22, 130] quadrupolar nuclei that have different values of ω_Q.

3.2 Coherence and Phase Cycling

We have seen how coherence relates to bulk transverse magnetisation caused by nuclear magnetic moments precessing in synchrony with each other. Coherence can be generalised to indicate a transition between two spin-states, $|r\rangle$ and $|s\rangle$, such that the coherence order is denoted:

$$p_{rs} = M_r - M_s \tag{3-7}$$

where M is the magnetic quantum number [43].

Transverse magnetisation (e.g. $\hat{I}_x$) is a special case where $p = \pm 1$. Population states (e.g. $\hat{I}_z$) and zero-quantum coherence (e.g. $\hat{I}^+\hat{S}^-$) have a coherence

order of zero, $p = 0$. During free precession the coherence order cannot change—only pulses can transfer magnetisation between states. A 90°-pulse will excite all possible coherence orders in a spin system and a 180°-pulse will convert p to $-p$.

For quadrupolar or coupled spin $I = 3/2$ nuclei there are coherence orders and population states that cannot be visualised as a vector [118]. Using the irreducible spherical tensor operators developed in §2.9, the density matrix can be visualised as spherical harmonics, both during free precession and RF pulses [247].

At a basic level we can see that by applying 90°- and 180°-pulses we have control over the magnetisation of the nuclear spins. But applying RF seems to be an all-or-nothing approach, exciting or inverting all coherence orders or none. The method of *phase cycling* can be used to precisely select the desired coherence transfer.

The phase refers to the ϕ term in Eq. (3-2). Not only can the spectrometer generate RF pulses with different phases, but it can also receive different phases too. We know that if a coherence is undergoing a change in coherence order of Δp then it experiences a phase shift of $-\Delta\phi\Delta p$. Matching the receiver phase with this phase shift ($\Delta\phi_\mathrm{r} = -\Delta\phi\Delta p$) allows us to select a particular coherence, (p) as over the course of a phase cycle the undesired coherences will experience different phase shifts and be summed to zero. Further information and examples can be found in Refs. [134, §6.3] and [100, §6.3]. For now, phase cycles will be discussed when required to explain particular experiments, as a concrete example can often be more informative than general abstract rules.

Different pulse sequences with certain phase cycling—routing the magnetisation along different coherence transfer pathways—are the source of a great variety of NMR experiments, each designed to make use of specific interactions to extract information from the nuclei. Each experiment can be represented by a schematic diagram showing the types of pulses (commonly 90° and 180°) and the coherence transfers selected by the phase cycling of such pulses. We will encounter several of these diagrams below, such as in Fig. 3-2.

Determination of phase cycles can be accomplished and optimised by several approaches. The conventional method described by Bodenhausen, Kogler

and Ernst [43] can be easily computed and visualised [156] as well as optimised to give phase cycles of minimum length [241]. This type of phase cycling is employed in this thesis. Cogwheel phase cycling was invented [189] and optimised [138] by Levitt's group. Instead of incrementing multiple pulse phases consecutively in a *nested* phase cycle, all the pulse phases can be incremented simultaneously. This can cause a substantial reduction in the number of phase cycle steps required and, consequently, the duration of the whole experiment. Both these methods of phase cycling can be *multiplexed*, where each transient is stored separately and processed afterwards to yield the desired coherence transfer pathway [148]. Multiplex phase cycling also reduces the number of phase cycles required, as well as allowing multiple NMR experiments to be extracted from the same data set.

Phase cycling calculations are helped by two physical facts. First, only transverse magnetisation can generate an EMF. As stated above, this corresponds to the specific coherence order $p = \pm 1$. We can choose which coherence ($p = +1$ or -1) when we sample the induced EMF using quadrature detection[5]. The corollary of this first fact is that all coherence pathway transfer diagrams must end at $p = +1$ or -1. Secondly, all coherence pathway transfer diagrams begin in the population state, $p = 0$, because of longitudinal relaxation returning the system to the equilibrium state of longitudinal magnetisation.

3.3 Longitudinal Relaxation—T_1

The spin state at thermal equilibrium was given in Eq. (2-28) as $\hat{\boldsymbol{\rho}}(0) \propto \hat{I}_z$ and we have just seen how RF pulses can convert this longitudinal magnetisation into transverse magnetisation. The irreversible evolution of a spin system toward thermal equilibrium is called spin-lattice, or longitudinal, relaxation.

For NMR to be useful the spin system needs to return to thermal equilibrium in a reasonable time, ready for the next pulse. Relaxing too fast—around the μs scale—would damp the FID causing the spectrum to appear very broad. Relaxing too slowly limits the repetition rate of an experiment as applying RF pulses before the system has relaxed can lead to saturation of the energy levels

[5] See §3.5

and no FID being received at all. Typical spin-lattice recovery times are of the order $\sim$ s, although exceptionally long times of hours or days can sometimes be found. There are various relaxation mechanisms depending on the state of matter, nucleus type, sample temperature, paramagnetic purity level, electronic environment and whether or not external fields are applied, such as radio waves, micro waves, ultrasound or X-rays.

A basic overview is provided by Levitt [187, §2.6]. Ernst et al. discuss relaxation at four increasingly fundamental levels of physical significance [100, §2.3]. Two descriptive formalisms are given by Slichter [283, Chs. 5 & 6]. Abragam covers many of the mechanisms [1, Ch. IX], of particular interest is §II where the relaxation mechanism is caused by fixed paramagnetic impurities. Abragam and Goldman elaborated the description of this mechanism [2, Ch. 6]. Goldman has recently described a formal theory of spin-lattice relaxation using Hamiltonian theory and the Liouville–von Neumann equation (given above in §2.1), which leads to the synthesis of a master equation describing spin-lattice relaxation [116].

Van Kranendonk had previously discussed quadrupolar relaxation [296] and this work was continued by Andrew and Tunstall [16]. More experimental detail of quadrupolar relaxation came from nuclear quadrupolar resonance, where the Van Kranendonk mechanism was vindicated, but only for low[6] temperatures [152]. The Van Kranendonk mechanism was shown not to apply for quadrupolar nuclei in amorphous materials, where another quadrupolar relaxation mechanism is much more efficient at relaxing the nuclei [114, 291]. Multiexponential quadrupolar relaxation was expected and Jaccard et al. experimentally and theoretically studied this mechanism [149].

The materials studied in this thesis are insulating crystals or glasses, therefore the main relaxation mechanisms are either due to paramagnetic impurities or various forms of quadrupolar relaxation. Specific mechanisms are discussed below in §6.4 but for now it is appropriate to discuss the most basic level of formalism; the phenomenological Bloch equations.

If an ensemble of NMR-active nuclei with no initial magnetisation is

[6] $<$90 K for the case of observing chlorine nuclei in K_2PtCl_6.

suddenly subjected to a B_0 field, the magnetisation is given by:

$$M_z(t) = M_{eq}\left(1 - \mathrm{e}^{-t/T_1}\right) \tag{3-8}$$

where M_z is the bulk magnetisation along the z-axis at time t and M_{eq} is the bulk magnetisation at equilibrium, that is, fully relaxed. The key parameter is the longitudinal, or spin-lattice, relaxation time constant, T_1.

At time $t = T_1$ the magnetisation will be only 63.2% relaxed, at $5 \times T_1$ the magnetisation will be a more complete 99.3% relaxed. From a standpoint of reproducibility in quantitative studies, the spin system should be left to relax at least $5 \times T_1$ between phase cycle steps.

Multiexponential relaxation can be accommodated by using a weighted sum of $\left(I + \frac{1}{2}\right)$ exponentials [114]:

$$M_z(t) = \sum_{n=0}^{I+1/2} M_{eq}^n \left(1 - \mathrm{e}^{-t/T_1^n}\right) \tag{3-9}$$

3.3.1 The Saturation-Recovery Experiment

We have seen how the Zeeman interaction (§2.5) splits the nuclear magnetic energy levels and how we can use radio wave pulses (§3.1) to generate coherences (§3.2) between these energy transitions. Now is an appropriate time to bring together all these ideas to describe a basic NMR experiment that can measure the T_1 relaxation time of a given nuclear species in a sample. The saturation-recovery experiment is shown in Fig. 3-2, in the form of a pulse sequence and coherence transfer pathway diagram.

The pulse sequence starts with a series of high-power pulses, called a pulse comb. As the duration between the pulses is much less than the relaxation time (T_1) all the energy levels of the resonant nucleus will be saturated. No coherences or population states will exist after the pulse comb. This highlights the necessity of waiting for a suitable duration between phase-cycle steps.

After the pulse comb the spin system starts to relax back to equilibrium. For spin $I = 1/2$ nuclei, the longitudinal relaxation was given by Eq. (3-8). For long relaxation times the magnetisation of the spin system will be entirely in the population state I_z, which corresponds to $p = 0$, as shown in Fig. 3-2.

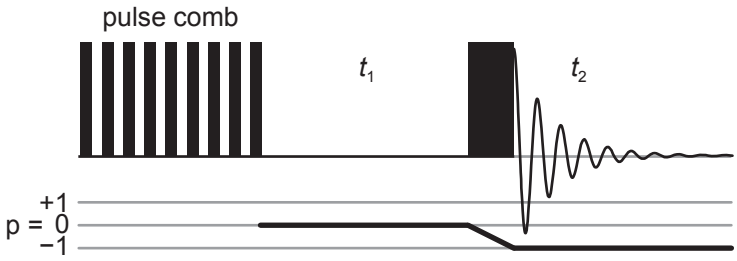

Figure 3-2. Pulse sequence (top) and coherence transfer pathway diagram (bottom) of the saturation-recovery experiment. The black rectangles signify RF pulses whilst the durations in between are periods of free precession, labelled t_1 and t_2. Pulse sequence diagrams are schematic and not to scale. Actual RF pulses typically last around a µs, whereas t_2 is measured in ms and t_1 in s. See §3.3.1 for further details.

Next, a 90°-pulse is applied. The RF will excite all coherences for the specific resonant nuclei. All other spins are unaltered. In some cases, e.g. double-resonance experiments, there would be more than one coherence transfer pathway diagram corresponding to the separate RF channels. Despite the presence of all coherences, quadrature detection only detects the $p = -1$ pathway—a fact elucidated in §3.5. The magnitude of the detected signal is directly proportional to the amount of resonant nuclei, making NMR a quantitive technique. After a suitable duration of detection time ($\sim$ ms) the experiment can be repeated. If the t_1 time was fixed, every subsequent 90°-pulse will be acting on the same starting magnetisation and the experiment will be consistent throughout.

The T_1 time of the resonant nuclei in a sample can be measured by repeating the experiment shown in Fig. 3-2 several times, each with a different t_1 duration. When t_1 is near zero we expect very little signal. When t_1 is much longer than T_1 we expect a full signal. Values of t_1 in between these extremes will map out a curve according to Eq. (3-8), hence by fitting this curve the value of T_1 can be ascertained. The form of the "signal" does not matter for this experiment and is covered below in §3.5.

For solution-state NMR, longitudinal and transverse magnetisation relaxation times can be similar. Rarely though, does the longitudinal relax faster than the transverse [17]. For solid-state NMR, the transverse magnetisation almost always decays long before the longitudinal magnetisation has relaxed because of the dephasing of transverse magnetisation.

3.4 Transverse Relaxation—T_2

In addition to T_1, another relaxation time constant is T_2. The *coherence dephasing time* can be imagined using the vector model as individual precessing magnetic moments falling out of synchronisation with each other. This can be visualised as many vectors in the rotating frame initially pointing along a single direction in the x-y plane. As time progresses the vectors spread out evenly across the whole x-y plane to give zero net transverse magnetisation.

Ideally, the bulk magnetisation of fully relaxed nuclei after a perfect 90°-pulse and no other interactions is described below, in the laboratory frame:

$$\begin{aligned} M_x(t) = &\quad M_{eq}\sin(\omega_0 t)\left(\mathrm{e}^{-t/T_2}\right) \\ M_y(t) = &- M_{eq}\cos(\omega_0 t)\left(\mathrm{e}^{-t/T_2}\right) \end{aligned} \tag{3-10}$$

Equation (3-10) describes an exponentially damped bulk magnetic moment, precessing with angular frequency ω_0 in the x-y plane.

In reality, there will be a spread of precession frequencies causing a broadening of the spectrum. This obviously has a detrimental effect on the resolution but also masks the informative interactions and true transverse relaxation with equipment-specific dephasing. The experimentally measured peak width in a spectrum will be $\propto 1/T_2^*$. The true transverse relaxation (T_2) along with the interaction and equipment-specific dephasing (T_2') contributions make up the measured dephasing time like so:

$$\frac{1}{T_2^*} = \frac{1}{T_2} + \frac{1}{T_2'} \tag{3-11}$$

Most often in solid-state NMR $T_2' \ll T_2$, therefore the true transverse relaxation is rarely measured and the explanation of its cause is not required here. The T_2' term encompasses factors such as imperfect apparatus and nuclear spin interactions, e.g. the residual heteronuclear dipolar interaction not removed by ^{1}H decoupling and multiple non-commuting homonuclear dipolar couplings.

A spin-echo can be used to measure T_2' by removing or *refocusing* the inhomogeneous broadening caused by the equipment as well as chemical shift offsets. Only the factors that incoherently dephase the transverse magnetisation remain, such as the true transverse relaxation and, e.g. the heteronuclear dipolar

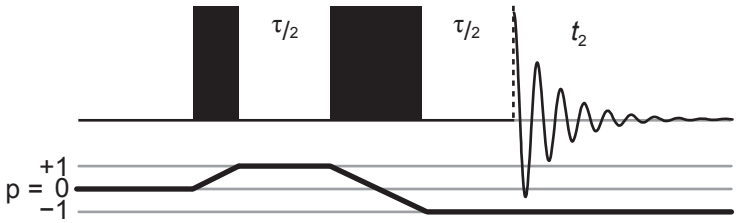

Figure 3-3. Pulse sequence and coherence transfer pathway diagram of the spin-echo experiment. See §3.4.1 for details.

interaction. But as stated above $T_2^{'} \ll T_2$, henceforth the assumption will be that spin-echo experiments measure $T_2^{'}$.

3.4.1 The Spin-Echo Experiment

A spin-echo experiment is shown in Fig. 3-3. After a suitably long relaxation delay the magnetisation will be fully longitudinal. A 90°-pulse excites a single quantum (SQ) coherence, chosen by phase-cycling. The magnetisation precesses according to Eq. (3-10), but there is a spread of ω_0 values—some spins are "fast" and some are "slow". After a duration of $\tau/2$ a 180°-pulse is applied, which reverses the direction of the precession. Now the fast spins are quickly "undoing" their previous evolution whilst the slow spins slowly undo theirs. After another $\tau/2$ all the respective evolutions of the spins are back where they started and detection of the signal begins. The coherent dephasing effects[7] are refocussed by the 180°-pulse, but any irreversible dephasing from interesting spin-spin interactions[8] will cause a reduction in signal. By repeating the experiment with varying τ duration, the coherence dephasing time $\left(T_2^{'}\right)$ of the nucleus under study can be determined. If varying experimental conditions changes the dephasing time then additional information about the interactions can be extracted.

Mathematically, the features of coherence transfer echoes are discussed below (§3.8) with regard to refocussing the fourth-rank portion of the second-order quadrupolar interaction. Application of the given theory can be elementarily applied in this case of single-quantum coherences with equal evolution and detection times.

[7] E.g., magnetic inhomogeneity, chemical shift offsets.
[8] E.g., noncommuting homonuclear dipolar couplings, quadrupolar-dipole interactions.

Modifications to this basic spin-echo theory for application to quadrupolar nuclei involves modifying Eq. (3-10) to accommodate multiexponential relaxation. In addition, the multiple quantum coherences are best dealt with using a density matrix formalism rather than the vector model [63].

There are many practical uses for a spin-echo beyond measuring T_2'. For rapidly dephasing transverse magnetisation (from natural broad spectral lines), a spin-echo can remove the signal loss and phase problems by avoiding the spectrometer dead-time after a pulse. A series of echoes can enhance sensitivity of quadrupolar lineshapes, in what is termed a QCPMG[9] experiment [181]. As the J-coupling is not refocused by a spin-echo, detection of a cosinusoidal factor to the exponential decay can reveal this interaction [82].

3.5 Signal Detection

We have seen that by applying an RF pulse—that is not exactly 180°—to an ensemble of spins we will have converted some of the longitudinal magnetisation ($p = 0$) to transverse magnetisation ($p = \pm 1$). As this bulk transverse magnetisation precesses in the static magnetic field, RF is detected in the coil surrounding the sample. A typical wavelength of a, for example, 300 MHz, radio wave is $\simeq 1$ m. The coil that envelopes the sample is on a scale 100 times smaller than this wavelength. Therefore, the idea that the NMR signal is predominantly caused by coherent spontaneous emission (radio waves) is incorrect. The NMR signal can be explained as a near-field phenomenon by Faraday's law, as a rotating magnetic moment induces an electromotive force (EMF) in a nearby open circuit [135, 136].

This current is the aforementioned signal, which contains a wealth of information as the exact frequencies present disclose the active spin interactions. After preamplification, the signal is *mixed down* with the carrier wave frequency so the electronics only have to deal with frequencies up to ~ 0.5 MHz instead of ~ 500 MHz. This is conveniently equivalent to viewing the interactions in the rotating frame.

[9] This quadrupolar experiment is a modification to the eponymous pulse sequence invented by Carr, Purcell [61], Meiboom and Gill [223].

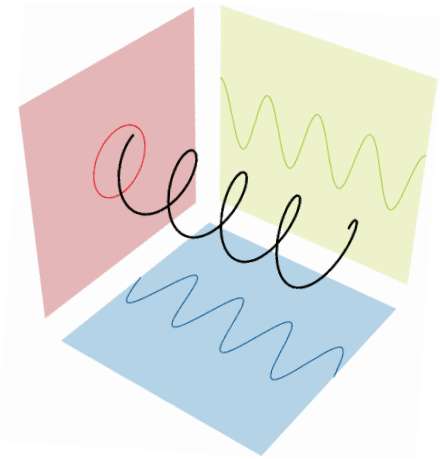

Figure 3-4. The black curve follows the tip of the bulk magnetisation vector as it precesses in time. The quadrature detectors are represented by the two projections shown in green and blue. It is clear that if there was only one detector it would not be possible to determine the direction in which the magnetisation was precessing. Figure calculated in Mathematica™.

Disregarding relaxation, the bulk transverse magnetisation propagates according to $e^{i\omega t}$, which can be written as $\cos(\omega t) + i\sin(\omega t)$. Both real and imaginary components must be measured to separate $+\omega$ from $-\omega$. This is achieved by using two phase-sensitive detectors set 90° out of phase, such that one effectively measures the x-axis magnetisation and the other measures the y-axis magnetisation. A schematic bulk magnetic moment propagating in time is shown in Fig. 3-4, along with projections that represent the phase-sensitive detectors.

Referring back to §2.1, we know that the magnetisation is physically observable and proportional to an expectation value, either $\langle \hat{I}_- \rangle$ or $\langle \hat{I}_+ \rangle$. This might be alarming as for an individual spin we cannot know the magnetisation (quantised angular momentum) in the x and y directions simultaneously. However, the current in the coil is caused by the bulk magnetisation from the spin ensemble and hence this macroscopic property avoids violating Heisenberg's principle.

The signal can be calculated[10] by taking the trace of the scalar product

[10] See, e.g. Ref. [295, Eq. (2.15)].

between the density matrix and the appropriate[11] physical observable:

$$\begin{aligned} s(t) &= \left\langle \hat{I}_-^\dagger \,\middle|\, \hat{\boldsymbol{\rho}}^{\mathrm{rot}}(t) \right\rangle \\ &= \mathrm{Tr}\left[\hat{I}_+ \, \hat{\boldsymbol{\rho}}^{\mathrm{rot}}(t)\right] = \mathrm{Tr}\left[\hat{\boldsymbol{\rho}}^{\mathrm{rot}}(t) \, \hat{I}_+\right] \end{aligned} \tag{3-12}$$

In the following spin $I = 1/2$ example, the initial density matrix is set to $\hat{I}_x = \left[\begin{smallmatrix} 0 & 1/2 \\ 1/2 & 0 \end{smallmatrix}\right]$ and the Hamiltonian is only a frequency offset, $\hat{\mathscr{H}} = \Omega \hat{I}_z = (\omega_0 - \omega_{\mathrm{RF}})\hat{I}_z$. Propagation using Eq. (2-5) gives $\hat{\boldsymbol{\rho}}(t)$. Then taking the scalar product with the raising operator gives:

$$\hat{\boldsymbol{\rho}}^{\mathrm{rot}}(t) \, \hat{I}_+ = \begin{pmatrix} 0 & \frac{1}{2}\mathrm{e}^{-\mathrm{i}\Omega t} \\ \frac{1}{2}\mathrm{e}^{\mathrm{i}\Omega t} & 0 \end{pmatrix} \cdot \begin{pmatrix} 0 & 1 \\ 0 & 0 \end{pmatrix} = \begin{pmatrix} 0 & 0 \\ 0 & \frac{1}{2}\mathrm{e}^{\mathrm{i}\Omega t} \end{pmatrix} \tag{3-13}$$

Our quadrature detected signal is therefore, according to Eq. (3-12):

$$s(t) = \tfrac{1}{2}\mathrm{e}^{\mathrm{i}\Omega t} = \tfrac{1}{2}(\cos(\Omega t) + \mathrm{i}\sin(\Omega t)) \tag{3-14}$$

which is what we see in a complex oscillation—two signals separated in phase by 90°. These two signals are digitised at a sampling rate given by the required spectral width. To transform these complex signals into a spectrum we can apply a discrete-time Fourier transform operation.

3.6 Fourier Transform

The Fourier transform has a long history in NMR [99, 195] and has been covered extensively in textbooks, [1, p. 114], [150, Ch. 3.10], [107, Ch. II].

The signal is a digitised list of complex numbers, $s[n]$, where n goes from zero to the number of acquired points, TD. The discrete-time Fourier transform is then used:

$$S(\omega) = \sum_{n=0}^{TD-1} s[n] \, \mathrm{e}^{-\mathrm{i}\omega n} \tag{3-15}$$

As an ideal case we can use a signal, at frequency Ω, with relaxation rate $R = 1/T_2$. Such a signal is described by:

$$s(t) = \mathrm{e}^{\mathrm{i}\phi} \, \mathrm{e}^{\mathrm{i}\Omega t} \, \mathrm{e}^{-tR} \tag{3-16}$$

[11] We choose $\hat{I}_-$ which corresponds to $p = -1$ coherence. The expectation value is the transposed and conjugated detection operator, which in this case is $\hat{I}_-^\dagger = \hat{I}_+$. In §5.3, pNMRsim simulations are introduced where we have to specify a detection operator. Choosing `Ip` ($\hat{I}_+$) accomplishes the selection of $p = -1$ coherence [26, Eq. (17)].

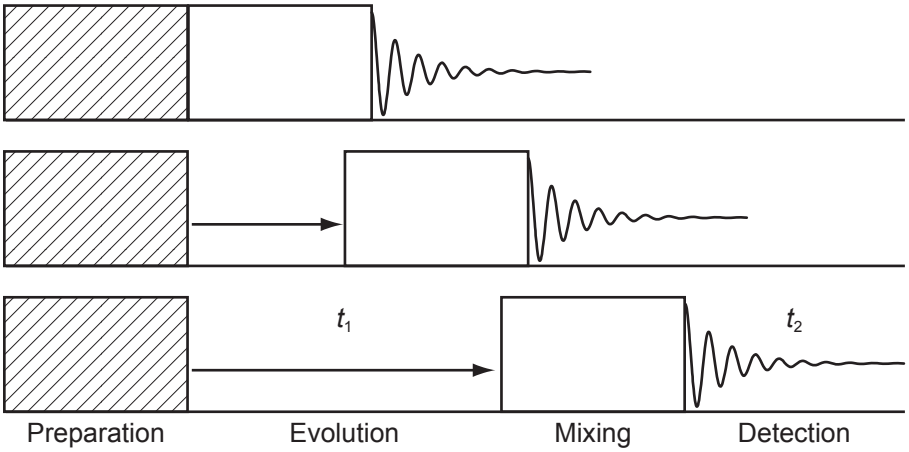

Figure 3-5. Defining times in a two-dimensional experiment. During the preparation time RF pulses and/or delays generate the desired coherences. These coherences evolve for variable time, t_1, which is incremented in a series of otherwise identical experiments. This forms what is called the *indirect* dimension. Further RF pulses and/or delays mix, or convert, the evolved coherences into a detectable coherence. This signal is then acquired during the second variable time, t_2, or *direct* dimension.

where $e^{i\phi}$ is an arbitrary phase factor.

Fourier transforming this ideal signal, where $\phi = 0$, yields a complex spectrum that comprises of two parts, historically termed absorptive and dispersive:

$$S(\omega) = \mathcal{A}(\omega) + i\mathcal{D}(\omega) \tag{3-17}$$

where

$$\begin{aligned} \mathcal{A}(\omega) &= \frac{R}{R^2 + (\Omega - \omega)^2} \\ \mathcal{D}(\omega) &= \frac{(\Omega - \omega)}{R^2 + (\Omega - \omega)^2} \end{aligned} \tag{3-18}$$

The lineshapes described by Eq. (3-18) are Lorentzian, centred at frequency Ω. The absorptive lineshape has a full-width at half-maximum of $2R = {}^{2}/_{T_2}$ (in $\mathrm{rad\,s^{-1}}$) $= {}^{1}/_{\pi T_2}$ (in Hz).

The arbitrary phase factor, caused by instrumental factors, has the effect of mixing the absorptive and dispersive components of $S(\omega)$. This is easily corrected by multiplying the signal by $e^{-i\phi}$, with the aim of obtaining a purely absorptive spectrum—a process referred to as *phasing*.

For two-dimensional (2D) experiments there are two periods of evolution, shown in Fig. 3-5. Ignoring phase factors and relaxation the form of the signal

is:

$$s(t_1, t_2) \propto \mathrm{e}^{\mathrm{i}\Omega_1 t_1}\, \mathrm{e}^{\mathrm{i}\Omega_2 t_2} \tag{3-19}$$

which Fourier transform to give a 2D spectrum:

$$\begin{aligned} S(\omega_1, \omega_2) &\propto (\mathcal{A}_1 + \mathrm{i}\mathcal{D}_1)(\mathcal{A}_2 + \mathrm{i}\mathcal{D}_2) \\ &\propto (\mathcal{A}_1\mathcal{A}_2 - \mathcal{D}_1\mathcal{D}_2) + \mathrm{i}(\mathcal{A}_1\mathcal{D}_2 + \mathcal{A}_2\mathcal{D}_1) \end{aligned} \tag{3-20}$$

The real part of this spectrum is a product of absorptive and dispersive components that cannot be separated by multiplying the signal with a corrective phase factor; it is a *phase-twisted* lineshape and shown in Fig. 3-6b. The $\mathcal{D}_1\mathcal{D}_2$ component has especially broad wings and therefore undesirably reduces spectral resolution. As mentioned in the introduction, there are two methods that extend the idea of quadrature detection to a second dimension. One method is termed time proportional phase increment (TPPI) and is described elsewhere [211]. The 2D spectra presented in this thesis use the States-Haberkorn-Ruben method, or "States" for short [287]. A prerequisite for this method is an *amplitude modulated* experiment, the hallmark of which is that both $+p$ and $-p$ coherences are allowed to evolve during t_1[12]. The t_1 duration along with other defining times in a two-dimensional experiment were given in Fig. 3-5.

The acquired signal of an amplitude-modulated experiment, ignoring relaxation, is similar to Eq. (3-19) but with two contributions from the t_1 evolution period:

$$s_{\cos}(t_1, t_2) \propto \left(\mathrm{e}^{\mathrm{i}\Omega_1 t_1} + \mathrm{e}^{-\mathrm{i}\Omega_1 t_1}\right) \mathrm{e}^{\mathrm{i}\Omega_2 t_2} = 2\cos(\Omega_1 t_1)\, \mathrm{e}^{\mathrm{i}\Omega_2 t_2} \tag{3-21}$$

Unlike Eq. (3-19) the modulation in t_1 is governed by a cosine term rather than a phase term—the spectrum is modulated in t_1 in amplitude rather than phase [54, §2.3.2]. Note that a Fourier transform of this signal will give purely absorptive lineshapes, but is unable to determine the sign of Ω_1 as only a single indirect detection has been used.

The pseudo-quadrature States detection appears when the whole experiment is repeated, with the preparatory portion (as defined in Fig. 3-5) phase-

[12] These coherences will propagate as $\mathrm{e}^{\mathrm{i}p\Omega t_1}$, which is accounted for by the choice of Ω_1.

shifted[13] by $e^{i\pi/2} = 90°$. The signal for this experiment is:

$$s_{\sin}(t_1, t_2) \propto \left(e^{i\pi/2}\, e^{i\Omega_1 t_1} + e^{-i\pi/2}\, e^{-i\Omega_1 t_1}\right) e^{i\Omega_2 t_2} = -2\sin(\Omega_1 t_1)\, e^{i\Omega_2 t_2} \tag{3-22}$$

Fourier transforming the t_2 dimension for each experiment gives:

$$\begin{aligned} s_{\cos}(t_1, \omega_2) &\propto \quad 2\cos(\Omega_1 t_1)\,(\mathcal{A}_2 + i\mathcal{D}_2) \\ s_{\sin}(t_1, \omega_2) &\propto -2\sin(\Omega_1 t_1)\,(\mathcal{A}_2 + i\mathcal{D}_2) \end{aligned} \tag{3-23}$$

which expresses two signals 90° out of phase and almost identical to Eq. (3-14), which described the quadrature-detected FID. To make Eq. (3-23) equivalent to Eq. (3-14) we can discard the imaginary parts ($i\mathcal{D}_2$) and reverse the sign of the sine component. Now we can set the real-only sine component to the "imaginary" channel, which is a neat trick that helps determine the sign of the frequency, Ω, in the indirect dimension. Thus:

$$\begin{aligned} s_{\text{total}}(t_1, \omega_2) &\propto 2\cos(\Omega_1 t_1)\,\mathcal{A}_2 + 2i\sin(\Omega_1 t_1)\,\mathcal{A}_2 \\ &\propto 2\, e^{i\Omega_1 t_1}\mathcal{A}_2 \end{aligned} \tag{3-24}$$

a final Fourier transform of the t_1 dimension gives:

$$S(\omega_1, \omega_2) \propto (\mathcal{A}_1 + i\mathcal{D}_1)\mathcal{A}_2 \tag{3-25}$$

The spectrum described by Eq. (3-25) has a real part that is purely absorptive and has the Ω-frequency sign-discriminated. A comparison of this, much narrower, lineshape to the phase-twisted lineshape described by Eq. (3-20), is presented in Fig. 3-6.

3.7 The Spin Diffusion Experiment

The spin diffusion experiment is the base on which the results of Ch. 7 stand. The origins of the term *spin diffusion* can be traced back to §5 of Bloembergen's 1949 article on spin-lattice relaxation [42]. However, the kind of spin diffusion covered in this thesis involves an exchange of magnetisation between inequivalent spins and is termed *spectral* spin diffusion. This is because the process can be considered as diffusion in frequency space [198, 289].

[13] Practically the phase-shift depends on the coherence order during t_1 evolution and is given by $90°/|p|$, but the receiver phase follows this (see §3.2) hence the acquired signal is always 90° out of phase as Eq. (3-22) shows.

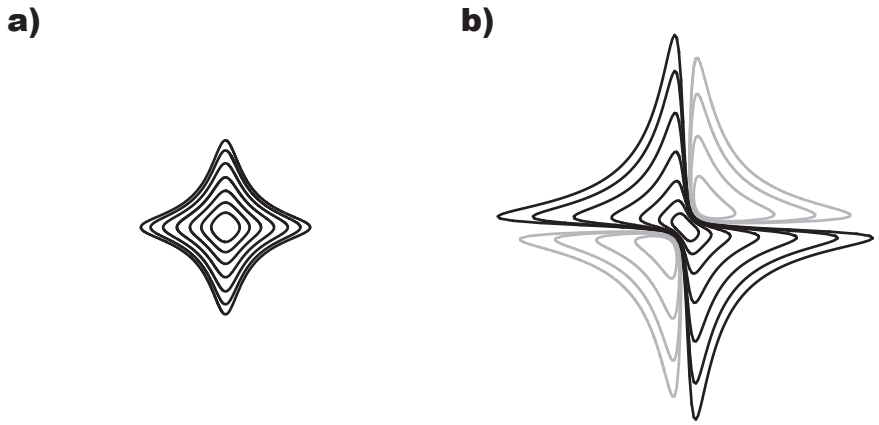

Figure 3-6. Real components of simulated 2D lineshapes recorded with; a) amplitude-modulation to obtain pure absorptive mode in both dimensions, b) single pathway (phase modulation) and complex 2DFT, which gives a phase-twist lineshape described by Eq. (3-20). Both lineshapes are plotted to the same scale with 200 Hz Lorentzian broadening. Contours increase by ×2 from a base of 3% of the maximum intensity.

Spectral spin diffusion can be used to obtain spatial proximity information in solids. This is similar to nuclear Overhauser effect spectroscopy (NOESY) in solution-state NMR, in fact, the pulse sequences are identical; cf. Fig. 3-7 and [151, Fig. 1]. However, it is the fast tumbling motion of the molecules in a liquid that cause the NOE—an incoherent relaxation phenomenon not found in solids [150, §5.12]. Another cause of spin diffusion that will not be pursued is chemical exchange, whereby an atom physically moves to another chemical site and in doing so has a different chemical shift but no magnetisation is actually transferred [199].

Spin diffusion requires some kind of energy conserving process if the magnetisation is to hop between spins. To explain this, first consider two degenerate transitions—overlapping spectral lines—and the flip-flop part of the dipolar Hamiltonian, $\left(\hat{I}^{+}\hat{S}^{-} + \hat{I}^{-}\hat{S}^{+}\right)$ given in Eq. (2-37). Magnetisation will oscillate between the nearby spins because it costs nothing to do so. However, if there are additional interactions then this oscillation may be strongly damped.

Now, if the two spins have different resonance frequencies then the flip-flop process is not energy conserving, therefore an additional source of energy has to be present to enable spin diffusion to continue [224]. These sources are many and varied, including: an abundance of strongly coupled high-γ nuclei

(proton-driven spin diffusion), a radio frequency field (RF-driven spin diffusion), macroscopic rotation (rotational resonance), any interaction (Λ) where the spin-part of the irreducible spherical tensor operator ($\hat{T}_\Lambda$) does not commute with the spin-part of the homonuclear dipolar coupling operator[14] ($\hat{T}_{20}$), multiple strong and non-coincident homonuclear dipolar couplings.

This last mechanism is responsible for broadening proton spectra [59, 330]. The effect on most other nuclei is negligible under MAS, but broadening can be seen for moderately high-γ nuclear species if sufficiently abundant, e.g. ^{11}B NMR spectra in Fig. 6-9. This broadening appears in 2D spin diffusion spectra as well and plays a part in driving the spin diffusion. Multiple noncommuting homonuclear couplings truncate the dipolar interaction by dominating the weak couplings between far-apart nuclei. This effect causes difficulty in quantitative distance measurements, even for three spin $I = 1/2$ nuclei [34].

Additional spin-diffusion mechanisms that can be disregarded for the remainder of this thesis include; molecular tumbling (applicable to liquids), CSA-driven (does not usually dominate in quadrupolar cases [93, 209]) and quadrupole-dipole interaction cross-terms[15] (typically small, but because of the presence of an isotropic component cannot be removed by spinning around any axis [19, 309]).

With an understanding of the various mechanics of spectral spin diffusion we can now introduce a 2D NMR experiment to probe this phenomenon. The pulse sequence and coherence transfer pathway diagram of the spin diffusion experiment is shown in Fig. 3-7. There are various phase-cycling schemes to achieve this coherence transfer pathway. Only two of the three pulses need to be phase-cycled. This can be achieved by phase-cycling the last two pulses and using TPPI [158, Tab. 1]. However, as the experiment is amplitude-modulated, States can be employed. A phase cycle where the first and third pulses are cycled instead of the latter two was used in this thesis. The phase cycle is given in Tab. A-2.

For application to half-integer quadrupolar nuclei, soft pulses are used and the system can notionally be thought of as fictitious spin $I = 1/2$ nuclei

[14] Given in Eq. (2-35)

[15] Cross-terms here are second-order entities and do not refer to the noncommutation of the quadrupolar and dipolar interactions separately.

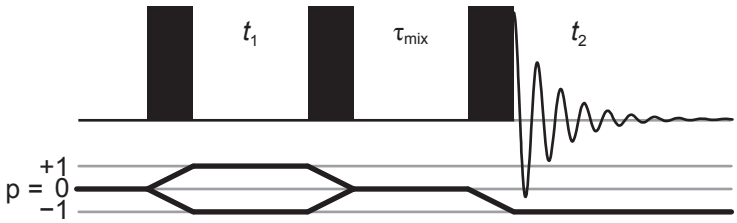

Figure 3-7. Pulse sequence and coherence transfer pathway diagram of the spin-diffusion (NOESY-like) experiment. See §3.7 for details.

[301]. Of course, the quadrupolar interaction is still present and may even be driving the spin diffusion, but multiple-quantum coherences do not need to be considered as they are not selected by the phase cycling. The spin diffusion experiment only correlates single-quantum with single-quantum and, contrastingly, we shall see below (§4.1) homonuclear correlation experiments that seek to correlate different quanta.

The first 90°-pulse in the sequence, and subsequent t_1 time, allows the single-quantum (SQ) magnetisation to precess at a characteristic frequency and is similar to the one-pulse experiment described in §3.3.1. The second 90°-pulse converts the SQ coherence into a population state. This state is maintained for a duration, τ_{mix}, called the mixing time, as it is during this period that the individual spins can exchange magnetisation. For zero mixing time it is expected that there will be no magnetisation exchange and for long mixing times it is expected that the magnetisation will reach an equilibrium between the different chemical sites. After the mixing time a third 90°-pulse is applied, the spins once again precess at their characteristic frequencies and a signal is detected. This procedure is repeated as many times as required to satisfy the phase-cycle with States and to acquire a suitable number of t_1 times for the indirect dimension.

After a Fourier transformation of both t_1 and t_2 time dimensions is performed, a 2D spectrum is obtained. Magnetisation that has not been exchanged will have precessed at the same characteristic frequency during both times, giving rise to a peak on the diagonal of the spectrum. Magnetisation that has been exchanged between chemically inequivalent sites will have precessed at one frequency during t_1 and another during t_2. A peak will appear off-diagonal in the spectrum and at the direct-dimension chemical shift of the spin where the mag-

netisation has finally resided. These two cases give rise to diagonal *auto-peaks* and *cross-peaks*, respectively [198].

Seeing a cross-peak in a spin-diffusion spectrum provides two pieces of information:

(i) Magnetisation has exchanged between chemically inequivalent sites that are close in space.

(ii) There exists an energy-balancing mechanism to allow such an exchange to occur.

Further information can be extracted about (i) by performing the spin diffusion experiment multiple times with varying mixing time. Integrating the cross-peak area and plotting as a function of mixing time yields a buildup curve, potentially containing information about the average distance between the spins[16]. But we know for $\tau_{\text{mix}} \gg T_1$ there will be no signal as the spin system will have fully relaxed and dephased. Such longitudinal relaxation will occur during the mixing time, affecting the whole signal. To produce a "normalised" buildup curve, the integrated cross-peak areas can be divided by the auto-peak areas. Then, for long mixing times before total dephasing, the magnetisation is seen to equilibrate between the spins, as expected from a stochastic diffusion process.

To be confident that the distance information obtained is accurate the cause of (ii) should be known. There are ways to help determine this cause. For example, if there are protons in the sample, does decoupling[17] reduce or remove the cross-peaks? If changing to different static magnetic field changes the rate of buildup then the CSA or second-order quadrupolar interaction might be the mechanism, rather than the first-order quadrupolar interaction that is not B_0 dependent [93, Tab. 1]. However, with a different field the spectral lines will be separated by a different frequency, which could cloud matters if rotational resonance is involved. Changing the spinning speed will also give information about this cause, but as nearly all the mechanisms depend on spinning speed the outcome may be tricky to interpret. As the dipolar interaction is

[16] This is theoretically true assuming no chemical exchange, otherwise the experiment measures kinetic rate constants.

[17] Disrupting the heteronuclear dipolar field using RF pulses.

coupling the spins we know that increasing the MAS rate will certainly affect the spin diffusion, with very fast MAS removing the interaction—and therefore cross-peaks—entirely. In a multiple noncommuting homonuclear dipolar coupled system, increasing the MAS rate will suppress the effective dipolar coupling monotonically. Therefore, if the buildup rate peaks at a certain spinning speed then the energy-balance mechanism at this point could probably be an incoherent resonance between an anisotropic interaction (e.g. quadrupolar) or a coherent resonance due to the rotation of the sample [259].

At a rotational-resonance condition the energy difference required[18] to balance the spin flip-flop is taken from the coherent mechanical rotation of the sample around the magic angle [224, §V.D]. Such conditions occur when the difference in isotropic chemical shift[19] is equal to an integer multiple of the spinning speed, i.e. $\Delta\delta_{\text{iso}} = n\nu_{\text{r}}$. The special case of $n = 0$ rotational-resonance corresponds to overlapping lineshapes. For the other conditions, $n > 0$, the behaviour of magnetisation transfer can be approximated as if the inequivalent spins were actually overlapping lineshapes.

The rotational-resonance conditions for dilute spin $I = {}^1/_2$ nuclei (e.g. ^{13}C nuclei) are comparatively narrow, $\sim 10\,\text{Hz}$ wide [66, Fig. 3]. Consequently, two lineshapes can be completely enveloped by the rotational-resonance condition and, in this case, rapid oscillatory exchange of longitudinal magnetisation occurs between the sites. The time evolution of the oscillation can be used for measuring internuclear distance (up to 5 Å) between the sites with considerable accuracy [314]. The method has aided structural characterisation of, amongst other compounds, an enzyme-inhibitor complex, a membrane protein structure and a receptor-bound neurotransmitter embedded in its native membrane environment [70, 220, 315].

If there are more than two peaks in the spectrum then it is likely that only two will fall under the rotational-resonance condition. For a 2D experiment this will enhance their respective cross-peak and without sensible interpretation such an enhancement could be misconstrued to mean these sites were much closer than they are in reality.

[18] In frequency units this is equal to the chemical shift difference.
[19] $\Delta\delta_{\text{iso}} = |\delta_{\text{iso},1} - \delta_{\text{iso},2}|$

Because of the narrowness of the rotational-resonance condition, second-order broadened half-integer quadrupolar lineshapes are unlikely to be completely covered by the condition. This either precludes the use of rotational resonance to deliberately enhance the spin diffusion between half-integer quadrupolar nuclei, or could lead to distorted cross-peaks. Nijman et al. proposed a method for using rotational resonance on half-integer quadrupolar nuclei whereby the MAS rate is swept to achieve a broader coupling condition [238]. They also note that only the central transitions of the coupled nuclei significantly contribute toward the magnetisation transfer, justifying the decision to use soft pulses in spin diffusion experiments.

There is a state in which half-integer quadrupolar nuclei are not second-order broadened; under DOR. In such an experiment the rotational-resonance effect could be fully used to enhance spin diffusion. However, changing the spinning speed to match the condition is severely limited by the narrow range at which the DOR outer rotor can spin (500 Hz to 2000 Hz). Reciprocally, the low spinning speed often entails that the homonuclear dipolar coupling is not fully averaged away and so spin diffusion proceeds at a swift rate, without the requirement for a rotational-resonance enhancement.

Spin diffusion experimental details are given in §5.2.3 and spectra can be found in Ch. 7.

3.8 The Multiple Quantum MAS Experiment

Definitively, a quadrupolar nucleus has more than two energy levels. This implies—according to Eq. (3-7)—that the spin of a quadrupolar nucleus can support a coherence order $p > 1$, termed *multiple quantum* coherence.

We have seen previously (§2.10.1) how quadrupolar nuclei can suffer from a second-order broadened central transition. Besides DOR, another method to remove this broadening is to use multiple quantum coherences to refocus the second-order quadrupolar interaction. Multiple quantum MAS (MQMAS) is a technique that operates under similar principles to the spin-echo (§3.4) experiment, which refocussed evolution under an offset. This refocussing effect is now put on a firm mathematical footing in terms of the spin interactions and

coherence order present under evolution and detection periods, specifically for an MQMAS experiment.

For example, consider the two-pulse sequence in Fig. 3-8. The range of coherence orders considered has been expanded to account for the increased number of energy levels available to, in this example, a spin $I = {}^3/_2$ nucleus. The first pulse prepares triple-quantum (3Q) coherence for the evolution time, t_1. The second pulse mixes the coherences for detection, physically constrained to be the SQ coherence $p = -1$. All coherences will be excited by the first hard pulse and a six-step[20] phase-cycle is employed to select only the evolution of the coherences of interest (± 3). The signal [Eq. (3-12)] depends on the Hamiltonian that has been propagated, according to Eq. (2-5). As we are under MAS conditions, consider just the Zeeman and second-order quadrupolar interactions. Referring to Fig. 3-8, there is a 3Q evolution time for duration t_1 and a SQ evolution time for t_2. In general, for half-integer quadrupolar nuclei, the signal will be:

$$s(t_1, t_2) \propto \mathrm{e}^{\mathrm{i}\omega^{(2)}_{m,-m} t_1}\, \mathrm{e}^{\mathrm{i}\omega^{(2)}_{m,-m} t_2} \tag{3-26}$$

where $\omega^{(2)}_{m,-m}$ is the frequency shift of the coherence order ($|\pm m\rangle \leftrightarrow |\mp m\rangle$) caused by the second-order quadrupolar interaction and is given in Eq. (2-62), which is $\propto \hat{\mathscr{H}}_{\mathrm{Q}}$. Explicitly:

$$\begin{aligned} s(t_1, t_2) \propto\; & \mathrm{e}^{\mathrm{i}\left(A^I_{3/2} Q^0 + C^I_{3/2} Q^4 d^4_{00}(\beta_{RL})\right) t_1} \\ & \times \mathrm{e}^{\mathrm{i}\left(A^I_{1/2} Q^0 + C^I_{1/2} Q^4 d^4_{00}(\beta_{RL})\right) t_2} \end{aligned} \tag{3-27}$$

where, assuming MAS and rotor synchronisation, the middle term containing d^2_{00} was averaged to zero after one rotor period and therefore not present in Eq. (3-27). The isotropic term, Q^0, will shift every crystallite equally and does not contribute to the broadening, but importantly, is not refocussed by the MQMAS-echo. The fourth-rank anisotropic term, Q^4, was given in Eq. (2-63) and for a certain η_{Q} and crystallite orientation, evaluates to a scalar. Since we are at the magic angle $d^4_{00}(\arctan\sqrt{2}) = -\frac{7}{18}$, evidently a scalar as well.

The scalar coefficients, $C^I_{3/2}$ and $C^I_{1/2}$ are given in Tab. A-1. These values are the key to refocussing the anisotropic broadening as they are the only portions in Eq. (3-27) that differ between the evolution and detection periods. The

[20] $\phi_1 = 0°, 60°, 120°, 180°, 240°, 300°$. $\phi_{\mathrm{R}} = 0°, 180°, 0°, 180°, 0°, 180°$.

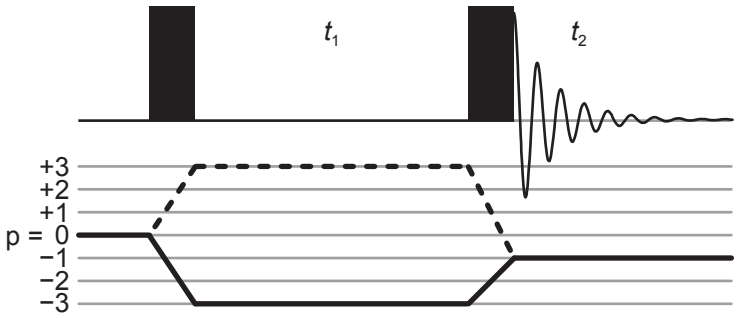

Figure 3-8. Pulse sequence and coherence transfer pathway diagram of an MQMAS experiment [221].

fourth-rank portion of Eq. (3-27), ignoring the factors d^4_{00} and Q^4, is:

$$s(t_1, t_2) \propto \mathrm{e}^{\left(C^I_{3/2} t_1 + C^I_{1/2} t_2\right)} \tag{3-28}$$

Evidently if $C^I_{3/2} t_1 = -C^I_{1/2} t_2$ the whole term would evaluate to unity and the anisotropic broadening would disappear. For a given t_1 duration this refocusing would appear at a time in t_2 given by:

$$t_2 = -\frac{C^I_{3/2}}{C^I_{1/2}} t_1 \tag{3-29}$$

For our example involving a spin $I = 3/2$ nucleus, $C^{3/2}_{3/2} = -3/20$ and $C^{3/2}_{1/2} = 27/140$, making the ratio $-7/9$. Substitution into Eq. (3-29) indicates that a refocussed echo will form when $t_2 = \frac{7}{9} t_1$. This example corresponds to the solid-line coherence transfer pathway in Fig. 3-8. Another solution exists indicated by the dotted line, which forms what is termed an *antiecho* at time $t_2 = -\frac{7}{9} t_1$, i.e. before the second pulse[21]. Consider another example, this time for a spin $I = 5/2$ nucleus. Looking up the coefficients in Tab. A-1 we find the ratio to be $19/12$—a different sign to the spin $I = 3/2$ case. In this case the echo and antiecho pathways in Fig. 3-8 are reversed and the refocussed echo forms at positive time $t_2 = \frac{19}{12} t_1$.

As the MQMAS-echo does not refocus isotropic terms, such as δ_{iso} and those $\propto Q^0$, inequivalent sites will be separated but appear unbroadened.

As higher-order spins can support higher-order quantum coherences it is possible to perform MQMAS experiments that evolve under these instead of the 3Q example presented above [8, 248]. There is a potential advantage in

[21] The antiecho can be recorded by adding a single-quantum spin-echo pulse after the MQMAS experiment.

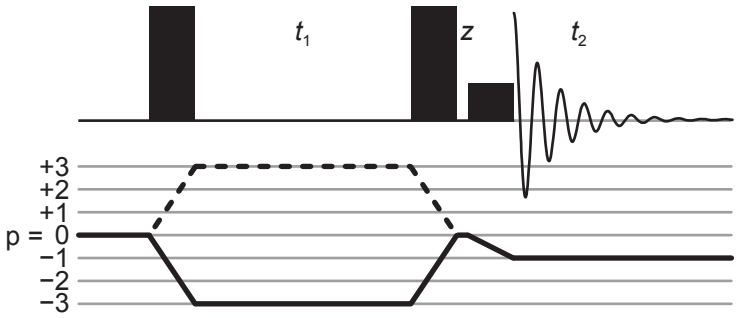

Figure 3-9. Pulse sequence and coherence transfer pathway diagram of an MQMAS experiment with a z-filter to provide amplitude-modulation. The first two pulses should use high-power RF for maximum 3Q excitation and conversion efficiency. The last pulse should be a selective 90°-pulse.

gaining resolution that must be weighed against the disadvantage of a sensitivity reduction involved in exciting these higher-order coherences.

Based on §3.5 we might expect to perform this experiment with States to give purely absorptive peaks in both dimensions because both $\pm p$ coherences are evolving during t_1. However, this is not the case as the coherence transfer pathways are asymmetric[22]. Two methods to obtain purely absorptive MQMAS spectra are to record the whole echo [58], or add a z-filter [285]. The pulse sequence for the latter method is shown in Fig. 3-9.

Using a z-filter achieves symmetric coherence transfer pathways, hence giving amplitude modulation and pure absorption-mode 2D lineshapes [10]. Further improvements in lineshape and sensitivity can be found by using rotor synchronised acquisition [214].

The spectral lineshapes in these 2D MQMAS experiments still contain the quadrupolar information in the broadened anisotropic direction. These lines appear angled on the spectrum, according to the ratio given in Eq. (3-29) [227]. If we wish to have the anisotropic direction parallel to the (direct) F_2-axis and the isotropic direction parallel to the (indirect) F_1-axis, then a shearing transformation must be performed [54, §6.1].

The split-t_1 approach circumvents the need for shearing by, as the name suggests, splitting the t_1 duration between MQ coherence evolution and SQ

[22] Generally, purely absorptive lineshapes would fail to be acquired due to the difference of efficiencies caused by the different change in coherence transfer, Δp. In the special case of using 3Q coherence on a spin $I = 3/2$ nucleus these efficiencies *can* be matched with carefully optimised RF power and tipping angle [9, Fig. 4A].

coherence evolution [56]. This allows the refocussing of the anisotropy to be fixed at $t_2 = 0$ for any value of t_1. The exact ratio of split duration and positions in the modified pulse sequence depend on the nuclear spin number, I, and which MQ coherence is being excited.

Since these founding efforts established robust pulse sequences for refocussing the second-order quadrupolar broadening, further development has been toward increasing sensitivity and resolution. To this end there are reports of using rotation-induced adiabatic coherence transfer (RIACT) to enhance 3Q↔SQ coherence transfer [323] by spin-locking the magnetisation [299]. Similarly, double frequency sweeps (DFS) can efficiently transfer 3Q→SQ coherences [147, 170] as can fast amplitude modulation (FAM) of pulses [200]. A rotary resonance between the RF field and the sample rotation has also been used to enhance 3Q preparation and mixing pulses in a scheme called FASTER-MQMAS [302]. Often these enhancement techniques can be used together [201]. For spectrometers supporting multiplex phase cycling [148] multiple coherence transfer pathways can be recorded at once and, suitably mixed, provide a signal enhancement [109]. Recently, comparisons of these—and other—techniques have been directly compared with regard to signal and resolution enhancement [162, 294].

As we have seen there are many variants of the MQMAS experiment and it would be helpful to introduce now the type used later in this thesis, which is an amplitude-modulated split-t_1 z-filtered 3QMAS with FAM. The pulse sequence is shown in Fig. 3-10 and the 96-step phase cycle can be found in the literature [58, Tab. A3]. The MQMAS spectrum is given in §6.3.3.

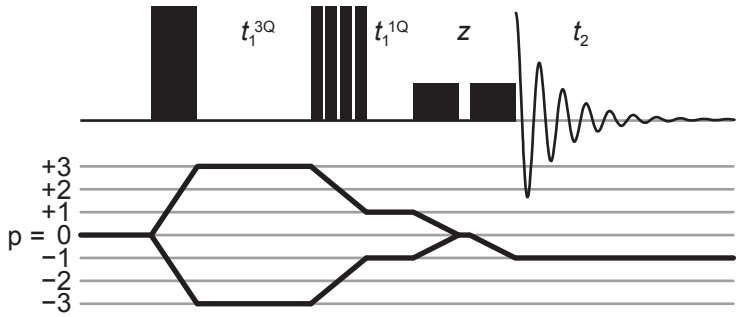

Figure 3-10. Pulse sequence and coherence transfer pathway diagram of an MQ-MAS experiment. This variant is amplitude-modulated split-t_1 z-filtered 3QMAS with FAM. As the coherence path lengths are symmetric the experiment is amplitude modulated. Split-t_1 experiments evolve during the t_1 dimension partly through 3Q coherence and partly through SQ coherence. This avoids having to shear the spectrum during processing as the isotropic dimension will already be parallel to F_2-axis. FAM provides efficient $\Delta p = \pm 2$ coherence transfer.

CHAPTER 4

Review of Correlation Experiments

> Knowledge is of two kinds. We know a subject ourselves, or we know where we can find information upon it.
>
> Samuel Johnson

NMR-active nuclei can be correlated via the dipolar (through-space) or the J (through-bond) interactions. Correlation between like isotopes is homonuclear, whilst dissimilar isotopes can have a heteronuclear correlation. Homonuclear correlation between half-integer quadrupolar nuclei is the main concern of this thesis. Correlation using the dipolar interaction is covered first. Edén has recently reviewed this field, with a focus on double-quantum dipolar recoupling [90]. In the concluding section, correlation using the J-coupling is examined, an area in which Amoureux et al. have reviewed the recent developments [11]. Although often involved in these experiments for half-integer quadrupolar nuclei, enhancement techniques (e.g. DFS, FAM, RAPT, HS) have been discussed in detail elsewhere [281].

4.1 Homonuclear Dipolar Correlation

4.1.1 Effect on 1D Spectra

Whilst perhaps not exactly a true correlation, the dipolar coupling strength between two half-integer quadrupolar nuclei can be found by examining their spectral lineshapes, in special cases. As we saw in §2.7.1 for an isolated pair of spin $I = 1/2$ nuclei, the dipolar coupling is perfectly removed by MAS after one rotor period; there will be no dipolar linebroadening. The quadrupolar case is different. Because the I_z^2 portion of the first-order quadrupolar interaction [Eq. (2-49)] does not commute with the $I^{\pm}$ portion of the dipolar interaction [Eq. (2-37)] the perfect removal of the dipolar interaction by MAS is thwarted. This noncommutation leads to a linebroadening as the quadrupolar interaction is reintroducing, or *recoupling*, the dipolar interaction that MAS would otherwise remove. Edén and Frydman noted that this type of dipolar recoupling is most prominent for overlapping lineshapes that have small C_Q and large Larmor frequencies [92]. Facey et al. also used first-order quadrupolar driven recoupling to measure ^{2}H–^{2}H distances by observing the broadening of MAS lineshapes [101]. However, care is needed when fitting lineshapes as several broadening mechanisms can act at once, not least the noncommutation of multiple homonuclear dipole interactions [34, §II]. An approach avoiding this pitfall is to observe the transfer of magnetisation rather than fit lineshapes. Gan was able to extract ^{2}H–^{2}H distances and tensor orientations for α-glycine via this method [108].

Linebroadening due to the dipolar interaction also affects the isotropic dimension in MQMAS experiments. This phenomenon has been used by Duer to gain structural information on Na_2SO_4 by simulating the high-resolution spinning sideband pattern [78]. Wi and Frydman developed the theory of heteronuclear and homonuclear dipolar coupling between quadrupolar spins and were able to simulate ^{11}B MQMAS spectra of various boron containing organic samples [309]. By comparing simulations to experiment, the dipolar coupling strength between the boron nuclei, and hence the distance, was found. In this case a diborane complex was chosen as it contains directly bonded boron nuclei as an isolated spin-pair.

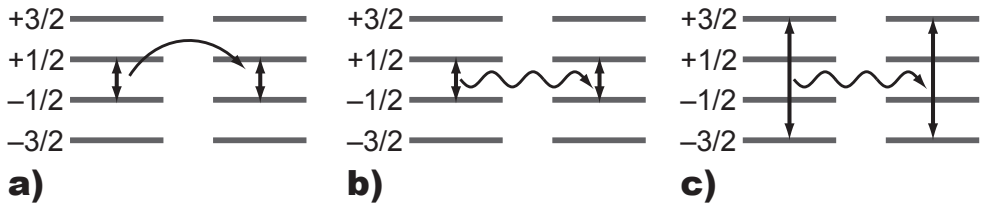

Figure 4-1. Schematic energy level diagrams to aid visualisation of homonuclear dipole correlation between two spin $I = 3/2$ nuclei; a) shows a single quantum transfer from one central transition to another, b) shows a double quantum coherence between two central transitions, c) shows a six quantum coherence between two outer satellite transitions.

4.1.2 Spin Diffusion

Under MAS, spin diffusion spectra that correlate SQ with SQ (schematically shown in Fig. 4-1a) will suffer from second-order quadrupolar broadening. However, by exciting triple-quantum for the t_1 evolution period, such that the coherence transfer pathway is $0 \rightarrow \pm 3 \rightarrow 0 \rightarrow -1$, the second-order quadrupolar interaction can be refocussed and the resulting cross-peaks will contain information on the relative tensor orientations between the coupled half-integer quadrupolar nuclei. Comparison with simulation to extract this information was first presented by Dowell et al. [74, 75] and then by Liu, Deng and Ding [191]. The report by Liu et al. investigates the effect of pulse strength, duration and MAS rate on spin diffusion, all of which have significant effect on the cross-peak lineshape determined by the quadrupolar tensor orientations. Various energy-conserving mechanisms were given in §3.7 and their understanding will now be cemented by a review of published experimental work.

Proton Driven

Recoupling the homonuclear dipolar interaction can be achieved by a strong heteronuclear dipolar field, such as an abundance of protons. Multiply connected dipolar couplings are not completely averaged to zero after a complete MAS rotation, but they will be suppressed. This means, like most recoupling mechanisms, proton driven recoupling is spinning speed dependent [93, Tab. 1]. This effect does not depend on the static magnetic field strength. Proton driven recoupling also has the advantage of optional suppression by decoupling techniques. Proton driven spin diffusion between spin $I = 3/2$ nuclei has been inves-

tigated [73, 191], used for tensor orientation information [74, 75] and locating bound ions (^{23}Na) in organic molecules such as a DNA quadruplex [265].

Off Angle MAS

Instead of finding mechanisms to reintroduce the dipolar interaction that magic-angle spinning removes, an ingenious solution is to not spin at the magic angle in the first place. This was first demonstrated as a suitable method of correlating half-integer quadrupolar nuclei by Hartmann, Jäger and Zwanziger [128]. Evolution during t_1 and t_2 times are at the magic angle but for the mixing time the rotor is switched away from 54.74° by 1°–25°. Joo, Werner-Zwanziger and Zwanziger call this method 2DAC for 2-dimensional anisotropy-correlated spectroscopy and have used it to observe spin diffusion in glassy and crystalline B_2O_3 [159]. Through comparison of the buildup rates they were able to measure the fraction of boron in boroxol rings in the glass to be $f = 0.66$—a topic discussed further in §6.1.3—thus demonstrating the potential of homonuclear correlation experiments to provide real structural information about disordered materials.

By combining spinning away from the P_2 magic angle with multiple quantum techniques, Ajithkumar and Kentgens devised a new experiment called MQP_4MAS [6, 7]. This involves spinning the sample at one of the angles at which $P_4(\cos\theta) = 0$, namely 30.56° or 70.12° to the static magnetic field. The fourth-rank second-order broadening caused by the quadrupolar interaction can then be removed without also removing the dipolar interaction that mediates spin diffusion. This method also fails to remove the CSA interaction which the authors argue can be used as an extra structural parameter. Ajithkumar, van Eck and Kentgens subsequently compare MQP_4MAS with a dynamic angle spinning (DAS) exchange experiment [7]. The advantage of the DAS experiment is that it does not require exciting multiple quantum coherences, so offers greater sensitivity at the cost of more specialised hardware.

Rotational Resonance

Recoupling the homonuclear dipolar interaction using coherent mechanical rotation was explained above in §3.7. As rotational resonance depends quite finely

on the exact chemical shift difference [66] its application to the broadened central transitions of half-integer quadrupolar nuclei might be curtailed. However, Nijman et al. recorded a 2D spin diffusion spectrum for ^{27}Al by using adiabatic-passage rotational-resonance recoupling [238]. This involved sweeping the MAS rate through the rotational-resonance condition to achieve a broader recoupling condition and a more complete transfer of magnetisation.

Simulations on the spin dynamics of quadrupolar nuclei at rotational resonance conditions were presented by Walls, Lim and Pines [303]. Depending on the relative magnitudes of the quadrupolar interaction strength and the spinning speed, different transitions contribute to the magnetisation transfer [18, §5.1]. For the common case where $\omega_{\mathrm{Q}} \gg \omega_{\mathrm{r}}$ only the central-transitions have significant magnetisation transfer $\left(\left|\pm\tfrac{1}{2}\right\rangle \leftrightarrow \left|\mp\tfrac{1}{2}\right\rangle\right)$.

Another important effect of rotational resonance can occur when a small magic-angle offset broadens the satellite transition peaks, thus changing the satellite transition rotational-resonance condition and leading to strong effects on line broadening, spin-echo dephasing and T_1 relaxation [180]. If a dipole-dipole homonuclear correlation technique requires effective dipole interaction removal by MAS, then precise setting of the magic angle can be critical if the results are to be meaningfully interpreted.

RF Driven

Spin-locking, or rotary resonance recoupling, involves a coupling between the energy changes caused by the physical rotation of the sample with the energy of a RF pulse, e.g. $\omega_{\mathrm{nut}} = n\omega_{\mathrm{r}}$ [27]. Theory and experiment of rotary resonance recoupling for half-integer quadrupolar nuclei were investigated by Wi et al., where they explored its use for dipolar recoupling [311, 312]. In 2005, Edén used symmetry-based techniques to recouple the dipolar interaction during the spin diffusion mixing time [91]. Many symmetry-based homonuclear dipolar recoupling sequences can be constructed from theory and the evaluation of such sequences can readily be found in the literature for spin $I = 1/2$ NMR [51]. Active recoupling transfers magnetisation substantially faster than would normally occur due to, say, quadrupolar driven recoupling.

Quadrupolar Driven

In the absence of more efficient energy-conversing mechanisms, the noncommutation of the quadrupolar and dipolar interactions will provide the energy balance needed to transfer magnetisation between spins [93, §2]. Whereas proton- or RF-driven transfers take a few ms, a hallmark of quadrupolar driven recoupling is that it can take up to 1000 ms for the magnetisation to reach equilibrium across the coupled spins [93, 236, 309].

Combining the three-pulse spin diffusion experiment with DOR has been demonstrated by Kentgens et al. for ^{23}Na in Na_2SO_3 [169, Fig. 6] and by Hung et al. for ^{27}Al to determine the crystal structure of an aluminium borate [139]. The SQ nature of these experiments is advantageous because of the higher sensitivity compared with exciting multiple-quantum coherences. Nevertheless, Edén, Grinshtein and Frydman obtained high-resolution homonuclear correlation spectra using an MQMAS sequence before the spin diffusion mixing time. The 2D MQMAS plus the τ_{mix} dimension makes this a pseudo-3D experiment [94].

4.1.3 Six Quantum Coherence and DQHDR

To be certain of observing a coherence that has been mediated by the dipolar interaction, it is sufficient to excite a $4I$ coherence [18, §5.1.3]. In the spin $I = 3/2$ case, this is a 6Q coherence as shown in Fig. 4-1c. Duer and Painter presented a $4I$ quantum filter experiment that consists of two pulses; one to excite the 6Q coherence and another to convert 6Q→SQ for detection [81]. The experiment is simple to use, interpret and using a 6Q coherence indicates correlation between two dipolar coupled spin $I = 3/2$ nuclei. In high-resolution applications, a 6Q coherence can be used as a dipolar filter, allowing only coupled nuclei to appear in the spectrum [205]. However, by using 6Q coherence, these techniques suffer from very poor signal-to-noise because of very inefficient 6Q excitation and conversion, therefore it is preferable to use lower-order coherences instead.

Double quantum homononuclear dipolar recoupling (DQHDR) correlates DQ coherence between two spins (Fig. 4-1b) with SQ coherence. When applied to quadrupolar nuclei it is important to be sure the DQ coherence is between

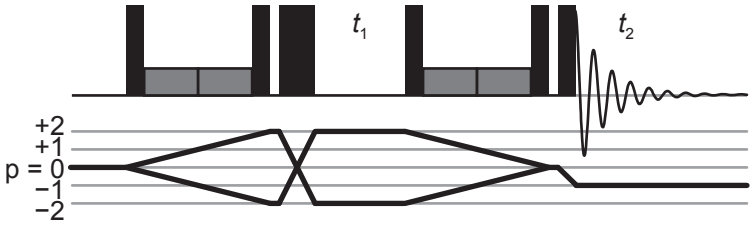

Figure 4-2. Pulse sequence and coherence transfer pathway diagram of a Double-Quantum Homonuclear Dipolar Recoupling experiment. Bracketed recoupling (spin-lock or symmetry based) fragments are used to excite and reconvert DQ coherence. A 180°-pulse, combined with phase-cycling, removes single-spin DQ coherences. A z-filter and selective readout pulse complete the sequence [204].

two nuclei and not on a single spin. Initial DQ techniques correlated SQ with DQ and relied on the fact DQ coherence excitation efficiency peaks for a certain pulse length. To avoid unwanted SQ coherence, a short period of free precession was included to filter out the broader SQ signal [242].

A pulse sequence for DQHDR is shown in Fig. 4-2. Note that with the inclusion of a selective 180°-pulse and judicious phase cycling the single-spin DQ coherences can be filtered out. This enables efficient homonuclear correlation of half-integer quadrupolar nuclei, no longer dependent on the inefficient excitation of $4I$ coherence.

Initially, spin-locking was used by Mali to excite and convert double quantum coherences for use in homonuclear dipolar recoupling experiments [203, 204]. However, spin-locking quadrupolar nuclei under MAS is particularly tricky [22]. Symmetry-based pulse fragments have been shown to be more efficient at DQ excitation and conversion and are now commonly used in DQHDR experiments [89, 95, 96, 193, 206, 304]. DQHDR has been combined with a 6Q filter by Mali and Kaučič for improved resolution [205]. More recently Brinkmann et al. have implemented the DQHDR sequence under DOR [50].

4.2 *J*-Coupling Correlation

4.2.1 Heteronuclear

Since its discovery and explanation in the 1950s [120, 261], *J*-couplings have commonly been used in solution-state NMR to detect connectivities between

unlike nuclei. In solid-state NMR, the detection of J-couplings involving half-integer quadrupolar nuclei is not so common, an early example being in 1982 [225]. Massiot et al. have recently reviewed J-coupling in solid-state NMR [216], noting that while there are numerous experiments involving one quadrupolar nucleus and one spin $I = 1/2$ nucleus, very few are between two quadrupolar nuclei.

Detection of J-coupling can be in the form of a visible lineshape splitting [327], especially if high-resolution techniques are used [322]. However, the high-resolution techniques make second-order isotropic shifts due to cross-terms more significant [19]. Detection can also be accomplished by extracting a modulation caused by the J-coupling upon a spin-echo dephasing curve, as shown by Hung et al. for $J_{^{13}C^{17}O}$ and $J_{^{15}N^{17}O}$ [141].

True 2D correlation experiments involving J-couplings are often based on either the J-HMQC (through-bond multiple-quantum correlation) [186] or INEPT (insensitive nuclei enhanced by polarisation transfer) [292] techniques developed for spin $I = 1/2$ nuclei. The study of the product operators for this class of experiment involving spin $I = 3/2$ nuclei [113, 293] assisted the development of experiments correlating spin $I = 1/2$ and half-integer quadrupolar nuclei [12, 163, 215, 313]. Despite issues of resolution and sensitivity, through-bond heteronuclear correlations have been performed between two half-integer quadrupolar nuclei, specifically ^{27}Al and ^{17}O [146, 184, 217]. Previously, before these true 2D methods were developed, researchers had compared MQMAS experiments to simulation to "detect" a $J_{^{11}B^{75}As}$-coupling of 650 Hz [310].

4.2.2 Homonuclear—Solution-State NMR

Homonuclear J-coupling has long been observed in liquids through the splitting of spectral lines, regardless of spin number. In 1971, Odom, Ellis and Walsh measured $J_{^{11}B^{11}B}$ in B_5H_9 to be $19.4\,\text{Hz} \pm 0.2\,\text{Hz}$ directly from the NMR spectrum [239]. Anderson et al. executed a study on linked polyhedral boranes and measured $J_{^{11}B^{11}B}$ in $[B_5H_8]_2$ to be $\simeq 150\,\text{Hz}$ [13]. However, this is a rather large ^{11}B–^{11}B J-coupling and most studies measure the boron J-coupling in other compounds to be considerable less. For tetrachlorotetraborane, the spectral

splitting is absent, which, combined with knowledge of relaxation times and the linebroadening of ^{10}B, led to a result that $J_{^{11}\mathrm{B}^{11}\mathrm{B}}$ is around 3.0 Hz to 7.5 Hz in this compound [166]. There are many additional reports of boron–boron J-couplings in the literature [213, Ch. 8 §3.3][262].

Correlation spectroscopy (COSY) makes use of 2DFT methods to correlate nuclei through-bond, in direct analogue with how the NOESY experiment correlates nuclei through-space. Goodreau and Spencer have presented several ^{11}B–^{11}B COSY spectra revealing the J-coupling in phosphapentaboranes [117]. Clearly, ^{11}B–^{11}B J-coupling in some compounds is straightforward to detect in solution-state NMR.

Another experiment for detecting nuclei that are connected through-bond is termed the incredible natural abundance double quantum transfer experiment (INADEQUATE) and was reported in 1980 by Bax, Freeman and Kempsell [33]. By cleverly suppressing the overpowering signal from solitary ^{13}C nuclei they were able to observe the J-coupled ^{13}C–^{13}C signal. Nowadays, phase-cycling to select a DQ coherence is routine and the INADEQUATE experiment has enjoyed great success in many forms, both in solution- and solid-state NMR for spin $I = 1/2$ nuclei [119]. To date, there have been no reports of a successful implementation of an INADEQUATE experiment for half-integer quadrupolar nuclei.

4.2.3 Homonuclear—Solid-State NMR

Spin $I = 1/2$

Solid-state NMR INADEQUATE experiments use MAS to remove the homonuclear dipolar coupling to detect J-couplings between isolated spin pairs. Under these conditions Fayon et al. measured $^2J_{^{31}\mathrm{P}^{31}\mathrm{P}}$ in crystalline and amorphous samples, providing clear structural information and noting that the disorder does not affect the efficiency of the experiment [103]. This is an important conclusion for those seeking through-bond correlations in disordered materials. Spin-echo experiments have been used for many years to measure J-couplings, also under MAS to remove the dipolar coupling. The solid-state NMR literature has reports of ^1J and ^2J values alike, such as $^1J_{^{15}\mathrm{N}^{15}\mathrm{N}} = 12\,\mathrm{Hz} \pm 1\,\mathrm{Hz}$ in a fully

labelled organic compound[1] [57]. Unlike solution-state NMR, solid-state NMR can also measure J-coupling between chemically equivalent sites [62, 82].

As the theory of J-coupling is well understood, first principles calculations can be performed to determine the strengths of J-coupling in heteronuclear and homonuclear cases for spin $I = 1/2$ and quadrupolar nuclei alike [160].

Quadrupolar

There have been very few reports of homonuclear J-coupled quadrupolar nuclei in solid-state NMR [18, §6]. This contrasts strongly with the plentiful $J_{^{11}\mathrm{B}^{11}\mathrm{B}}$ reports found in solution-state NMR [213, Ch. 8].

Hung et al. have recently reported a $^2J_{\mathrm{OO}}$-coupling of 8.8 Hz ± 0.9 Hz in ^{17}O-labelled glycine·^{2}HCl, which was determined by fitting a spin-echo dephasing curve with an appropriate J-modulated decay function [141]. A spin-echo experiment in nuclear quadrupole resonance (NQR) of As_2S_3 has also seen modulations, in this case from $^2J_{^{75}\mathrm{As}^{75}\mathrm{As}}$-coupling [307]. As NQR is static the dephasing curve should be strongly affected by the dipolar coupling, but in this instance $|b_{jk}/2\pi| < 100$ Hz, whereas the ^2J-coupling was measured to be 122 Hz to 250 Hz. Wi and Frydman simulated the MQMAS spectrum of a bispinacolate diborate complex, simultaneously obtaining the quadrupolar parameters, tensor orientations and a $^1J_{^{11}\mathrm{B}^{11}\mathrm{B}}$-coupling of 85 Hz ± 20 Hz [309]. They performed the same treatment for a spin $I = 5/2$ nucleus, ^{55}Mn, in dimanganese decacarbonyl to obtain a $^1J_{^{55}\mathrm{Mn}^{55}\mathrm{Mn}}$-coupling of 65 Hz ± 5 Hz.

There are experiments that succeed in detecting homonuclear J-coupling by first relaying the through-bond magnetisation via an intermediate spin $I = 1/2$ nucleus. This homonuclear-heteronuclear single quantum correlation experiment (H-HSQC) was reported by Deschamps et al. in 2008 and consists of back-to-back INEPT sequences [71]. Deschamps et al. used H-HSQC to correlate ^{27}Al–^{27}Al via $^2J_{^{27}\mathrm{Al}^{31}\mathrm{P}}$–$^2J_{^{31}\mathrm{P}^{27}\mathrm{Al}}$, showing that small J-couplings do persist in MAS NMR. The H-HSQC experiment was naturally extended by Dechamps and Massiot to three-dimensions by adding an additional evolution time to encode the ^{31}P isotropic dimension [72]. The extra information gained comes

[1] N-({[5-(phenylamino)methylene]-1, 3-cyclopentadien-1-yl} methylene)-1,2,4-triazole-4-amine.

at the price of greatly extended experimental duration. Hu, Amoureux and Trébosc proposed a new, shorter, experimental methodology they call two-dimensional indirect covariance (2D-IC) [137]. This approach is even more obviously not a true homonuclear correlation experiment because the technique is to generate a homonuclear spectrum from a heteronuclear one. In their article, they use a MQ-filtered refocused INEPT sequence to correlate ^{27}Al–^{31}P before generating a ^{27}Al–^{27}Al correlation spectrum.

These latter techniques do indeed correlate J-coupled quadrupolar nuclei in solid-state NMR, but if there are no intermediary spin $I = 1/2$ nuclei to relay the magnetisation the experiments will fail. The spin-echo technique seems to be the most robust for the detection of direct quadrupole–quadrupole J-coupling. However, there are a notable lack of reports in the solid-state NMR literature. Important questions remain, such as; why can solid-state NMR readily detect $^{2}J_{^{31}\mathrm{P}^{31}\mathrm{P}}$ but not $^{2}J_{^{11}\mathrm{B}^{11}\mathrm{B}}$?

A tentative answer might be that most of the compounds examined so far have naturally small J-couplings and that, even under MAS, the residual dipolar coupling is causing rapid dephasing—too fast to reliably extract J-modulation from a spin-echo curve. With the ability to calculate J-coupling strengths from first principles we can show that previous negative results are due to J-couplings being undetectably small. We can also search for compounds to study that should have significant J-coupling strength, such as the small molecules studied by Wi and Frydman. However, this latter approach will not particularly assist the immediate search for homonuclear correlation of disordered materials, such as technologically useful glasses.

CHAPTER 5

NMR Experiment and Simulation Details

SSNMR spectroscopists do it at the magic angle

5.1 NMR Experimental Hardware

Cutting-edge nuclear magnetic resonance research, capable of studying atomic structures, characterising chemicals and discovering dynamic processes, is an expensive enterprise. The superconducting cryomagnets that are used to create very strong and highly homogeneous magnetic fields can cost over £1 000 000. Spectrometer consoles, which synthesize and amplify RF pulses with nanosecond timing of duration and phase, typically cost over £100 000. Another costly component is the probe that fits in the bore of the magnet, containing a delicate nest of electronics and pneumatics to deliver high-power RF to the sample whilst it rapidly rotates at speeds up to 2×10^6 rpm.

The technology, engineering and physical principles that have gone toward designing such equipment is extremely interesting and there are numerous texts on every aspect. Unfortunately it is beyond the scope of this thesis to

Table 5-1. Static magnetic field strengths with associated proton and boron Larmor frequencies and specific spectrometer consoles used. $\gamma(^1\mathrm{H}) = 26.752\,212 \times 10^7\,\mathrm{rad\,s^{-1}\,T^{-1}}$, $\gamma(^{11}\mathrm{B}) = 8.584\,704 \times 10^7\,\mathrm{rad\,s^{-1}\,T^{-1}}$ [126].

B_0 in T	$\nu_0(^1\mathrm{H})$ in MHz	$\nu_0(^{11}\mathrm{B})$ in MHz	Console
7.05	300.09	96.30	Varian Infinityplus
11.74	500.01	160.45	Bruker Avance III
14.09	599.98	192.53	Bruker Avance II+
14.10	600.14	192.58	Bruker Avance III[a]

[a]Located at the University of St Andrews

present even the most fascinating facet of this area. Instead, for a general introduction to NMR hardware, the following general references are given, in reverse chronological order; [150, Ch. 3], [187, Ch. 4], [197, Ch. 3], [107, Ch. IV], [127, Ch. 2].

5.1.1 Magnets and Consoles

^{11}B solid-state NMR experiments were carried out at static magnetic field strengths of 7.05 T to 14.10 T and on various spectrometers, listed in Tab. 5-1. Probe-specific room temperature shims were used to ensure optimal magnetic field homogeneity. $\lambda/4$ cables were RF matched for maximum signal sensitivity. All NMR experiments were performed at room temperature.

Referencing

^{11}B chemical shifts were calibrated using boron phosphate, BPO_4, (−3.6 ppm) or sodium borohydride, $NaBH_4$, (−42.06 ppm) as secondary references [131]. The primary reference for ^{11}B is boron trifluoride diethyl etherate, $BF_3{\cdot}Et_2O$ [126].

5.1.2 Solid-State NMR Probes

MAS experiments were performed using Bruker wide-bore 3.2 mm or 4 mm MAS probes. DOR experiments at 14.1 T used a Samoson-built probe. Some probes use boron-nitride stators, which give a boron background signal if not refocussed. For these spectra the background was removed by subtracting the signal

from an empty rotor. The high-Q RF circuit contained in the probe was tuned to a specific frequency corresponding to the Larmor frequency of the desired isotope for a given static magnetic field. The frequencies for ^{1}H and ^{11}B are given in Tab. 5-1. Tuning was achieved by slightly varying the capacitance of the circuit, the effects of which were visible as a absorption peak of reflected power on a network analyser. The capacitance of the RF circuit was then fine-tuned *in situ* by minimising the power reflected back from the probe during a pulse, using an in-line directional coupler connected to an oscilloscope. For experiments involving spinning, pressurised dried air was used from a storage tank; to damp pressure waves from the air compressor. For MAS, the spinning speed was detected optically and regulated by Bruker spinning-speed controllers, with typical pressures for a 4 mm rotor to spin at 10 kHz being $\simeq 3 \times 10^5$ Pa for the bearing and $\simeq 1 \times 10^5$ Pa for the drive. These automatic units allow precise and stable (± 1 Hz) spinning speeds to be achieved almost indefinitely. For DOR the spinning speed was detected part-optically, part-acoustically and also computer controlled.

5.1.3 Sample Preparation For NMR

Hygroscopic samples (see §6.2) were kept in a vacuum desiccator until required. The samples were then finely ground in either a porcelain or agate mortar and packed into a zirconia rotor with a Kel-F®[1] cap. Once packed the samples are protected from atmospheric moisture. Proton NMR revealed negligible signal from a sample packed over two years previously.

5.2 Pulsed Experiments

Computer software controlling the spectrometers were Spinsight and TopSpin for Infinityplus and Avance spectrometers, respectively. Both spectrometer control software programs allow precise ns-control of RF amplitudes, phase and duration, giving infinite flexibility for "spin-engineering". The saturation spin-echo (SATSE, see §5.2.5) experiment was self-written for Infinityplus and Avance spectrometers. All other pulse sequences were pre-programmed.

[1] Polychlorotrifluoroethylene

5.2.1 Spin-Lattice Relaxation—T_1

Measuring the T_1 time can be achieved by several experiments [100, §4.6.1]. The saturation-recovery experiment was explained above in §3.3.

^{11}B MAS NMR saturation-recovery experiments were performed at 14.1 T on vitreous and polycrystalline lithium diborate (see §6.2), containing no paramagnetic doping, to determine their respective T_1 times. Ninety-nine hard pulses 1 µs apart were used for the pulse comb, followed by a variable relaxation delay and a further hard pulse to convert the current population state to an observable coherence. The pulse duration used was 0.8 µs. The spectral width was rotor-synchronised to 10 kHz. The relaxation time was doubled between experiments, ranging from 10 ms to 81.92 s for the glass sample and 40 ms to 81.92 s for the crystalline sample. The results are presented in §6.4.

90°-pulse-recovery experiments were performed on copper- and cobalt-doped polycrystalline lithium diborate at 11.74 T. The solid-90° pulse duration was 4.65 µs giving $\nu_{\text{nut}} = 61.5$ kHz. The spectral width was rotor-synchronised to 10 kHz. The relaxation time was doubled between experiments, ranging from 0.1 ms to 409.6 s for the cobalt-doped sample and 0.1 ms to 3276.8 s for the copper-doped sample. A recycle delay of 70 s or 360 s was used for the cobalt- and copper-doped samples respectively. The results are presented in §6.4.

5.2.2 MQMAS

Based on the theory explained in §3.8, the MQMAS pulse sequence shown in Fig. 3-10 was performed on polycrystalline barium diborate. The excitation pulse was optimised starting from a hard 270°-pulse. The FAM pulse duration, number of FAM cycles and z-filter pulse duration were subsequently optimised. The spectrum and further experimental details are given in §6.3.3.

5.2.3 Spin Diffusion

The spin diffusion experiment was introduced above in §3.7. Two-dimensional spin-diffusion ^{11}B MAS spectra were recorded using the pulse sequence shown in Fig. 3-7. Unless otherwise stated all spin diffusion spectra were recorded on polycrystalline lithium diborate, $Li_2O{\cdot}2B_2O_3$, under the following conditions.

Experiments were performed in a rotor-synchronised fashion, that is, the spectral width was set equal to the MAS frequency in both dimensions. Incorrect baseline correction can lead to baseline roll, which manifests itself as small positive or negative intensity at frequencies outside the lineshape regions. An 8-step phase cycle was used, as shown in Tab A-2, to select $\Delta p = \pm 1$ on the first 90°-pulse and $\Delta p = -1$ on the last 90°-pulse. Sign discrimination was achieved in the F_1-dimension using the States method [287]. The magic angle was set with KBr or deuterated oxalic acid. The transmitter frequency was placed at 6 ppm—between the two peaks in lithium diborate. Soft pulses were used, $\nu_{\text{nut}} \simeq 6$ kHz. The recycle delay was 28 s. In t_2, 512 points were acquired with a digital filter, co-adding 8 transients for each of 256 t_1 slices. Both dimensions were Lorentzian broadened by 20 Hz. The spectra were plotted with 8 contour levels starting at 2% of the maximum intensity and increasing by a factor of 1.75 between adjacent contours.

A diverse selection of spin diffusion spectra are presented in Ch. 7, at different fields, MAS rates, mixing times and isotopic enrichments. DOR spin diffusion spectra recorded by Dr Ivan Hung at 14.1 T are presented in §7.3. The outer magic-angle rotor rate was 1.5 kHz, the inner rotor rate was 5 kHz, the spectral width was 10 kHz in both dimensions, moderately soft 3.75 µs pulses were used and the recycle delay was 2 s. In t_2, 512 points were acquired with a digital filter, co-adding 32 transients for each of 512 t_1 slices. Odd-ordered sidebands were suppressed [269]. The spectra are plotted with 8 contour levels starting at 40% of the maximum intensity and increasing by a factor of 1.14 between adjacent contours.

5.2.4 DQHDR

Double quantum homonuclear dipolar recoupling was introduced above in §4.1.3 and a pulse sequence and coherence transfer pathway diagram was shown in Fig. 4-2. DQHDR was performed with the assistance of Dr Ivan Hung on vitreous and polycrystalline lithium diborate, at 14.1 T and 10 kHz MAS rate. The spectral widths were rotor synchronised in both dimensions. Selective 90°-pulses of 22 µs duration bracketed the dipole-interaction recoupling spin-locks.

A suitable weak spin-lock was found by optimising the RF power level. The mixing duration lasted one rotor period. The selective 180°-pulse was twice the duration of the selective 90°-pulse. A 10 ms z-filter duration was used. The States method achieved sign discrimination in the indirect dimension.

For the glass the recycle delay was 1.5 s. In t_2, 256 points were acquired, co-adding 32 transients for each of 64 t_1 slices.

For the crystal the recycle delay was 15 s. In t_2, 256 points were acquired, co-adding 48 transients for each of 128 t_1 slices.

Both dimensions were Lorentzian broadened by 50 Hz. The spectra are plotted with 8 contour levels starting at 5.6% of the maximum intensity and increasing by a factor of 1.5 between adjacent contours. The results are presented in §7.6.

5.2.5 Spin-Echo Coherence Dephasing—T_2'

^{11}B MAS NMR spin-echo experiments were carried out at 14.1 T on polycrystalline lithium diborate of varying ^{11}B isotopic abundance and MAS rate. The samples contained no paramagnetic doping.

The measurement of the coherence dephasing time required multiple experiments with varying durations of rotor-synchronised dephasing time, $\tau/2$. Plotting peak integrated intensity against τ and fitting the results to Eq. (3-10) determined the T_2' time. For this measurement to be accurate, each experiment must start from the same initial conditions. With crystalline materials the T_1 time is inconveniently long, as we shall see in §6.4. Repeating the experiment faster than approximately $5\times T_1$ distorts the spin-echo dephasing curve, leading to inaccurate measurements of T_2', as the starting bulk magnetisation would be different for each experiment. As the usual route of letting the system fully relax between pulses would take too much time and the signal from ^{11}B is strong enough to detect even from a 25% relaxed[2] sample, the spin-echo pulse sequence was modified by adding a pulse comb. This pulse sequence is shown in Fig. 5-1 and herein termed SATSE.

The SATuration-Spin-Echo experiment uses a pulse comb to saturate the

[2]Corresponding to $0.3\times T_1$

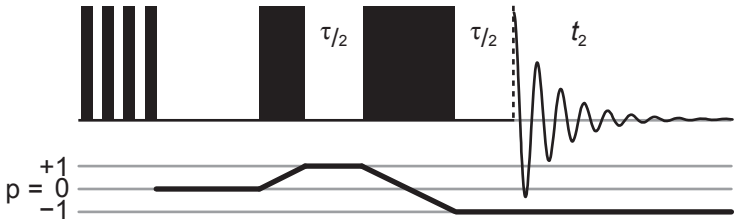

Figure 5-1. Pulse sequence and coherence transfer pathway diagram of the saturation spin-echo experiment. Following a pulse comb (to saturate the magnetisation) and consistent recycle delay, a 90°-pulse excites a SQ coherence state. After a duration of $\tau/2$, a refocusing 180°-pulse is applied and a spin-echo forms: detection starts $\tau/2$ after the refocusing pulse, coinciding with the echo top. By repeating the experiment with varying τ duration, the transverse decoherence can be studied. Note that $\tau/2$ needs to be rotor-synchronised and will be of the order of ms, whereas the RF pulses are much briefer, $\sim$ µs.

magnetisation; the energy levels become equally populated and no bulk magnetisation exists for this spin species. The system then relaxes for a fraction of the T_1 time before the 90°—$\tau/2$—180°—$\tau/2$ echo sequence begins. This ensures each echo experiment starts from the same initial conditions so comparing intensities between experiments is meaningful.

A 16-step nested phase cycle was used [179], as shown in Tab. A-3. The first pulse selects $\Delta p = +1$ with a 4-step cycle. This also selects $\Delta p = -3$, but with a short pulse length and low ν_{nut}, 3Q excitation efficiency will be very low. The second pulse selects $\Delta p = -2$, also with a 4-step cycle. Technically, the $\Delta p = +2$ coherence transfer is also selected, but realistically the tiny 3Q coherence will undergo an inefficient conversion to the observable SQ coherence as 3Q→SQ conversion-pulse lengths are optimal for <90°, not 180°, tipping angles in the case of spin $I = 3/2$ nuclei [8].

For the results presented in Ch. 8, thirty-three hard pulses 11 µs apart were used for the saturation comb, followed by a relaxation delay of 32 s. Hard pulses had 90°-pulse duration of 2.1 µs giving $\nu_{\text{nut}} = 120$ kHz. The soft 90°-pulse duration was 12.5 µs, half the refocusing 180°-pulse duration, giving $\nu_{\text{nut}} = 20$ kHz. The spectral width was 50 kHz. Spectra were baseline corrected before integration. Transients were acquired with a digital filter and co-added 96, 384 or 640 times for 100%, 25% and 5% ^{11}B samples, respectively. The $\tau/2$ durations were integer multiples of the rotor period, which avoids the unwanted introduction of modulation from chemical shift anisotropy [240]. If the magic angle is

mis-set even by ≈0.5° the T_1 and T_2' times will be increased for lineshapes at the $n = 0$ rotational resonance [180]. The magic angle was set as accuractely as possible by maximising the number of spinning sidebands of KBr.

5.3 Simulation

Computer simulations have long been used to model all manner of physical systems. In NMR, the Hamiltonians that describe the energy of a nuclear spin system are very accurately known [283]. By propagating these Hamiltonians on an initial density matrix the state of the spin system at any point in the future can be determined [86]. This principle was described generally in §2.1.

The size of the initial density matrix depends on the spin, I, and number, n, of coupled nuclei, such that the matrix will consist of $(2I+1)^n \times (2I+1)^n$ elements. For example, four ^{11}B nuclei are described by a 256×256 matrix with 65 536 elements. If an extra ^{11}B nucleus is added to the system, the number of matrix elements jumps to over a million. Hence, the size of system these simulations can model is limited by current computational resources.

SIMPSON is an open-source program for accurate numerical simulation of solid-state NMR experiments. SIMPSON has been in serious academic use for over a decade and thoroughly tried and tested by the NMR community [26]. However, for large systems, especially those involving quadrupolar nuclei, SIMPSON can be inefficient.

pNMRsim performs mostly the same tasks as SIMPSON, but often significantly faster [132]. However, as this modern software is still being improved upon, all important results are cross-checked against SIMPSON.

Both simulation programs can model spinning systems, used commonly for MAS simulations [87]. Vitally, the programs can repeat the calculations with different angles between the spin system and the static magnetic field [88]. This approach corresponds to the powder average seen in solid-state NMR experiments. The simulations were powder-averaged according to the ZCW scheme [65, 67, 328]. Broader lineshapes require that more crystallites are calculated to accurately simulate the experimental lineshape, thus taking longer to compute. The simulation programs take an input file specifying the spin

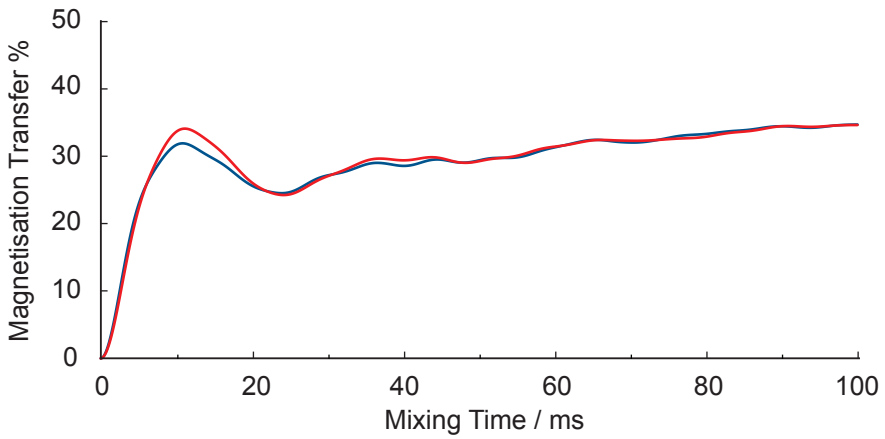

Figure 5-2. Buildup curve simulation comparing different detection matrices in pNMRsim. Two spin, 1st order, $I = 3/2$, $\omega_r/2\pi = 10\,\text{kHz}$, $\Delta\delta_{iso} = 0$, CSA $= 0$, $C_Q = 2560\,\text{kHz}$, $\eta_Q = 0$, $b_{jk}/2\pi = -1\,\text{kHz}$, parallel quadrupolar tensors perpendicular to dipolar vector. Direct `I1z` → `I2z` simulation is shown in red. For pulsed `I1z` → `I2c` simulation, $t_{90} = 1.25\,\mu\text{s}$ making $\nu_{nut} = 200\,\text{kHz}$, and is shown in blue.

system, interactions, experimental variables and the various pulses and delays that make up a specific NMR experiment. Unlike experimental NMR, there is no need to implement phase cycling as the coherences can be filtered from the density matrix as required, greatly shortening the computational time. Another key difference is the lack of relaxation in the simulations—the nuclei never return to thermal equilibrium and are unperturbed by the true T_2 relaxation such that simulated FIDs continue forever. Other dephasing phenomena can still be simulated, such as multiple noncommuting dipolar couplings, but the standard approach is to artificially damp the FID to broaden the simulated lineshapes—a process known as *apodisation*.

An example input file for pNMRsim of a 2D MAS NMR simulation for a spin diffusion experiment involving two dipolar coupled ^{11}B nuclei is shown in §C.1. Simulated FIDs are processed in the same manner as experimental data; with suitable broadening and Fourier transformation.

Full 2D spin diffusion experiments can be simulated. However, if only the magnetisation transfer is of interest then an input file can be constructed to start with z-magnetisation on one spin, evolve in time and detect z-magnetisation on the other spin. By detecting `Iz` on a spin, the program reads off the trace of the Hamiltonian density matrix in a similar manner to Eq. (3-12). This trace

includes the satellite transitions, which are usually not present in experiment because of the smaller excitation bandwidth of the readout pulse. A more realistic simulation would include the effect of a soft 90°-pulse at the end of the mixing period, followed by normal central-transition (`Ic`) detection. The difference between these detection regimes is shown in Fig. 5-2. There is a good comparison between the direct transfer and the pulse-detect variant simulations.

Despite the added realism, the Hamiltonian for an RF pulse contains off-diagonal elements (as compared to a free evolution Hamiltonian). A disproportionate amount of computational time must then be spent diagonalising the matrix, prolonging such simulations considerably [331, §2.2]. As the results show a strong consistency between both detection methods the simulations presented herein will be of the direct $z \rightarrow z$ sort and not involve a pulsed readout.

CHAPTER 6

Borate Crystals and Glasses

> The deepest and most interesting unsolved problem in solid state theory is probably the theory of the nature of glass and the glass transition.
>
> Philip Warren Anderson

6.1 Introduction To Borates

6.1.1 Practical Value and General Uses of Boron Compounds

Boron is a critical constituent in borosilicate glass, primarily added to improve thermal shock resistance and aid melting. Pyrex® is probably the most famous example of borosilicate glass, a material which has not escaped the scrutiny of NMR [254]. Other practical uses for boron can be found in sodium borohydride, a versatile reagent discovered by English chemist Herbert Brown (Nobel Prize, 1979) [52, 53] and utilised in solid-state NMR as an ^{11}B chemical shift reference.

Because of the excellent hardness, thermal and chemical stability of boron nitride, various forms are used in high-temperature equipment [306], to coat

heavy-duty tools instead of chrome-plating and to construct stators and rotor caps in some NMR MAS probes. Alloyed with neodymium and iron, boron produces the strongest permanently-magnetic material known [182]. Boron doped diamond electrically conducts, allowing sensors to operate in environments in which no other material could survive [29]. The proximity of ^{11}B nuclei in diamond has been studied with spin diffusion NMR experiments [235].

The other stable isotope of boron, ^{10}B, is an excellent neutron absorber and used in the control rods of some nuclear reactors as a moderator. The nuclear industry is also familiar with borosilicate glass for the immobilisation of high-level nuclear waste [244]. Molten alkali borosilicates are very corrosive, efficiently dissolving nuclear waste, which can be readily vitrified to immobilise the waste for, hopefully, æons. Such an unalterable configuration—important to avoid clustering or leaching of radionuclides—is not possible in real crystals, where atoms can move along dislocations.

Important and numerous properties of non-crystalline solids, such as borate glass, are explained by the glass-defining structural disorder—a state in need of further study. As a local probe of bulk material, NMR is suited to study the proximities and connectivities in disordered materials. Such a study will begin on a model compound of known structure, such as a crystal, before being applied to glasses.

6.1.2 The Glass Transition

Consider cooling a liquid. Regardless of cooling rate, at a well-defined temperature a phase transition could occur (releasing latent heat), whereby the atoms crystallise to a long-range ordered structure. Alternatively, the molecular motion of the liquid gets increasingly slower, until the measurement of flow rate becomes infeasible and the material is left in a metastable state; a glass [68].

Unlike a crystal, glasses have no long-range order and the formation of glass evolves no latent heat. Furthermore, this peculiar glass transition does not occur at a well-defined temperature—slower cooling rates lower the transition temperature, shown in Fig. 6-1. There are numerous other parameters (temperatures, energies) that describe glass forming [212] but are not pivotal

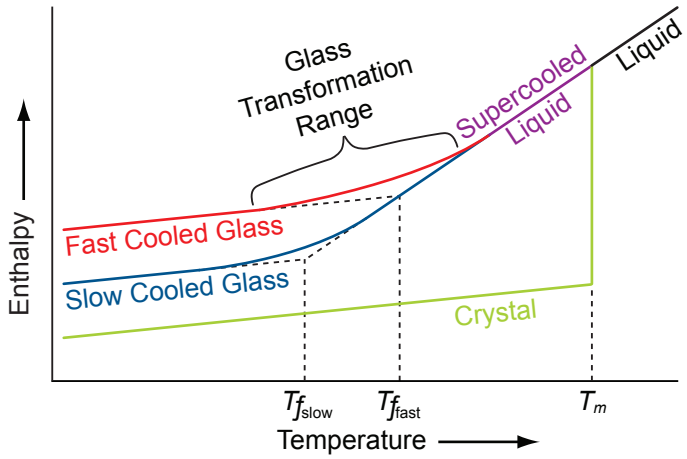

Figure 6-1. Idealised diagram showing the effect of temperature on the enthalpy (which behaves similarly to volume) of a glass-forming melt [280, Fig. 1.1]. Extrapolating the cooled-glass and supercooled-liquid lines lead to an intersection defined as the fictive temperature, where the structure of the glass would be the same as in the equilibrium liquid.

to the immediate discussion.

Although glasses are disordered, they are not completely random and bonding between the atoms will be similar to a corresponding crystalline phase. Zachariasen argued in 1932 that if the internal energies of these two phases are similar then so are the oxygen polyhedra and hence gave four requirements for "A_mO_n" oxide glass formation [326]:

(i) An oxygen atom is linked to not more than two atoms A.

(ii) The number of oxygen atoms surrounding atoms A must be small.

(iii) The oxygen polyhedra share corners with each other, not edges or faces.

(iv) At least three corners in each oxygen polyhedron must be shared.

Borate glasses obey these rules. Thus for local probes such as NMR, glass spectra appear similar to those of the corresponding crystal because the bonding and short-range order are similar. This crucial fact allows us to develop NMR experiments using model crystalline compounds, then apply the "calibrated" methods to disordered materials for the extraction of new information.

Diffraction techniques using X-rays or neutrons are reliably used to determine the crystallinity of a sample. However, careful analysis is required to avoid the mistaken interpretation of extended order when applied to glasses

[267, 318]. But unlike other oxide glasses, such as silicate and phosphate glass, borate glass *does* possess a medium range order [157].

The medium range order in borates extends from 5 Å to 15 Å and takes the form of superstructural units [320]. These rigid units are distributed randomly in a glass and are also found in most borate crystal structures. The question of why glass-forming liquids like borates solidify into structures far from a random distribution is still open.

6.1.3 Borate Anomalies and Superstructural Units

Pure B_2O_3 has been studied by NMR through T_1 relaxation [266], MQMAS [144] and recently DOR [140, 317]. Neutron scattering [290], Raman scattering [161, 222], mechanical properties [175], infrared spectroscopy [218], molecular dynamics and density functional theory [105, 173, 332] have all helped characterise B_2O_3. Despite considerable debate on the existence of boroxol rings [84, §6] the question is now: what fraction of BO_3 triangles are part of these rings? The answers from NMR and neutron scattering suggest $f = 0.6$–0.8 [144, 157, 178, 317], with the most recent result provided by DOR giving $f = 0.73 \pm 0.01$ [140].

The boron atoms in B_2O_3 are solely three-coordinated (B3), which is a charge-balanced state. Adding conventional network modifiers leads initially to the formation of BO_4 tetrahedra rather than non-bridging oxygens. Hence unlike "normal" silicate glass, network modifiers act as network strengtheners, giving rise to increased connectivity. The four-coordinated boron atoms (B4) are negative-charge centres, which are balanced by interstitial cations. This dual valence nature of boron is responsible for a wide variety of superstructural units, some of which are shown in Fig. 6-2 [320]. From energy considerations, only certain superstructural units can stably exist [171].

Superstructural units were, as recently as ten years ago, an "extremely controversial" issue [321], but now have been accepted by the borate glass community in light of increasing evidence [325] and success in explaining various borate anomalies. These anomalies are often in the form of minima or maxima of physical properties as the fraction of alkali doping is increased, such as

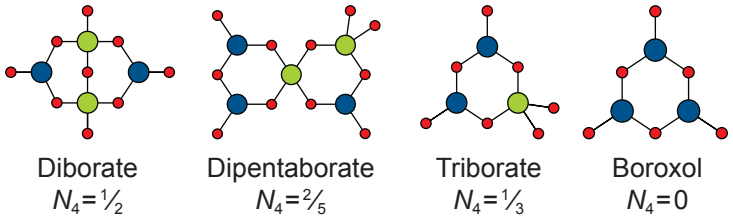

Figure 6-2. A selection of superstructural units that can exist in borate glasses and crystals. Three-coordinated boron is shown in blue, four-coordinated boron is shown in green and bridging oxygen is shown in red. Corresponding N_4 fraction is given, see §6.1.3 for details.

thermal expansion [279] or ultrasound velocity [174, 175].

Further anomalies are seen in the N_4 fraction, defined from the quantities of B3 and B4 atoms as $N_4 = \frac{\mathrm{B4}}{\mathrm{B3+B4}}$. This property shows a maximum around $\sim$ 35 mol% alkali modifier [329]. NMR has proved instrumental in the quantitative determination of the N_4 fraction in borates [5, 48, 49, 64, 77, 79, 104, 153, 154, 178, 202, 226, 245, 298] but has not yet been able to directly explore the superstructural units. Neutron scattering offers a window on superstructural units, determining unit types in addition to overall N_4 fractions for glasses [69, 282, 290, 319]. Raman scattering is particularly well suited to detect the distinct breathing mode frequencies of the different superstructural units [83, 161, 176, 222], but is not a quantitative technique. Attempts have been made to correspond the N_4 fraction measured by NMR with the superstructural unit assignments measured by Raman scattering [31].

The study of the medium range order seen in borate glasses is a key motivator in this thesis, which aims to develop homonuclear correlation experiments for solid-state NMR. Heteronuclear experiments have already been demonstrated in this area [4, 36]. As the superstructural units are rigid, the specific boron–boron bond lengths and angles could fingerprint each unit, allowing quantification. To this end, a model crystalline compound was chosen to develop the techniques with the longer-term aim being application to disordered materials.

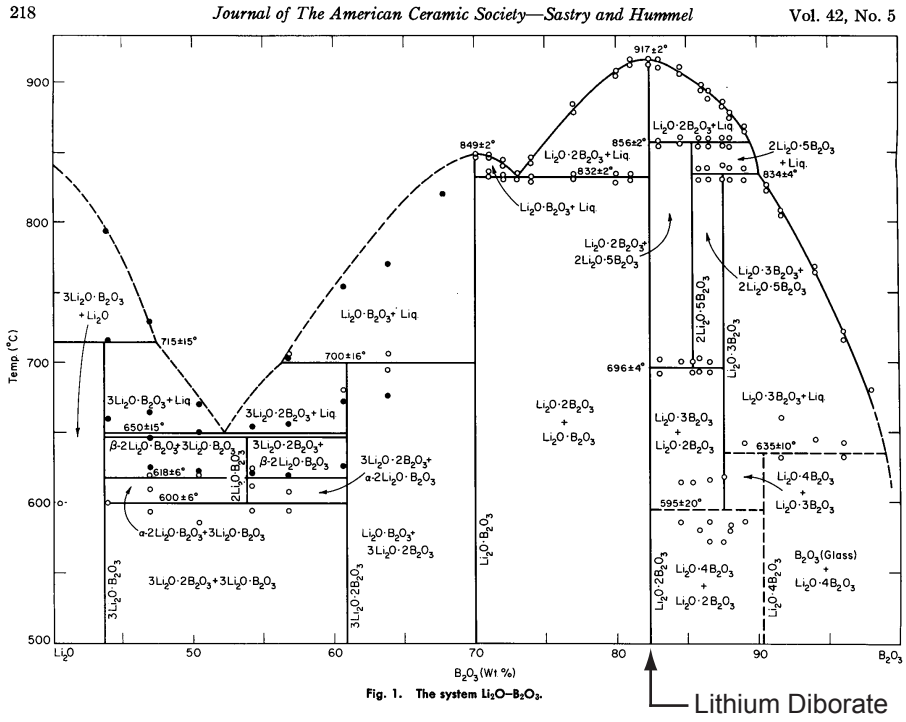

Figure 6-3. Li_2O–B_2O_3 phase diagram [272, 273].

6.1.4 Lithium Diborate

Of all possible alkali metal dopants, lithium is most suited to further investigations. The lithium borate phase diagram has been thoroughly explored, revealing a range of crystalline phases—see Fig. 6-3. This system has been shown to form glasses over a wider doping range than the other alkali metals [321]. As a glass, the several borate anomalies appear most extremely in the lithium system, which has the deepest minima in linear thermal expansion coefficient [279] and is almost[1] the only system to show a decrease in molar volume as the fraction of dopant is increased [30]. Lithium borate samples have a low density, which reduces the stress on the MAS rotors enabling faster spinning speeds to be safely reached with this system.

$Li_2O{\cdot}2B_2O_3$ was chosen as the model crystalline compound. The lithium diborate structure is well known [277] and is comprised solely of superstructural diborate units[2], as shown in Fig. 6-4. Structural information about the boron atoms in $Li_2O{\cdot}2B_2O_3$ is given in Tab. 6-1. The diborate group is the only su-

[1] The potassium system also shows this trend, but to a lesser extent.

[2] $ZnO{\cdot}2B_2O_3$ and $MgO{\cdot}2B_2O_3$ are also comprised solely of diborate units [282, Tab. 1], but for reasons stated in the text the lithium system is preferred.

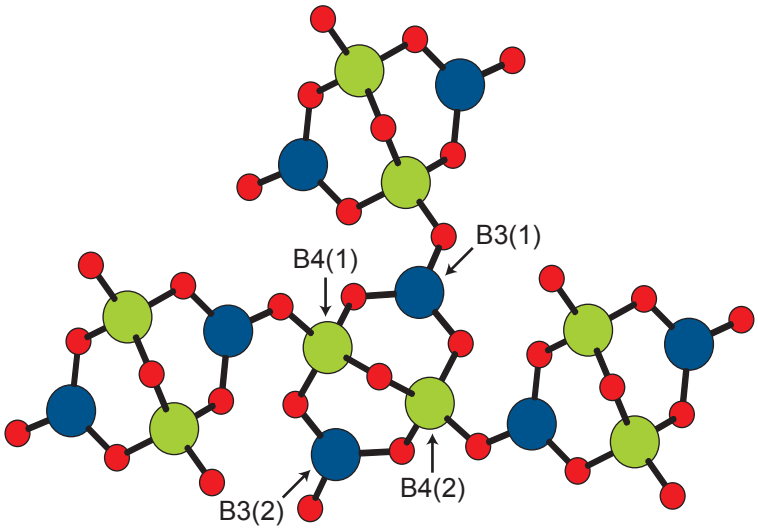

Figure 6-4. Ball and stick model of the crystal structure of lithium diborate [258], showing it to consist solely of diborate units. Three-coordinated boron is shown in blue, four-coordinated boron is shown in green, oxygen is shown in red and lithium ions are not shown. The labelling of boron atoms used in Tab. 6-1 is indicated.

Table 6-1. Boron–boron distances, corresponding dipolar coupling strength and Euler angles between different boron atoms in the diborate group. Bracketed numbers are used to differentiate between different boron atoms in the same superstructural group, as indicated in Fig. 6-4.

Nuclei	Separation[a]	Dipolar coupling[b]	Euler Angles in degrees[c]		
	in Å	$(-b_{jk}/2\pi)$ in Hz	α	β	γ
B3(1)–B4(1)	2.44	848	93.4	119.9	−83.2
B3(1)–B4(2)	2.49	801	49.7	119.3	−150.1
B3(1)–B3(2)	3.58	269	90.0	90.0	−117.1
B4(1)–B4(2)	2.36	937	−90.0	90.0	154.5
B4(1)–B3(2)	2.49	801	130.3	60.7	−150.1
B4(2)–B3(2)	2.44	848	86.6	60.1	−83.2

[a]Distances were extracted from the known crystal structure [258]
[b]The dipole-coupling constants were calculated using Eq. (2-32)
[c]Euler angles, relative to the *c*-axis of the crystal file, were determined using mPackages for Mathematica™[188]

perstructural unit containing equal measures of B3 and B4 [282]. Remarkably, the structure is a rare example of stable B4–O–B4 bonding, which is normally energetically unfavourable due to the repulsion between negatively charged BO_4 tetrahedra.

Crystalline lithium diborate is worthy of study in its own right as a non-linear optical material [97], gamma radiation detector [286] and due to its

Figure 6-5. Partially reacted reagents overflowing a crucible because of rapid water and carbon dioxide evolution. This can cause loss of sample or contamination. Weight-loss measurements can help detect such losses.

negative thermal expansion coefficient at temperatures <0 °C [3]. However, for this thesis, the rigid structural arrangement of the B3 and B4 atoms is the fundamental factor for examining this model crystalline compound.

6.2 Synthesis of Lithium Borates

6.2.1 Natural Abundance

$$Li_2CO_3 + 2B_2O_3 \xrightarrow{\text{heating}} Li_2O{\cdot}2B_2O_3 + CO_2 \tag{6-1}$$

Polycrystalline lithium diborate, $Li_2O{\cdot}2B_2O_3$, was prepared by mixing lithium carbonate (Alfa Aesar® #013418, 99%) and boron oxide (Alfa Aesar® #089964, 99.98%) in the correct stoichiometric ratio (see Tab. B-1 for $x = 1/3$). After agitating the mixture to ensure homogeneity the reactants were transferred to a platinum-rhodium crucible and placed in a normal-atmosphere electric furnace at 100 °C. The temperature was ramped at 5 °C/ min for 3 h to 1000 °C. This temperature was chosen as it is above the congruent melting temperature of lithium diborate—given as 917 °C ± 2 °C [272]. The slow ramping rate allows time for water vapour and carbon dioxide to evolve, which leads to foaming. On heating, the (approximately four times) volume expansion can cause the material to be pushed out of a too-small crucible—see Fig. 6-5. Weight-loss measurements of the cooled product should indicate at most 4%

weight loss from the desired product, significantly more loss would require remaking the batch as the stoichiometry might not be as desired. After twenty minutes at 1000 °C, the melt was poured onto a room-temperature steel plate. It is noted that if the melt is left in the crucible to cool more slowly, unexpectedly, crystallisation does not occur. Because molten glass is a good solvent, heterogeneities on the platinum crucible in contact with the melt probably dissolve during processing. Hence, when the melt is allowed to cool in the crucible, glass formation ensues because there are few (if any) heterogeneous particles in contact with the melt [115, §2.2]. But when the melt is poured, heterogeneous crystallisation occurs.

Various lithium borate glasses, $x = 0$–40, $x\mathrm{Li_2O}\cdot(100-x)\mathrm{B_2O_3}$, were also made using the above method and stoichiometric ratios given in Tab. B-1. Although for $x < 0.3$ the poured melts readily form a glass, the melts were splat-quenched between steel plates to ensure this outcome and consistency. Beneficially, the thin glass pieces are easier to grind into powder for X-ray diffraction and NMR measurements. Confirmation of crystallinity (or its absence) and phase purity was provided by powder X-ray diffraction. A scanning electron microscope (SEM) image of lithium diborate is shown in Fig. 6-6, revealing that different cooling rates lead to glass or crystal formation.

6.2.2 Isotopically Altered $^{10}B/^{11}B$

$$\mathrm{Li_2CO_3} + 4\mathrm{B(OH)_3} \xrightarrow{\text{heating}} \mathrm{Li_2O}\cdot 2\mathrm{B_2O_3} + \mathrm{CO_2} + 6\mathrm{H_2O} \qquad (6\text{-}2)$$

Polycrystalline lithium diborate samples with varying degrees of ^{11}B enrichment were prepared by mixing the powders lithium carbonate (Sigma-Aldrich® #255823, ≥99.0%), boric-^{10}B acid (Sigma-Aldrich® #426156, 99%) and boric-^{11}B acid (EaglePicher™ #Bl-EV-95-10, 99.27%) in the correct stoichiometric ratio (see Tab. B-2). The reagents were thoroughly mixed in a 5% gold-platinium crucible and placed in a normal-atmosphere electric furnace at 1000 °C. Evolution of water vapour and carbon dioxide was rapid, but the mixture quickly melts so volume expansion was reduced. After fifteen minutes the crucible was removed and left to cool. The lithium diborate invariably solidified transparent, indicating an amorphous state. Weight-loss measurements were performed

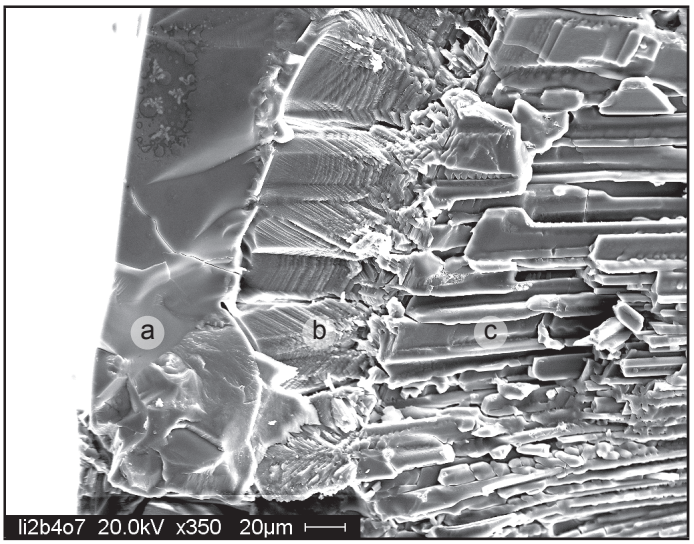

Figure 6-6. SEM image of a cross-section of iron-doped lithium diborate that has been poured from a melt onto a steel plate. a) Contact area with plate, $\approx 70\,\mu m$ deep, which has quickly cooled leaving the lithium diborate in an amorphous state. b) Striated region of intermediary cooling and partial crystallinity. c) Polycrystalline lithium diborate throughout the sample bulk where cooling rates were slower.

to check the expected reaction had occurred. The crucible was placed into a furnace at the higher temperature of 1100 °C to decrease the viscosity of the melt before pouring. After five minutes the melt was poured onto a room-temperature steel plate and allowed to crystallise.

6.3 Solid-State NMR of Borates

6.3.1 1D MAS of $Li_2O{\cdot}2B_2O_3$

The crystal structure of lithium diborate shown in Fig. 6-4 indicates one chemically distinct three-coordinated boron site and one chemically distinct four-coordinated boron site. Representative ^{11}B MAS NMR spectra of polycrystalline $Li_2O{\cdot}2B_2O_3$ are shown in Fig. 6-7 for two different static magnetic field strengths. The B3 and B4 lineshapes are clearly visible in both spectra and are distinctly resolved in the high-field case. Integration of the two lineshapes in quantitative spectra directly provide the value of the N_4 fraction. Care must be taken to include the intensity of the spinning sidebands if the spectra are not rotor-synchronised.

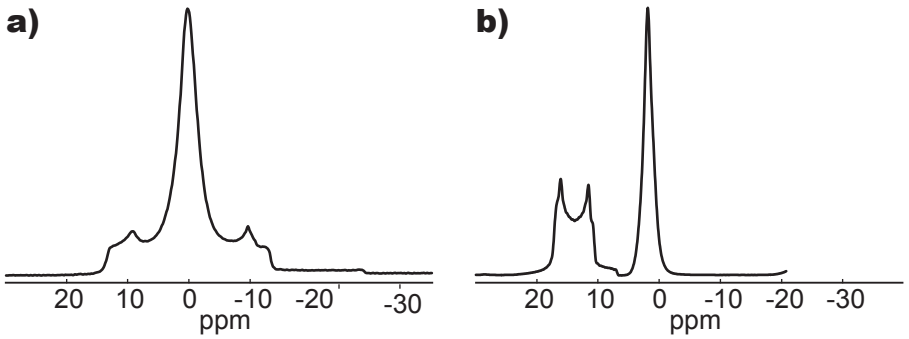

Figure 6-7. ^{11}B MAS (10 kHz) NMR spectra of polycrystalline lithium diborate, $Li_2O{\cdot}2B_2O_3$, recorded at a) 7.05 T and b) 14.1 T. At high-field the B3 (left lineshape, around 15 ppm) and B4 (right peak, around 2 ppm) sites appear as distinct spectral lineshapes, whereas at low-field the B3 is broadened such that the two lineshapes overlap. The broadening is a direct consequence of the $1/\omega_0$ dependence that the second-order central transition energy level has, given by Eq. (2-62). The fourth-rank portion of the second-order quadrupolar interaction is not removed by MAS and responsible for the specific spectral lineshapes.

As the four-coordinated boron is in a tetrahedrally symmetric environment the electric field gradient at the nucleus will be low and hence the quadrupolar coupling constant, C_Q, will be low too. Conversely, the three-coordinated boron occupies a site with trigonal planar symmetry. There will be a large electric field gradient at the nucleus, as there is less charge density above and below the trigonal plane, giving rise to a large C_Q for the B3 site.

Fitting the ^{11}B NMR spectra to calculated lineshapes allows physical parameters to be determined, such as the isotropic chemical shift (δ_iso) and the quadrupolar coupling (C_Q and η_Q). These parameters, obtained from fits of polycrystalline lithium diborate, are given in Tab. 6-2. Under MAS, the isotropic chemical shift is always at higher ppm values than the centre of gravity of the quadrupolar lineshape. As revealed in Eq. (2-62), the central transition of a half-integer quadrupolar nucleus is subject to an isotropic second-order quadrupolar shift—an energy change due to the second-order quadrupolar interaction that is not affected by spinning around any axis. The centre of gravity of an MAS lineshape is given by:

$$\delta_\mathrm{cog} = \delta_\mathrm{iso}^\mathrm{CS} + \delta_\mathrm{iso}^{(2)} \tag{6-3}$$

where $\delta_\mathrm{iso}^{(2)}$ for a nucleus with spin I is [229, Eq. (2)]:

$$\delta_\mathrm{iso}^{(2)} = -\frac{3}{40}\left(\frac{C_\mathrm{Q}}{\nu_0}\right)^2 \left(\frac{I(I+1)-{}^3\!/_4}{I^2(2I-1)^2}\right)\left(1+\frac{\eta_\mathrm{Q}^2}{3}\right)\times 10^6 \tag{6-4}$$

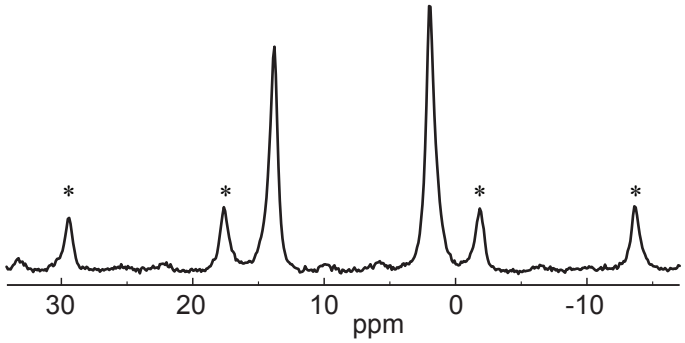

Figure 6-8. ^{11}B DOR NMR spectrum of polycrystalline lithium diborate recorded at 14.1 T by Dr Ivan Hung. Inner rotor rate was 5 kHz. The outer magic-angle rotor rate was 1.5 kHz, which was not sufficient to fully remove the anisotropic interactions, thus spinning sidebands were present in the spectrum (indicated by asterisks). Sideband suppression was used to minimise the odd-ordered sidebands [269]. The peak appearing around 14 ppm is the B3 site, with no second-order broadening. Likewise, the B4 peak is around 2 ppm.

where ν_0 is the Larmor frequency of the nucleus and C_Q and η_Q were defined in Eq. (2-42). The third term, for a spin $I = 3/2$ nucleus, is $1/3$. Compared with Eq. (2-62), the numerical prefactor reassuringly evaluates[3] to that given in Tab. A-1 for the isotropic second-order shift.

6.3.2 1D DOR of $Li_2O{\cdot}2B_2O_3$

As understood from §2.10.2, double rotation can remove the second-order quadrupolar broadening. A ^{11}B DOR NMR spectrum of $Li_2O{\cdot}2B_2O_3$ is shown in Fig. 6-8. The remaining lineshape broadening of this natural abundance sample is predominantly caused by multiple noncommuting homonuclear dipole couplings. Under DOR the quadrupolar lineshapes appear at the centre of gravity of the MAS peak [Eq. (6-3)] rather than the "correct" isotropic chemical shift of the line. The calculated and observed peak positions are given in Tab. 6-2 and agree well.

Anisotropic interactions and the relative orientations of the quadrupolar principal axis system can be extracted from spinning sideband intensities in favourable cases [142]. The DOR spectrum in Fig. 6-8 is reproducible in simulations by choosing an appropriate chemical shift, C_Q, η_Q, CSA and effective dipole coupling between B3 and B4 sites. Knowledge of the effective dipolar

[3] i.e. $2 \times -3/40 \times 1/3 = -1/20 = A_{1/2}^{3/2}$

Table 6-2. ^{11}B NMR parameters for polycrystalline lithium diborate, which are in agreement with published values [125]. δ_{cog} was calculated from the first three columns of data and Eq. (6-3). At 14.1 T, $\nu_0(^{11}B) = 192.54$ MHz.

	MAS				DOR
Site	δ_{iso} in ppm	C_Q in MHz	η_Q	δ_{cog} in ppm	δ_{obs} in ppm
B3	18.2±0.5	2.60±0.05	0.18±0.04	13.9±0.5	13.8±0.1
B4	2.0±0.5	0.50±0.02	0.50±0.50	1.8±0.5	1.8±0.1

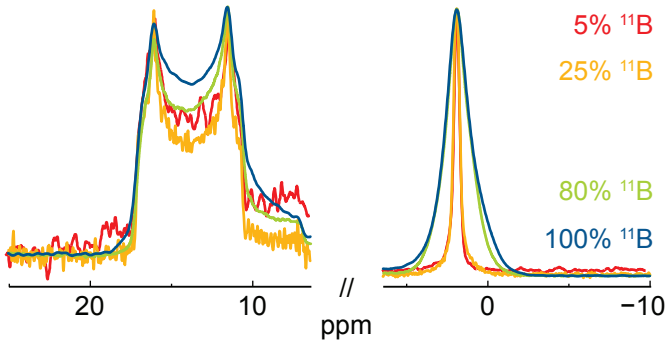

Figure 6-9. ^{11}B MAS NMR spectra of polycrystalline lithium diborate with varying levels of isotropic enrichment; 5% ^{11}B (red), 25% ^{11}B (orange), 80% ^{11}B (green) and 100% ^{11}B (blue). Recorded at 14.1 T. MAS rate was 10 kHz. Line broadening was 10 Hz. Long recycle delays and small tipping angles were used to provide quantitive measurement. Boron background was subtracted by acquiring boron signal from an empty rotor with identical experimental settings. Spectra are normalised to the same vertical height.

coupling would be beneficial in analysing homonuclear correlation experiments. However, in this case there are too many variables to extract an unambiguous set of parameters from the DOR spectrum.

Isotopically Altered ^{10}B/^{11}B

Using the method described in §6.2.2, $Li_2O{\cdot}2B_2O_3$ samples were made with 5%, 25% and 100% ^{11}B, to complement the 80% ^{11}B natural abundance sample.

Comparative 1D ^{11}B MAS NMR spectra are shown in Fig. 6-9. Altering the isotopic abundances has not affected the chemistry or structure of lithium diborate. The 1D ^{11}B MAS NMR spectra show a marked change in lineshape broadening, as well as a predictable reduction in the signal-to-noise ratio. The significant remaining (after MAS) broadening mechanisms are due to the second-order quadrupolar interaction and multiple noncommuting homonuclear dipolar couplings. The B3 lineshape is principally affected by the quadrupolar

Table 6-3. Connectivity probabilities for three- and four-coordinated boron atoms in crystalline lithium diborate for differing degrees of ^{11}B isotope. Probabilities given for no neighbours, exactly one neighbour, and so on. The 25% ^{11}B composition maximises the chance that an ^{11}B4 will have just one ^{11}B neighbour. The maximum for the B3 site occurs at 33.3̇% ^{11}B composition.

^{11}B	Site	Zero	One	Two	Three	Four
5%	B3	85.7%	13.5%	0.7%	0%	
5%	B4	81.5%	17.1%	1.4%	0%	0%
25%	B3	42.2%	42.2%	14.1%	1.6%	
25%	B4	31.6%	42.2%	21.1%	4.7%	0.4%
33.3̇%	B3	29.6%	44.4%	22.2%	3.7%	
33.3̇%	B4	19.8%	39.5%	29.6%	9.9%	1.2%
80%	B3	0.8%	9.6%	38.4%	51.2%	
80%	B4	0.2%	2.6%	15.4%	41.0%	41.0%
100%	B3	0%	0%	0%	100%	
100%	B4	0%	0%	0%	0%	100%

broadening mechanism, showing little variation in width as a function of isotopic abundance. The B4 lineshape, with a relatively small C_Q, is predominately affected by the multiple noncommuting homonuclear dipolar broadening mechanism. With only 25% ^{11}B, the nuclei are significantly spaced apart such that any neighbouring ^{11}B nuclei can be considered as spin pairs. The 5% ^{11}B sample is a similar case, but with less ^{11}B in general. The ^{11}B nuclei in the natural abundance sample are necessarily clustered, such that multiple nuclei are connected by the dipolar interaction. Consequently, MAS failed to completely remove the dipolar interaction and some broadening remained. This behaviour, which is well know from ^{1}H MAS NMR [55, 330], was even more pronounced for the 100% ^{11}B sample.

The probabilities[4] are given in Tab. 6-3, revealing two regimes of whether or not the system can be described by isolated spin pairs. For 5% and 25% ^{11}B isotopic abundances a given ^{11}B nucleus will most likely have one or zero ^{11}B neighbours. For 80% and 100% ^{11}B isotopic abundances, two or more ^{11}B neighbours are most likely. These two regimes will have important consequences for homonuclear correlation experiments, as we shall see later in spin diffusion

[4]Calculated from binomial probabilities, e.g. for only 25% ^{11}B, the probability an ^{11}B3 will have exactly one ^{11}B neighbour is $\left(\frac{1}{4}\right)^1 \times \left(\frac{3}{4}\right)^2 \times 3 = \frac{27}{64}$. For 33.3̇% ^{11}B, the probability an ^{11}B4 will have exactly two ^{11}B neighbours is $\left(\frac{1}{3}\right)^2 \times \left(\frac{2}{3}\right)^2 \times 6 = \frac{8}{27}$.

(Fig. 7-11) and spin-echo (Fig. 8-1) experiments on these isotopically altered compounds.

For 100% ^{11}B abundance, the root-sum-squared dipolar coupling can be calculated from Eq. (2-32), the crystal structure [277] and the following equation [330, Eq. (3)]:

$$b_{\mathrm{rss}} = \sqrt{\sum_{j \neq k} b_{jk}^2} \tag{6-5}$$

Considering out to 10 Å; for the B3 site $b_{\mathrm{rss}} = 1613$ Hz and for the B4 site $b_{\mathrm{rss}} = 1818$ Hz. The similarity of these values indicates that any residual dipolar-interaction phenomena (e.g. linebroadening or spin-echo dephasing) will affect both sites to the same degree.

6.3.3 MQMAS of $BaO{\cdot}2B_2O_3$

Multiple quantum MAS experiments were introduced in §3.8 and yield high-resolution spectra, similar to DOR, but also retain second-order broadened lineshapes that can be fitted to give quadrupolar parameters. $Li_2O{\cdot}2B_2O_3$ has only one B3 site and one B4 site, which are resolved in high-field spectra. For lithium diborate, MQMAS would not provide any more information than a 1D MAS spectrum. An MQMAS spectrum of lithium diborate has recently been published [64, Fig. 3]. There have been no reports of performing the MQMAS experiment on barium diborate, to the best knowledge of the author.

Crystalline barium diborate comprises equal proportions of dipentaborate (B_5O_{11}) and ditriborate (B_3O_8) superstructural units, which share a bridging oxygen [41, Fig. 1]. As is clear by examining the units themselves, or referring to the crystal structure as a whole, there are four chemically distinct B3 atoms and four chemically distinct B4 atoms as well. The barium diborate system represents a good test case for more advanced homonuclear correlation experiments, where separation of different superstructural units could be achieved.

As the multiple B3 and B4 sites overlap, a high-resolution spectrum can help determine which lineshape is caused by which chemical site. An MQMAS spectrum of $BaO{\cdot}2B_2O_3$ is presented in Fig. 6-10. In the top-right of the spectrum the B4 sites were broadened into each other; a case where reducing

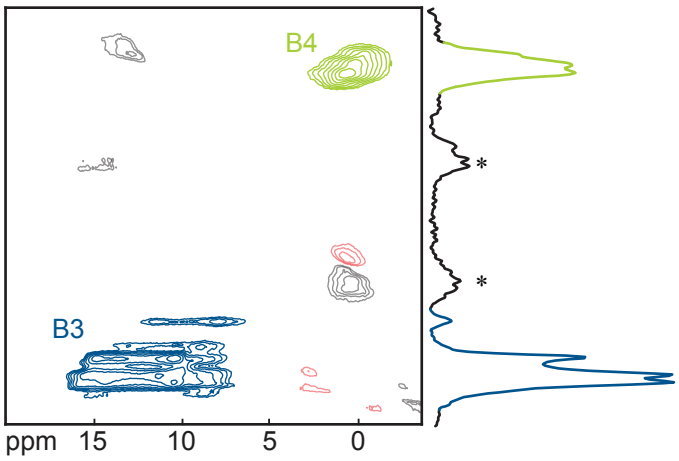

Figure 6-10. An ^{11}B amplitude-modulated split-t_1 z-filtered 3QMAS [58] with FAM [200] spectrum of polycrystalline barium diborate. The pulse sequence was shown in Fig. 3-10. Recorded at 14.1 T and 10 kHz MAS rate. The B3 peaks are blue and the B4 peaks are green. Spectral width was rotor synchronised for the direct dimension and three times the MAS rate for the indirect dimension. The excitation pulse was 4.25 µs. Three FAM repetitions were used, with a FAM pulse duration of 0.9 µs. The selective 90°-pulse duration was 27 µs. The recycle delay was 5.2 s. In t_2, 1024 points were acquired with a digital filter, co-adding 96 transients for each of 256 t_1 slices. The States method achieved sign discrimination in the indirect dimension. Both dimensions were Lorentzian broadened by 10 Hz. The spectrum is plotted with 8 contour levels starting at 5% of the maximum intensity and increasing by a factor of 1.43 between adjacent contours. Faded peaks and asterisks indicate spinning sidebands, the origins of which are detailed elsewhere [210][196, §8].

the amount of ^{11}B would enhance resolution. Several B3 sites were clearly discernible, allowing extraction of quadrupolar parameters. However, the spectrum could contain more than the four expected B3 lineshapes, which may indicate a mixture of crystalline phases. Recently a second phase, β-$BaO{\cdot}2B_2O_3$, was reported [246]. From this preliminary investigation, the phase purity was not investigated and further research is required.

6.4 T_1 Relaxation of Glasses and Crystals

Saturation-recovery experiments (§3.3) were performed on polycrystalline and vitreous lithium diborate, to determine their ^{11}B T_1 relaxation time in the absence of paramagnetic species. Experimental details are given in §5.2.1 and the results are presented in Fig. 6-11. Initial recovery was governed by a power law (most clearly seen on the log-log scale) as was expected from previous studies

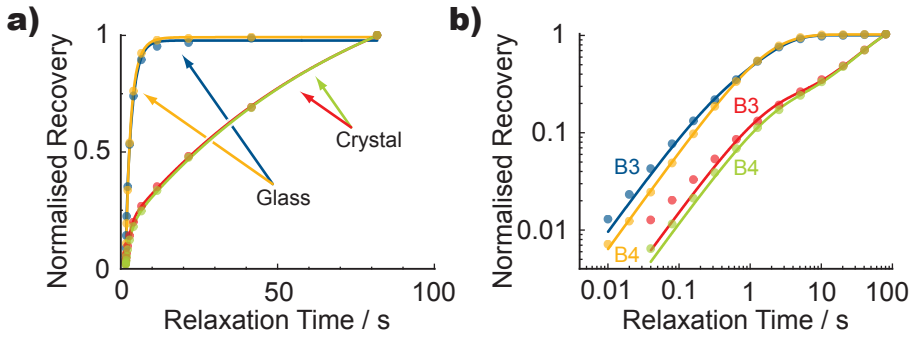

Figure 6-11. Room temperature saturation-recovery ^{11}B NMR experiments on polycrystalline and vitreous lithium diborate recorded at 14.1 T. MAS rate was 10 kHz. No paramagnetic species were present in the samples. The high static magnetic field allowed separate rates to be calculated for B3 (blue and red) and B4 (green and orange) chemical sites. Results are plotted a) linearly and b) on a log-log scale. The disordered material relaxes around thirty times faster, with little variation between chemical sites. Data were fitted to Eq. (6-6), the parameters of which are given in Tab. 6-4.

Table 6-4. Parameters fitted to Eq. (6-6) for T_1 relaxation in polycrystalline and vitreous lithium diborate shown in Fig. 6-11. Correlation coefficients are given in Tab. A-4.

State	Site	A	p	T_1^a in s	T_1^b in s
Crystal	B3	1.46±0.07	0.87±0.01	79.9 ±7.8	1.31±0.14
Crystal	B4	1.44±0.03	0.89±0.01	77.6 ±3.5	1.61±0.09
Glass	B3	0.98±0.01	0.86±0.04	2.10±0.13	0.25±0.09
Glass	B4	0.99±0.01	0.46±0.16	2.66±0.41	1.15±0.15

[276]. The glass sample was shown to fully relax, whereas the crystal sample was still recovering magnetisation at 81.92 s. Saturation-recovery data were fitted to the function:

$$S(t) = A\left(p\left(1-\mathrm{e}^{-t/T_1^a}\right)+\left(1-p\right)\left(1-\mathrm{e}^{-t/T_1^b}\right)\right) \tag{6-6}$$

where $S(t)$ is the normalised integrated intensity of the lineshape, $0 \leq p \leq 1$ describes the proportion of the slow-relaxation component, A is a normalising constant and t is the recovery time.

Examination of T_1^a values in Tab. 6-4 reveal that the ^{11}B nuclei in disordered lithium diborate relaxed 30–50 times faster than the polycrystalline material. This was in agreement with studies on disordered and polycrystalline B_2O_3 [266]. Multiexponential buildup, with $2I$ components, was expected for quadrupolar nuclei as they possess $2I$ energy transitions [16]. However, this

multiexponential behaviour is relatively weak in solid-state NMR [45, §2] and therefore the multiexponential behaviour arises from the separate relaxation mechanisms that can exist for quadrupolar nuclei [114]. The presence and comparative strength of each mechanism will determine the relaxation behaviour and suitable fitting function. However, based on the accuracy of the fit evident in Fig. 6-11 and previous quadrupolar relaxation studies [275, §IV.B] a bi-exponential fit was suitable for the glass in this case.

In NMR, shorter recycle delays between phase cycle steps shorten the total experimental time, as the recycle delay is usually the rate limiting step. Borate crystals are the model compounds that are to be studied before moving on to more complicated disordered materials. The long ^{11}B spin-lattice relaxation, compared to the vitreous phase, inhibits the rapid acquisition of data. Fortunately, the recycle delays for polycrystalline lithium diborate were only measured in tens of seconds rather than hours; the latter would render 2D NMR experiments infeasible. Nevertheless, the unsolved problem of long relaxation in crystals is of broad importance and worthy of some investigation.

The structural differences between crystal and glass cause the nuclei to relax through different mechanisms, prolonging the T_1 relaxation for those in the crystal lattice. Different relaxation mechanisms were briefly covered in §3.3 but will be elaborated upon here. The dominant cause of relaxation in insulating crystals, such as lithium diborate, is a two-phonon quadrupolar relaxation Raman process, first reported by Van Kranendonk [296]. In this process, an incident phonon is annihilated at the nuclear site, the nuclear spin is flipped and an energy-conserving phonon is created [266, §2]. The mechanism has a specific temperature dependence and experiments with chlorine nuclei provide supporting evidence for this mechanism [152]. In amorphous materials, the Van Kranendonk mechanism has been shown to be negligible by Szeftel and Alloul [291]. A more efficient relaxation mechanism is described as being due to the abundant existence of two-level defects. Bridging oxygen atoms tunnelling between two potential wells cause a modulation of the electric field gradient at the nuclear site. This changing field is a more efficient process at relaxing the nuclear spins than the Van Kranendonk mechanism [231, 232].

To be confident in the assignment of these relaxation mechanisms for

Table 6-5. Selected ionic "Shannon" radii [278].

Ion	Charge	Coordination	Spin State	Ionic Radius in Å
Li	1+	4		0.59
Li	1+	6		0.76
Cu	2+	4		0.57
Cu	2+	6		0.73
Co	2+	4	High Spin	0.58
Co	2+	6	High Spin	0.65
Co	2+	6	Low Spin	0.75
Fe	3+	4	High Spin	0.49
Fe	3+	6	Low Spin	0.55
Fe	3+	6	High Spin	0.54

lithium diborate crystal and glass, the temperature dependence of T_1 would need to be sought. Regardless of these mechanisms an additional, overriding, mechanism can be introduced; relaxation through paramagnetic centres [1, Ch. IX §II.A].

6.4.1 Paramagnetic Doping

The presence of a large electric field, such as that which forms around a paramagnetic ion, causes rapid relaxation to nuclei that are close enough to dipole-couple with an unpaired electron spin. Further away nuclear spins then relax via spin diffusion to the paramagnetic centre [172, §II.B]. Mortuza, Dupree and Holland have shown that tiny amounts (<0.5 mol%) of paramagnetic impurities can drastically reduce the T_1 time in glasses without affecting the structure [228]. Relaxation through paramagnetic centres also affects the coherence dephasing, with excessive (>2 mol%) dopant causing severe broadening of spectral lines [31, Fig. 11].

A suitable paramagnetic ion will have many unpaired electrons and be small enough to substitute for a Li^{1+} ion. The ionic size of selected ions is given in Tab. 6-5. For a given coordination number, Cu^{2+}, Co^{2+} and Fe^{3+} are small enough to substitute for Li^{1+}. Sources of these ions can be found in copper(II) oxide, cobalt(II,III) oxide and iron(III) oxide, respectively. The first and last compounds melt above the firing temperature of 1100 °C, at temperatures of 1201 °C and 1566 °C. However, the oxides readily dissolve in the corrosive borate

glass melt. Above 895 °C, cobalt(Ⅱ,Ⅲ) oxide decomposes into CoO, containing the cobalt(Ⅱ) ion:

$$2Co_3O_4 \xrightarrow{\text{heating}} 6CoO + O_2 \tag{6-7}$$

If 0.1 mol% of copper(Ⅱ) oxide provided solely Cu^{2+} ions, which have one unpaired electron, there would be at most 0.1 mol% of unpaired electrons contributing to the electronic moment. However, the same amount of cobalt(Ⅱ,Ⅲ) oxide could provide 0.3 mol% of Co^{2+} ions, which have either one or three unpaired electrons depending on the spin-state. Therefore, either 0.3 mol% or 0.9 mol% of unpaired electrons could contribute to the electronic moment in the cobalt-doped case. Iron(Ⅲ) oxide has five unpaired electrons, therefore 0.1 mol% of Fe_2O_3 could contribute 1 mol% of unpaired electrons.

Two samples of polycrystalline lithium diborate with either 0.1 mol% CuO or 0.1 mol% Co_3O_4 were synthesised using the boric acid method (§6.2.2). The crystallised solids appeared brown-green and blue for the copper- and cobalt-doped samples, respectively. Polycrystalline lithium diborate with nominally 0.1 mol% iron(Ⅲ) oxide (Sigma-Aldrich, #310050, ≥99%) was synthesised using the boron oxide method (§6.2.1). Before melting, the well-mixed powders appeared light pink in colour and after melting the crystallised solid appeared light brown.

All three paramagnetic-doped lithium diborate samples were investigated with ^{11}B MAS NMR, using identical experimental parameters. NMR spectra, with the boron-background subtracted, are shown in Fig. 6-12. Assuming the samples are otherwise identical, any change in linewidth is attributable to relaxation (coherence dephasing rather than spin-lattice) through the paramagnetic centres. The full-width at half-maximum for the B4 peaks were: iron-doped 322 Hz ± 12 Hz, copper-doped 318 Hz ± 12 Hz, cobalt-doped 386 Hz ± 12 Hz.

6.4.2 T_1 Relaxation of Doped Crystals

90°-pulse-recovery experiments were performed on 0.1 mol% copper- and cobalt-doped polycrystalline $Li_2O{\cdot}2B_2O_3$ to determine their ^{11}B T_1 relaxation time. The data are shown in Fig. 6-13, fitted to the mono-exponential:

$$S(t) = A(1 - e^{-t/T_1}) + c \tag{6-8}$$

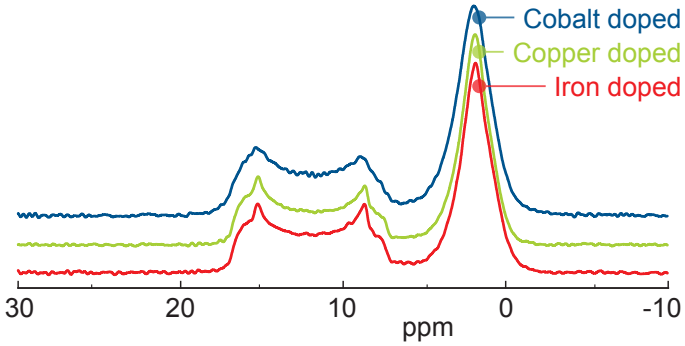

Figure 6-12. ^{11}B MAS NMR spectra of polycrystalline lithium diborate recorded at 11.74 T. MAS rate was 10 kHz. Various paramagnetic dopants are shown to have negligible effect on the NMR spectra when present at the 0.1 mol% level.

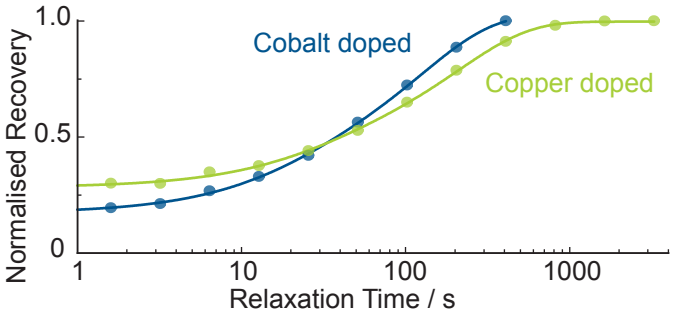

Figure 6-13. Room temperature saturation-recovery ^{11}B NMR experiment at 11.74 T and 10 kHz MAS rate. The semi-log plot shows the recovery curves of the B4 site for 0.1 mol% cobalt- and copper-doped polycrystalline lithium diborate. The data were fitted to Eq. (6-8), the parameters of which are given in Tab. 6-6.

where A and c are variables that vertically scale and shift the function. The significant magnetisation at short relaxation times was accommodated the c term. Compared to Eq. (6-6), c can be thought of as a second component that recovers extremely fast.

The signal at very short (0.1 s, not plotted) relaxation durations were similar to that at 1.6 s for both samples. Careful baseline correction excludes an artificial explanation for such significant signal intensity. The rapid recovery could indicate that some paramagnetic ions are present near ^{11}B nuclei. The presence of such a baseline offset does not affect the determination of T_1 times, as indicated by the low correlation of the c variable in Tab. A-5.

The overriding result was that both the copper- and cobalt-doping failed to reduce the T_1 relaxation time significantly. The cobalt-doped lithium diborate had a slightly wider B4 lineshape and faster relaxation than the copper-

Table 6-6. Fit parameters for T_1 relaxation in 0.1 mol% copper- and cobalt-doped polycrystalline lithium diborate. Only data for the B4 site are given and were fitted to Eq. (6-6). Correlation coefficients are given in Tab. A-5.

Dopant	A	T_1 in s	c
Cobalt	0.79±0.02	82.9± 6.4	0.18±0.01
Copper	0.69±0.01	145.5±10.9	0.30±0.01

doped sample. Cobalt was a slightly more effective relaxation agent than copper, arguably because the cobalt(Ⅱ,Ⅲ) oxide provided more unpaired electrons. By this argument the iron-doped sample should be the most effective of three dopants, but the linewidth of the iron-doped sample in Fig. 6-12 was similar to that of the copper-doped. T_1 relaxation data was not collected for the iron-doped sample, but preliminary tests indicated the relaxation time was the same order of magnitude as the cobalt- and copper-doped samples.

The metal oxides effectively dissolved in the melt, as seen in cases where the melt forms a glass. Additionally, the dopant ions had a high probability of being in paramagnetic states. If these points hold true, then the simplest explanation for the lack of significant relaxation seen in Fig. 6-13 is that the crystal lattice does not readily accept these dopants. Plausibly, the 2+ charge state of the cobalt and copper dopants inhibited their substitution into the Li^{1+} ion location. For Fe^{3+}, even more so. However, Co^{2+} and Fe^{3+} ions have been shown previously to be accepted into a glass matrix [31].

Once again, a difference between glasses and crystals becomes apparent as the ionic acceptance is explained by the much greater disorder in the glass network. In a rigid crystal lattice such ions could be restricted by the valence imbalance. It is briefly noted that, even in a glass, the chance of Fe^{3+} substituting for B^{3+} can be neglected based on the large difference in metal-oxide bond length. As paramagnetic species were included in the crystal synthesis but not detected near most of the boron nuclei, a question is raised as to the location of the paramagnetic species.

Scanning electron microscopy (SEM) was used to observe the surface of polycrystalline lithium diborate doped with 5 mol% Fe_2O_3. The results are shown in Figs. 6-14 and 6-15. The SEM results indicated that a significant

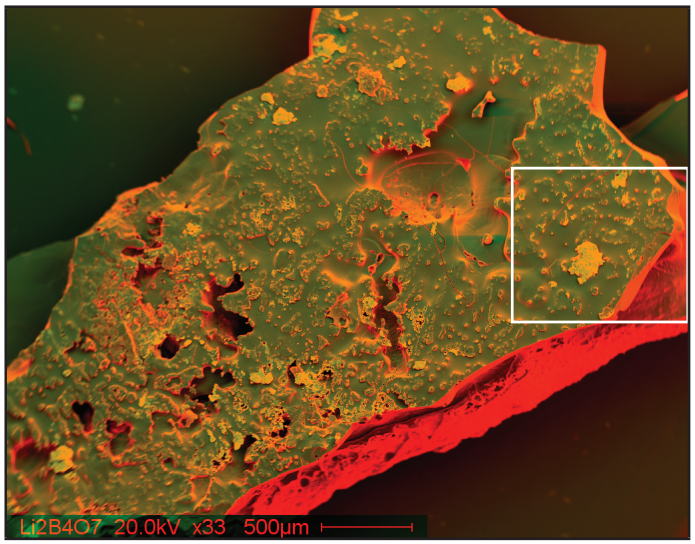

Figure 6-14. SEM image of a shard of 5 mol% iron-doped polycrystalline lithium diborate. The white box indicates the region shown in Fig. 6-15.

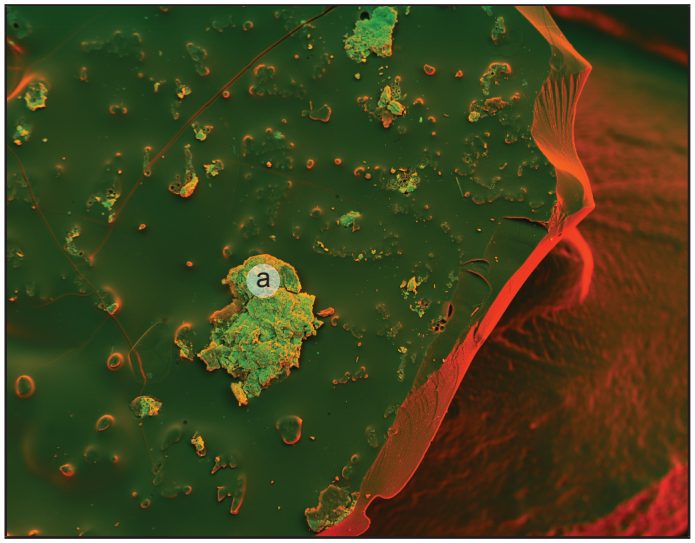

Figure 6-15. Magnified SEM image of Fig. 6-14. Patches of different material, such as (a), are clearly visible on the surface. Energy-dispersive X-ray spectroscopy indicates these are composed of mostly iron oxide. In between these regions, negligible elemental iron was detected on the surface.

amount of the iron oxide did not enter the crystal lattice and remained in clusters of varying microscopic size. As most boron atoms were very far from the paramagnetic centres this result largely accounts for the lack of enhanced spin-lattice relaxation.

Further investigation could, potentially, successfully introduce paramagnetic centres into polycrystalline material to reduce the nuclear spin-lattice relaxation time. Further methods, not involving paramagnetic centres, involve

creating defects in the crystal lattice. However, this ultimately will transform the crystal into an amorphous material, which cannot function as a model compound for investigations on homonuclear correlation between half-integer quadrupolar nuclei.

CHAPTER 7

Homonuclear Correlation Experiments

> In theory, there is no difference
> between theory and practice.
> But, in practice, there is.
>
> Jan L. A. van de Snepscheut

Using polycrystalline lithium diborate as a model compound, homonuclear correlations involving the half-integer quadrupolar nucleus ^{11}B were investigated. Two-dimensional spin diffusion experiments (§3.7, §5.2.3) are used to observe the transfer of nuclear magnetisation, mediated by the dipolar interaction. An intricate interplay of dipole and quadrupole effects means the interpretation of such spectra is not always straightforward. In the two-site case of lithium diborate, there are three potential correlations: B3–B4, B3–B3, B4–B4. As the B3 site has significant second-order quadrupolar broadening there is opportunity to detect spin diffusion between inequivalent B3 sites by observing cross-peaks between the singularities of the B3 lineshape. Any cross-peaks between inequivalent B4 sites would be hidden under the featureless auto-peak. Double-quantum homonuclear dipolar recoupling experiments are presented at the end of this chapter, where all three correlations can be detected.

7.1 MAS Spin Diffusion at 14.1 T

7.1.1 Varying Mixing Time at Fixed MAS Rate

Two-dimensional spin diffusion ^{11}B NMR experiments at MAS rates of 4716 Hz, 6160 Hz and 7602 Hz are presented in Figs. 7-1, 7-2 and 7-3, respectively.

One-dimensional row slices through the B4 site of all the spectra are presented in Figs. 7-4, 7-5 and 7-6. For maximum consistency, all spectra for a given spinning speed were recorded contiguously.

Examination of the spectra at zero mixing time revealed all the intensity was in auto-peaks along the diagonal. Auto-peaks are created by magnetisation that has not exchanged. Hence, a diagonal slice of a spin diffusion spectrum at 14.1 T will be representative of the 1D MAS spectrum shown in Fig. 6-7b. From this we can assign the bottom-left peak to be the large-C_Q B3 site and the top-right peak to be the small-C_Q B4 site. The B3–B4 and B4–B3 cross-peaks were clearly visible for long mixing times at the off-diagonal intersection of the B3 and B4 auto-peaks. The appearance of cross-peaks indicate there was a spin diffusion mechanism at work, balancing the energy needed for a dipolar flip-flop of spins. The bottom-right B3–B4 cross-peak was formed from magnetisation that evolved on a B3 nucleus, was exchanged during the mixing time and detected on a B4 nucleus. The top-left B4–B3 cross-peak was, *vice versa*, formed the same way. Intensity was also seen between the singularities of the B3 lineshape, indicating a B3–B3 cross-peak.

For different MAS rates, there was a difference in broadening of the peaks, which can be assigned to the effect of multiple noncommuting homonuclear dipolar couplings. At 14.1 T and the three MAS rates of 4716 Hz, 6160 Hz and 7602 Hz, the broadness of the diagonal peaks decreased for faster spinning speeds. Note the relative widths of the B3 auto-peaks at 0 ms in Figs. 7-1a, 7-2a and 7-3a. As MAS can only completely remove the dipolar interaction between isolated spin pairs these multiple noncommuting couplings, in effect, reintroduce the dipolar interaction. Faster MAS suppresses these residual dipolar interactions more effectively [330].

At a MAS rate of 4716 Hz, the B3–B4 cross-peaks were seen to grow quickly, starting from a mixing time of 3 ms. The B3–B3 cross-peaks appeared

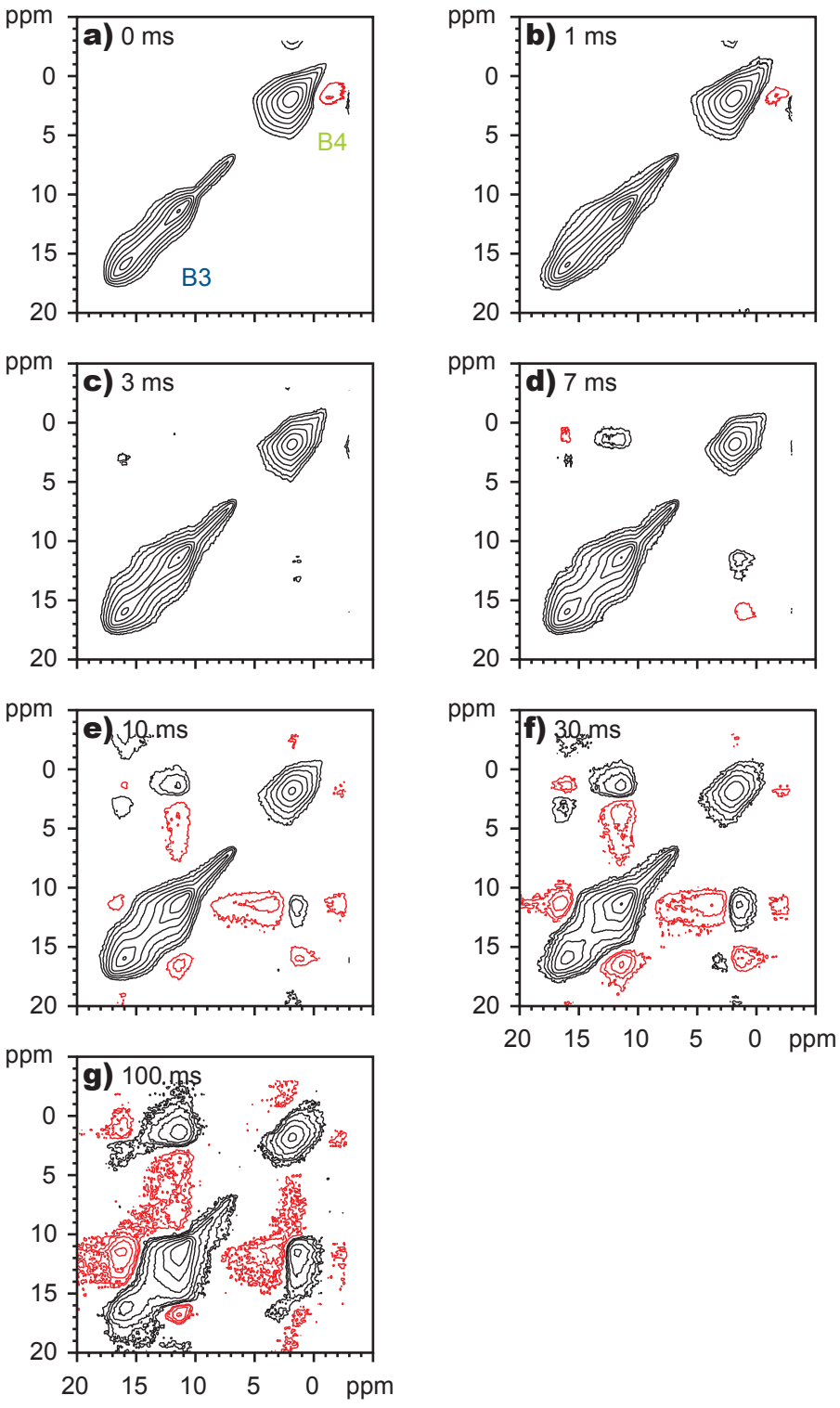

Figure 7-1. ^{11}B MAS NMR rotor-synchronised spin diffusion spectra of polycrystalline lithium diborate. Recorded at 14.1 T. MAS rate was 4716 Hz. The mixing times were a) 0 ms, b) 1 ms, c) 3 ms, d) 7 ms, e) 10 ms, f) 30 ms, g) 100 ms. Contours increase by ×1.75 from a base of 2% of the maximum intensity.

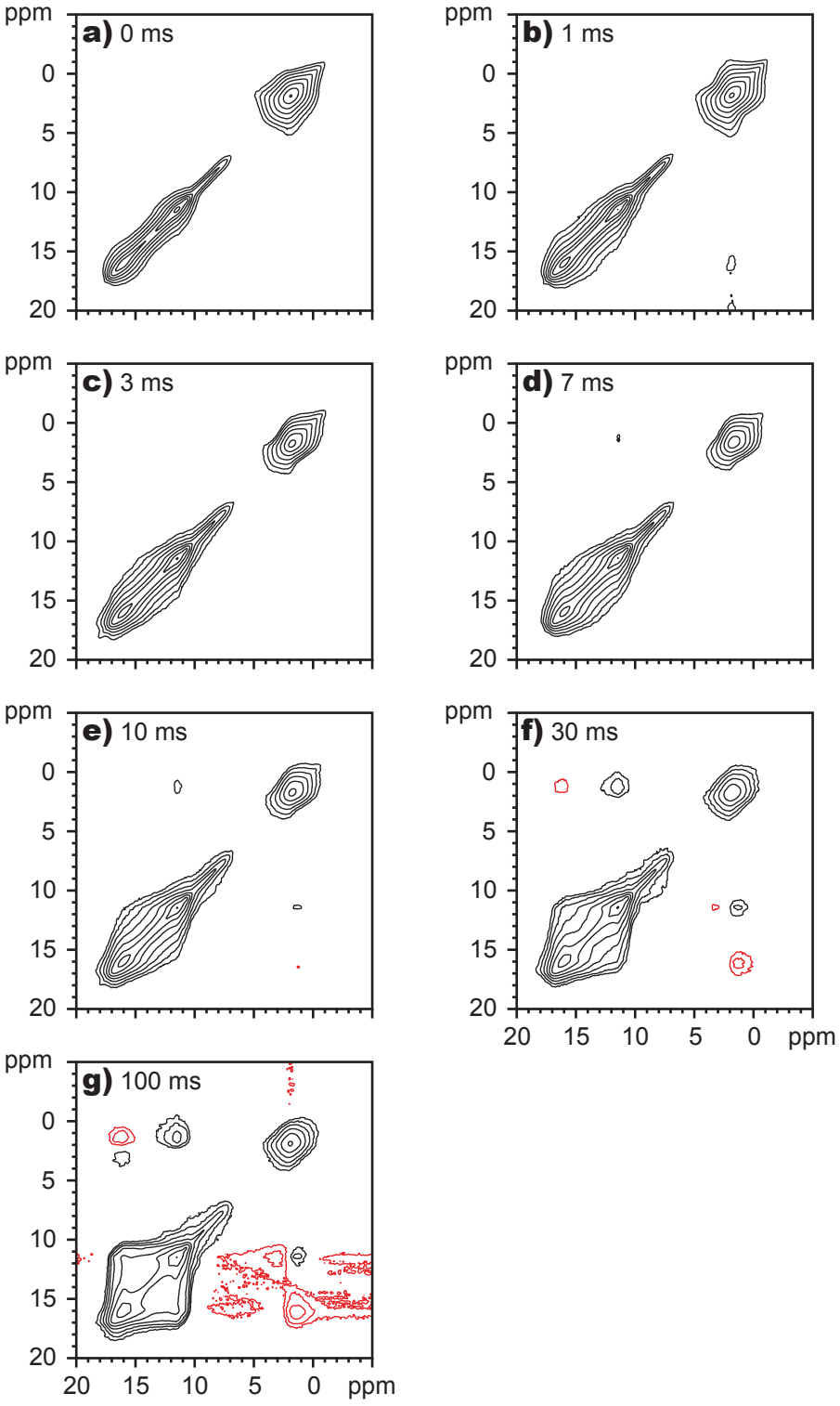

Figure 7-2. ^{11}B MAS NMR rotor-synchronised spin diffusion spectra of polycrystalline lithium diborate. Recorded at 14.1 T. MAS rate was 6160 Hz. The mixing times were a) 0 ms, b) 1 ms, c) 3 ms, d) 7 ms, e) 10 ms, f) 30 ms, g) 100 ms. Contours increase by ×1.75 from a base of 2% of the maximum intensity.

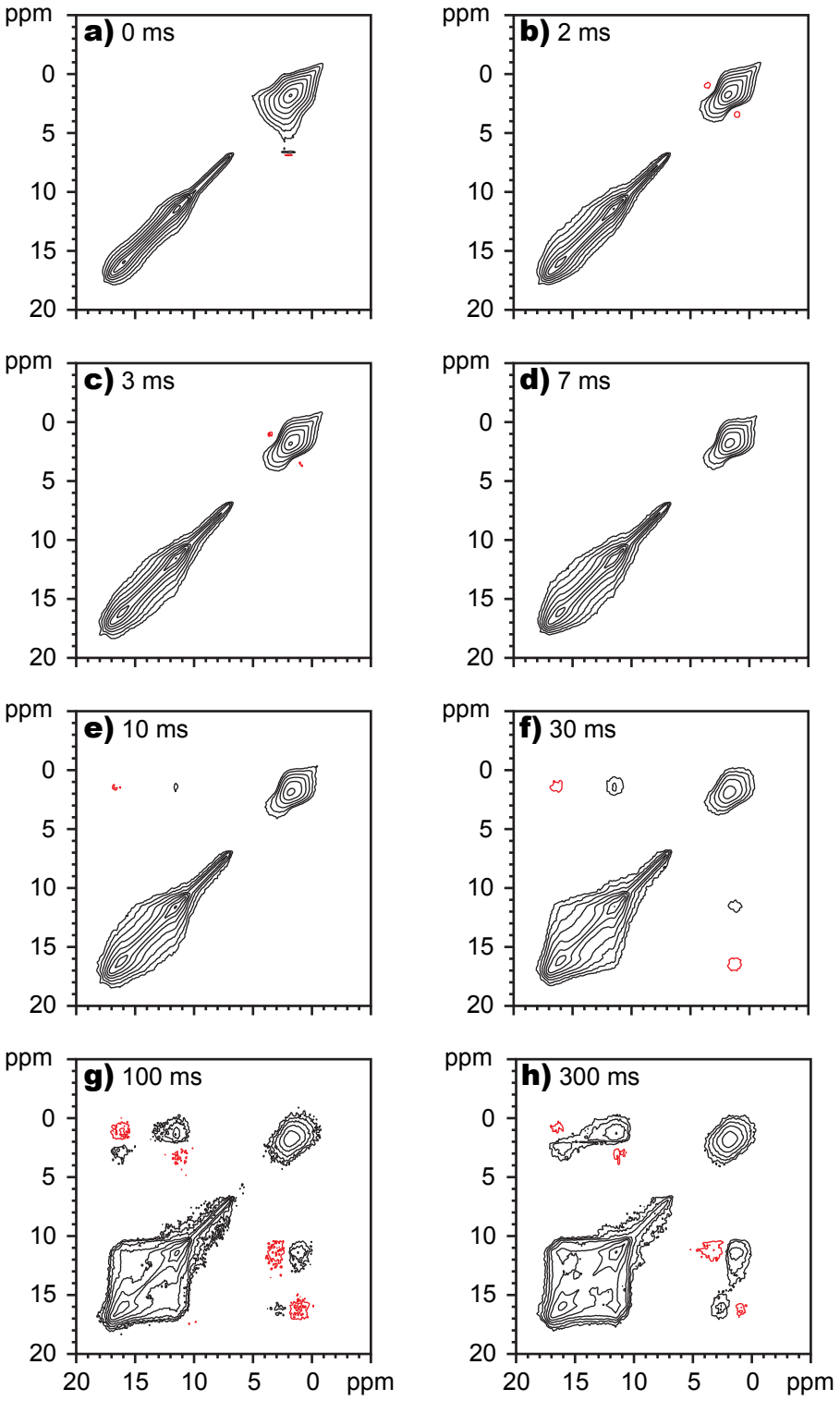

Figure 7-3. ^{11}B MAS NMR rotor-synchronised spin diffusion spectra of polycrystalline lithium diborate. Recorded at 14.1 T. MAS rate was 7602 Hz. The mixing times were a) 0 ms, b) 2 ms, c) 3 ms, d) 7 ms, e) 10 ms, f) 30 ms, g) 100 ms, h) 300 ms. Contours increase by ×1.75 from a base of 2% of the maximum intensity.

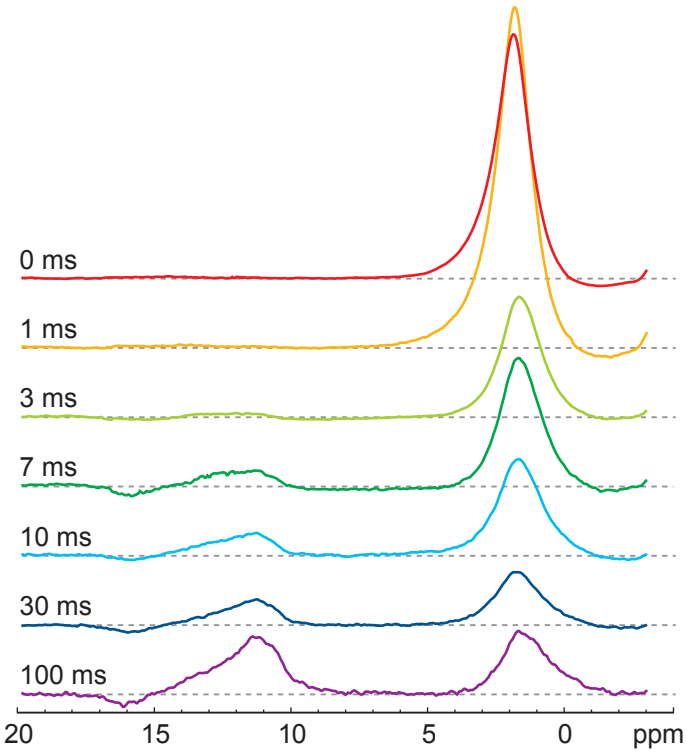

Figure 7-4. Slices taken through the rows (parallel to ω_2) at 1.4 ppm in Fig. 7-1. Recorded at 14.1 T. MAS rate was 4716 Hz. Numbers next to the slices indicate the mixing time.

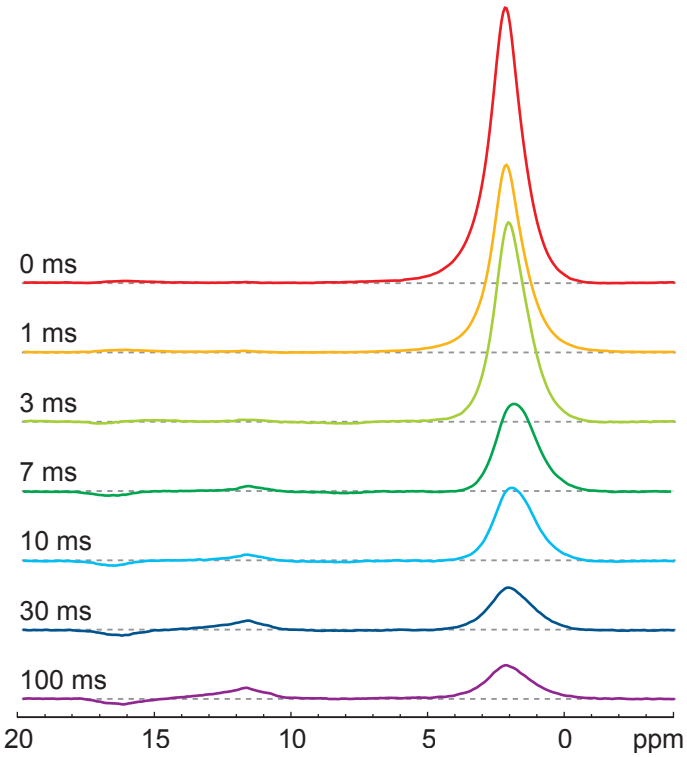

Figure 7-5. Slices taken through the rows (parallel to ω_2) at 1.4 ppm in Fig. 7-2. Recorded at 14.1 T. MAS rate was 6160 Hz. Numbers next to the slices indicate the mixing time.

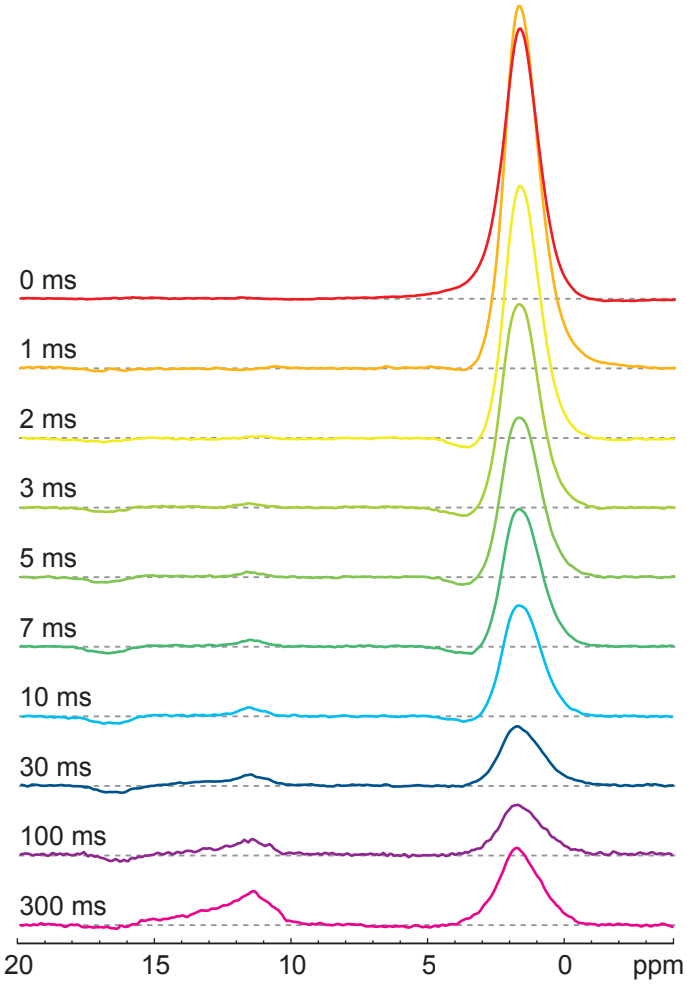

Figure 7-6. Slices taken through the rows (parallel to ω_2) at 1.4 ppm in Fig. 7-3. Recorded at 14.1 T. MAS rate was 7602 Hz. Numbers next to the slices indicate mixing the time.

with mixed positive and negative intensity, which grew at a similar rate as the B3–B4 cross-peaks. The B3–B4 cross-peaks had an interesting shape, also showing regions of mixed positive and negative intensity. Examination of the slices in Fig. 7-4 indicated this shape persisted for different mixing times.

The most striking difference at the slightly higher spinning speed of 6160 Hz was that the B3–B3 cross-peaks were only positive in intensity. Yet the B3–B4 cross-peak shape was the same $\binom{-+}{+-}$ pattern seen at a MAS rate of 4716 Hz. Comparing cross-peak intensities at $\tau_{\text{mix}} = 10$ ms for 4716 Hz and 6160 Hz MAS rates, the cross-peak buildup took longer at the faster MAS rate. Also, comparing the slices at $\tau_{\text{mix}} = 100$ ms, the overall cross-peak to auto-peak intensity was reduced at the faster MAS rate. However, the B3–B3 cross-peak intensity was higher than the B3–B4 cross-peak intensity.

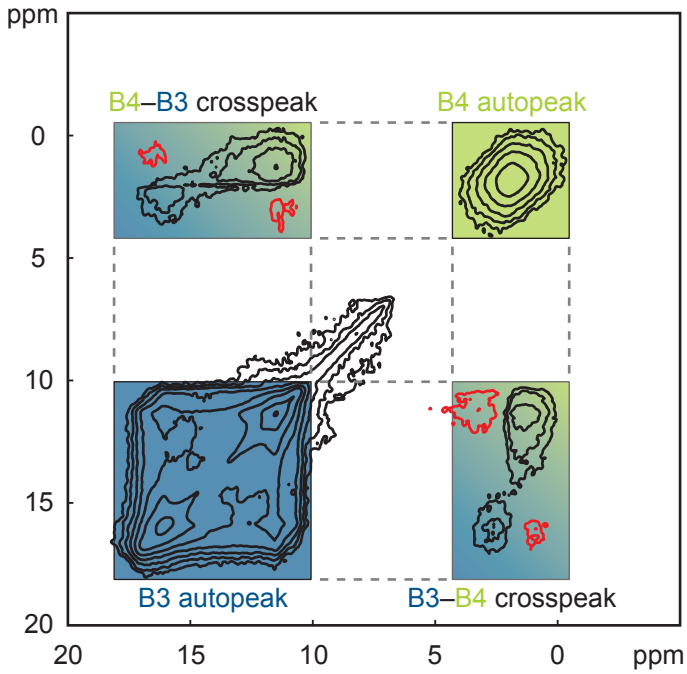

Figure 7-7. An ^{11}B MAS NMR spin diffusion spectrum of polycrystalline lithium diborate recorded at 14.1 T. The MAS rate was 7602 Hz and the mixing time was 300 ms. Further experimental details were given in §5.2.3. The spectrum is repeated from Fig. 7-3h.

At the MAS rate of 7602 Hz a spectrum was recorded for a mixing time of 300 ms, see Fig. 7-3h. For $\tau_{\text{mix}} = 300$ ms all cross-peak intensities were greater than the cross-peak intensities at $\tau_{\text{mix}} = 100$ ms, showing the transfer of magnetisation was still occurring. Comparing cross-peak intensities at $\tau_{\text{mix}} = 30$ ms for 6160 Hz and 7602 Hz MAS rates, the cross-peak buildup took longer at the faster MAS rate.

The spectrum from Fig. 7-3h is enlarged and shown in Fig. 7-7. Labelled on the figure are the broadly defined auto- and cross-peak regions. Presence of a cross-peak indicates magnetisation has been transferred between the B3 and B4 sites, whether the peak is positive or negative. The labelled areas shown in Fig. 7-7 were volume-integrated in absolute mode to yield total absolute peak intensity.

A buildup curve can be made by volume-integrating (in absolute mode) the auto- and cross-peaks of the spectra in Fig. 7-3 for a MAS rate of 7602 Hz. The magnetisation transfer as a function of mixing time is shown in Fig. 7-8. Generally, the curve follows the expected behaviour for magnetisation that is stochastically diffusing. For zero mixing time, there should be no magnetisation

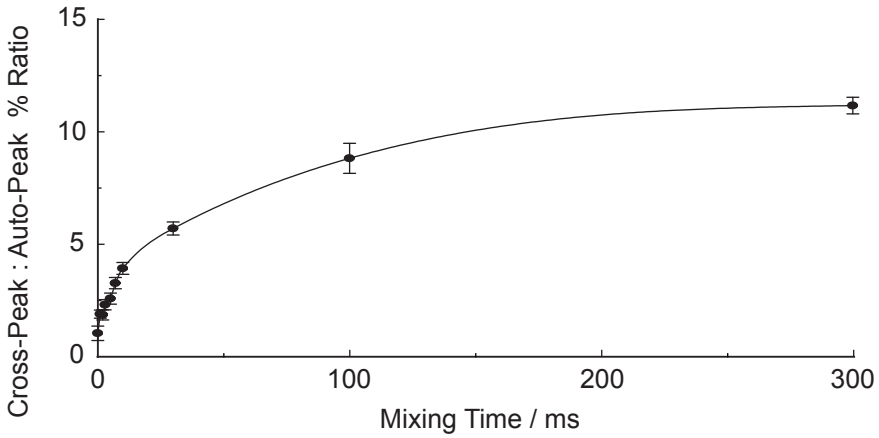

Figure 7-8. The ratio of absolute cross-peak intensity to absolute auto-peak intensity under MAS (7602 Hz) as a function of mixing time. The spectra were shown in Fig. 7-3. There was rapid initial buildup, followed by a slower increase to an eventual plateau around 10% magnetisation transferred. The points are joined by a spline curve as a guide to the eye.

transfer and the finite but small (∼1%) value indicated in Fig. 7-8 is an unfortunate consequence of using a magnitude spectrum for integration—the random noise in the cross-peak regions are being falsely counted as actual cross-peak intensity. An area of noise was also integrated to provide an indication of measurement uncertainty. The integrated intensity of the cross-peaks were normalised to account for relaxation by dividing by the integrated intensity of the auto-peaks. Note that in this definition the integrated intensity of the auto-peaks also include the B3–B3 and B4–B4 cross-peaks, which is a limitation of this basic approach.

7.1.2 Varying MAS Rate at Fixed Mixing Time

Figure 7-9 shows spin diffusion spectra at the long mixing time of 100 ms for varying MAS rates from 4427 Hz to 7602 Hz. The slowest spinning speed corresponds to 23 ppm, which is slightly larger than the lineshape separation. At spinning speeds slower than ≈ 4427 Hz, some of the resonances would fall outside the rotor-synchronised spectral width. The experimental conditions were given in §5.2.3. All spectra were processed and displayed equivalently except for Fig. 7-9a, which had a base contour level of 13% as opposed to 2% otherwise.

Concentrating on the B3–B4 cross-peaks, the $\binom{-+}{+-}$ shape appeared to be present at all tested MAS rates. For the slowest spinning speed, the cross-peak

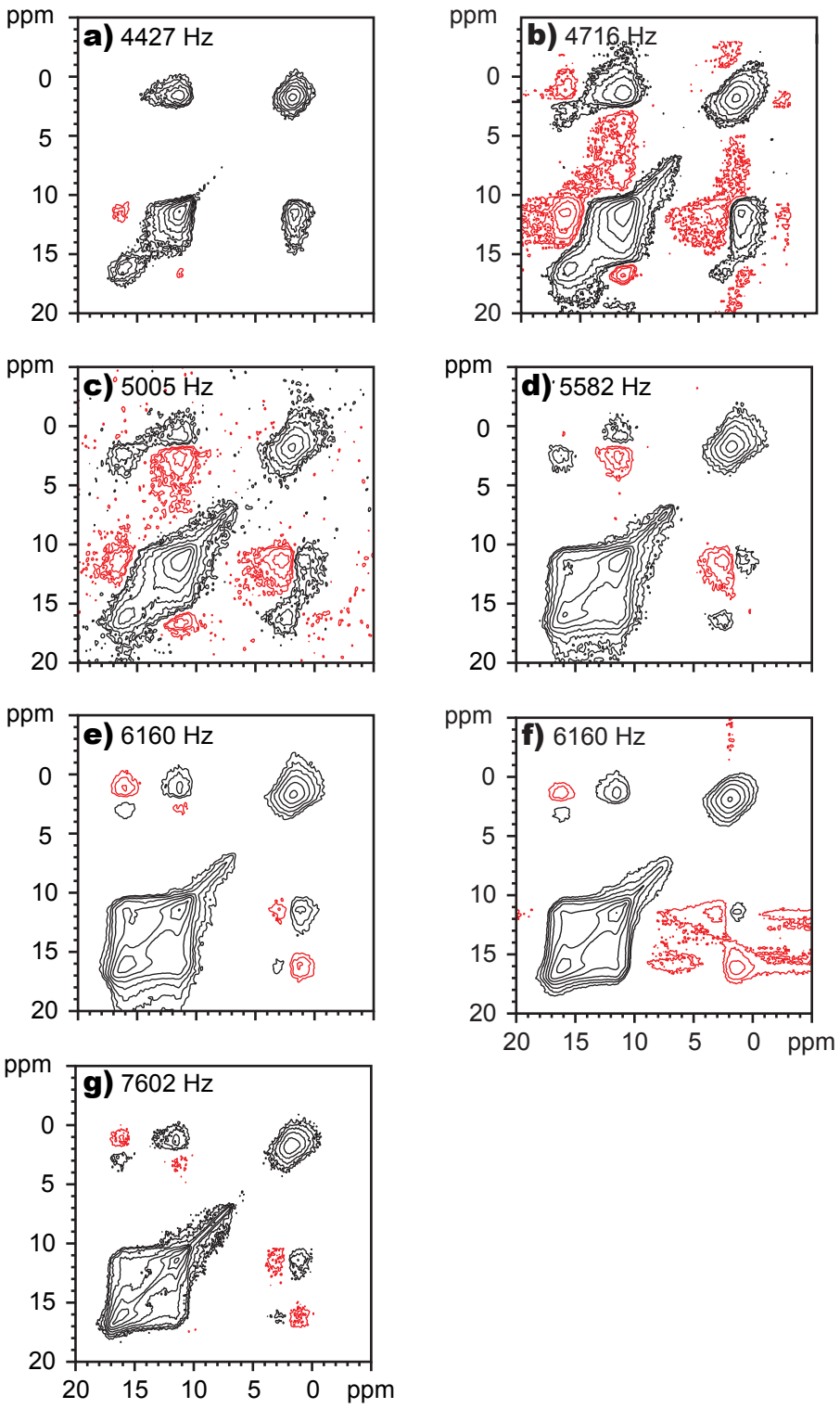

Figure 7-9. ^{11}B MAS NMR spin diffusion spectra of polycrystalline lithium diborate. Recorded at 14.1 T. The mixing time was 100 ms. MAS rates were a) 4427 Hz, b) 4716 Hz, c) 5005 Hz, d) 5582 Hz, e) 6160 Hz (Warwick), f) 6160 Hz (St Andrews), g) 7602 Hz. Contours increase by ×1.75 from a base of 2% [a) 13%] of the maximum intensity.

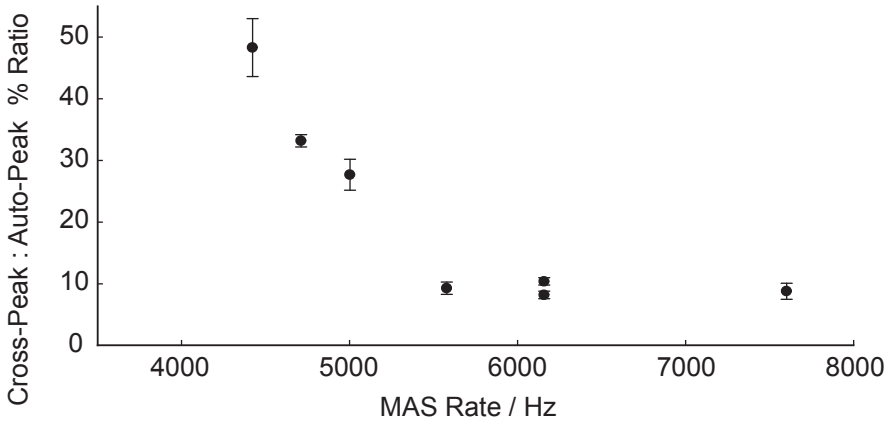

Figure 7-10. The ratio of absolute cross-peak intensity to absolute auto-peak intensity at 100 ms mixing time as a function of MAS rate. The spectra were shown in Fig. 7-9.

shape was not so clear, but the cross-peaks were certainly not purely in-phase absorptive across their entire span. The B3–B3 cross-peaks had roughly the same relative intensity, regardless of spinning speed. However, for MAS rates $\leq$5005 Hz the B3–B3 cross-peaks showed mixed positive and negative intensity.

By visual inspection of the contour-level difference between the auto- and cross-peaks for the slower (Fig. 7-9b) and fastest (Fig. 7-9g) spinning speeds, it is clear that faster spinning reduced magnetisation transfer. This result was confirmed by plotting the ratio of absolute cross-peak intensity to absolute auto-peak intensity as a function of spinning speed, as shown in Fig. 7-10.

7.2 Isotopically Altered $^{10}B/^{11}B$ Spin Diffusion

In the 2D spin diffusion spectra presented above for lithium diborate at natural abundance (80% ^{11}B), each ^{11}B nucleus will have several other ^{11}B nuclei nearby. The consequences of the ^{11}B nuclei not existing as well-isolated spin pairs was already seen in Fig. 6-9, whereby the multiple noncommuting homonuclear dipolar couplings caused lineshape broadening [330]. Polycrystalline lithium diborate with only 25% ^{11}B was synthesised as described in §6.2.2. At this concentration there was a preponderance of ^{11}B–^{11}B spin pairs—see Tab. 6-3. There were also less ^{11}B nuclei to detect, so the number of co-added transients was increased from 8 to 36, such that each spin diffusion experiment took 72 h to acquire.

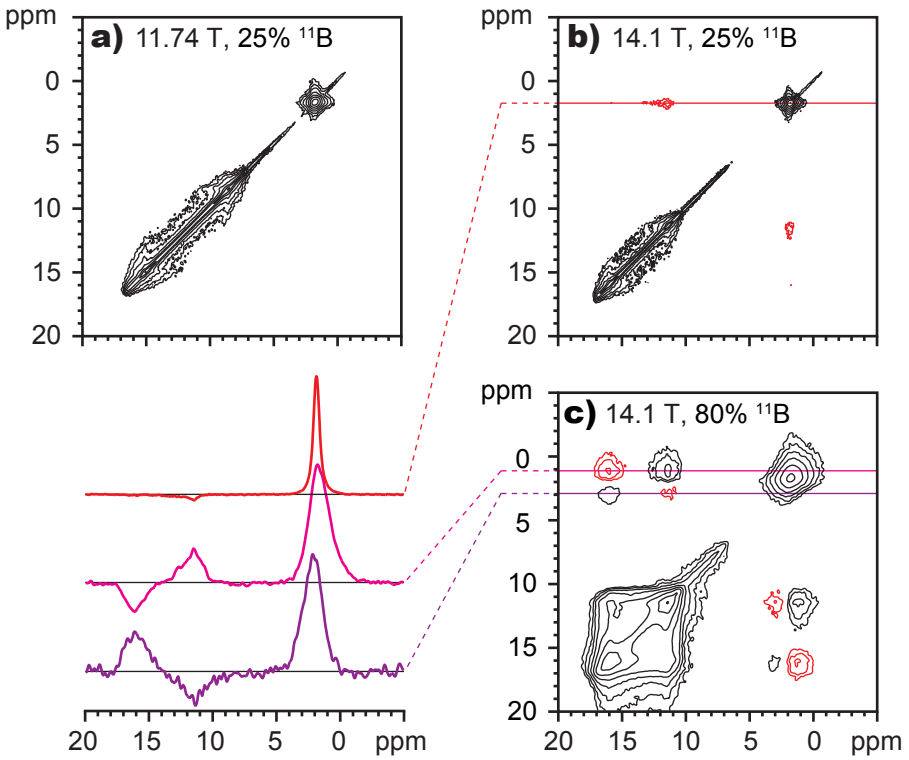

Figure 7-11. ^{11}B MAS NMR rotor-synchronised spin diffusion spectra of lithium diborate at a MAS rate of 6160 Hz and long mixing time of 100 ms. a) 25% ^{11}B, 11.74 T, b) 25% ^{11}B, 14.1 T, c) 80% (natural abundance) ^{11}B, 14.1 T (repeated from Fig. 7-9e). Small negative cross-peaks were visible in spectrum (b) between the B3 and B4 sites. The row slices were normalised to the same B4 peak intensity.

7.2.1 At 14.1 T and 11.74 T

For the long mixing time of 100 ms and a spinning speed of 6160 Hz, two spin diffusion spectra are compared at static magnetic fields of 11.74 T and 14.1 T in Fig. 7-11. The B3 and B4 lineshapes were distinctly resolved at both of these magnetic field strengths. The important differences between the spectra were: the B3 site is narrower at the higher field—as a consequence of the $1/\omega_0$ dependence of the second-order quadrupolar broadening given in Eq. (2-62)—and there were small, negative, cross-peaks in the higher-field spectrum. The intensity of B3–B4 cross-peaks in Fig. 7-11a was, if present at all, far below the 2% base contour level. The B4 auto-peak in Figs. 7-11a and 7-11b, for the 25% ^{11}B sample, much more resembled the theoretical 2D Lorentzian lineshape shown in Fig. 3-6a.

Further information can be deduced by comparison of Fig. 7-11b and its natural abundance equivalent in Fig. 7-11c. The reduction in ^{11}B nuclei

near other ^{11}B nuclei had a substantial effect on the cross-peak intensities. The B3–B4 cross-peaks had noticeably reduced intensity and were negative. A curious feature of these B3–B4 cross-peaks was their specific location, being exactly in line with the B4 auto-peak. Compared to the natural abundance spectrum where the B3–B4 cross-peaks had a $\left(\begin{smallmatrix}-&+\\+&-\end{smallmatrix}\right)$ shape, the reduced-^{11}B spectrum seemed to have purely negative B3–B4 cross-peaks and no mixed positive-negative character at all.

7.2.2 Varying Mixing Time at Fixed MAS Rate

6160 Hz MAS Rate and 11.74 T

For a MAS rate of 6160 Hz, spin diffusion experiments of varying τ_{mix} were recorded at 11.74 T and are presented in Fig. 7-12. With the exception of $\tau_{\text{mix}} =$ 3 ms, spectra are presented for the same mixing times as for the natural abundance lithium diborate at 14.1 T in Fig. 7-2. For consistency, and due to the increased number of co-added transients, this dataset was collected over 18 days contiguously.

With 25% ^{11}B, the auto-peaks were significantly narrower. The sparsity of ^{11}B nuclei greatly reduced the chance of multiple noncommuting homonuclear dipolar couplings. Cross-peaks were conspicuously absent in this series of spectra. At $\tau_{\text{mix}} = 10$ ms, the signal still appeared completely along the diagonal, as in the spectrum at zero mixing time. Compare this result to the equivalent spectrum (Fig. 7-2e) for the natural abundance sample (and 20% higher B_0), which had clear indication of B3–B3 and B3–B4 cross-peaks by 10 ms mixing time. Even for the long mixing time of 100 ms, there was no significant cross-peak intensity.

7.3 DOR Spin Diffusion at 14.1 T

7.3.1 Varying Mixing Time under DOR

From §2.10.2, we know that under DOR the quadrupolar lineshapes are not broadened by the second-order quadrupolar interaction. A diagonal slice of a spin diffusion spectrum will be representative of the 1D DOR spectrum in Fig. 6-

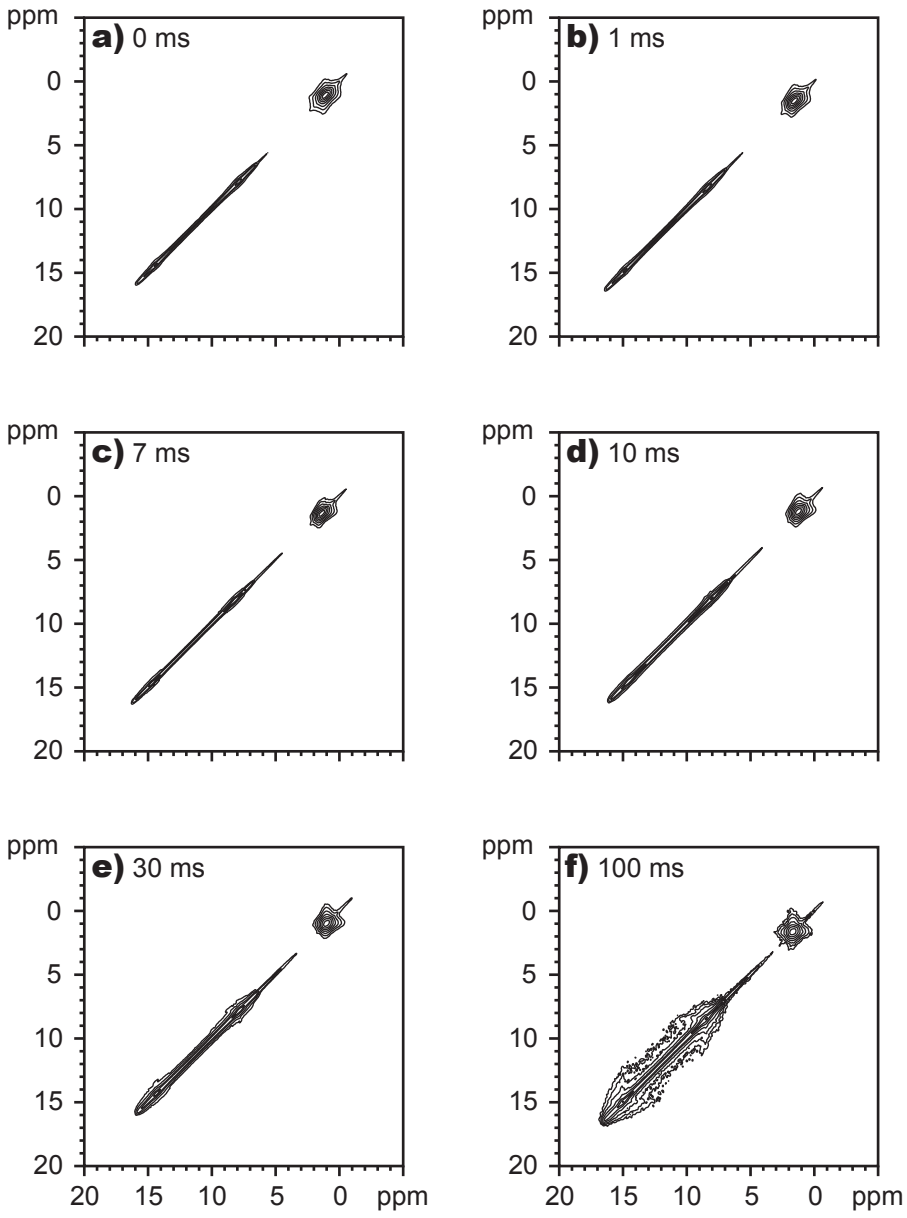

Figure 7-12. ^{11}B MAS NMR rotor-synchronised spin diffusion spectra recorded at 11.74 T. The MAS rate was 6160 Hz. This polycrystalline lithium diborate had an ^{11}B to ^{10}B ratio of 25:75, compared to the natural abundance 80:20 ratio. The transmitter frequency was at 10.8 ppm. As the amount of ^{11}B in the sample was reduced, the number of co-added transients recorded was increased to 36. Both dimensions were Lorentzian broadened 5 Hz. The mixing times were a) 0 ms, b) 1 ms, c) 3 ms, d) 7 ms, e) 10 ms, f) 30 ms, g) 100 ms. Contours increase by $\times$1.75 from a base of 2% of the maximum intensity.

8. In this regime, spin diffusion experiments of varying τ_{mix} were recorded, as shown in Fig. 7-13.

Note that the DOR figures are plotted with a relatively high (40%) base contour level. This was necessary to see the signal peaks above the noise for longer mixing times where dephasing was a severe issue. For $\tau_{\text{mix}} = 1\,\text{ms}$, the noise ceiling was 4% of the maximum signal, compared to 0.4% in the comparable MAS case. The poor signal-to-noise under DOR was partly circumstantial (only using a 2 s recycle delay) and partly due to the smaller sample volume and reduced filling factor available.

For $\tau_{\text{mix}} \geq 50\,\text{ms}$, cross-peaks were clearly present, indicating spin diffusion was occurring. Only the B3–B4 cross-peaks were visible because of the narrow and featureless auto-peaks of the B3 and B4 sites under DOR. For $\tau_{\text{mix}} < 50\,\text{ms}$, cross-peaks were very weak. This contrasts with the MAS case at the similar spinning speed of 4716 Hz, where B3–B4 cross-peaks were detectable after only 3 ms mixing time.

A buildup curve showing magnetisation transfer as a function of mixing time under DOR is shown in Fig. 7-14. The magnetisation transfer under DOR was more complete than under MAS. For the MAS case shown in Fig. 7-8 the cross-peak : auto-peak ratio was $\approx 10\%$ at $\tau_{\text{mix}} = 300\,\text{ms}$. Under DOR, the plateau of magnetisation transfer was around 100%, meaning that the cross-peak : auto-peak ratio was balanced and magnetisation had equilibrated amongst the different sites.

There was an intensity imbalance between the B3 and B4 auto-peaks. Initially, at $\tau_{\text{mix}} = 1\,\text{ms}$, the B4 site had only 84% of the integrated intensity of the B3 site. By $\tau_{\text{mix}} = 1000\,\text{ms}$, this ratio had tipped such that the B4 site was 274% of the intensity of the B3 site. For $\tau_{\text{mix}} = 500\,\text{ms}$, the transfer was measured to be >100%, which is not a feasible steady-state condition. However, at this long mixing time the rapidly-relaxing B3 site is markedly diminished in intensity. This reduction of total auto-peak integrated-intensity artificially skews the ratio, giving rise to—apparently—greater magnetisation transfer.

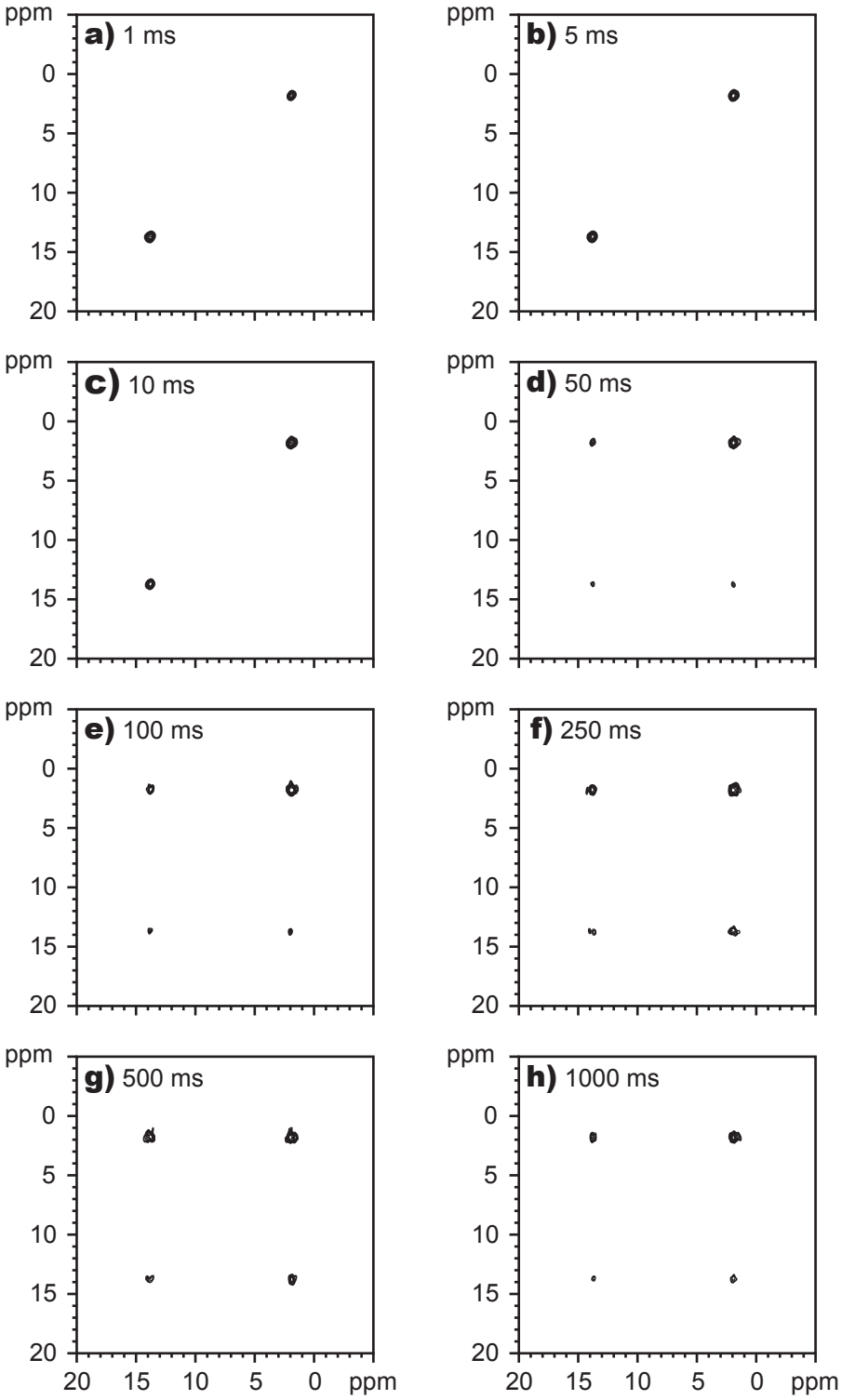

Figure 7-13. ^{11}B DOR NMR spin diffusion spectra recorded at 14.1 T. The mixing times were a) 1 ms, b) 5 ms, c) 10 ms, d) 50 ms, e) 100 ms, f) 250 ms, g) 500 ms, h) 1000 ms. Contours increase by ×1.14 from a base of 40% of the maximum intensity. Dr Ivan Hung is acknowledged for acquiring the DOR data.

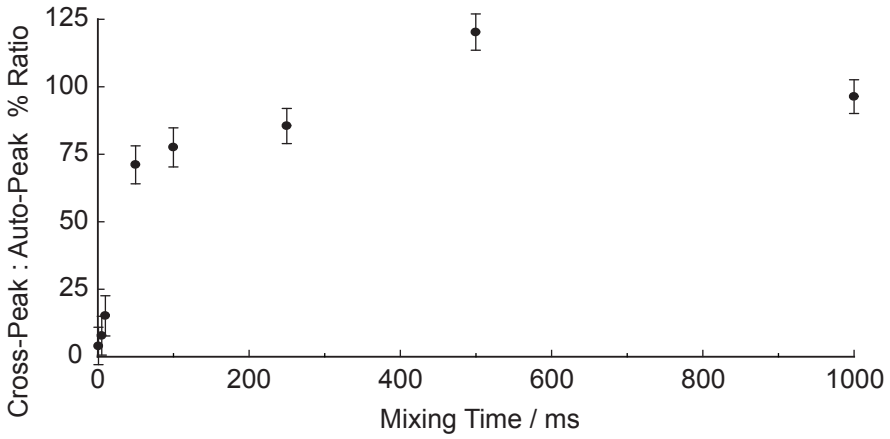

Figure 7-14. The ratio of absolute cross-peak intensity to absolute auto-peak intensity under DOR as a function of mixing time, for spectra shown in Fig. 7-13.

7.4 MAS Spin Diffusion at 7.05 T

For a fixed MAS rate and long mixing time, an ^{11}B spin diffusion spectrum of polycrystalline lithium diborate recorded at 7.05 T is shown in Fig. 7-15. A diagonal slice corresponds to the 1D MAS spectrum in Fig. 6-7a. From this we can assign the small-C_Q B4 site to be peaking around 0 ppm and the singularities of the large-C_Q B3 site around 11 ppm and −9 ppm. The low-intensity tail of the B3 site extends along to the top edge of the spectrum and becomes folded back in. The B3–B4 cross-peaks are most prominent in the spectrum, appearing to the top, bottom, left and right of the B4 peak. Although these peaks could be B3–B3 cross-peaks, such a shape was not seen in the higher field spectra. The centre of the B3 lineshape also had relatively low intensity, such that the cross-peaks related to this area would have also had a similarly low intensity.

The strong B3–B4 cross-peaks seen at 7.05 T in Fig. 7-15 were due to the two chemical sites overlapping. At this $n = 0$ rotational-resonance condition, the dipolar flip-flop transition needed no additional energy balance. If the magnetisation was confined to only the frequency where the lineshapes overlap then the cross-peaks could only appear under the B4 auto-peak. During the course of a rotor period an individual crystallite will be changing direction with respect to the static magnetic field and consequently will be changing frequency too. This frequency is given by Eq. (2-63) and shows that a given crystallite frequency will oscillate, moving back and forth through the lineshape. As all

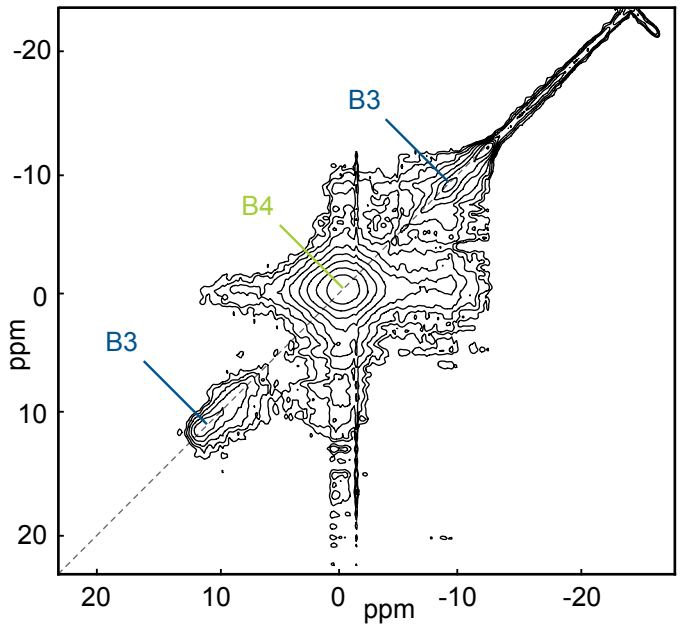

Figure 7-15. An ^{11}B MAS NMR rotor-synchronised spin diffusion spectrum of polycrystalline lithium diborate. Recorded at 7.05 T. The MAS rate was 10 kHz. ^{11}B nutation frequency was around 50 kHz. The recycle delay was 18 s. In t_2, 128 points were acquired and 128 slices in t_1 with 2 co-added transients each. The mixing time was 114 ms. Contours increase by $\times 1.4$ from a base of 2% of the maximum intensity.

possible angles are represented in the powder pattern there are numerous opportunities for crossing crystallites to exchange magnetisation and hence spread the magnetisation across the entire lineshape. Thus, there was efficient exchange of longitudinal magnetisation between the B3 and B4 sites aided by the $n = 0$ rotational-resonance condition.

At 7.05 T, even at long mixing time, the B3–B3 cross-peaks were negligible. This result can be explained aided by comparison with similar spectra at 14.1 T, such as Fig. 7-3h, where B3–B3 cross-peaks were detected. The main difference in experimental conditions was the static magnetic field strength. The central transition is not affected by the first-order quadrupolar interaction [Eq. (2-59)] and there was no change in homonuclear dipolar coupling strength or the rotational-resonance condition. There was a suppression of B3–B3 cross-peak intensity going to lower field because the lineshape was broadened and the isotropic shift was increased. The second-order quadrupolar interaction spread out the frequencies of the crystallites, making efficient exchange of magnetisation between them less likely. The same effect has been noted before on pure

B_2O_3 where B3–B3 cross-peaks were seen at 11.7 T but not 4.7 T [93, Fig. 14].

7.5 Discussion

Spin diffusion in polycrystalline lithium diborate has been investigated under MAS for varying magnetic field strength, varying spinning speed, varying mixing time, differing isotopic abundance and under DOR. Spin diffusion was allowed to proceed naturally—no attempt was made to actively recouple the dipolar interaction with RF. To summarise the key experimental observations:

- Spin diffusion (B3–B3 and B3–B4) was reduced by faster MAS rates, both in the buildup rate and final magnetisation transfer.
- At long mixing times for MAS rates from 4427 Hz to 7602 Hz at 14.1 T, the B3–B4 cross-peaks had a $\binom{-+}{+-}$ shape. Mixed positive and negative intensity was also observed for the B3–B3 cross-peaks at MAS rates of 4427 Hz and 5005 Hz at 14.1 T.
- At zero mixing time for natural abundance ^{11}B, faster spinning narrowed the auto-peaks.
- Reducing the ^{11}B isotopic abundance to 25% (where isolated spin-pairs are predominant) diminished the intensity of the B3–B4 cross-peaks.
- The auto-peaks were much narrower for reduced ^{11}B isotopic abundance.
- Spin diffusion under DOR at 14.1 T was efficient with ≈100% magnetisation transfer at $\tau_{\text{mix}} = 1000$ ms.
- The B3 and B4 lineshapes overlap at 7.05 T—the $n = 0$ rotational resonance condition—giving rise to strong B3–B4 cross-peaks.
- B3–B3 cross-peaks were not evident at 7.05 T.

7.5.1 Spin Diffusion at Long Mixing Time

For the natural abundance sample at long mixing times and 14.1 T, B3–B3 and B3–B4 cross-peaks were visible at the tested MAS rates and under DOR, as

presented in, e.g. , Figs. 7-1g, 7-2g, 7-3h and 7-13h. The presence of cross-peaks indicated that magnetisation exchange occurred, implying that the involved nuclei were close in space and an energy-balancing mechanism was present.

Compared to the high-field natural abundance spectra shown in Fig. 7-2, at a magnetic field strength of 7.05 T only the B3–B4 cross-peaks were visible in Fig. 7-15. Thus, the B3–B3 spin diffusion mechanism depended on the field strength. With depleted ^{11}B a severe reduction of cross-peak intensity was seen in Fig. 7-12f, attributable to the diminished probability of ^{11}B nuclei being close in space. Where strong cross-peaks were seen in other spectra, the potential spin diffusion mechanisms can be examined. These mechanisms were initially mentioned in §3.7. For lithium diborate, there were no protons in the sample so a strong heteronuclear dipolar field was not the spin diffusion mechanism. The CSA and cross terms[1] were negligible. No RF was applied during mixing. The remaining spin diffusion mechanisms were the first- and second-order quadrupolar interactions, strong noncommuting homonuclear dipolar couplings and rotational-resonance conditions.

Generally, the shape of the cross-peaks contains information about the relative tensor orientation between the quadrupolar nuclei [75]. Such an analysis is beyond the scope of this thesis. Note that DFT calculations have given the ^{11}B quadrupolar tensor orientations for lithium diborate [124, Fig. 4a].

For the higher field of 14.1 T the B3 and B4 lineshapes did not overlap because of the decreased second-order quadrupolar broadening and isotropic shift. An energy balance mechanism must have been involved to explain the presence of B3–B4 cross-peaks. The spinning speeds used were much greater than the $n = 1$ rotational-resonance condition, occurring between 1600 Hz to 2900 Hz MAS rate. Hence the remaining possible spin diffusion mechanisms were multiple noncommuting homonuclear dipolar couplings and the quadrupolar interaction. The latter mechanism prevents MAS from completely averaging the dipolar interaction to zero because of the noncommutation of the I_z^2 term in the quadrupolar interaction [Eq. (2-53)] with the flip-flop portion of the dipolar interaction [Eq. (2-37)].

[1] Such as $\hat{\mathscr{H}}^{\mathrm{L}}_{\mathrm{Q}\times\mathrm{D}}$ that arise from the full quadrupolar and dipolar Hamiltonians in the laboratory frame.

Effect of Isotopic Enrichment

A dramatic effect occurred when the abundance of ^{11}B in the sample was reduced from 80% to 25%; this almost entirely removed the multiple noncommuting homonuclear couplings that broaden the auto-peaks and could contribute to magnetisation exchange. For the same spinning speed and magnetic field strength two degrees of ^{11}B abundance were presented in Fig. 7-11. Both showed B3–B4 cross-peaks. For the 25% ^{11}B sample these cross-peaks were much reduced in intensity and showed small negative intensity, for the 80% ^{11}B sample the B3–B4 cross-peaks had a distinctive $\binom{-+}{+-}$ shape.

Varying MAS Rate

For a long mixing time, the effect of varying MAS rate was shown in Fig. 7-9. Both B3–B3 and B3–B4 cross-peaks were detectable at MAS rates of 4427 Hz to 7602 Hz. The B3–B4 cross-peaks all appeared with a similar $\binom{-+}{+-}$ pattern over the MAS rates tested as well as for different spectrometers[2] and additional samples of polycrystalline lithium diborate, variously doped with iron, copper or cobalt (not shown). At faster spinning speeds, the B3–B4 cross-peak intensity was slightly reduced, which hints at an involvement of multiple noncommuting dipolar couplings as discussed on the following page.

The B3–B3 cross-peaks were positive for MAS rates *geq* 5582 Hz and negative for MAS rates less than this, over the experimental range presented. The absence of negative intensity and increase in cross-peak intensity as the MAS rate was increased is not characteristic of multiple noncommuting dipolar couplings. However, the process of forming cross-peaks containing regions of negative intensity, at certain MAS rates, is not yet understood.

7.5.2 Varying Mixing Time

Having examined spin diffusion spectra at zero and long mixing times, now the focus will be on the changes that occur during the transition between these extremes. Three MAS rates and one DOR case were presented in Figs. 7-1, 7-2, 7-3 and 7-13 along with a complementary buildup series at 11.74 T and only

[2]Some experiments were performed in St Andrews, still at 14.1 T.

25% ^{11}B in Fig. 7-12. In all cases where spin diffusion was detected, the process took tens or hundreds of ms to reach an equilibrium. Note that proton- or RF-driven spin diffusion, which are not acting here, occurs much faster than this, on the ms timescale. Where detectable, both B3–B3 and B3–B4 cross-peaks build up over a similar timescale.

For faster spinning speeds the rate of magnetisation transfer was slower. The first visible[3] B3–B4 cross-peaks were at 3 ms for a MAS rate of 4716 Hz, 7 ms for 6160 Hz and 10 ms for 7602 Hz. Quadrupolar-driven spin diffusion and multiple noncommuting homonuclear dipolar couplings would both be expected to be affected by a change in MAS rate.

Another, briefly mentioned, mechanism not affected by any spinning is the quadrupole-dipole cross-term, $\hat{\mathscr{H}}^{\mathrm{L}}_{\mathrm{Q}\times\mathrm{D}}$. The terms in this Hamiltonian are proportional to $C_{\mathrm{Q}}b_{jk}/\omega_0$ [309, Eq. (19)]. As the quadrupolar interaction is not squared as the other second-order terms are, this mechanism only has a strength of a few Hz in lithium diborate at this field. Therefore, despite its constant presence, the transfer of magnetisation is expected to be uninfluenced by such quadrupole-dipole cross-terms. This mechanism is not further considered.

The effect of varying mixing time under DOR was shown in Figs. 7-13 and 7-14. Notably, the detected B3–B4 cross-peaks were positive throughout. Compare this to MAS, where the second-order quadrupolar broadening is present and a $\left(\begin{smallmatrix}-&+\\+&-\end{smallmatrix}\right)$ shape appeared. Whether or not the second-order quadrupolar interaction is causing the mixed positive and negative intensity under MAS, the second-order quadrupolar broadening was required to observe the shape of the cross-peaks. The lack of cross-peak detail under DOR precludes the extraction of tensor orientations, but does give information on the number and distribution of sites. In lithium diborate there is just one B3 and one B4 site. If there were a distribution of B3 sites, such as in vitreous B_2O_3, they could be clearly separated and potential spin diffusion between the sites can be detected [140, Fig. 3].

[3] i.e. cross-peak intensity > 2%

7.5.3 On The Origins of Negative Cross-Peaks

In a spin diffusion experiment without active recoupling, mixed positive and negative cross-peaks between quadrupolar nuclei have not been seen before, to the best knowledge of the author. Concerning ^{11}B, previous reports include B_2O_3 at 11.7 T and 10 kHz/14.5 kHz MAS rates [93], BCN at 21.8 T and 10 kHz/16 kHz MAS rates [236], as well as borax at 11.7 T and 20 kHz MAS rate [235]. Where cross-peaks were seen, none had negative intensity or resemblance to a $\left(\begin{smallmatrix}-&+\\+&-\end{smallmatrix}\right)$ pattern.

Negative cross-peaks are, however, commonly seen in solution-state NMR where there is fast molecular motion and it is the nuclear Overhauser effect that causes the magnetisation transfer [198, §4(a)(i)]. Such a mechanism cannot be possible in solid-state NMR, where any motion at all would be far from the ns timescale required.

Regardless of transfer mechanism, zz antiphase magnetisation can exist if the proximate nuclei also have a J-coupling. For the spin $I = 1/2$ case this can be seen in the product operator formalism given in §A.2. Critically, the existence of a resolved J-coupling between the two nuclei is a sufficient and necessary condition for the appearance of zz signals [44]. As the J-coupling between the B3 and B4 nuclei in lithium diborate is negligible[4], zz signals are unlikely to account for the $\left(\begin{smallmatrix}-&+\\+&-\end{smallmatrix}\right)$ shape seen in the spin diffusion spectra presented above. Additionally, comparison with Ref. [44, Fig. 4c] indicates the polarity of the cross-peak shape caused by this mechanism is reversed from that seen above, which further reduces the likelihood that this particular mechanism is involved.

It is known that the double-quantum *flop-flop* Hamiltonian gives rise to negative cross-peaks. This has been shown for isolated pairs of spin $I = 1/2$ nuclei where RF pulses were used to disrupt the MAS averaging of the dipolar interaction and promote DQ coherences [28]. The DQ nature of the magnetisation exchange means that cross-peaks from direct exchange have negative intensity, whilst exchange via a mutual coupling results in a positive cross-peak [288]. Also, the cross-peaks would appear in several ms rather than tens or

[4]The J-coupling magnitude is revealed in §8.2.2.

hundreds of ms, because of the efficiency of the RF-driven exchange. RF-driven exchange between half-integer quadrupolar nuclei also results in negative cross-peak intensities, because of the DQ recoupling effect [27]. However, in the experiments above no RF is applied during the mixing time and the phase cycle explicitly excludes DQ coherences, ruling out involvement from the flop-flop Hamiltonian.

Without RF-driven DQ recoupling, J-coupling or the nuclear Overhauser effect, what other mechanism exists to explain negative cross-peaks in the spin diffusion experiment? A high-order 4-spin process could become dominant if the normal 2-spin process is suppressed. This was observed in ^{19}F spectra of inorganic fluorides, at 4.7 T/8.4 T and 23 kHz/18 kHz MAS rates, respectively [76]. Simulations of this phenomena are given below in §9.3.

The 4-spin process involves four coupled spins, divided into two groups of two. Each pair has a similar chemical shift and the groups themselves are separated apart. The exchange occurs when both pairs flip-flop simultaneously, e.g. $|\alpha\beta\beta\alpha\rangle \leftrightarrow |\beta\alpha\alpha\beta\rangle$. Thus, it is the polarisation difference between a spin-pair that exchanges with another pair. Importantly, the theory of 4-spin exchange reveals that the pattern of the four cross-peaks has a $\left(\begin{smallmatrix}-&+\\+&-\end{smallmatrix}\right)$ shape [76, Eqs. (28) and (29)]. This is the same pattern as the two-site spin diffusion seen between quadrupolar nuclei above. In this quadrupolar case, however, the four peaks are not from four separate spins but two separated sites, one of which has significant second-order quadrupolar broadening. If two B3 spins and two B4 spins were in a favourable arrangement, maybe this 4-spin process could occur. The idea is feasible for certain, instantaneous, crystallite orientations, but the effect MAS will have—continually changing a crystallite's frequency—on the process is unclear at this stage.

The B3–B4 cross-peaks maintained a $\left(\begin{smallmatrix}-&+\\+&-\end{smallmatrix}\right)$ shape regardless of mixing time. This is most clearly seen in the row slices of the spectra shown in Figs. 7-4, 7-5 and 7-6. The mechanism or mechanisms responsible for this shape appear to have acted at the same rate during the mixing time.

Furthermore, from the 25% ^{11}B spin diffusion results presented in Fig. 7-11b there were negative B3–B4 cross-peaks that did not appear in a $\left(\begin{smallmatrix}-&+\\+&-\end{smallmatrix}\right)$ shape. With this level of isotopic abundance the probability of four ^{11}B nuclei in close

proximity is very small (3%), which discounts the spin diffusion mechanisms of multiple homonuclear dipolar coupling and possibly a high-order 4-spin process. Notably, for the decreased magnetic field strength of 11.74 T the B3–B4 cross-peaks disappear entirely. This field-dependent behaviour was seen for the B3–B3 cross-peaks which were determined to be driven by the quadrupolar interaction. The implication is that the mixed positive and negative B3–B4 cross-peaks are allowed to be seen by the second-order quadrupolar broadening. Therefore, the full $\binom{-+}{+-}$ shape seen in the spin diffusion spectra of lithium diborate was a result of the complicated interplay involving various quadrupolar and dipolar interactions.

7.5.4 Outlook

Where the spin diffusion mechanism is known, such as in a spin $I = 1/2$ case with chemical exchange, the auto- and cross-peak integrals can be used to determine a rate matrix from just one mixing time [158]. Because of the added complications imposed by solid-state NMR, the quadrupolar interaction and multiply connected spins, this quantitative approach was not employed here. Nevertheless, by varying the mixing time closer spins will exchange magnetisation faster for a given spin diffusion mechanism.

Ideally, there would be a quantitative model describing the spin diffusion between the B3 and B4 sites as well as accounting for the relaxation suffered during the mixing time. Then, for a given mixing time, the relaxation-corrected spectrum at zero mixing time could be subtracted leaving only the areas where magnetisation had transferred. By integrating these areas and fitting the resultant curve to the free parameters of a spin diffusion model, the internuclear distances could be extracted. In practice, even for a model compound, this approach is complicated by the intricate interplay of quadrupolar and dipolar interactions as well as the multiple noncommuting spins. The latter detail inhibits a direct application of theory constructed for isolated spin pairs and there is need for further research.

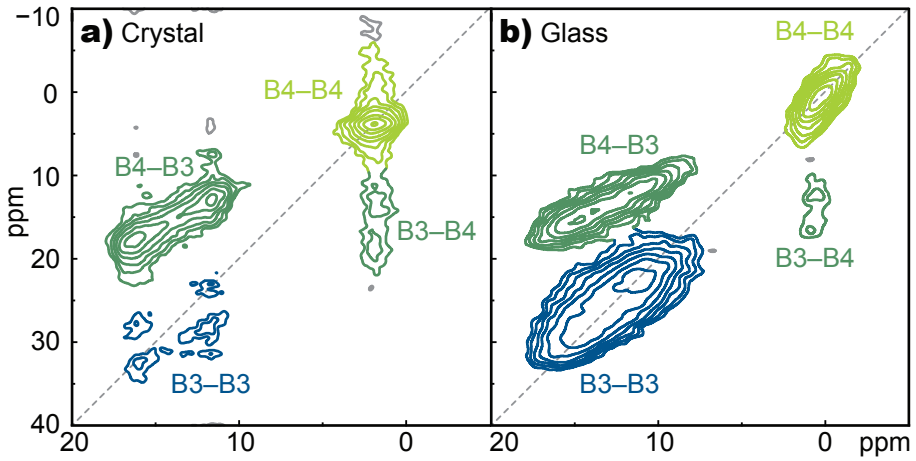

Figure 7-16. ^{11}B MAS NMR double-quantum homonuclear dipolar recoupling spectrum of a) polycrystalline $Li_2O{\cdot}2B_2O_3$ and b) $x = 25$, $xLi_2O{\cdot}(100-x)B_2O_3$ glass. Recorded at 14.1 T and an MAS rate of 10 kHz. Further experimental details were given in §5.2.4. Spectra were recorded collaboratively with Dr Ivan Hung.

7.6 Double Quantum Homonuclear Dipolar Recoupling

Experiments such as spin diffusion (e.g. NOESY-like) correlate single-quantum coherences. When integrating volumes it is not obvious how much of a diagonal peak is auto-peak and how much is a self cross-peak. For lineshapes without any second-order quadrupolar broadening the entire cross-peak would lie beneath the auto-peak, making a through-space correlation impossible to verify. Double-quantum correlation experiments escape this problem by only recording magnetisation due to pairs of coupled nuclei; there are no auto-peaks.

The double-quantum homonuclear dipolar recoupling experiment (§5.2.4) was performed on polycrystalline $Li_2O{\cdot}2B_2O_3$ and $x = 25$, $xLi_2O{\cdot}(100-x)B_2O_3$ glass. The spectra are presented in Fig. 7-16. All three correlations are clearly visible; B3–B4, B3–B3, B4–B4. The latter correlation proving conclusively that the B4 sites in lithium diborate have a through-space dipolar coupling; a fact hidden by the auto-peak in a spin diffusion experiment.

Comparing the spectra of the glass to that of the crystal, the same correlation peaks are visible. However, the B3–B3 correlation peak is attenuated for the crystal. This is because the glass structure consists of several connected superstructural units such as; boroxol, triborate and dipentaborate groups—

shown in Fig. 6-2. These units all contain a B3 atom bonded (via one oxygen atom) directly to another B3 atom. However, in the crystal structure the B3 atoms are always bonded via B4 atoms and never directly, as can be seen from the crystal structure given in Fig. 6-4. This increased distance between the B3 sites causes the attenuation of the B3–B3 correlation peak seen in Fig. 7-16a.

The peaks are broader in the spectrum of the vitreous compound because of the inherent disorder of the glass network. All sites show chemical shift dispersion, especially the B4–B4 peak that is narrow in the crystal, indicating a range of bond lengths and angles between the boron and oxygen atoms. The B3 peaks exhibit a combination of chemical shift dispersion and second-order quadrupolar broadening.

Further notable features in the comparison of the spectra are the shift of the B4 site to higher ppm values upon crystallisation, showing small structural changes to this high symmetry site. This effect has recently been noted for the same system studied here, $Li_2O{\cdot}2B_2O_3$ [64].

CHAPTER 8

Spin Echoes, Dephasing and J-Coupling

Spin-echo MAS experiments (§3.4) are used here to investigate the refocussed (T_2') coherence dephasing time in polycrystalline lithium diborate as a function of spinning speed and isotopic abundance. Dephasing mechanisms are examined and parallels to spin diffusion mechanisms were noted because of the similar involvement of the dipolar and quadrupolar interactions. J-modulation of the spin-echo dephasing curve, that would reveal through-bond connectivities, was not seen; a result commensurate with the very small J-couplings as revealed by first-principles calculations.

8.1 Spin-Echo Dephasing

Using ^{11}B MAS NMR, spin-echo experiments were performed on polycrystalline lithium diborate with three degrees of ^{11}B isotopic abundance; 5%, 25% and 100%. The long T_1 relaxation time of ^{11}B nuclei in this sample (§6.4) necessitated that saturation pulses were used, as previously detailed in §5.2.5. The synthesis method of the samples was given above in §6.2.2. Normalised spin-echo dephasing curves at 14.1 T and 20 kHz MAS rate for these samples are presented in Fig. 8-1. At 14.1 T the B3 and B4 lineshapes are distinct, as shown in Fig. 6-7b, hence separate dephasing behaviour can be determined for the B3 and B4 sites. Note that the chief difference between the sites is C_Q—2.56 MHz

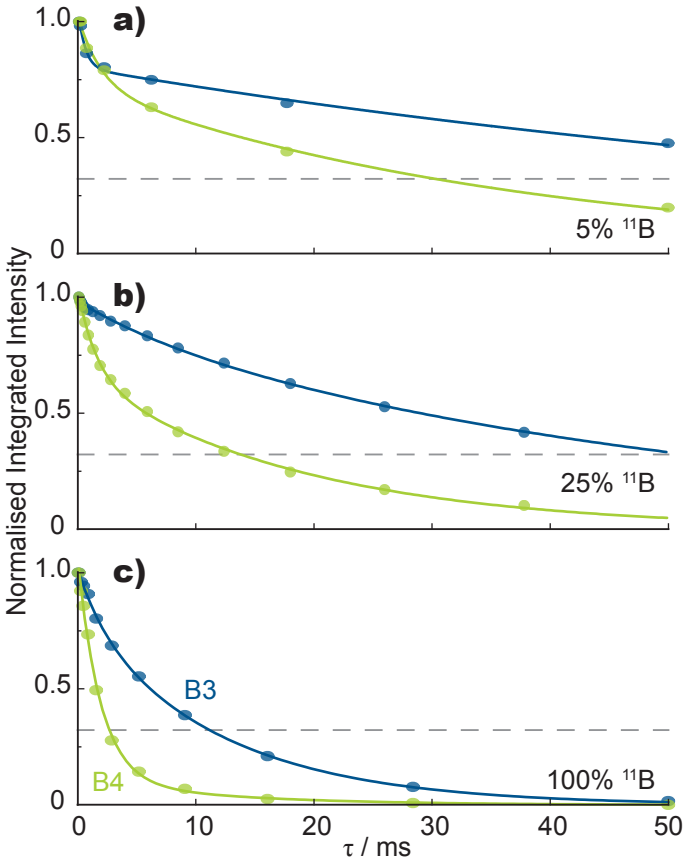

Figure 8-1. Normalised spin-echo dephasing curves for polycrystalline lithium diborate at 14.1 T and 20 kHz MAS rate, with varying degrees of ^{11}B abundance; a) 5% ^{11}B, b) 25% ^{11}B, c) 100% ^{11}B. The high field allows separate dephasing rates to be measured for the resolved B3 (blue) and B4 (green) chemical sites. For the shortest τ, times the signal-to-noise ratio was >100 for both B3 and B4 sites in all samples, therefore the associated uncertainty in the integrated intensity is well within the shown datapoints. The data were fitted (solids lines) to the bi-exponential function given by Eq. (8-2) with the fit parameters in Tab. 8-1.

for B3 and 0.51 MHz for B4.

For the 100% ^{11}B enriched polycrystalline lithium diborate sample, spin-echo experiments were performed at MAS rates of 5 kHz, 10 kHz, 16 kHz and 20 kHz. These spinning speeds correspond to initial[1] τ durations of 400 µs, 200 µs, 125 µs and 100 µs, respectively. The normalised spin-echo dephasing curves are presented in Fig. 8-2. For a given number of measurement points and final τ value, the number of rotor-synchronised τ points were spaced logarithmically to improve resolution at shorter τ times where dephasing is fastest.

A normalised spin-echo dephasing curve with τ durations up to 250 ms for 25% ^{11}B polycrystalline lithium diborate at 14.1 T and 20 kHz MAS rate is

[1] One rotor period

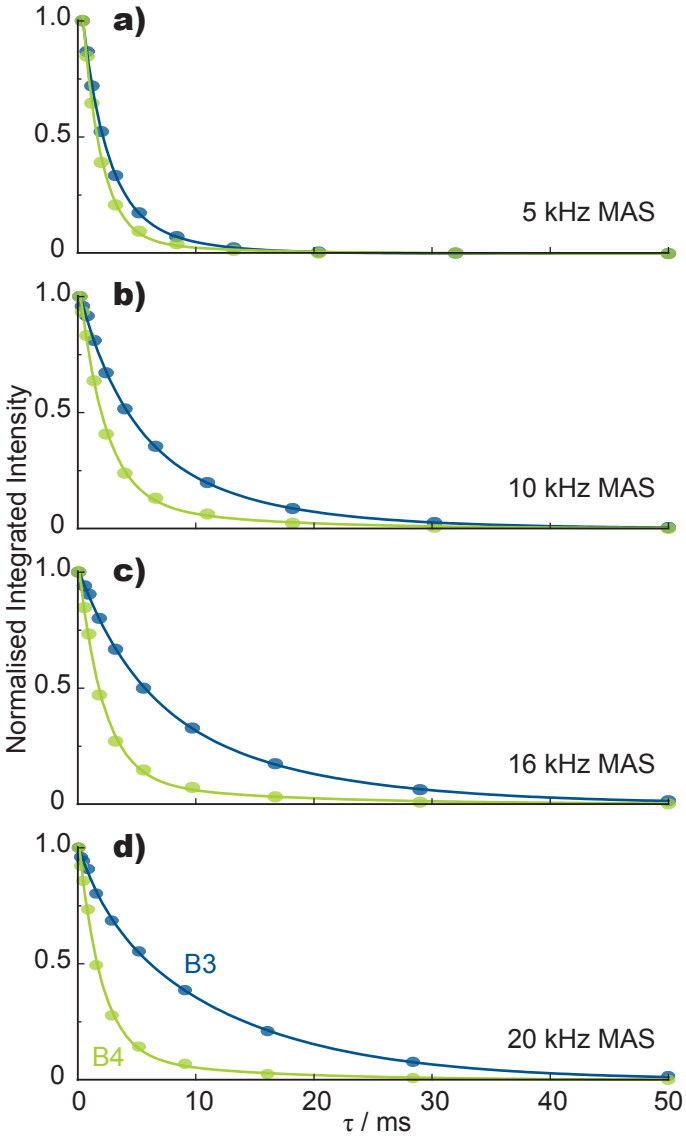

Figure 8-2. Normalised spin-echo dephasing curves for 100% ^{11}B polycrystalline lithium diborate at 14.1 T. MAS rates were; a) 5 kHz, b) 10 kHz, c) 16 kHz, d) 20 kHz. For the shortest τ times the signal-to-noise ratio was >200 for both B3 and B4 sites, therefore the associated uncertainty in the integrated intensity is well within the shown datapoints. The bi-exponential best-fit curves (solids lines) are parameterised in Tab. 8-2.

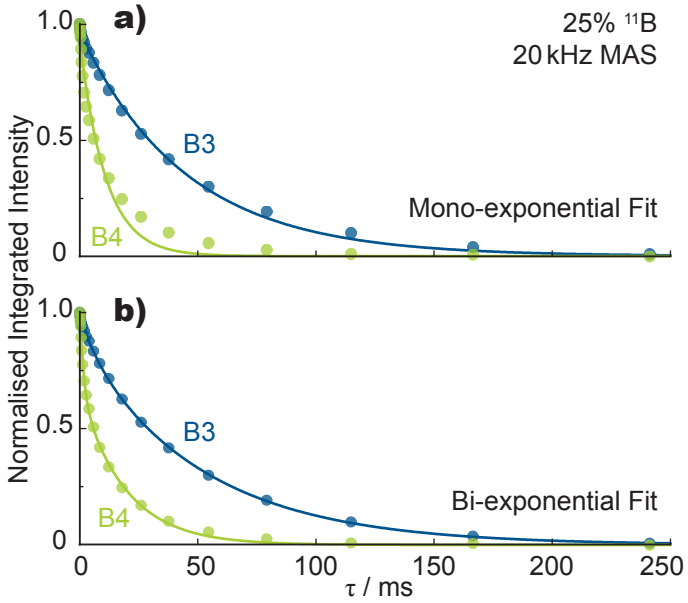

Figure 8-3. Normalised spin-echo dephasing curves for 25% ^{11}B polycrystalline lithium diborate at 14.1 T, 20 kHz MAS rate, for the B3 site (blue) and the B4 site (green). a) Ill-fitting mono-exponential fit, b) Bi-exponential fit.

shown in Fig. 8-3. Two non-linear curves were separately fitted to the data; a mono-exponential curve given by Eq. (8-1) and a bi-exponential curve given by Eq. (8-2).

$$S(\tau) = A\mathrm{e}^{-\tau/T_2'} \tag{8-1}$$

$$S(\tau) = A\left(p\mathrm{e}^{-\tau/T_{2a}'} + (1-p)\mathrm{e}^{-\tau/T_{2b}'}\right) \tag{8-2}$$

where $0 \leq p \leq 1$ describes the proportion of the faster dephasing component, A is a normalising constant and τ is the rotor-synchronised spin-echo duration from the first 90°-pulse to acquisition as described in Fig. 5-1.

There was a poor fit for the mono-exponential decay curve shown in Fig. 8-3a, especially for the B4 site at longer τ times. A bi-exponential decay curve fitted to the same data produced very good best-fit curves. Parameters of the bi-exponential best-fit for the data shown in Figs. 8-1 and 8-2 are given in Tabs. 8-1 and 8-2. Although T_{2b}'—the slow-dephasing component—was small, it was crucial to fit the data satisfactorily. The correlation coefficients of the fits are given in Tab. 8-3 revealing a high correlation between p and the T_2' times. Care must be taken when interpreting variations in p between different fits.

Considering Figs. 8-1 and 8-2 as well as Tabs. 8-1 and 8-2, the key obser-

Table 8-1. Fit parameters to Eq. (8-2) of spin-echo dephasing curves for polycrystalline lithium diborate with varying degrees of ^{11}B abundance, at 14.1 T and 20 kHz MAS rate, as shown in Fig. 8-1.

Site	^{11}B	A	p	$T_{2a}^{'}$ in ms	$T_{2b}^{'}$ in ms
B3	5%	1.04±0.02	0.23±0.02	0.6±0.1	92.7±6.6
B3	25%	0.98±0.01	0.11±0.02	7.8±2.1	51.8±1.6
B3	100%	1.02±0.01	0.20±0.05	2.2±0.7	12.1±0.7
B4	5%	1.02±0.02	0.29±0.04	1.9±0.6	37.2±4.2
B4	25%	1.03±0.01	0.35±0.02	1.6±0.1	19.0±0.7
B4	100%	1.07±0.02	0.90±0.07	1.9±0.2	12.4±9.9

Table 8-2. Fit parameters to Eq. (8-2) for spin-echo dephasing in 100% ^{11}B polycrystalline lithium diborate, at 14.1 T for varying MAS rate, as shown in Fig. 8-2. Correlation between $T_2^{'}$ values and p are all > 0.9.

Site	MAS in kHz	A	p	$T_{2a}^{'}$ in ms	$T_{2b}^{'}$ in ms
B3	5	1.19±0.01	0.79±0.12	2.0±0.2	5.8± 1.8
B3	10	1.04±0.01	0.53±0.19	3.8±0.8	10.3± 2.1
B3	16	1.02±0.01	0.52±0.13	4.8±0.8	13.6± 1.8
B3	20	1.02±0.01	0.20±0.02	2.2±0.7	12.1± 0.7
B4	5	1.29±0.04	0.95±0.07	1.6±0.2	9.4±12.5
B4	10	1.11±0.02	0.88±0.10	2.2±0.3	11.4± 8.7
B4	16	1.08±0.02	0.90±0.08	2.1±0.3	13.8±12.6
B4	20	1.07±0.02	0.90±0.07	1.9±0.2	12.4± 9.9

Table 8-3. Correlation coefficients of variables used to fit bi-exponential spin-echo dephasing curves in Figs. 8-1 and 8-2. ^{11}B column indicates level of isotopic abundance, MAS rate is in kHz. Values close to ±1 indicate the two parameters are correlated, whilst a zero value indicates that the two parameters are independent.

^{11}B	MAS	Site	Ap	$AT_{2a}^{'}$	$AT_{2b}^{'}$	$pT_{2a}^{'}$	$pT_{2b}^{'}$	$T_{2a}^{'}T_{2b}^{'}$
100%	5	B3	−0.56	−0.72	−0.49	0.97	0.97	0.91
100%	5	B4	−0.50	−0.77	−0.40	0.90	0.94	0.78
100%	10	B3	−0.42	−0.55	−0.37	0.97	0.98	0.92
100%	10	B4	−0.41	−0.63	−0.33	0.92	0.94	0.80
100%	16	B3	0.39	−0.34	−0.53	−0.98	−0.97	0.91
100%	16	B4	−0.34	−0.60	−0.26	0.89	0.92	0.76
100%	20	B3	0.27	−0.29	−0.59	−0.93	−0.89	0.79
100%	20	B4	0.35	−0.28	−0.60	−0.92	−0.90	0.76
25%	20	B3	0.18	−0.22	−0.49	−0.92	−0.87	0.76
25%	20	B4	0.08	−0.24	−0.65	−0.85	−0.70	0.65
5%	20	B3	−0.70	−0.15	−0.74	−0.37	0.23	0.37
5%	20	B4	−0.05	−0.18	−0.56	−0.79	−0.64	0.58

vations were:

- The B3 site dephased slower than the B4 site in lithium diborate at all investigated spinning speeds.
- The dephasing time was shortened for both sites as the ^{11}B isotopic abundance was enriched.
- Speeding up the MAS rate from 5 kHz to 20 kHz prolonged the spin-echo dephasing time for the B3 site much more significantly than the B4 site.

These observations are discussed further in §8.3 after the effects of pulse duration and strength are presented.

Recalling Fig. 3-1, sites with greater values of C_{Q} nutate faster than those with lesser values. As the spin-echo experiment calls for a 180°-pulse there is a choice of which site to optimise. The data shown above were optimised for the B3 site. With identical experimental variables, except pulse length, the spin-echo experiments shown in Figs. 8-2a and 8-2d were repeated. A longer pulse length was used to optimise the 180°-pulse for the B4 site. However, it was found that the duration of the soft pulse had essentially no effect on the normalised integrated intensity dephasing curves. In this context, a 16-step phase cycle ensured only the $0 \rightarrow +1 \rightarrow -1$ coherence transfer pathways were selected. Thus, imperfect 180°-pulses are only expected to affect the intensity and not the rate of coherence dephasing.

The spin-echo experiments above used soft pulses, such that $\omega_{\mathrm{Q}} \gg \omega_{\mathrm{nut}}$. The effect on the spin-echo dephasing curve of increasing the RF pulse power to approach the hard pulse limit is shown in Fig. 8-4. The comparative soft pulse data from Fig. 8-2d is overlaid.

Hard pulses reduced the coherence dephasing time. The reduction was greater for the B4 site, which was more in the hard-pulse limit than the B3 site. That is, for the B4 site: $\frac{\omega_{\mathrm{Q}}/2\pi}{\omega_{\mathrm{nut}}/2\pi} = \frac{85\,\mathrm{kHz}}{120\,\mathrm{kHz}} = 0.7$, whereas for the B3 site: $\frac{\omega_{\mathrm{Q}}/2\pi}{\omega_{\mathrm{nut}}/2\pi} = \frac{426\,\mathrm{kHz}}{120\,\mathrm{kHz}} = 3.5$, which is merely near the hard pulse limit. As hard pulses can alter the populations of the satellite transitions, conceivably this provides an additional mechanism through which the central transition coherence can relax and dephase. As the satellite transitions of the B4 site were more affected

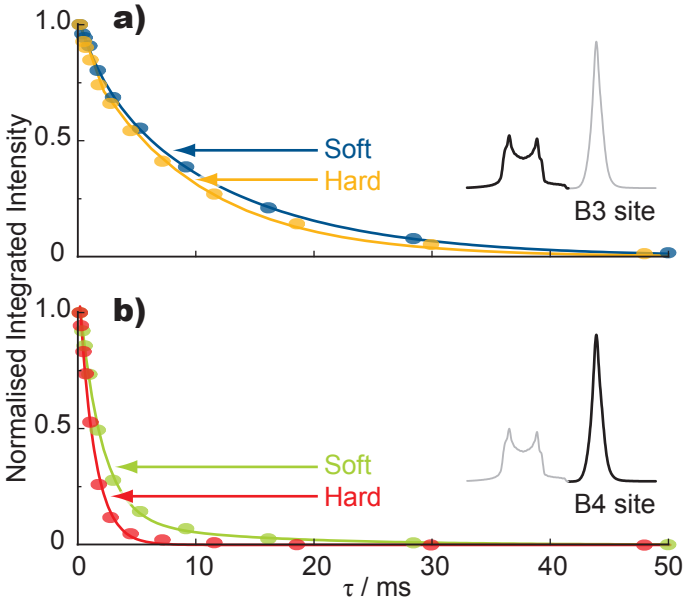

Figure 8-4. Normalised spin-echo dephasing curves as in Fig. 8-2d—at 20 kHz MAS for a) the B3 site, and b) the B4 site. The difference between hard (red and orange) and soft (green and blue) pulses is shown.

by the hard pulses the increase in dephasing was enhanced, compared to the B3 site. Differences in spin-echo dephasing between the B3 and B4 sites are addressed by simulations in Ch. 9.

8.2 J-Coupling

8.2.1 Spin-Echo Experiment

Spin-echo experiments could, in principle, detect a $^2J_{\mathrm{BB}}$-coupling via a cosine-modulation of the dephasing curve that would lead to zero crossings. For the 25% ^{11}B, sample 22 τ points were recorded out to 250 ms. The results of this 75 h spin-echo experiment are presented in Fig. 8-5 on a semi-log plot.

Despite near-ideal conditions a zero-crossing was not seen. This puts an upper limit on the size of $^2J_{\mathrm{BB}}$ to be approximately $\frac{1}{2\tau} = 5$ Hz. In fact the upper limit can be made even smaller than this if the requirement is to detect even slight J-modulation of the dephasing curve via a least-squares fit. As no modulation was found it is determined that $^2J_{\mathrm{BB}} < 3$ Hz in polycrystalline lithium diborate.

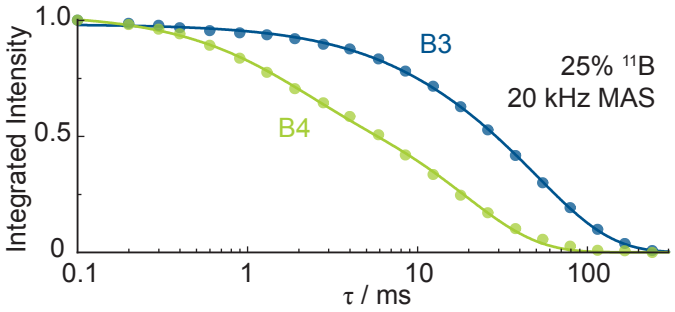

Figure 8-5. A semi-log plot of Fig. 8-3b to emphasise the initial τ values.

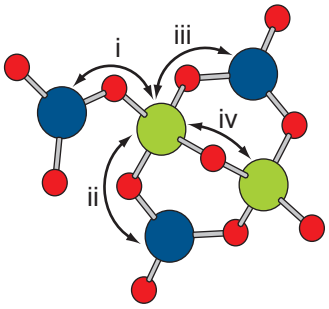

Figure 8-6. A diborate unit, with an extra neighbouring B3 atom, from a $Li_2O{\cdot}2B_2O_3$ crystal structure [277]. All four distinct $^2J_{BB}$-couplings are indicated. Three-coordinated boron is shown in blue, four-coordinated boron is shown in green and bridging oxygen is shown in red.

8.2.2 *J*-Coupling Calculations

First-principles calculations [160] performed by Dr Jonathan Yates were used to determine the J-coupling in crystalline lithium diborate. The four distinct two-bond boron–boron J-couplings are shown in Fig. 8-6. The couplings denoted i–iii are B4–O–B3, and have values; $^2J_{\mathrm{i}} = 2.65\,\mathrm{Hz}$, $^2J_{\mathrm{ii}} = 0.95\,\mathrm{Hz}$, $^2J_{\mathrm{iii}} = 1.20\,\mathrm{Hz}$. The fourth coupling (iv) is B4–O–B4 with a value of $^2J_{\mathrm{iv}} = -0.07\,\mathrm{Hz}$.

8.3 Conclusions

In all spin-echo experiments presented above, the large-C_{Q} B3 site dephased slower than the smaller-C_{Q} B4 site. Primarily, this effect is not due to the B4 site having greater dipolar couplings than the B3 site. The b_{rss} calculation given in §6.3.2 showed that the difference between B3 and B4 is not substantial enough to explain the discrepancy in dephasing times.

Both chemical sites will be subject to the same heteronuclear dipolar

field as well, which is expected to be negligible in lithium borates. Other negligible differences between the sites include the chemical shift, both isotropic and anisotropic, as well as motion of the spins. Motion of the spins would appear as a narrowing of lineshapes [233], not seen in any room-temperature solid-state NMR of lithium borates. The remaining difference is the quadrupolar coupling. Using Eq. (2-43) we find for the B3 site, $\omega_Q/2\pi = 427\,\text{kHz}$ and for the B4 site, $\omega_Q/2\pi = 85\,\text{kHz}$. These values represent the magnitude of the first-order quadrupolar interaction. Edén and Frydman have shown that when $\omega_Q \approx \omega_r$ the first-order quadrupolar interaction recouples the dipolar interaction [92, §II.A]. The effect on linewidth is pronounced when this is the case. However, the spin-echo experiments presented above were conducted in the regime where $\omega_Q \gg \omega_r$ and no linewidth change was seen for the spin-echo spectra under varying MAS rate. Additionally, this first-order phenomenon would affect the B4 site more than the B3 site, whereas in experiment the B4 dephasing time hardly changes.

The change in coherence dephasing time as the degree of ^{11}B isotopic abundance is varied can be explained by the presence of multiple noncommuting homonuclear dipolar couplings. With 5% ^{11}B the mean probability of a given ^{11}B nucleus being near more than one ^{11}B nuclei is only ≈1%. Increasing the ^{11}B abundance to 25% the same probability increases to ≈21%, see Tab. 6-3. Hence, coherence dephasing took much longer with only 5% ^{11}B in the sample because of the considerable reduction in multiple noncommuting homonuclear dipolar couplings. This coherence dephasing effect was also seen in lineshapes of Fig. 6-9 where significant multiple noncommuting homonuclear dipolar couplings caused broadening. The B3 site was still seen to dephase slower than the B4 site for long τ times.

The lineshape intensity at long τ times was suppressed by irreversible dephasing caused by multiple noncommuting homonuclear dipolar couplings. In the absence of this dephasing mechanism, other phenomena can dephase the coherence; but at long τ times they were hidden by this faster mechanism. For 100% ^{11}B enrichment every ^{11}B nucleus will be maximally connected to other ^{11}B nuclei, there being no other isotope of boron present. Multiple noncommuting homonuclear dipolar couplings were the chief cause of spin-echo dephasing for this degree of enrichment. The high correlation coefficients in

this case (Tab. 8-3) showed the fitted function was barely bi-exponential as the dephasing mechanism was dominated by the multiple noncommuting homonuclear dipolar couplings. For 100% abundant ^{11}B the quickness of dephasing would only allow J-couplings stronger than ~ 15 Hz to be detected.

The 25% ^{11}B composition had three comparative advantages for detecting a J-modulation of the spin-echo. First, a dramatic reduction of multiple connected ^{11}B nuclei increased dephasing time from that of the 100% composition, enhancing the J-coupling sensitivity. Secondly, with five times more ^{11}B nuclei than in the 5% composition the signal-to-noise ratio was higher, allowing more τ points to be recorded. Thirdly, the probability of two ^{11}B nuclei bonded to a mutual oxygen was near-maximal compared to all other compositions. Despite these advantages there was no observable J-modulation in the spin-echo experiments. Based on the first-principles calculations of §8.2.2, the lack of observed modulation was due to the small $^2J_{\mathrm{BB}}$ in the diborate unit.

For 5% ^{11}B, the curves are very clearly not mono-exponential, with distinct fast and slow dephasing rates visible. The separation of these regimes is qualified above, by the low correlation between p and the $T_2^{'}$ times. From the shape of the dephasing curve for the 5% ^{11}B enriched sample, as well as the relevant correlation coefficients, there were clearly at least two mechanisms contributing to the overall dephasing.

When varying the MAS rate for the 100% ^{11}B sample, the longest dephasing time, $T_{2b}^{'}$, increased from 2 ms to 12 ms as the MAS rate was sped-up for the large-C_{Q} B3 site. This behaviour has been reported before in the case of proton spectra as the dephasing is primarily caused by the multiple noncommuting homonuclear dipolar couplings [330]. $T_{2b}^{'}$ for the B4 site was largely unaffected by the change in MAS rate, having an average of 2 ms dephasing time—always less than the B3 site over the tested spinning speeds. As the B4-site dephasing was not dramatically affected by the change in MAS rate, the primary dephasing mechanism is probably not due to multiple noncommuting homonuclear dipolar couplings.

Insight into the interplay between the quadrupolar interaction and multiple noncommuting homonuclear dipolar couplings is provided by simulations presented in the following chapter.

CHAPTER 9

Simulations of Magnetisation Exchange and Dephasing

> You must understand a thing completely before you can safely ignore it.
>
> James Geary

The previous chapters have shown how varying some experimental parameters can alter spin diffusion and coherence dephasing behaviour. With computer simulations, the effect of varying different parameters can be systematically considered. Notably, the intricate interplay of dipole and quadrupole interactions can be investigated.

9.1 Factors Affecting Magnetisation Transfer: Model 2-Spin Systems

Consider two quadrupolar spins in a strong[1] magnetic field undergoing MAS. To monitor magnetisation transfer experimentally, it is sufficient to frequency encode the spins in the t_1 dimension before converting the bulk magnetisation

[1] $\omega_Q \ll \omega_0$

back along the z-axis for a mixing time, τ_{mix}. Then, a third pulse is required to convert the z-magnetisation into a detectable single-quantum coherence, where the spins evolve again to provide frequency information in the t_2 dimension. After a 2DFT operation any transferred magnetisation will be visible as a spectral cross-peak, such as those seen in the spectra of Ch. 7.

With simulation, a direct approach is available by only simulating the mixing time; z-magnetisation is started on one spin and z-magnetisation is detected on another spin some time later. This approach removes the need to simulate pulsing, which would require more computation time. Explicitly, the start matrix would be `I1z` and the detect matrix would be `I2z`. In matrix form only the diagonal elements would be nonzero. When the trace of diagonal is taken to determine the signal, elements corresponding to the satellite transitions will also be included. However, as shown in §5.3, their inclusion had a negligible effect on the initial buildup rate and final magnetisation transfer.

The following curves, produced by pNMRsim [132], plot the longitudinal magnetisation transfer from one spin to another, through time. By starting with the simplest cases and gradually introducing interactions, the nature of the quadrupolar and dipolar interactions is clarified. The simulations only considered the first-order quadrupolar interaction of dipolar coupled spin $I = 3/2$ nuclei. Thus the lineshapes resembled Fig. 2-10c rather than MAS lineshapes of Fig. 2-10a, since there was no second-order broadening or second-order isotropic shift of any transition. However, the satellite transitions were still broadened by the first-order interaction and it follows that different spin numbers, I, produced different transfer characteristics. The following general simulations were identical for all spin $I = 3/2$ nuclei, from ^{7}Li to ^{201}Hg. Neither relaxation or J-coupling is taken into account. CSA was also absent making these simulations B_0 independent[2].

There are a few trivial cases of magnetisation transfer:

(i) With only one spin there is nowhere to transfer the magnetisation.

(ii) Without dipolar (or J) coupling there is no mechanism to transfer magnetisation.

[2] see [93, Tab. 1] for recoupling mechanism dependencies on MAS rate and B_0.

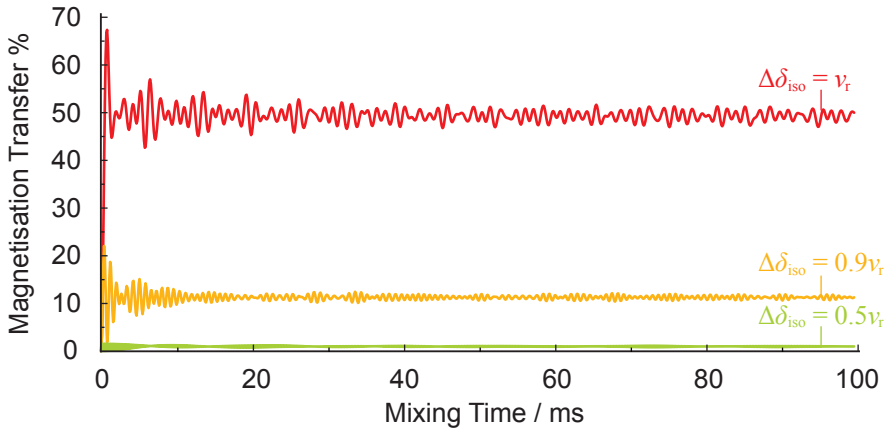

Figure 9-1. Simulated (pNMRsim) $z \rightarrow z$ buildup curves varying $\Delta\delta_{iso}$. Two spin, 1st order, $I = 3/2$, $\omega_r/2\pi = 10\,\text{kHz}$, $C_Q = 0$, CSA $= 0$, $b_{jk}/2\pi = -1\,\text{kHz}$. $\Delta\delta_{iso} = 10\,\text{kHz}$ (red), $9\,\text{kHz}$ (orange), $5\,\text{kHz}$ (green).

(iii) When the dipolar vector is coincident with the quadrupolar (or CSA) tensors and $\Delta\delta_{iso} = 0$ there is no transfer as the spins are in chemically identical sites.

The results presented below start to explore the vast parameter space remaining, with either two or four spins to avoid case (i), these spins were dipolar coupled together to avoid case (ii) and case (iii) was also easily broken by setting $\Delta\delta_{iso} \neq 0$ or rotating the β-angle between the quadrupole and dipole tensors, $\beta_{Q\rightarrow D}$.

9.1.1 $\Delta\delta_{iso}$—Isotropic Chemical Shift Difference

The effect of varying $\Delta\delta_{iso}$ with fixed $|b_{jk}|$ and ω_r in the absence of a quadrupolar interaction are shown in Fig. 9-1. The top red curve had $\Delta\delta_{iso} = \nu_r$; magnetisation transfer was very rapid and the two spins quickly reached an equilibrium, each having 50% of the available magnetisation. This condition corresponds to $n = 1$ rotational resonance, which is known—from $I = 1/2$ solid-state NMR—to recouple the dipolar interaction [190, 238, 259]. The orange curve in the middle had $\Delta\delta_{iso} = 0.9\nu_r$, which still gave a rapid buildup but the final magnetisation transfer was much reduced, demonstrating the two regimes (early and late) are not necessarily related. The green curve near the bottom of the figure had $\Delta\delta_{iso} = 0.5\nu_r$ and gave very little magnetisation transfer.

Evidently, from Fig. 9-1 the initial rate of transfer and final magnetisation

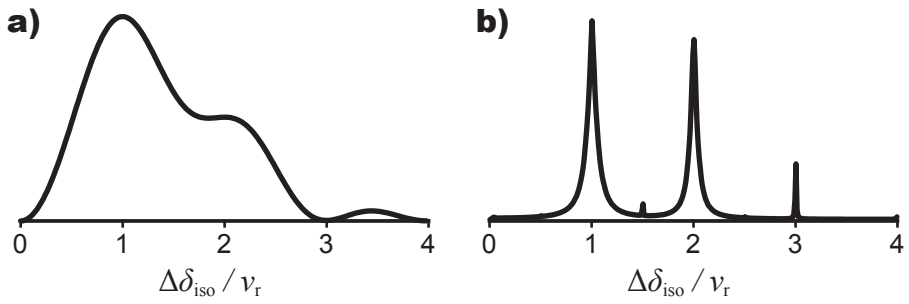

Figure 9-2. Analysis of simulated (pNMRsim) $z \rightarrow z$ buildup. a) Initial magnetisation transfer, corresponding to the magnetisation transferred after one rotor period. b) Final magnetisation transfer, taken at 100 ms. These are shown against isotropic chemical shift separation (divided by MAS rate) and are valid for all I where $b_{jk} \ll \omega_r$. $\omega_r/2\pi = 10$ kHz, C_Q and CSA were zero. In a specific case where $I = 3/2$ and $b_{jk}/2\pi = -1$ kHz, a) peaks at 32% magnetisation transfer per ms and b) peaks at 50% final magnetisation transfer.

depended on the isotropic chemical shift difference relative to the MAS rate. This relationship is explored in Fig. 9-2 by monitoring the two regimes separately. Initial buildup (Fig. 9-2a) measured the first point of the curve—after one rotor period. This measure is connected with the rate at which the recoupling mechanism (if present) acts. The final magnetisation transfer (Fig. 9-2b) was determined by taking the mean of the last ten points of the buildup-curve—at 100 ms. These are plotted against varying isotropic chemical shift difference divided by fixed MAS rate. Only the ratio of these variables is important so long as $b_{jk} \ll \omega_r$.

Defining $n = \Delta\delta_{iso}/\nu_r$ as in Ref. [190] we can see that the $n = 1$ rotational resonance gave the most rapid buildup and the highest final magnetisation transfer. At $n = 2$ the final magnetisation was comparable but the buildup took longer. These two conditions were fairly broad. Higher rotational resonance conditions exist (and become significant if the spins have finite CSA) but are narrow and weak [190].

Evidently, when $n = 1$ or $n = 2$ there will be enhanced magnetisation transfer. This effect has important consequences for spin diffusion experiments. As rotational resonance is narrowband, with two spins there is a choice of actively recoupling, or not, the dipolar interaction. With three or more spins then only two spins could be at a specific rotational resonance, giving enhanced magnetisation transfer and thus the illusion that these spins are closer in space. For

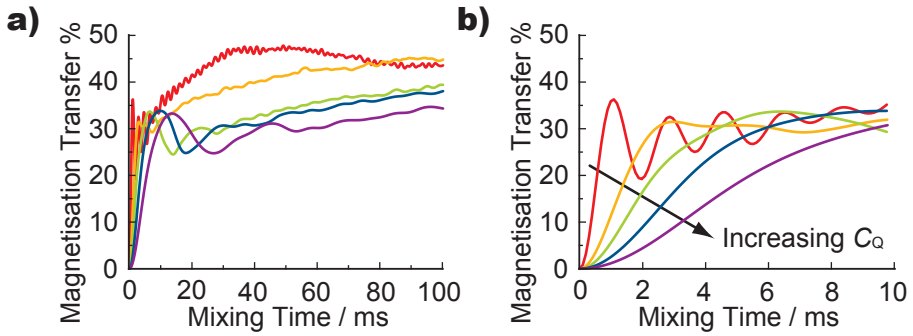

Figure 9-3. Simulated (pNMRsim) $z \rightarrow z$ buildup curves varying C_Q. Two spin, 1st order, $I = 3/2$, $\omega_r/2\pi = 10\,\text{kHz}$, $\Delta\delta_{iso} = 0$, CSA = 0, $b_{jk}/2\pi = -1\,\text{kHz}$, parallel quadrupolar tensors perpendicular to dipolar vector. $C_Q = 100\,\text{kHz}$ (red), 200 kHz (orange), 800 kHz (green), 1600 kHz (blue), 3200 kHz (purple).

a given spin system and magnetic field strength the MAS rate must be chosen wisely to select or avoid rotational resonance conditions and obviate spurious results.

9.1.2 C_Q—Quadrupolar Coupling

Figure 9-3 shows the effect of varying the quadrupolar coupling strength of the two overlapping lineshapes in the regime $\omega_Q > \omega_r$ and $\Delta\delta_{iso} = 0$. The relation between C_Q and ω_Q was given in Eq. (2-43). Whereas C_Q relates, physically, to the strength of the electric field gradient, ω_Q corrects for the spin number to describe the general behaviour of all quadrupolar nuclei.

For the values of C_Q tested significant magnetisation transfer was seen, around 30%–50%, indicating efficient dipolar recoupling. The initial magnetisation transfer was slower than the no-C_Q rotational-resonance cases shown in Fig. 9-1, occurring over several ms. Increasing C_Q for both spins in the $\omega_Q > \omega_r$ regime gradually suppressed both the initial buildup rate as well as the final magnetisation transfer.

To further explore this enhanced dipole recoupling a plot showing how initial buildup rate varies with ω_Q/ω_r is presented in Fig. 9-4. Zero C_Q was a trivial case of no transfer. The fastest initial magnetisation transfer occured where $\omega_Q/\omega_r \simeq 1$. After this peak, the initial buildup rate tailed off as C_Q was increased against MAS rate, as shown in Fig. 9-3. Enhanced buildup rate

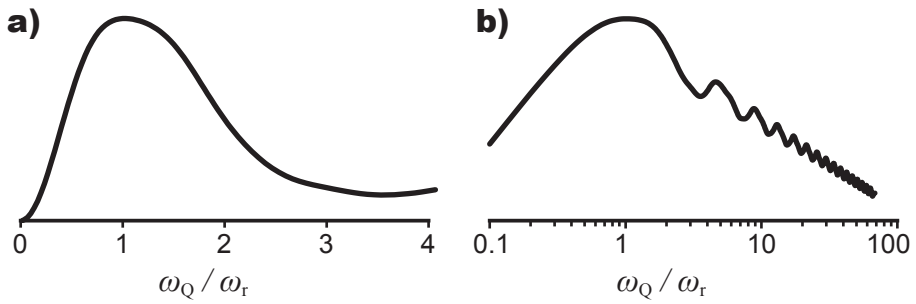

Figure 9-4. Analysis of simulated (pNMRsim) $z \rightarrow z$ buildup. The rate of initial buildup as a function ω_Q/ω_r, valid for all quadrupolar nuclei to the first order. MAS rate was fixed and C_Q varied. $\Delta\delta_{iso}$ and CSA are zero and $|b_{jk}| \ll \omega_r$. a) Linear plot, b) log-log plot.

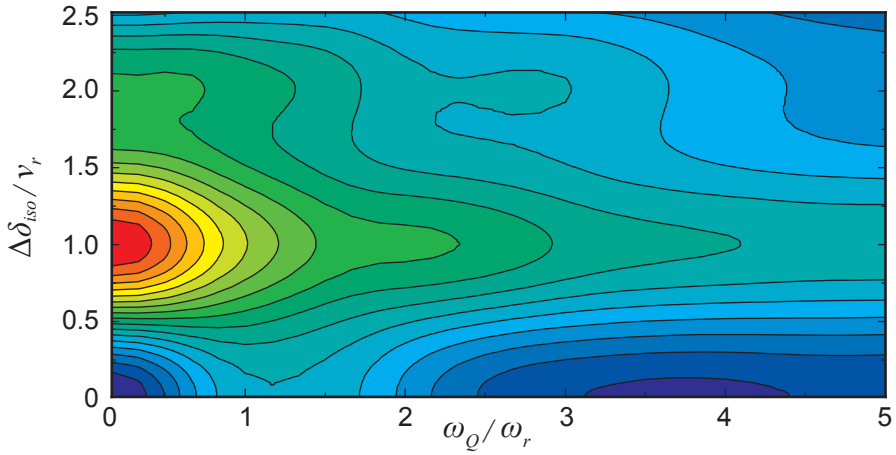

Figure 9-5. The rate of initial buildup as a function ω_Q/ω_r and $\Delta\delta_{iso}/\nu_r$, taken from 62 500 pNMRsim $z \rightarrow z$ buildup simulations. Valid for all quadrupolar nuclei to the first order. Red values indicate most rapid buildup, in this example where $b_{jk}/2\pi = -1$ kHz, this corresponds to 32% magnetisation transfer per ms. Eighteen contour levels are linearly spaced from 0% to 32% magnetisation transfer per ms.

is indicative of a stronger effective dipolar coupling. When ω_Q is of a similar magnitude to ω_r the first-order quadrupolar coupling was more effective at reintroducing the dipolar interaction removed by MAS.

The previous plot can be expanded to incorporate chemical shift difference. Such a two-dimensional plot is presented in Fig. 9-5. Note the buildup rate was enhanced for all values of ω_Q at the $n = 1$ rotational resonance condition. For overlapping lineshapes and very small $\Delta\delta_{iso}$, introducing quadrupolar coupling allowed magnetisation to transfer, peaking in effectiveness just after $\omega_Q/\omega_r = 1$. The first row ($\Delta\delta_{iso} = 0$) slice was shown in Fig. 9-4 and the first column ($\omega_Q = 0$) slice was shown in Fig. 9-2a.

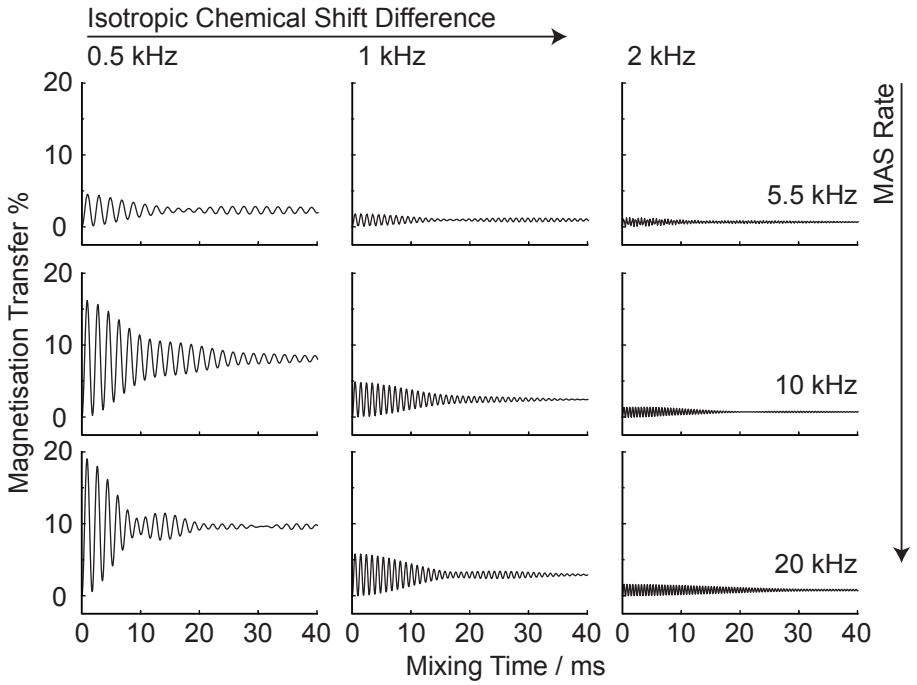

Figure 9-6. Simulated (pNMRsim) $z \rightarrow z$ buildup curves for direct comparison with Ref. [93, Fig. 3]. Two spin, $I = 3/2$, parallel quadrupolar tensors perpendicular to dipolar vector, $C_\mathrm{Q} = 100\,\mathrm{kHz}$, $b_{jk}/2\pi = -500\,\mathrm{Hz}$, $\Delta\delta_\mathrm{iso}$ and $\omega_\mathrm{r}/2\pi$ as indicated.

The effect of a small first-order quadrupolar coupling was to enhance the magnetisation transfer when the quadrupolar coupling (ω_Q) strength was of similar magnitude to the MAS rate (ω_r). At this condition, the MAS modulation of the quadrupolar interaction more effectively recouples the dipolar interaction, allowing enhanced transfer despite the faster spinning speed. For quadrupolar nuclei, ω_Q is usually considerably greater than ω_r so this effect is only significant for fast spinning of nuclei with small C_Q.

With the addition of a small quadrupolar coupling, the effect on magnetisation transfer as a function of isotropic chemical shift separation and MAS rate is shown in Fig. 9-6. The figure is presented in the same manner as Ref. [93, Fig. 3] to aid comparison. The exact resemblance attests to the accuracy of pNMRsim simulation under the stated conditions. Smaller values of $\Delta\delta_\mathrm{iso}$ gave greater magnetisation transfer as there was less energy difference for the spin diffusion mechanism to compensate. The magnetisation transfer oscillations proceeded at a frequency almost equal to the chemical shift difference, but slightly faster due to the additional quadrupolar interaction. The final magnetisation transfer was greater for MAS rates of 10 kHz and 20 kHz because of a

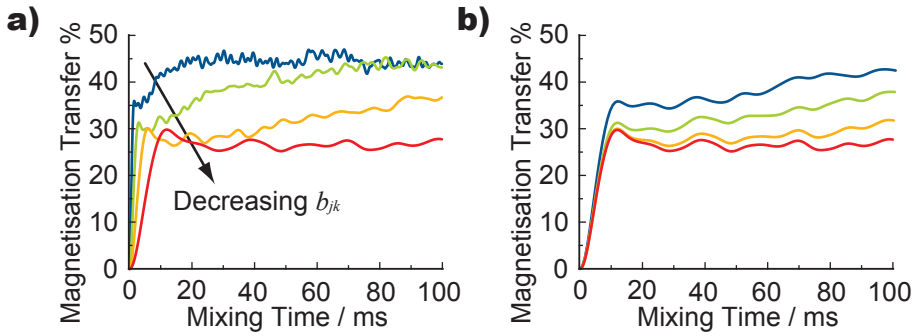

Figure 9-7. Simulated (pNMRsim) $z \rightarrow z$ buildup curves varying $b_{jk}/2\pi$. Two spin, 1st order, $I = 3/2$, $\omega_r/2\pi = 10\,\text{kHz}$, $\Delta\delta_{iso} = 0$, CSA = 0, $C_Q = 200\,\text{kHz}$, parallel quadrupolar tensors perpendicular to dipolar vector. $b_{jk}/2\pi = -250\,\text{Hz}$ (red), $-500\,\text{Hz}$ (orange), $-1000\,\text{Hz}$ (green), $-2000\,\text{Hz}$ (dark blue). a) Unmodified buildup curves. b) Curves stretched along time axis by amount $(b_{jk}/2\pi)/-250\,\text{Hz}$.

"resonance" between the first-order quadrupolar interaction and the MAS rate.

9.1.3 b_{jk}—Dipolar Coupling

Figure 9-7 shows buildup curves where b_{jk} was doubled for successive simulations. From Eq. (2-32) we can see that doubling the dipolar coupling strength has the physical corollary of moving the nuclear spins a factor of $\sqrt[3]{2} \simeq 1.26$ closer. Increasing the dipolar coupling strength affected the buildup curves linearly; they kept the same characteristics but the initial buildup is faster and final magnetisation transfer is enhanced. This is made clearer in Fig. 9-7b where the curves have been stretched along the time axis. Directly changing the dipolar coupling strength had a linear effect on the initial buildup rate. Therefore, the initial buildup rate is probably a good indicator of the residual effective dipolar coupling strength that MAS could not remove.

The monotonic relationship between buildup rate (or final magnetisation transfer) and the average nuclei separation is the factor that adds value to dipolar homonuclear correlation experiments; the promise of extracting actual atomic distances using NMR. However, although the dipolar coupling strength behaves in a straightforward manner for $\Delta\delta_{iso} = 0$, the other factors affecting magnetisation transfer are much more complicated.

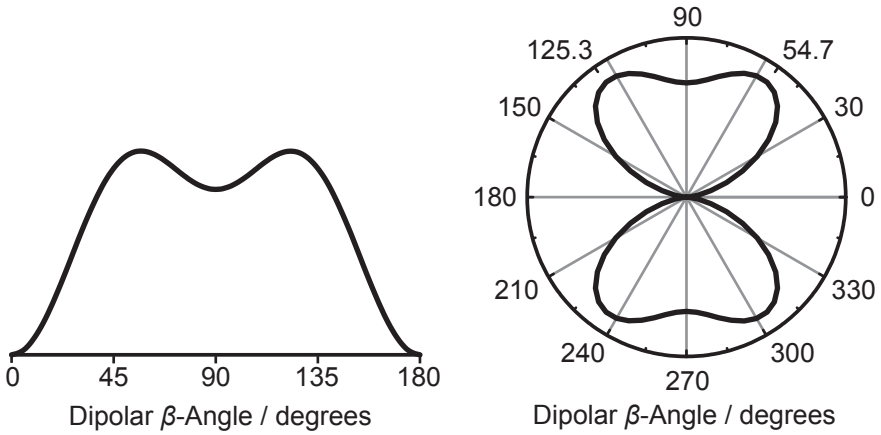

Figure 9-8. Analysis of simulated (pNMRsim) $z \rightarrow z$ buildup showing the initial magnetisation transfer rate as a function of the β-angle between parallel quadrupolar tensors and the dipolar vector. C_{Q} and ω_{r} are finite, $\Delta\delta_{\mathrm{iso}} = 0$. The curve is the same shape for all quadrupolar nuclei.

9.1.4 $\beta_{\mathrm{Q}\rightarrow\mathrm{D}}$ Angle

For dipolar-coupled spins of identical chemical shift, the initial rate of magnetisation transfer is strongly dependent on the β-angle between (coincident) quadrupolar tensors and the dipolar vector. Fig. 9-8 reveals how the effective dipolar coupling strength changed as the $\beta_{\mathrm{Q}\rightarrow\mathrm{D}}$ angle was varied. When all the vectors were coincident (i.e. 0° or 180°) there was no initial transfer and, overall, no magnetisation transfer took place. Initial magnetisation transfer rate peaked at the magic angle, hinting at the involvement of the P_2 Legendre polynomial. Varying the spin number, I, or dipolar coupling strength, b_{jk}, did not change the shape of the curve—only the magnitude. Importantly, this angular dependence would only be significant in reality for a truly isolated spin pair.

Summary

The following effects magnetisation transfer were observed:

- For $C_{\mathrm{Q}} = 0$, rotational resonance greatly enhanced the efficiency of magnetisation transfer, but was only strongly effective around the $n = 1$ or $n = 2$ conditions.

- First-order quadrupolar coupling recoupled the dipolar interaction regardless of chemical shift separation but the initial buildup rate and final mag-

netisation transfer were less, compared to a rotational resonance case.

- First-order quadrupolar-driven recoupling of the dipolar interaction was most effective around $\omega_{\mathrm{Q}} \approx \omega_{\mathrm{r}}$.
- The initial rate of magnetisation transfer was directly proportional to effective dipolar coupling.
- Varying the $\beta_{\mathrm{Q}\rightarrow\mathrm{D}}$ strongly affected the rate of initial magnetisation transfer, especially around the case of coincident vectors.

The most interesting point is that, ignoring rotational resonance, the effective dipolar coupling was strongest when $\omega_{\mathrm{Q}} \approx \omega_{\mathrm{r}}$. As the dipolar coupling causes broadening of the lineshapes and dephasing of spin-echo curves, these effects are expected to be greatest around this condition. Lineshape broadening caused by the recoupling of the dipolar interaction by the first-order quadrupolar interaction was observed by Edén and Frydman [92].

9.2 Comparison to Experimental Magnetisation Transfer

For a real material it is impossible to change the dipolar and quadrupolar coupling strengths or angular relations between the nuclei. Within limits it is possible to change the isotropic chemical shift difference by moving to higher or lower static magnetic fields, but this requires access to another NMR magnet. The easiest variable to change experimentally so as to help probe the spin dynamics of homonuclear dipolar coupled nuclei is the spinning speed. However, comparing magnetisation transfer at different MAS rates can make it hard to extract mechanism information because many relations vary simultaneously. To assist understanding, the MAS rate can be varied in simulation over a much greater range than experimentally possible.

For typical ^{11}B–^{11}B dipolar couplings, $b_{jk}/2\pi \approx -1\,\mathrm{kHz}$, in which case spinning faster than 10 kHz would suppress the dipolar coupling greatly unless it is recoupled by other interactions. Most NMR of quadrupolar nuclei will be in the regime where $\omega_{\mathrm{Q}}/\omega_{\mathrm{r}} \gg 1$. For example, an ^{11}B nucleus with $C_{\mathrm{Q}} = 500\,\mathrm{kHz}$

equates to $\omega_Q/2\pi = 83.3\,\text{kHz}$ which is much greater than a typical MAS rate of 10 kHz. Referring to Fig. 9-4, this regime is beyond the $\omega_Q/\omega_r \simeq 1$ peak.

The most significant effect on dipolar recoupling when varying the MAS rate will be seen at the rotational-resonance conditions, as shown in Fig. 9-2. For spin $I = 1/2$ nuclei there is a definite isotropic chemical shift separation. For half-integer quadrupolar nuclei there are transitions that are under the influence of quadrupolar broadening, spreading the lineshapes over a wider spectral region. Considering the second-order quadrupolar interaction broadened central transition of separated sites, the rotational-resonance condition cannot be met by the whole lineshape at a given instant in time. Thus, such conditions are expected to be spread out for half-integer quadrupolar nuclei exhibiting second-order quadrupolar broadening of the central transition.

9.2.1 Two-Spin Simulations

The central transitions of the simulated first-order lineshapes in pNMRsim are not broadened. Two-spin simulations, based on NMR parameters similar to those found in lithium diborate at 14.1 T (except without CSA, which is insignificant in this case) are presented in Fig. 9-9, which shows the final magnetisation transfer as a function of spinning speed. As with previous figures, this involves calculating separate buildup curves and taking the last point, corresponding to $\tau_{mix} = 100\,\text{ms}$. As the spectral width is rotor synchronised the (dwell) time between data points varies as the MAS rate changes. To ensure the last point is fixed at 100 ms the number of points computed was set equal to a tenth of the MAS rate. As each point in Fig. 9-9 is a discrete simulation, only a fraction of the buildup-curve information is represented.

The highest magnetisation transfer occurred at $n = 1$ rotational resonance, 3080 Hz, where $\Delta\delta_{iso} = \nu_r$. In a 1D NMR experiment at 14.1 T, considering the effect of second-order quadrupolar broadening, this would place the spinning sidebands of one peak over the other. For a 2D SQ–SQ spin diffusion experiment the spinning sidebands for both peaks would appear at the cross-peak location, preventing the identification of a real cross-peak.

The small peaks either side of the $n = 1$ rotational resonance were a

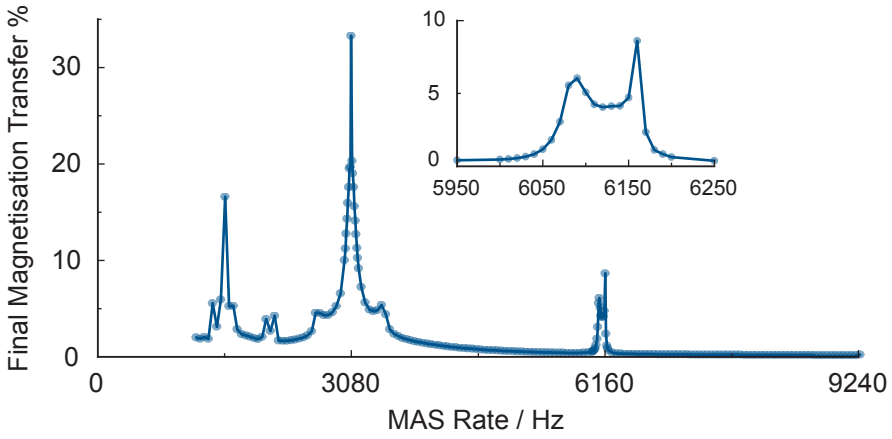

Figure 9-9. Analysis of simulated (pNMRsim) $z \rightarrow z$ buildup showing final magnetisation transfer as a function of MAS rate. Two spin, 1^{st} order, $I = 3/2$, $\Delta\delta_{iso} = 3080\,Hz$, CSA $= 0$, $C_Q = 2560\,kHz$ and $520\,kHz$, $b_{jk}/2\pi = -848\,Hz$, parallel quadrupolar tensors were at angle (93.4°, 119.9°, −83.2°) to the dipole vector. Spin system was representative of B3 and B4 nuclei in a diborate unit, see Tab. 6-1.

consequence of the quadrupolar interaction broadening the matching condition. The $n = 2$ rotational resonance at 1540 Hz also showed an increase in final magnetisation transfer because of the efficient recovery of the dipolar interaction at that spinning speed. At 6160 Hz where $n = 1/2$, there was a small region of magnetisation transfer. The shape (see inset) of this region was dependent on the relative quadrupolar tensor angles (results not shown).

The $n = 1/2$ match condition is suitable for experiment as the spinning sidebands will be displaced from the cross-peaks, allowing easy measurement of spin diffusion. Note, however, that these simulations are first-order only and in a real second-order broadened lineshape only a fraction of the crystallites will be at the exact $n = 1/2$ condition. Experimentally, the MAS rate could be swept to ensure all crystallites experienced the match condition, as demonstrated by Nijman et al. [238].

9.2.2 Four-Spin Simulations

Simulations were also performed for four spins representative of boron nuclei in a diborate superstructural group, using dipolar strengths and Euler angles between the spins as given in Tab. 6-1. The z-magnetisation was started on the two spins with greater quadrupolar coupling—corresponding to the B3 sites in

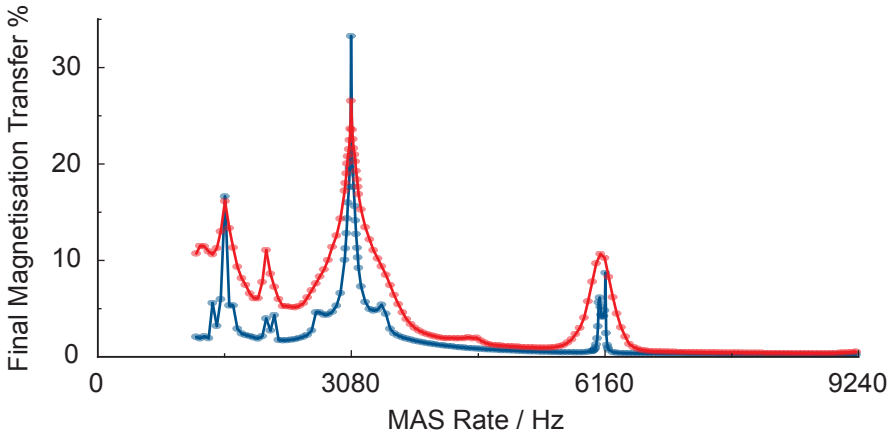

Figure 9-10. Analysis of simulated (pNMRsim) $z \rightarrow z$ buildup showing final magnetisation transfer as a function of MAS rate for two spins (blue, repeated from Fig. 9-9) and four spins (red). 1^{st} order, $I = 3/2$, no CSA. The same randomly generated quadrupolar tensor orientations were used throughout. Dipolar coupling strengths and Euler angles between spins are taken from the diborate superstructural unit as listed in Tab. 6-1.

a diborate group—and detected on the corresponding B4 spin sites. A direct comparison with the above two-spin case is revealed in Fig. 9-10, showing final magnetisation transfer as a function of MAS rate. The four-spin case showed familiar features to the two-spin case but was slightly broadened as more spins opened up more pathways for the magnetisation to transfer. Neither the two- or four-spin case reached a maximal 50% magnetisation transfer, indicating that the given quadrupolar coupling strengths were not totally effective in recoupling the dipolar interaction.

As described in §5.3 the four-spin density matrix contains over 65 000 elements. Consequently, the simulations took over 1 h each to run on a 3.6 GHz Intel® Pentium® 4 processor. Five spin simulations are feasible, but as the basis of these simulations is the diborate superstructural unit—which contains four boron atoms—the simulations were sensibly limited to these four spins.

The full buildup curves for two- and four-spin cases at three specific MAS rates are presented in Fig. 9-11. Significant magnetisation transfer occurred only at rotational-resonance conditions. With four spins, the buildup curves were smoother than the two spin case. These more realistic simulations showed buildup occurring over tens of milliseconds, as seen experimentally in Fig. 7-8.

The plot of final magnetisation transfer against MAS rate for four spins

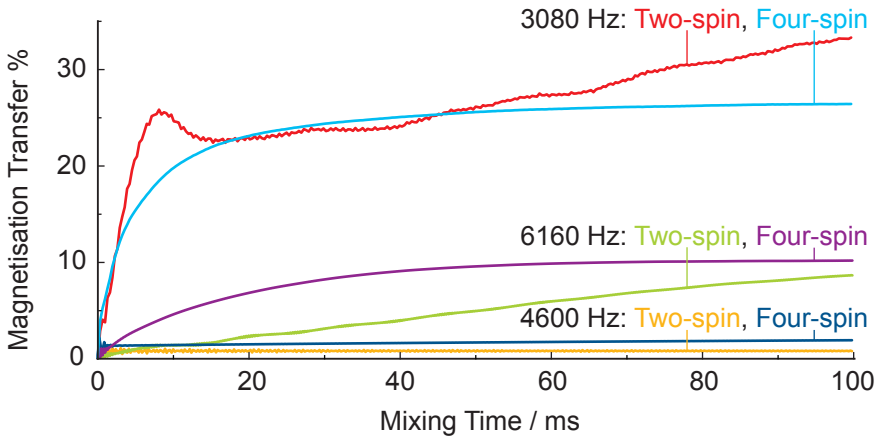

Figure 9-11. Simulated (pNMRsim) $z \rightarrow z$ buildup comparing two-spin and four-spin curves at three different MAS rates. Two- and four-spin parameters are the same as in Fig. 9-10. Two spin; $\omega_r/2\pi = 3080\,\text{Hz}$ (red), 4600 Hz (orange), 6160 Hz (green). Four spin; $\omega_r/2\pi = 3080\,\text{Hz}$ (light blue), 4600 Hz (dark blue), 6160 Hz (purple).

shown in Fig. 9-10 only took into account the first-order quadrupolar interaction. Without the second-order quadrupolar interaction, the spectrum of lithium diborate would consist of two sharp Lorentzian lines 16 ppm apart, as shown in Fig. 2-10c. At 14.1 T this separation corresponds to a frequency of 3080 Hz[3], so sharp rotational-resonance lines appeared at precise integer multiples of this frequency. In reality, the second-order quadrupolar interaction broadens and shifts the lineshapes, according to Eq. (2-62), so we would expect the rotational-resonance conditions to be broadened also. To reproduce the effect of the second-order interaction, the four-spin case in Fig. 9-10 was convoluted with a second-order broadened lineshape of lithium diborate.

The convolution first assumed the B4 site is a sharp line, shown as the black vertical line in Fig. 9-12a. The unbroadened B3 site would appear 3080 Hz away (16 ppm), but with the presence of the second-order interaction, the intensity at this point was very low. Hence, we can expect the rotational-resonance peaks to no longer appear around 3080 Hz and 6160 Hz. Conversely, the intensity at the point 1900 Hz (shown as the orange vertical line) from the B3 site has jumped from zero to a significant value. Now we can expect rotational-resonance peaks around 1900 Hz and 3800 Hz. The data in Fig. 9-10 were shifted by a factor 1900/3080 and scaled corresponding to the intensity at the matching

[3] 16 ppm × 192.53 MHz ≃ 3080 Hz

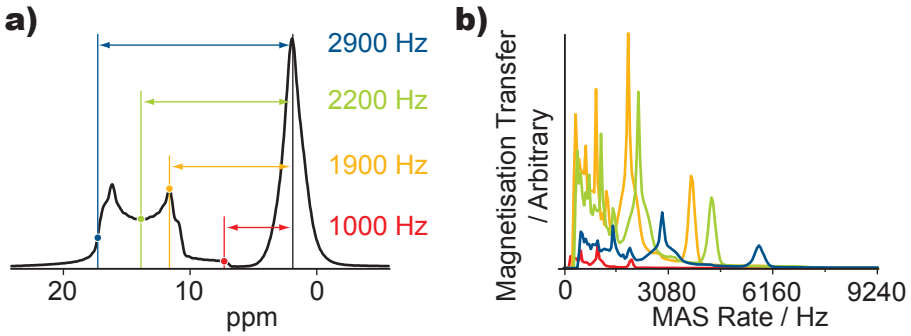

Figure 9-12. a) The second-order quadrupolar broadened lineshape from which the correct shift and intensity scaling can be computed. b) Shifted and scaled curves of Fig. 9-10 corresponding to the points shown in (a).

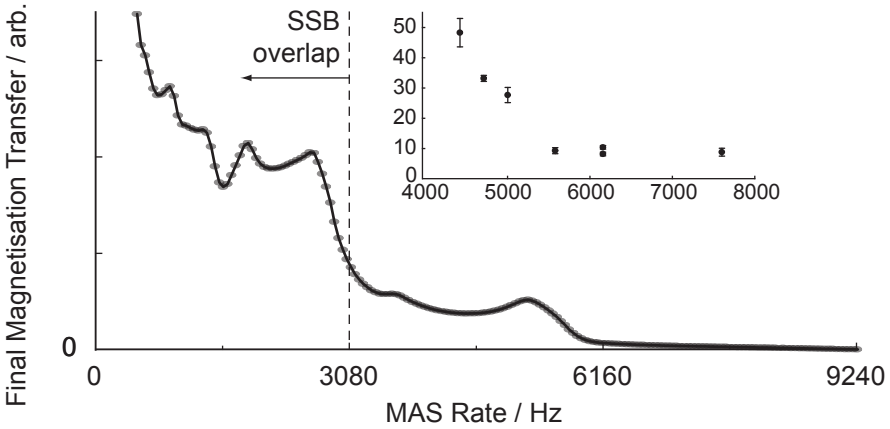

Figure 9-13. Analysis of simulated (pNMRsim) $z \rightarrow z$ buildup, showing final magnetisation transfer at 14.1 T as a function of MAS rate, approximating the second-order interaction by convoluting the lineshape of the B3 site shown in Fig. 6-7 with that of Fig. 9-10. The experimental intensity every 50 Hz from the B3 site was used to shift and scale an interpolated form of Fig. 9-10 in Mathematica™. These numerous curves were themselves interpolated and the intensity every 50 Hz was summed. See Fig. 9-12 and discussion in text for further details. Inset is the experimental data repeated from Fig. 7-10.

(orange) point to create a new graph shown as the orange curve in Fig. 9-12b.

Similarly, the shifting and scaling was performed for three other points 1000 Hz (red), 2200 Hz (green) and 2900 Hz (blue) from the B3 site. Their respective curves are also shown in Fig. 9-12b. Note how the red curve peaked at 1000 Hz and 2000 Hz with much reduced intensity. If all four shifted and scaled curves were added together, they would approximate the final magnetisation transfer against MAS rate graph with the second-order quadrupolar interaction.

Instead of only four points, a multitude of points were taken. By shifting and scaling many curves then adding them all together, a more accurate

approximation, shown in Fig. 9-13, was created. This graph shows a gradual fall-off in magnetisation transfer as MAS rate was increased, in agreement with the experimentally observed trends in Fig. 7-10.

The convoluted simulation data reveals that spinning slower than the $n = 1$ rotational-resonance condition (3080 Hz) gives strong magnetisation transfer and, therefore, cross-peak intensity. However, in this regime experimentally there would be many spinning sidebands, which would overlap with the second-order broadened peaks under MAS. DOR is capable of spinning an outer rotor in this regime (500 Hz to 2000 Hz) and has the other advantages of narrow quadrupolar lineshapes and odd-order sideband suppression. However, the outer rotor spinning speed can only be varied over a small range compared to MAS. The cross-peak : auto-peak ratio at long mixing time for DOR was ≈100% (see Fig. 7-14); a case where the outer rotor was spun at 1500 Hz. Under 4716 Hz MAS this ratio was reduced to ≈30% and by 6160 Hz MAS rate, reduced further to ≈10% (see Fig. 7-10). This trend is in agreement with the ratio of the comparative simulated transfer in Fig. 9-13.

All of the magnetisation transfer simulations showed positive-only transfer, giving no hint as to the cause of the mixed positive-negative cross-peaks seen experimentally.

9.3 Spin Diffusion—$Ba_2MoO_3F_4$

Simulating buildup curves represent just one dimension of a spin diffusion experiment—the mixing time. Sometimes it is instructive to simulate the complete experiment, to reproduce in two dimensions the lineshapes and patterns actually seen in experimental data. The power of this approach can be seen by reproducing the interesting case where Du, Levitt and Grey observed negative ^{19}F cross-peaks in the exchange spectrum of $Ba_2MoO_3F_4$ [76]. Spinning at 23 kHz greatly exceeds the $n = 1$ rotational-resonance condition of $\simeq 15$ kHz when in a 4.7 T field. They hypothesise a high-order spin diffusion process whereby four spins participate simultaneously.

A four-spin pNMRsim[4] simulation of this system is shown in Fig. 9-14.

[4]SIMPSON reproduced the same spectrum.

Table 9-1. NMR parameters for four-spin system representing $Ba_2MoO_3F_4$. CSA was determined by lineshape comparison to a 1D MAS NMR experimental spectrum [76, Fig. 1a], asymmetry was assumed to be zero. Spin labels are equivalent to those in Ref. [76].

	Chemical Shift in ppm		$-b_{jk}/2\pi$ in Hz		
Spin	Isotropic	Anisotropic	P2	P3	P4
P1	−24	80	5954	3704	4003
P2	−28	70		2527	3629
P3	−100	35			5426
P4	−104	50			

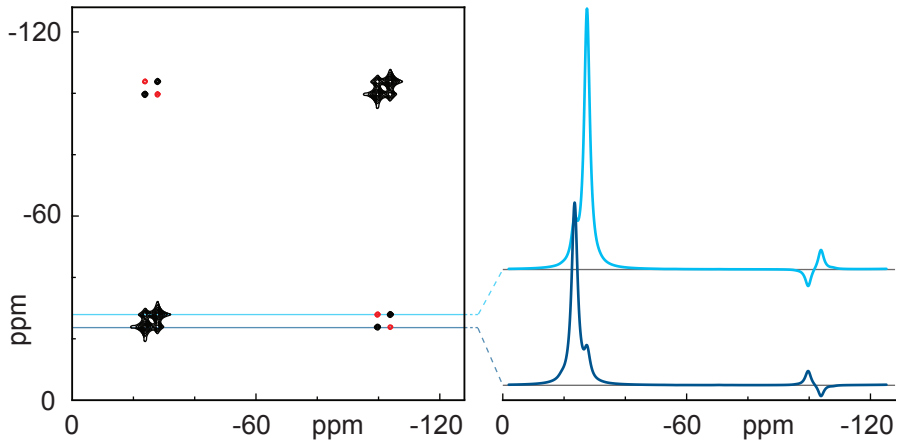

Figure 9-14. A four-spin pNMRsim simulation of a 2D ^{19}F MAS NMR rotor-synchronised spin diffusion spectrum of $Ba_2MoO_3F_4$ for comparison with experimental results presented in Ref. [76, Fig. 2c]. Analysis of the crystal structure [316] gave precise ^{19}F–^{19}F distances for calculation of dipolar coupling strengths using Eq. 2-32. Spin parameters are given in Tab. 9-1. $\nu_r = 23\,kHz$, $\nu_0(^{19}F) = 188.19\,MHz$, $\tau_{mix} = 10\,ms$. The entire pulse sequence was simulated (see §C.1) using ideal pulses and matrix filtering instead of phase cycling. The States method was used to achieve sign discrimination in the indirect dimension [287]. 200 Hz Lorentzian linebroadening was applied before the 2DFT. Contours increase by $\times 1.8$ from a base of 2% of the maximum intensity.

Negative cross-peaks were clearly seen between the outermost spins as well as the innermost spins, as detected experimentally [76, Fig. 2c]. When only two spins were simulated the cross-peaks were always positive. That is, adding together six separate simulations to describe all the dipole-dipole couplings between the four spins was not equivalent to one four-spin simulation. Separate $z \rightarrow z$ simulations of the ^{19}F–^{19}F buildup curves reproduce the correct intensity and sign of magnetisation transfer only when all four spins are involved. This evidence supports the high-order spin diffusion process hypothesis.

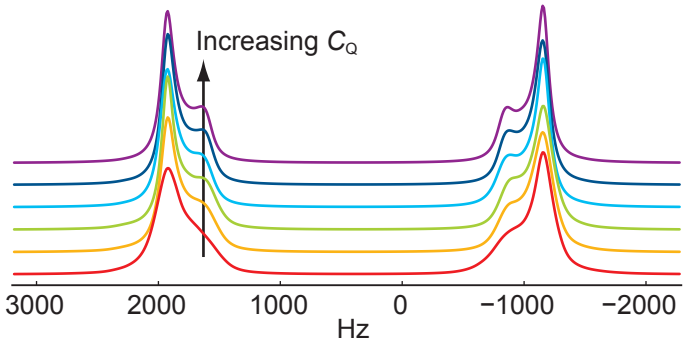

Figure 9-15. Two-spin pNMRsim simulated lineshapes, 1st order quadrupolar interaction, $\nu_0 = 192.54\,\text{MHz}$, $I = 3/2$, $\omega_r/2\pi = 10\,\text{kHz}$, SW = 10 kHz (rotor-synchronised), $\Delta\delta_{iso} = 3080\,\text{Hz}$, CSA = 0, $\eta_Q = 0$, $b_{jk}/2\pi = -3.2\,\text{kHz}$, 100 Hz Lorentzian broadened. All tensors were perpendicular. $C_Q = 512\,\text{kHz}$ and 512 kHz (red), $C_Q = 512\,\text{kHz}$ and 1280 kHz (orange), $C_Q = 512\,\text{kHz}$ and 2560 kHz (green), $C_Q = 1280\,\text{kHz}$ and 1280 kHz (light blue), $C_Q = 1280\,\text{kHz}$ and 2560 kHz (dark blue), $C_Q = 2560\,\text{kHz}$ and 2560 kHz (purple).

9.4 Dipolar Broadening

In the absence of quadrupolar or dipolar coupling, NMR lineshapes will have the form of a Lorentzian[5], as described by Eq. (3-18). For a dipolar coupled spin pair, adding first-order quadrupolar coupling reintroduces the dipolar interaction, causing broadening that is not removed by MAS. Quadrupolar recoupling is most effective when $\omega_Q/\omega_r \simeq 1$, as shown in Fig. 9-4 for initial $z \rightarrow z$ magnetisation transfer rate.

For a given MAS rate where $\omega_Q > \omega_r$, greater C_Q made the broadening more pronounced but did not significantly widen the observed lineshapes, as shown in Fig. 9-15. Changing η_Q had a minor effect. Varying the $\beta_{Q\rightarrow D}$ angle had a large effect, primarily by modifying the effective dipolar coupling as discussed above in §9.1.4. Random (non-linear) tensor orientations produced similar lineshapes to those presented in Fig. 9-15.

Strengthening the dipolar coupling drastically increased the broadening, in a linear fashion, as shown in Fig. 9-16. The high levels (broadening >1000 Hz) of quadrupolar-driven dipolar broadening were not seen experimentally in ^{11}B MAS NMR spectra of lithium diborate. The simulation result supports the root-sum-squared calculations of §6.3.2 by showing that $b_{jk}/2\pi \leq -1.6\,\text{kHz}$ in

[5] Assuming exponential dephasing.

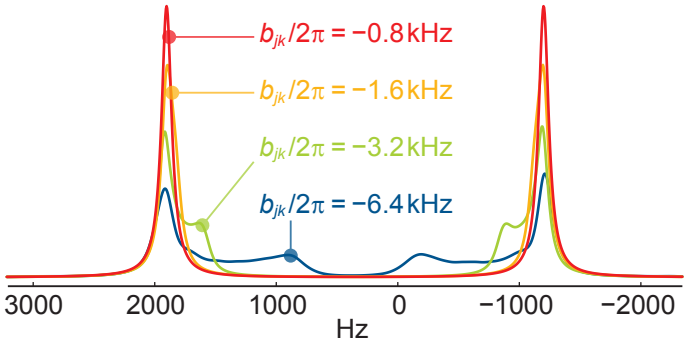

Figure 9-16. Two-spin pNMRsim simulated lineshapes, 1st order quadrupolar interaction, $\nu_0 = 192.54$ MHz, $I = 3/2$, $\omega_r/2\pi = 10$ kHz, SW = 10 kHz (rotor-synchronised), $\Delta\delta_{iso} = 3080$ Hz, CSA = 0, $\eta_Q = 0$, $C_Q = 2560$ kHz and 2560 kHz, 100 Hz Lorentzian broadened. All tensors were perpendicular. $b_{jk}/2\pi = -0.8$ kHz (red), $b_{jk}/2\pi = -1.6$ kHz (orange), $b_{jk}/2\pi = -3.2$ kHz (green), $b_{jk}/2\pi = -6.4$ kHz (blue).

this system.

The main spectral broadening mechanisms of the ^{11}B nuclei in lithium diborate are therefore multiple noncommuting homonuclear dipolar couplings (for high ^{11}B abundance samples) and fourth-rank second-order quadrupolar broadening. The effects of the quadrupolar interaction recoupling the dipolar interaction is therefore mostly hidden in the experimental 1D ^{11}B spectra (see Fig. 6-9).

For a given static magnetic field strength, the second-order broadening will not be affected. Changing the MAS rate will affect both remaining broadening mechanisms; multiple noncommuting couplings and the first-order quadrupolar interaction. However, faster spinning in the regime where $\omega_Q > \omega_r$ (as found in lithium diborate) causes opposing effects. Less effective multiple noncommuting homonuclear dipolar couplings will weaken the effective dipolar coupling and as ω_r approaches ω_Q the first-order quadrupolar interaction will become more effective at recoupling the dipolar interaction.

The effects of the first-order quadrupolar interaction for isolated spin-pairs will not only appear in 1D lineshapes. As described in §3.6 linebroadening is inversely related to T_2', therefore, broader lineshapes equate to faster coherence dephasing.

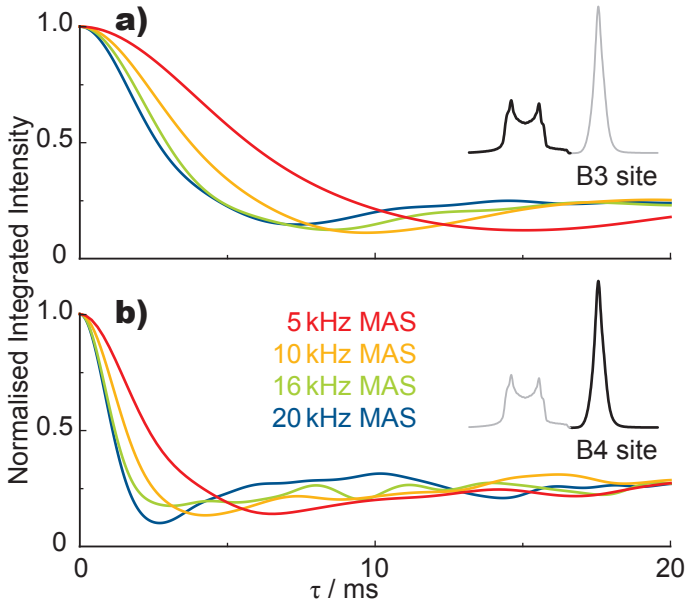

Figure 9-17. Simulated (pNMRsim) `Inx` → `Inc` two-spin spin-echo ($\tau/2$–π–$\tau/2$) dephasing curves, 1st order, $I = 3/2$, $b_{jk}/2\pi = -500\,\text{Hz}$, $\Delta\delta_{\text{iso}} = 0\,\text{Hz}$, CSA = 0. Parallel quadrupolar tensors were perpendicular to dipolar vector. $\omega_\text{r}/2\pi = 5\,\text{kHz}$ (red), $\omega_\text{r}/2\pi = 10\,\text{kHz}$ (orange), $\omega_\text{r}/2\pi = 16\,\text{kHz}$ (green), $\omega_\text{r}/2\pi = 20\,\text{kHz}$ (blue). a) $C_\text{Q} = 2560\,\text{kHz}$, b) $C_\text{Q} = 512\,\text{kHz}$.

9.5 Spin-Echo Dephasing

Quadrupolar-driven recoupling of the dipolar interaction will affect the dephasing of spin-echo curves as well as causing broadened lineshapes. Simulated spin-echo dephasing curves are presented in Fig. 9-17. The two-spin simulation parameters correspond to lithium diborate, the experimental spin-echo dephasing curves of which were shown in Fig. 8-2. As in experiment, the simulations show that the B3 site takes longer to dephase than the B4 site, over the MAS range investigated. Unlike experiment, speeding-up the MAS rate enhances the dephasing for both sites.

The difference in dephasing for a given MAS rate depends on the C_Q of the site. The intensity of the spin-echo for very short τ_mix times ($\approx 0.5\,\text{ms}$) is plotted against ω_Q in Fig. 9-18. The swiftest dephasing occurred around $\omega_\text{Q} \approx \omega_\text{r}$. For $\omega_\text{Q} = 0$ there was no dephasing. The similarities between spin-echo dephasing and initial buildup rate in magnetisation transfer experiments (Fig. 9-4) are striking.

For given values of ω_Q, the initial spin-echo intensity was plotted as a function of MAS rate in Fig. 9-19. For typically small values of quadrupolar

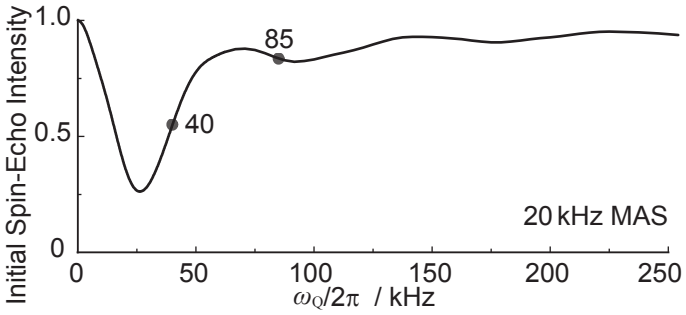

Figure 9-18. Analysis of simulated (pNMRsim) initial spin-echo intensity at ≈ 0.5 ms as a function of ω_Q at $\omega_r/2\pi = 20$ kHz. Other parameters as in Fig. 9-17. Highlighted points at $\omega_Q/2\pi = 40$ kHz and 85 kHz correspond to similar points in Fig. 9-19, to aid comparison. A lower value of initial spin-echo intensity corresponds to faster dephasing.

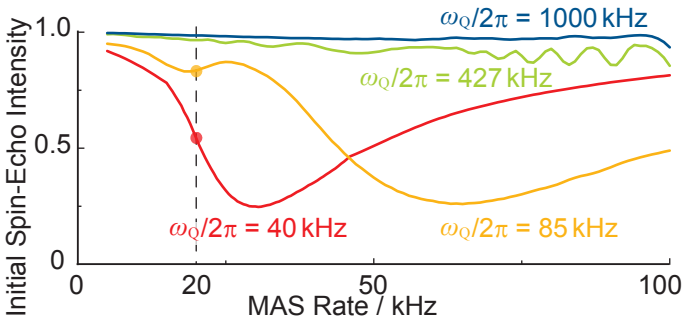

Figure 9-19. Analysis of simulated (pNMRsim) initial spin-echo intensity at ≈ 0.5 ms as a function of ω_r. $\omega_Q/2\pi = 40$ kHz (red), $\omega_Q/2\pi = 85$ kHz (orange, B4 site), $\omega_Q/2\pi = 427$ kHz (green, B3 site), $\omega_Q/2\pi = 1000$ kHz (blue). Other parameters as in Fig. 9-17. Highlighted points at $\omega_r/2\pi = 20$ kHz correspond to similar points in Fig. 9-18, to aid comparison. A lower value of initial spin-echo intensity corresponds to faster dephasing.

coupling ($\omega_Q/2\pi = 85$ kHz) and greater, spinning faster up to experimentally feasible rates enhances the quadrupolar-driven dephasing. The dephasing is more effective for smaller values of ω_Q. When ω_Q is very large there is only a small effect on the initial spin-echo dephasing.

The similarities between experiment and simulation—the smaller C_Q site dephases faster—can be explained by the first-order quadrupolar interaction recoupling the dipolar interaction more efficiently for sites with ω_Q/ω_r ratios closer to unity. Some differences between experiment and simulation are due to the lack of multiple couplings in the simulation.

Multiple noncommuting homonuclear dipolar couplings cause broadening, as shown in Fig. 6-9. The effects of multiple noncommuting homonuclear dipolar couplings on spin-echo dephasing were presented in Fig. 8-1. For lith-

ium diborate comprising of 100% abundant ^{11}B the main cause of $T_2^{'}$ dephasing was from multiple noncommuting homonuclear dipolar couplings. As the MAS rate was sped-up, the ability of the multiple noncommuting homonuclear dipolar couplings to recouple the dipolar interaction was suppressed, which led to longer dephasing times for the B3 site as presented in Fig. 8-2. This behaviour is not seen in the simulation data (Fig. 9-17) as multiple couplings are not present.

The two mechanisms—the first-order quadrupolar interaction and multiple noncommuting homonuclear dipolar couplings—will work against each other for abundant sites of typical ω_{Q}. The two-spin simulations presented above had no multiple couplings, such that without the quadrupolar coupling MAS would perfectly remove the dipolar interaction, giving no coherence dephasing at all. The importance of multiple noncommuting homonuclear dipolar couplings was seen experimentally for slow spinning whereby the dipolar interaction dephased sites almost irrespective of ω_{Q} value, as shown in Fig. 8-2a. For faster spinning speeds where the multiple noncommuting homonuclear dipolar couplings are suppressed, the first-order quadrupolar interaction is presumed to be dominant and causes faster dephasing for sites with $\omega_{\mathrm{Q}}/\omega_{\mathrm{r}}$ ratios closer to unity, as seen in Fig. 8-2d.

CHAPTER 10

Conclusions and Outlook

> It is a capital mistake to theorize before you have all the evidence. It biases the judgment.
>
> Sir Arthur Conan Doyle, A Study in Scarlet (1887)

10.1 Summary

This solid-state NMR study of half-integer quadrupolar nuclei focused on spin diffusion and spin-echo methods using an experimental and computer simulation approach to provide information about the role of dipolar and quadrupolar interactions in lithium diborate. Lithium diborate was used as a model crystalline compound and this study was enhanced by synthesising samples with a range of $^{10}B/^{11}B$ ratios. Specifically, by varying the ^{11}B isotopic abundance, the effect of multiple homonuclear dipolar couplings was investigated. Crystalline lithium diborate has two boron chemical sites, with high (B3) and low (B4) values of C_Q, also allowing the effect of quadrupolar coupling on the NMR spectra to be determined. This variety of known boron environment, combined with performing NMR under different MAS rates and static magnetic field strengths,

enabled a clearer study of the interplay between the dipolar and quadrupolar interactions.

An overview of the material in this thesis is now given in the order presented. The ^{11}B nuclei in glass and crystalline lithium diborate spin-lattice relax via different mechanisms, with the crystalline form taking 30–50 times longer. Adding 0.1 mol% of cobalt, copper or iron oxides to the melt failed to reduce the ^{11}B T_1 relaxation time in the crystalline form, presumable due to incomplete atomic-level mixing.

High levels of ^{11}B isotopic abundance broadened the ^{11}B NMR lineshapes due to the presence of multiple noncommuting homonuclear dipolar couplings, with faster MAS rates narrowing the lineshapes. Reduced ^{11}B isotopic abundance not only narrowed the lineshapes but also diminishing the cross-peak intensities in spin diffusion experiments. Spin diffusion between the boron nuclei was reduced by faster MAS rates, both in the buildup rate and final magnetisation transfer. Under the slower-spinning DOR, spin diffusion was more efficient than MAS at the same static magnetic field strength. At the lower field of 7.05 T the B3 and B4 lineshapes overlapped and rapid spin diffusion gave rise to strong cross-peaks. However, unlike at higher fields, no B3–B3 cross-peak intensity was evident. Under certain conditions the cross-peaks of lithium diborate had mixed positive and negative intensity. The origins of the $\left(\begin{smallmatrix}-&+\\+&-\end{smallmatrix}\right)$ pattern were explored, but no firm conclusions were reached.

Spin-echo dephasing curves also revealed the interplay between the quadrupolar and dipolar interactions. The dephasing time was shortened for increasing ^{11}B isotopic abundance, because of the enhanced dipolar interactions present. Over the spinning speeds investigated, the B4 site always dephased faster than the B3 site because the quadrupolar coupling strength (ω_{Q}) was more closely matched to the magnitude of the MAS frequency (ω_{r}). In this regime, MAS was prevented from fully removing[1] the dipolar interaction, leading to faster spin-echo dephasing. No $^2J_{\mathrm{BB}}$-coupling was detected in the modulation of spin-echo dephasing curves of lithium diborate.

Simulations were employed to model the dependence of magnetisation transfer over numerous NMR parameters ($\Delta\delta_{\mathrm{iso}}$, C_{Q}, b_{jk}, $\beta_{\mathrm{Q}\rightarrow\mathrm{D}}$, ω_r). Rota-

[1] Averaging the dipolar interaction between two spins to zero over one rotor period.

tional resonance conditions were seen to greatly enhance spin diffusion. First-order quadrupolar-driven recoupling was also shown to be most effective around $\omega_Q \approx \omega_r$. First-order simulations could not reproduce the mixed intensity cross-peaks for half-integer quadrupolar nuclei. However, a four-spin simulation of ^{19}F (spin $I = 1/2$) spin diffusion in $Ba_2MoO_3F_4$ accurately reproduced an experimental spectrum showing mixed positive and negative cross-peak intensities. Simulations of spin-echo dephasing of dipolar-coupled half-integer quadrupolar nuclei matched experiment regarding how ω_Q affects dephasing, with closer magnitudes to ω_r showing enhanced dephasing. However, when varying the MAS rate, opposite effects were observed between simulation and experiment. This discrepancy is explained by the two-spin simulations not representing multiple noncommuting homonuclear dipolar couplings.

10.2 Outlook

One of the more intriguing results presented in this thesis is that of the $\binom{-+}{+-}$ pattern seen in the spin diffusion cross-peaks of lithium diborate. There was a difference in shape depending on the degree of ^{11}B isotopic abundance. Hence, a natural extension would be to create more lithium diborate samples with ^{11}B isotopic abundances of 10 % to 90 % and compare the B3–B4 cross-peak shape as a function of $^{10}B/^{11}B$ ratio. More theoretical modelling could also be undertaken, to better understand the spin dynamics of half-integer quadrupolar nuclei exchanging magnetisation. This is especially important in the case where $\omega_Q \approx \omega_r$.

The problem that spin-lattice relaxation times are longer for crystalline materials than their amorphous counterparts still remains. Atomic-level mixing needs to be encouraged to avoid the clumping of material seen by microscopy. Further study into the paramagnetic doping of crystalline materials would look at a broader range of dopants and different synthesis techniques. For the cobalt- and copper-doped samples of Ch. 6, preliminary data were collected using a SQUID[2], which would aid such a further study by indicating the level of para-

[2]Superconducting Quantum Interference Device, used to measure the magnetic susceptibility of a material.

magnetism in each sample.

The presented simulations were four-spin and only considered the first-order quadrupolar interaction. Future simulations would include more spins as computer hardware improves. Further refinement of the simulation programs could lead to reliable results for dipolar-coupled spins with second as well as first-order quadrupolar interactions present. These improvements, combined with greater understanding of the interplay between dipolar and quadrupolar interactions, should lead to clearer interpretation of the experimental spin diffusion results present in this thesis.

Investigations of J-couplings between half-integer quadrupolar nuclei are at an early stage. The ability to calculate, *ab initio*, the value of J-couplings in materials should deliver good candidates for further experimental investigation. One such interesting study could compare the differences between the B3-O-B3 ^2J-coupling in boron oxide (B_2O_3) with that of B4-O-B4 ^2J-coupling for danburite ($CaB_2(SiO_4)_2$). Danburite, along with lithium diborate, is remarkable in containing joined BO_4 tetrahedra, which are usually energetically unfavourable.

From a NMR technique development viewpoint, the DQHDR experiment described in §7.6 shows particular promise for observing through-space homonuclear correlations between half-integer quadrupolar nuclei. The importance of researching this area is shown by the growing interest of researchers around the world.

Finally, it must not be forgotten that all these investigations should lead toward furthering the understanding of the structure of disordered materials, especially borate glasses. This fertile field of research still has many unanswered questions—questions that solid-state nuclear magnetic resonance of half-integer quadrupolar nuclei is more than capable of answering.

> A tremendous feeling of peace came over him. He knew that at last, for once and for ever, it was now all, finally, over.
>
> Douglas Adams
> *Mostly Harmless, Ch. 25*

APPENDIX A

NMR Theory Supplement

A.1 Spherical Spin Tensors for $I = 3/2$

$$\hat{T}_{20} = \sqrt{\frac{3}{2}} \begin{bmatrix} 1 & 0 & 0 & 0 \\ 0 & -1 & 0 & 0 \\ 0 & 0 & -1 & 0 \\ 0 & 0 & 0 & 1 \end{bmatrix}$$

$$\hat{T}_{21} = \sqrt{3} \begin{bmatrix} 0 & -1 & 0 & 0 \\ 0 & 0 & 0 & 0 \\ 0 & 0 & 0 & 1 \\ 0 & 0 & 0 & 0 \end{bmatrix} \quad \hat{T}_{2-1} = \sqrt{3} \begin{bmatrix} 0 & 0 & 0 & 0 \\ 1 & 0 & 0 & 0 \\ 0 & 0 & 0 & 0 \\ 0 & 0 & -1 & 0 \end{bmatrix}$$

$$\hat{T}_{22} = \sqrt{3} \begin{bmatrix} 0 & 0 & 1 & 0 \\ 0 & 0 & 0 & 1 \\ 0 & 0 & 0 & 0 \\ 0 & 0 & 0 & 0 \end{bmatrix} \quad \hat{T}_{2-2} = \sqrt{3} \begin{bmatrix} 0 & 0 & 0 & 0 \\ 0 & 0 & 0 & 0 \\ 1 & 0 & 0 & 0 \\ 0 & 1 & 0 & 0 \end{bmatrix}$$

A.2 The Spin Diffusion Experiment in Product Operator Formalism

This approach is for two spin $I = 1/2$ nuclei. If soft pulses are used, this approach extends to describing the central transition of coupled half-integer quadrupolar nuclei. Start with a fully relaxed spin system such that $\hat{\boldsymbol{\rho}}(0) = I_z$. Apply a 90°-pulse and allow free precession for duration t_1. A weak J-coupling is present, which is the cause of unwanted zero-quantum coherence.

$$I_z \xrightarrow{(90^\circ_x)_{\mathrm{IS}}} \xrightarrow{\Omega_{\mathrm{I}} t_1} \xrightarrow{\pi J_{\mathrm{IS}} t_1}$$

$$\begin{aligned} &-I_y \cos(\Omega_{\mathrm{I}} t_1)\cos(\pi J_{\mathrm{IS}} t_1) + 2I_x S_z \cos(\Omega_{\mathrm{I}} t_1)\sin(\pi J_{\mathrm{IS}} t_1) \\ &+I_x \sin(\Omega_{\mathrm{I}} t_1)\cos(\pi J_{\mathrm{IS}} t_1) + 2I_y S_z \sin(\Omega_{\mathrm{I}} t_1)\sin(\pi J_{\mathrm{IS}} t_1) \end{aligned}$$

With the t_1 evolution complete the mixing period begins with a second 90°-pulse.

$$\xrightarrow{(90^\circ_x)_{\mathrm{IS}}}$$

$$\begin{aligned} &-I_z \cos(\Omega_{\mathrm{I}} t_1)\cos(\pi J_{\mathrm{IS}} t_1) - 2I_x S_y \cos(\Omega_{\mathrm{I}} t_1)\sin(\pi J_{\mathrm{IS}} t_1) \\ &+I_x \sin(\Omega_{\mathrm{I}} t_1)\cos(\pi J_{\mathrm{IS}} t_1) + 2I_z S_y \sin(\Omega_{\mathrm{I}} t_1)\sin(\pi J_{\mathrm{IS}} t_1) \end{aligned}$$

Phase-cycling will select only $p = 0$ coherence orders.

$$\xrightarrow{\text{select } p=0}$$

$$-I_z \cos(\Omega_{\mathrm{I}} t_1)\cos(\pi J_{\mathrm{IS}} t_1) + ZQ_y \cos(\Omega_{\mathrm{I}} t_1)\sin(\pi J_{\mathrm{IS}} t_1)$$

During the mixing time, due to the dipolar interaction, spins I and S can exchange longitudinal magnetisation. This can be represented by $I_z \longrightarrow aI_z + bS_z$, where a and b will depend on the efficiency of the energy-transfer mechanism as well as the duration of the mixing time, τ_m. During the mixing time the unwanted zero-quantum coherence evolves:

$$\xrightarrow{(\Omega_{\mathrm{I}}+\Omega_{\mathrm{S}})\tau_m}$$

$$\begin{aligned} &-aI_z \cos(\Omega_{\mathrm{I}} t_1)\cos(\pi J_{\mathrm{IS}} t_1) - bS_z \cos(\Omega_{\mathrm{I}} t_1)\cos(\pi J_{\mathrm{IS}} t_1) \\ &+ZQ_y \cos(\Omega_{\mathrm{I}} t_1)\sin(\pi J_{\mathrm{IS}} t_1)\cos((\Omega_{\mathrm{I}} - \Omega_{\mathrm{S}})\tau_m) \\ &-ZQ_x \cos(\Omega_{\mathrm{I}} t_1)\sin(\pi J_{\mathrm{IS}} t_1)\sin((\Omega_{\mathrm{I}} - \Omega_{\mathrm{S}})\tau_m) \end{aligned}$$

Finally a third 90°-pulse is applied and the FID is detected:

$$\xrightarrow{(90^\circ_x)_{\mathrm{IS}}}$$

$$aI_y \cos(\Omega_{\mathrm{I}} t_1) \cos(\pi J_{\mathrm{IS}} t_1) + bS_y \cos(\Omega_{\mathrm{I}} t_1) \cos(\pi J_{\mathrm{IS}} t_1)$$
$$+\tfrac{1}{2}(2I_z S_x - 2I_x S_z) \cos(\Omega_{\mathrm{I}} t_1) \sin(\pi J_{\mathrm{IS}} t_1) \cos((\Omega_{\mathrm{I}} - \Omega_{\mathrm{S}})\tau_m)$$
$$-\tfrac{1}{2}(2I_x S_x - 2I_z S_z) \cos(\Omega_{\mathrm{I}} t_1) \sin(\pi J_{\mathrm{IS}} t_1) \sin((\Omega_{\mathrm{I}} - \Omega_{\mathrm{S}})\tau_m)$$

where aI_y is a purely absorptive auto-peak and bS_y is a purely absorptive cross-peak. Exactly the same treatment can be given to see the origin of auto-peaks and cross-peaks developing from magnetisation starting on the S spin instead. The $(2I_z S_x - 2I_x S_z)$ term is doubly dispersive and stems from the unwanted zero-quantum coherence caused by J-coupling or if a third spin participates in the spin diffusion. This term can be ignored if there is negligible J-coupling or the mixing time is sufficiently long enough such that the ZQ terms dephase. The $(2I_x S_x - 2I_z S_z)$ term does not induce an EMF in the coil and can be ignored.

Requisit matrix forms of the product operators are given:

$$I_x = \begin{bmatrix} 0 & 0 & \frac{1}{2} & 0 \\ 0 & 0 & 0 & \frac{1}{2} \\ \frac{1}{2} & 0 & 0 & 0 \\ 0 & \frac{1}{2} & 0 & 0 \end{bmatrix} \qquad I_y = \begin{bmatrix} 0 & 0 & -\mathrm{i}\frac{1}{2} & 0 \\ 0 & 0 & 0 & -\mathrm{i}\frac{1}{2} \\ \mathrm{i}\frac{1}{2} & 0 & 0 & 0 \\ 0 & \mathrm{i}\frac{1}{2} & 0 & 0 \end{bmatrix}$$

$$I_z = \begin{bmatrix} \frac{1}{2} & 0 & 0 & 0 \\ 0 & \frac{1}{2} & 0 & 0 \\ 0 & 0 & -\frac{1}{2} & 0 \\ 0 & 0 & 0 & -\frac{1}{2} \end{bmatrix} \qquad 2I_xS_y = \begin{bmatrix} 0 & 0 & 0 & -\mathrm{i}\frac{1}{2} \\ 0 & 0 & \mathrm{i}\frac{1}{2} & 0 \\ 0 & -\mathrm{i}\frac{1}{2} & 0 & 0 \\ \mathrm{i}\frac{1}{2} & 0 & 0 & 0 \end{bmatrix}$$

$$2I_zSy = \begin{bmatrix} 0 & -\mathrm{i}\frac{1}{2} & 0 & 0 \\ -\mathrm{i}\frac{1}{2} & 0 & 0 & 0 \\ 0 & 0 & 0 & -\mathrm{i}\frac{1}{2} \\ 0 & 0 & -\mathrm{i}\frac{1}{2} & 0 \end{bmatrix} \qquad ZQ_x = \begin{bmatrix} 0 & 0 & 0 & 0 \\ 0 & 0 & \frac{1}{2} & 0 \\ 0 & \frac{1}{2} & 0 & 0 \\ 0 & 0 & 0 & 0 \end{bmatrix}$$

$$ZQ_y = \begin{bmatrix} 0 & 0 & 0 & 0 \\ 0 & 0 & -\mathrm{i}\frac{1}{2} & 0 \\ 0 & \mathrm{i}\frac{1}{2} & 0 & 0 \\ 0 & 0 & 0 & 0 \end{bmatrix} \qquad 2I_zS_x = \begin{bmatrix} 0 & \frac{1}{2} & 0 & 0 \\ \frac{1}{2} & 0 & 0 & 0 \\ 0 & 0 & 0 & -\frac{1}{2} \\ 0 & 0 & -\frac{1}{2} & 0 \end{bmatrix}$$

$$2I_xS_z = \begin{bmatrix} 0 & 0 & \frac{1}{2} & 0 \\ 0 & 0 & 0 & -\frac{1}{2} \\ \frac{1}{2} & 0 & 0 & 0 \\ 0 & -\frac{1}{2} & 0 & 0 \end{bmatrix} \qquad 2I_xS_x = \begin{bmatrix} 0 & 0 & 0 & \frac{1}{2} \\ 0 & 0 & \frac{1}{2} & 0 \\ 0 & \frac{1}{2} & 0 & 0 \\ \frac{1}{2} & 0 & 0 & 0 \end{bmatrix}$$

$$2I_yS_y = \begin{bmatrix} 0 & 0 & 0 & -\frac{1}{2} \\ 0 & 0 & \frac{1}{2} & 0 \\ 0 & \frac{1}{2} & 0 & 0 \\ -\frac{1}{2} & 0 & 0 & 0 \end{bmatrix} \qquad 2I_zS_z = \begin{bmatrix} \frac{1}{2} & 0 & 0 & 0 \\ 0 & -\frac{1}{2} & 0 & 0 \\ 0 & 0 & -\frac{1}{2} & 0 \\ 0 & 0 & 0 & \frac{1}{2} \end{bmatrix}$$

A.3 Reduced Wigner *d*-Matrices

$$d^{\ell}_{m0}(\beta) = (-1)^m \sqrt{\frac{(\ell-m)!}{(\ell+m)!}}\, P^m_{\ell}(\cos\beta), \qquad m \geq 0 \tag{A-1}$$

When $m = 0$ this reduces to Eq. (2-14):

$$d^{\ell}_{00}(\beta) = P_{\ell}(\cos\beta) \tag{A-2}$$

For legibility the dependence on β can be made implicit, i.e. $d^{\ell}_{m'm}(\beta) \equiv d^{\ell}_{m'm}$.

The following relation can be used to calculate related Wigner d-matrices:

$$d^{\ell}_{m'm} = (-1)^{m-m'} d^{\ell}_{mm'} = d^{\ell}_{-m-m'} \tag{A-3}$$

$\ell = 1$

$d^1_{11} = \cos^2(\beta/2)$

$d^1_{10} = -\frac{1}{\sqrt{2}} \sin\beta$

$d^1_{1-0} = \sin^2(\beta/2)$

$\ell = 0$

$d^0_{00} = 1$

$d^1_{00} = \cos\beta$

$\ell = 2$

$d^2_{22} = \sin^4(\beta/2)$

$d^2_{21} = -\frac{1}{2}\big(\sin\beta(\cos\beta + 1)\big)$

$d^2_{11} = \frac{1}{2}(2\cos\beta - 1)(1 + \cos\beta)$

$d^2_{20} = \sqrt{\frac{3}{8}}\left(\sin^2\beta\right)$

$d^2_{10} = \sqrt{\frac{3}{2}}(\sin\beta\cos\beta)$

$d^2_{00} = \frac{1}{2}\left(3\cos^2\beta - 1\right)$

$d^2_{2-1} = \frac{1}{2}\big(\sin\beta(\cos\beta - 1)\big)$

$d^2_{1-1} = \frac{1}{2}(2\cos\beta + 1)(1 - \cos\beta)$

$d^2_{2-2} = \cos^4(\beta/2)$

$\ell = 4$ (Select terms)

$d^4_{00} = \frac{1}{8}\left(35\cos^4\beta - 30\cos^2\beta + 3\right)$

$d^4_{20} = -\frac{\sqrt{10}}{128}\left(14\cos^4\beta - 8\cos^2\beta - 6\right)$

$d^4_{40} = \frac{\sqrt{70}}{128}\left(\cos^4\beta - 4\cos^2\beta + 3\right)$

Complete terms for $\ell = 4, 6$ are given in Ref. [60].

A.4 Tables

Table A-1. Coefficients of the zeroth-, second-, and fourth-rank contributions to the second-order frequency shift, given in Eq. 2-62.

I	m	A_m^I	B_m^I	C_m^I
$3/2$	$1/2$	$-1/20$	$-1/7$	$27/140$
	$3/2$	$3/20$	0	$-3/20$
$5/2$	$1/2$	$-2/15$	$-8/21$	$18/35$
	$3/2$	$-1/10$	$-5/7$	$57/70$
	$5/2$	$5/6$	$5/21$	$-15/14$
$7/2$	$1/2$	$-1/4$	$-5/7$	$27/28$
	$3/2$	$-9/20$	$-12/7$	$303/140$
	$5/2$	$1/4$	$-10/7$	$33/28$
	$7/2$	$49/20$	1	$-69/20$
$9/2$	$1/2$	$-2/5$	$-8/7$	$54/35$
	$3/2$	$-9/10$	-3	$39/10$
	$5/2$	$-1/2$	$-25/7$	$57/14$
	$7/2$	$7/5$	-2	$3/5$
	$9/2$	$27/5$	$18/7$	$-279/35$

Table A-2. Phase cycle for a spin-diffusion experiment—see Fig. 3-7. The first and third pulse phases are shown in columns 1 and 2. The receiver phase is in column 4. The middle pulse is set to zero phase and not shown. Column 3 is the sum of the phase shifts. Based on the rule $\Delta\phi_\mathrm{r} = -\Delta\phi\Delta p$ given in §3.2, if the receiver is set to column 3 the correct coherence pathway will be selected

$\Delta\phi_1$	$\Delta\phi_3$	$\Delta\phi_1 + \Delta\phi_3$	$\Delta\phi_\mathrm{r}$
0	0	0	0
180	0	180	2
0	90	90	1
180	90	270	3
0	180	180	2
180	180	0	0
0	270	270	3
180	270	90	1

Table A-3. Phase cycle for both pulses (columns 1 and 3) and receiver (column 6) for a spin-echo experiment—see Fig. 5-1. Column 2 shows $-\Delta\phi_1$, the phase shift from a +1 coherence transfer. Column 4 shows $+2\Delta\phi_2$, the phase shift from a −2 coherence transfer. Column 5 is the sum of these phase shifts. Based on the rule $\Delta\phi_\mathrm{r} = -\Delta\phi\Delta p$ given in §3.2 if the receiver is set to column 6 the correct coherence pathway will be selected.

$\Delta\phi_1$	$-\Delta\phi_1$	$\Delta\phi_2$	$+2\Delta\phi_2$	$-\Delta\phi_1 + 2\Delta\phi_2$	$\Delta\phi_\mathrm{r}$
0	0	0	0	0	0
90	270	0	0	270	3
180	180	0	0	180	2
270	90	0	0	90	1
0	0	90	180	180	2
90	270	90	180	90	1
180	180	90	180	0	0
270	90	90	180	270	3
0	0	180	0	0	0
90	270	180	0	270	3
180	180	180	0	180	2
270	90	180	0	90	1
0	0	270	180	180	2
90	270	270	180	90	1
180	180	270	180	0	0
270	90	270	180	270	3

Table A-4. Correlation coefficients of variables in Tab. 6-4 used to fit bi-exponential saturation-recovery curves in Fig. 6-11. Values close to ±1 indicate the two parameters are correlated, whilst a zero value indicates that the two parameters are independent.

State	Site	Ap	AT_1^a	AT_1^b	pT_1^a	pT_1^b	$T_1^aT_1^b$
Crystal	B3	0.39	0.99	0.49	0.28	−0.36	0.54
Crystal	B4	0.08	0.99	0.52	−0.04	−0.57	0.58
Glass	B3	−0.23	0.45	0.18	−0.88	−0.90	0.72
Glass	B4	−0.34	0.43	0.30	−0.98	−0.99	0.94

Table A-5. Correlation coefficients of variables in Tab. 6-6 used to fit bi-exponential saturation-recovery curves in Fig. 6-8. Values close to ±1 indicate the two parameters are correlated, whilst a zero value indicates that the two parameters are independent.

Dopant	AT_1	Ac	T_1c
Cobalt	0.56	−0.26	0.39
Copper	0.25	−0.50	0.38

APPENDIX B

Stoichiometry

Table B-1. Stoichiometric ratios of reactants for the synthesis of $x\mathrm{Li_2O}\cdot(100-x)\mathrm{B_2O_3}$ following the method described in §6.2.1. To make a certain mass of product, measure out the ratios given multiplied by desired product mass. Valid for natural abundance boron (80% ^{11}B, 20% ^{10}B).

x	Li_2CO_3	:	B_2O_3
0.10	0.1126	:	0.9545
0.25	0.3095	:	0.8748
1/3	0.4369	:	0.8233
0.40	0.5501	:	0.7775
0.50	0.7426	:	0.6997

Table B-2. Stoichiometric ratios of reactants for the creation of $\mathrm{Li_2O}\cdot2\mathrm{B_2O_3}$ with varying ^{11}B isotope enrichment, following the method described in §6.2.2. To make a certain mass of product, measure out the ratios given multiplied by desired product mass.

^{11}B Fraction	Li_2CO_3	:	$^{11}B(OH)_3$	:	$^{10}B(OH)_3$
5%	0.4448	:	0.0747	:	1.3961
25%	0.4427	:	0.3716	:	1.0969
80%	0.4369	:	1.1737	:	0.2887
100%	0.4349	:	1.4603	:	0.0000

APPENDIX C

Example Input File

C.1 Example pNMRsim Input File

```
spinsys {
  nuclei 11B 11B                          #Two boron-11 nuclei
  channels 11B                            #One RF channel for 11B
  proton_frequency 600e6                  #Static magnetic field
                                          #in terms of 1H Larmor
  shift 1 18p                             #Chemical shift of 1st B
  shift 2  2p                             #CSA not specified = 0
  quadrupole 1 1 25600000 0.2 10 30 82    #Quadrupolar parameters
  quadrupole 2 1   512000 0.5 63 12 24    #1st order, CQ = 0.5 MHz
                                          #Eta = 0.5, random tens.
  dipole 1 2 -800 93.4 119.9 -83.2        #Coupling between spins
}                                         #1 and 2 of 800 Hz at
                                          #given Euler angles
par {
  spin_rate 6160                          #MAS rate
  sw 6160                                 #F2 spectral width
  sw1 6160                                #F1 spectral width
  crystal_file 3zcw30                     #Load crystallite file
  np 256                                  #Datapoints in t2
```

```
  ni 256 2                              #Slices in t1 (States)
  pulseid 5 50e3 y                      #Ideal pulse of 5us
                                        #with 50 kHz nutation
  store pulse90y                        #Save pulse propagator
  delay 10000                           #Calculate 10ms delay
  store mixtime                         #Save delay propagator
  variable Statesphase {0,90}           #Make phase list
  start_operator Inz                    #Initial density matrix
                                        #n = all spins, z = axis
  detect_operator Inc                   #Detect central trans.
  filter 10 [0]                         #ZQ coherence filter
  filter 11 [1,-1]                      #SQ coherence filter
}

pulseq {
  prop pulse90y+$Statesphase            #Propagate RF Ham. with
                                        #alternate States phase
  filter 11                             #Filter SQ coherences
  acq                                   #t1 acquisition
  prop pulse90y                         #Second pulse
  filter 10                             #Filter ZQ coherences
  prop mixtime                          #Mixing time
  prop pulse90y                         #Readout pulse
  acq -x                                #t2 acquisition
}

proc {
  save $(name).fid -simpson             #Store FID of filename
}                                       #in SIMPSON format
```

REFERENCES

[1] A. Abragam. *The Principles of Nuclear Magnetism*. Oxford University Press, Oxford, 1961. Cited on pages 24, 27, 44, 51, and 105.

[2] A. Abragam and M. Goldman. *Nuclear Magnetism: Order and Disorder*. Clarendon Press, Oxford, 1982. Cited on page 44.

[3] V. T. Adamiv, Y. V. Burak, and I. M. Teslyuk. The Crystal Structure of Li2B4O7 Compound in the Temperature Range 10–290k. *J. Alloy. Compd.*, 475(1-2):869–873, 2009. doi:10.1016/j.jallcom.2008.08.017. Cited on page 94.

[4] P. M. Aguiar and S. Kroeker. Medium-Range Order in Cesium Borate Glasses Probed by Double-Resonance NMR. *Solid State Nucl. Magn. Reson.*, 27(1-2):10–15, 2005. doi:10.1016/j.ssnmr.2004.08.009. Cited on page 91.

[5] P. M. Aguiar and S. Kroeker. Boron Speciation and Non-Bridging Oxygens in High-Alkali Borate Glasses. *J. Non-Cryst. Solids*, 353(18-21):1834–1839, 2007. doi:10.1016/j.jnoncrysol.2007.02.013. Cited on page 91.

[6] T. G. Ajithkumar and A. P. M. Kentgens. Homonuclear Correlation Experiments of Half-Integer Quadrupolar Nuclei Using Multiple-Quantum Techniques Spinning at a P-4 Magic Angle. *J. Am. Chem. Soc.*, 125(9):2398–2399, 2003. doi:10.1021/ja0292647. Cited on page 69.

[7] T. G. Ajithkumar, E. R. H. van Eck, and A. P. M. Kentgens. Homonuclear Correlation Experiments for Quadrupolar Nuclei, Spinning Away from the Magic Angle. *Solid State Nucl. Magn. Reson.*, 26(3-4):180–186, 2004. doi:10.1016/j.ssnmr.2004.03.005. Cited on page 69.

[8] J. P. Amoureux and C. Fernandez. Triple, Quintuple and Higher Order Multiple Quantum MAS NMR of Quadrupolar Nuclei. *Solid State Nucl. Magn. Reson.*, 10(4):211–223, 1998. doi:10.1016/S0926-2040(97)00027-1. Cited on pages 62 and 83.

[9] J. P. Amoureux, C. Fernandez, and L. Frydman. Optimized Multiple-Quantum Magic-Angle Spinning NMR Experiments on Half-Integer Quadrupoles. *Chem. Phys. Lett.*, 259(3-4):347–355, 1996. doi:10.1016/0009-2614(96)00809-3. Cited on page 63.

[10] J.-P. Amoureux, C. Fernandez, and S. Steuernagel. Z Filtering in MQMAS NMR. *J. Magn. Reson. Ser. A*, 123(1):116–118, 1996. doi:10.1006/jmra.1996.0221. Cited on page 63.

[11] J. P. Amoureux, J. Trébosc, L. Delevoye, O. Lafon, B. Hu, and Q. Wang. Correlation NMR Spectroscopy Involving Quadrupolar Nuclei. *Solid State Nucl. Magn. Reson.*, 35(1):12–18, 2009. doi:10.1016/j.ssnmr.2008.11.004. Cited on page 66.

[12] J. P. Amoureux, J. Trébosc, J. Wiench, and M. Pruski. HMQC and Refocused-INEPT Experiments Involving Half-Integer Quadrupolar Nuclei in Solids. *J. Magn. Reson.*,

184(1):1–14, 2007. doi:10.1016/j.jmr.2006.09.009. Cited on page 73.

[13] J. A. Anderson, R. J. Astheimer, J. D. Odom, and L. G. Sneddon. High Resolution Boron-11 Nuclear Magnetic Resonance Spectroscopy. 7. Use of Nuclear Magnetic Resonance to Investigate Bonding Interactions between Quadrupolar Nuclei. Boron-Boron Spin-Spin Coupling Constants in Linked Polyhedral Borane and Carborane Cages. *J. Am. Chem. Soc.*, 106(8):2275–2283, 1984. doi:10.1021/ja00320a011. Cited on page 73.

[14] E. R. Andrew, A. Bradbury, and R. G. Eades. Nuclear Magnetic Resonance Spectra from a Crystal Rotated at High Speed. *Nature*, 182(4650):1659–1659, 1958. doi:10.1038/1821659a0. Cited on page 3.

[15] E. R. Andrew, A. Bradbury, and R. G. Eades. Removal of Dipolar Broadening of Nuclear Magnetic Resonance Spectra of Solids by Specimen Rotation. *Nature*, 183(4678):1802–1803, 1959. doi:10.1038/1831802a0. Cited on page 3.

[16] E. R. Andrew and D. P. Tunstall. Spin-Lattice Relaxation in Imperfect Cubic Crystals and in Non-Cubic Crystals. *Proc. Phys. Soc.*, 78(1):1–11, 1961. doi:10.1088/0370-1328/78/1/302. Cited on pages 44 and 103.

[17] F. A. L. Anet, D. J. O'Leary, C. G. Wade, and R. D. Johnson. NMR Relaxation by the Antisymmetric Component of the Shielding Tensor: A Longer Transverse Than Longitudinal Relaxation Time. *Chem. Phys. Lett.*, 171(5-6):401–405, 1990. doi:10.1016/0009-2614(90)85237-7. Cited on page 46.

[18] S. E. Ashbrook and M. J. Duer. Structural Information from Quadrupolar Nuclei in Solid State NMR. *Concepts Magn. Res. A*, 28A(3):183–248, 2006. doi:10.1002/cmr.a.20053. Cited on pages 70, 71, and 75.

[19] S. E. Ashbrook, J. McManus, M. J. Thrippleton, and S. Wimperis. Second-Order Cross-Term Interactions in High-Resolution MAS NMR of Quadrupolar Nuclei. *Prog. Nucl. Magn. Reson. Spectrosc.*, 55(2):160–181, 2009. doi:10.1016/j.pnmrs.2009.04.002. Cited on pages 56 and 73.

[20] S. E. Ashbrook and S. Wimperis. SCAM-STMAS: Satellite-Transition MAS NMR of Quadrupolar Nuclei with Self-Compensation for Magic-Angle Misset. *J. Magn. Reson.*, 162(2):402–416, 2003. doi:10.1016/S1090-7807(03)00016-8. Cited on page 6.

[21] S. E. Ashbrook and S. Wimperis. High-Resolution NMR of Quadrupolar Nuclei in Solids: The Satellite-Transition Magic Angle Spinning (STMAS) Experiment. *Prog. Nucl. Magn. Reson. Spectrosc.*, 45(1-2):53–108, 2004. doi:10.1016/j.pnmrs.2004.04.002. Cited on page 6.

[22] S. E. Ashbrook and S. Wimperis. Spin-Locking of Half-Integer Quadrupolar Nuclei in Nuclear Magnetic Resonance of Solids: Creation and Evolution of Coherences. *J. Chem. Phys.*, 120(6):2719–2731, 2004. doi:10.1063/1.1638995. Cited on pages 41 and 72.

[23] A. D. Bain. Exact Calculation, Using Angular Momentum, of Combined Zeeman and Quadrupolar Interactions in NMR. *Mol. Phys.*, 101(21):3163–3175, 2003. doi:10.1080/00268970310001626298. Cited on page 25.

[24] A. D. Bain. A Simple Proof That Third-Order Quadrupole Perturbations of the NMR Central Transition of Half-Integral Spin Nuclei Are Zero. *J. Magn. Reson.*, 179(2):308–310, 2006. doi:10.1016/j.jmr.2006.01.007. Cited on page 30.

[25] A. D. Bain. Operator Formalisms: An Overview. *Concepts Magn. Res. A*, 28A(6):369–383, 2006. doi:10.1002/cmr.a.20067. Cited on page 10.

[26] M. Bak, J. T. Rasmussen, and N. C. Nielsen. SIMPSON: A General Simulation Program for Solid-State NMR Spectroscopy. *J. Magn. Reson.*, 147(2):296–330, 2000. doi:10.1006/jmre.2000.2179. Cited on pages 51 and 84.

[27] M. Baldus, D. Rovnyak, and R. G. Griffin. Radio-Frequency-Mediated Dipolar Re-

coupling among Half-Integer Quadrupolar Spins. *J. Chem. Phys.*, 112(13):5902–5909, 2000. doi:10.1063/1.481187. Cited on pages 70 and 134.

[28] M. Baldus, M. Tomaselli, B. H. Meier, and R. R. Ernst. Broadband Polarization-Transfer Experiments for Rotating Solids. *Chem. Phys. Lett.*, 230(4-5):329–336, 1994. doi:10.1016/0009-2614(94)01209-1. Cited on page 133.

[29] R. S. Balmer, J. R. Brandon, S. L. Clewes, H. K. Dhillon, J. M. Dodson, I. Friel, P. N. Inglis, T. D. Madgwick, M. L. Markham, T. P. Mollart, N. Perkins, G. A. Scarsbrook, D. J. Twitchen, A. J. Whitehead, J. J. Wilman, and S. M. Woollard. Chemical Vapour Deposition Synthetic Diamond: Materials, Technology and Applications. *J. Phys.: Condens. Matter*, 21(36):364221, 2009. doi:10.1088/0953-8984/21/36/364221. Cited on page 88.

[30] J. Banerjee, G. Ongie, J. Harder, T. Edwards, C. Larson, S. Sutton, A. Moeller, A. Basu, M. Affatigato, S. Feller, M. Kodama, P. M. Aguiar, and S. Kroeker. Structural Studies of Solution-Made High Alkali Content Borate Glasses. *J. Non-Cryst. Solids*, 352(6-7):674–678, 2006. doi:10.1016/j.jnoncrysol.2005.11.051. Cited on page 92.

[31] N. S. Barrow. Superstructural Units in Lithium Borate Glasses. *MPhys Dissertation, University of Warwick*, 2006. Cited on pages 91, 105, and 108.

[32] N. S. Barrow, S. E. Ashbrook, S. P. Brown, and D. Holland. Developing 11B Solid State MAS NMR Methods to Characterise Medium Range Structure in Borates. *Phys. Chem. Glasses-Eur. J. Glass Sci. Technol. B*, 50(3):201–204, 2009. Cited on page viii.

[33] A. Bax, R. Freeman, and S. P. Kempsell. Natural Abundance Carbon-13-Carbon-13 Coupling Observed via Double-Quantum Coherence. *J. Am. Chem. Soc.*, 102(14):4849–4851, 1980. doi:10.1021/ja00534a056. Cited on page 74.

[34] M. J. Bayro, M. Huber, R. Ramachandran, T. C. Davenport, B. H. Meier, M. Ernst, and R. G. Griffin. Dipolar Truncation in Magic-Angle Spinning NMR Recoupling Experiments. *J. Chem. Phys.*, 130(11):8, 2009. doi:10.1063/1.3089370. Cited on pages 56 and 67.

[35] E. D. Becker, C. L. Fisk, and C. L. Khetrapal. *The Development of NMR*, volume 1 of *Encyclopedia of Magnetic Resonance*. Wiley, Chicester, 1996. doi:10.1002/9780470034590.emrhp0001. Cited on page 2.

[36] M. Bertmer, L. Züchner, J. C. C. Chan, and H. Eckert. Short and Medium Range Order in Sodium Aluminoborate Glasses. 2. Site Connectivities and Cation Distributions Studied by Rotational Echo Double Resonance NMR Spectroscopy. *J. Phys. Chem. B*, 104(28):6541–6553, 2000. doi:10.1021/jp9941918. Cited on page 91.

[37] H. Bildsøe, J. P. Jacobsen, and K. Schaumburg. Application of Density Matrix Formalism in NMR Spectroscopy. I. Development of a Calculation Scheme and Some Simple Examples. *J. Magn. Reson.*, 23(1):137–151, 1976. doi:10.1016/0022-2364(76)90146-3. Cited on page 10.

[38] F. Bloch. Nuclear Induction. *Phys. Rev.*, 70(7-8):460, 1946. doi:10.1103/PhysRev.70.460. Cited on page 2.

[39] F. Bloch. *The Principle of Nuclear Induction*, volume 1 of *Encyclopedia of Magnetic Resonance*. Wiley, Chicester, 1996. doi:10.1002/9780470034590.emrhp0022. Cited on page 2.

[40] F. Bloch and A. Siegert. Magnetic Resonance for Nonrotating Fields. *Phys. Rev.*, 57(6):522, 1940. doi:10.1103/PhysRev.57.522. Cited on page 40.

[41] S. Block and A. Perloff. The Crystal Structure of Barium Tetraborate, BaO.2B2O3. *Acta Crystallogr.*, 19(3):297–300, 1965. doi:10.1107/S0365110X65003341. Cited on page 101.

[42] N. Bloembergen. On the Interaction of Nuclear Spins in a Crystalline Lattice. *Physica*, 15(3-4):386–426, 1949. doi:10.1016/0031-8914(49)90114-7. Cited on page 54.

[43] G. Bodenhausen, H. Kogler, and R. R. Ernst. Selection of Coherence-Transfer Pathways in NMR Pulse Experiments. *J. Magn. Reson.*, 58(3):370–388, 1984. doi:10.1016/0022-2364(84)90142-2. Cited on pages 4, 41, and 43.

[44] G. Bodenhausen, G. Wagner, M. Rance, O. W. Sørensen, K. Wüthrich, and R. R. Ernst. Longitudinal Two-Spin Order in 2D Exchange Spectroscopy (NOESY). *J. Magn. Reson.*, 59(3):542–550, 1984. doi:10.1016/0022-2364(84)90092-1. Cited on page 133.

[45] R. Böhmer and F. Qi. Spin Relaxation and Ultra-Slow Li Motion in an Aluminosilicate Glass Ceramic. *Solid State Nucl. Magn. Reson.*, 31(1):28–34, 2007. doi:10.1016/j.ssnmr.2006.11.002. Cited on page 104.

[46] G. J. Bowden and W. D. Hutchison. Tensor Operator-Formalism for Multiple-Quantum NMR. 1. Spin-1 Nuclei. *J. Magn. Reson.*, 67(3):403–414, 1986. Cited on pages 10 and 28.

[47] G. J. Bowden, W. D. Hutchison, and J. Khachan. Tensor Operator-Formalism for Multiple-Quantum NMR. 2. Spins-3/2, 2, and 5/2 and General-I. *J. Magn. Reson.*, 67(3):415–437, 1986. Cited on page 10.

[48] P. J. Bray. NMR Studies of the Structures of Glasses. *J. Non-Cryst. Solids*, 95-96(Part 1):45–59, 1987. doi:10.1016/S0022-3093(87)80098-4. Cited on page 91.

[49] P. J. Bray. NMR and NQR Studies of Boron in Vitreous and Crystalline Borates. *Inorg. Chim. Acta*, 289:158–173, 1999. doi:10.1016/S0020-1693(99)00066-3. Cited on page 91.

[50] A. Brinkmann, A. P. M. Kentgens, T. Anupõld, and A. Samoson. Symmetry-Based Recoupling in Double-Rotation NMR Spectroscopy. *J. Chem. Phys.*, 129(17):174507–11, 2008. doi:10.1063/1.3005395. Cited on page 72.

[51] A. Brinkmann, J. Schmedt auf der Günne, and M. H. Levitt. Homonuclear Zero-Quantum Recoupling in Fast Magic-Angle Spinning Nuclear Magnetic Resonance. *J. Magn. Reson.*, 156(1):79–96, 2002. doi:10.1006/jmre.2002.2525. Cited on page 70.

[52] H. C. Brown and S. Krishnamurthy. Forty Years of Hydride Reductions. *Tetrahedron*, 35(5):567–607, 1979. doi:10.1016/0040-4020(79)87003-9. Cited on page 87.

[53] H. C. Brown, H. I. Schlesinger, and A. B. Burg. Hydrides of Boron. XI. The Reaction of Diborane with Organic Compounds Containing a Carbonyl Group. *J. Am. Chem. Soc.*, 61(3):673–680, 1939. doi:10.1021/ja01872a041. Cited on page 87.

[54] S. P. Brown. Multiple-Quantum MAS NMR of Half-Integer Quadrupolar Nuclei. *Ph.D. Thesis, Merton College, Oxford*, 1997. Cited on pages 53 and 63.

[55] S. P. Brown. Probing Proton-Proton Proximities in the Solid State. *Prog. Nucl. Magn. Reson. Spectrosc.*, 50(4):199–251, 2007. doi:10.1016/j.pnmrs.2006.10.002. Cited on page 100.

[56] S. P. Brown, S. J. Heyes, and S. Wimperis. Two-Dimensional MAS Multiple-Quantum NMR of Quadrupolar Nuclei. Removal of Inhomogeneous Second-Order Broadening. *J. Magn. Reson. Ser. A*, 119(2):280–284, 1996. doi:10.1006/jmra.1996.0088. Cited on page 64.

[57] S. P. Brown, M. Perez-Torralba, D. Sanz, R. M. Claramunt, and L. Emsley. The Direct Detection of a Hydrogen Bond in the Solid State by NMR through the Observation of a Hydrogen-Bond Mediated 15N–15N *J* Coupling. *J. Am. Chem. Soc.*, 124(7):1152–1153, 2002. doi:10.1021/ja0172262. Cited on page 75.

[58] S. P. Brown and S. Wimperis. Two-Dimensional Multiple-Quantum MAS NMR of Quadrupolar Nuclei: A Comparison of Methods. *J. Magn. Reson.*, 128(1):42–61, 1997. doi:10.1006/jmre.1997.1217. Cited on pages 33, 63, 64, and 102.

[59] E. Brunner, D. Freude, B. C. Gerstein, and H. Pfeifer. Residual Linewidths of NMR Spectra of Systems under Magic-Angle Spinning. *J. Magn. Reson.*, 90(1):90–99, 1990. doi:10.1016/0022-2364(90)90367-I. Cited on page 56.

[60] H. A. Buckmaster. Tables of Angular Momentum Transformation Matrix Elements. *Can. J. Phys.*, 42(2):386–391, 1964. doi:10.1139/CJP-42-2-386. Cited on pages 12 and 5.

[61] H. Y. Carr and E. M. Purcell. Effects of Diffusion on Free Precession in Nuclear Magnetic Resonance Experiments. *Phys. Rev.*, 94(3):630, 1954. doi:10.1103/PhysRev.94.630. Cited on page 49.

[62] R. Challoner, T. Nakai, and C. A. McDowell. *J* Coupling in Chemically Equivalent Spin Pairs as Studied by Solid-State Nuclear Magnetic Resonance. *J. Chem. Phys.*, 94(11):7038–7045, 1991. doi:10.1063/1.460237. Cited on page 75.

[63] J. C. C. Chan. Spin Echoes in Half-Integer Quadrupole Systems. *Concepts Magn. Res.*, 11(6):363–377, 1999. doi:10.1002/(SICI)1099-0534(1999)11:6<363::AID-CMR2>3.0.CO;2-A. Cited on page 49.

[64] B. Chen, U. Werner-Zwanziger, M. L. F. Nascimento, L. Ghussn, E. D. Zanotto, and J. W. Zwanziger. Structural Similarity on Multiple Length Scales and its Relation to Devitrification Mechanism: A Solid-State NMR Study of Alkali Diborate Glasses and Crystals. *J. Phys. Chem. C*, 113(48):20725–20732, 2009. doi:10.1021/jp907259e. Cited on pages 91, 101, and 137.

[65] V. B. Cheng, H. H. Suzukawa, and M. Wolfsberg. Investigations of a Nonrandom Numerical Method for Multidimensional Integration. *J. Chem. Phys.*, 59(8):3992–3999, 1973. doi:10.1063/1.1680590. Cited on page 84.

[66] M. G. Colombo, B. H. Meier, and R. R. Ernst. Rotor-Driven Spin Diffusion in Natural-Abundance 13C Spin Systems. *Chem. Phys. Lett.*, 146(3-4):189–196, 1988. doi:10.1016/0009-2614(88)87429-3. Cited on pages 59 and 70.

[67] H. Conroy. Molecular Schrödinger Equation. VIII. A New Method for the Evaluation of Multidimensional Integrals. *J. Chem. Phys.*, 47(12):5307–5318, 1967. doi:10.1063/1.1701795. Cited on page 84.

[68] A. Cooper. The Ubiquitous Glass Transition. *J. Non-Cryst. Solids*, 95-96(Part 1):1–14, 1987. doi:10.1016/S0022-3093(87)80095-9. Cited on page 88.

[69] L. Cormier, G. Calas, and B. Beuneu. Structure of Single and Mixed Alkali Li-Rb Borate Glasses by Neutron Diffraction. *J. Non-Cryst. Solids*, 353(18-21):1779–1784, 2007. doi:10.1016/j.jnoncrysol.2007.02.045. Cited on page 91.

[70] F. Creuzet, A. McDermott, R. Gebhard, K. van der Hoef, M. Spijker-Assink, J. Herzfeld, J. Lugtenburg, M. Levitt, and R. Griffin. Determination of Membrane Protein Structure by Rotational Resonance NMR: Bacteriorhodopsin. *Science*, 251(4995):783–786, 1991. doi:10.1126/science.1990439. Cited on page 59.

[71] M. Deschamps, F. Fayon, V. Montouillout, and D. Massiot. Through-Bond Homonuclear Correlation Experiments in Solid-State NMR Applied to Quadrupolar Nuclei in Al-O-P-O-Al Chains. *Chem. Commun.*, 18:1924–1925, 2006. doi:10.1039/b600514d. Cited on page 75.

[72] M. Deschamps and D. Massiot. Three-Dimensional through-Bond Homonuclear-Heteronuclear Correlation Experiments for Quadrupolar Nuclei in Solid-State NMR Applied to 27Al-O-31P-O-27Al Networks. *J. Magn. Reson.*, 184(1):15–19, 2007. doi:10.1016/j.jmr.2006.09.011. Cited on page 75.

[73] S. W. Ding and C. A. McDowell. Spectral Spin-Diffusion of a Spin-3/2 System in Rotating Solids. *Mol. Phys.*, 85(2):283–298, 1995. Cited on page 69.

[74] N. G. Dowell, S. E. Ashbrook, J. McManus, and S. Wimperis. Relative Orientation of Quadrupole Tensors from Two-Dimensional Multiple-Quantum MAS NMR. *J. Am. Chem. Soc.*, 123(33):8135–8136, 2001. doi:10.1021/ja010681d. Cited on pages 68 and 69.

[75] N. G. Dowell, S. E. Ashbrook, and S. Wimperis. Relative Orientation of Quadru-

pole Tensors from High-Resolution NMR of Powdered Solids. *J. Phys. Chem. A*, 106(41):9470–9478, 2002. doi:10.1021/jp021315z. Cited on pages 68, 69, and 130.

[76] L.-S. Du, M. H. Levitt, and C. P. Grey. High-Order Spin Diffusion Mechanisms in 19F 2-D NMR of Oxyfluorides. *J. Magn. Reson.*, 140(1):242–249, 1999. doi:10.1006/jmre.1999.1849. Cited on pages 134, 163, and 164.

[77] L. S. Du and J. F. Stebbins. Solid-State NMR Study of Metastable Immiscibility in Alkali Borosilicate Glasses. *J. Non-Cryst. Solids*, 315(3):239–255, 2003. doi:10.1016/S0022-3093(02)01604-6. Cited on page 91.

[78] M. J. Duer. Determination of Structural Data from Multiple-Quantum Magic-Angle Spinning NMR Experiments. *Chem. Phys. Lett.*, 277(1-3):167–174, 1997. doi:10.1016/S0009-2614(97)00929-9. Cited on page 67.

[79] M. J. Duer. *Solid-State NMR Spectroscopy: Principles and Applications*. Blackwell Publishing, Oxford, 2002. Cited on page 91.

[80] M. J. Duer. *Introduction to Solid-State NMR Spectroscopy*. Blackwell Publishing, Oxford, 2004. Cited on pages 20 and 25.

[81] M. J. Duer and A. J. Painter. Correlating Quadrupolar Nuclear Spins: A Multiple-Quantum NMR Approach. *Chem. Phys. Lett.*, 313(5-6):763–770, 1999. doi:10.1016/S0009-2614(99)01043-X. Cited on page 71.

[82] L. Duma, W. C. Lai, M. Carravetta, L. Emsley, S. P. Brown, and M. H. Levitt. Principles of Spin-Echo Modulation by *J*-Couplings in Magic-Angle-Spinning Solid-State NMR. *ChemPhysChem*, 5(6):815–833, 2004. doi:10.1002/cphc.200301213. Cited on pages 49 and 75.

[83] B. P. Dwivedi, M. H. Rahman, Y. Kumar, and B. N. Khanna. Raman Scattering Study of Lithium Borate Glasses. *J. Phys. Chem. Solids*, 54(5):621–628, 1993. doi:10.1016/0022-3697(93)90242-J. Cited on page 91.

[84] H. Eckert. Structural Characterization of Noncrystalline Solids and Glasses Using Solid-State NMR. *Prog. Nucl. Magn. Reson. Spectrosc.*, 24:159–293, 1992. doi:10.1016/0079-6565(92)80001-V. Cited on pages 6 and 90.

[85] M. Edén. Solid-State NMR of Multiple-Spin Systems. *Ph.D. Thesis, Stockholm University, Sweden*, 1999. Cited on page 20.

[86] M. Edén. Computer Simulations in Solid-State NMR. I. Spin Dynamics Theory. *Concepts Magn. Res. A*, 17A(1):117–154, 2003. doi:10.1002/cmr.a.10061. Cited on pages 10 and 84.

[87] M. Edén. Computer Simulations in Solid-State NMR. II. Implementations for Static and Rotating Samples. *Concepts Magn. Res. A*, 18A(1):1–23, 2003. doi:10.1002/cmr.a.10064. Cited on page 84.

[88] M. Edén. Computer Simulations in Solid-State NMR. III. Powder Averaging. *Concepts Magn. Res. A*, 18A(1):24–55, 2003. doi:10.1002/cmr.a.10065. Cited on page 84.

[89] M. Edén. Determination of Absolute Quadrupolar Tensor Orientations by Double-Quantum NMR on Powders. *Chem. Phys. Lett.*, 470(4-6):318–324, 2009. doi:10.1016/j.cplett.2009.01.061. Cited on page 72.

[90] M. Edén. Homonuclear Dipolar Recoupling of Half-Integer Spin Quadrupolar Nuclei: Techniques and Applications. *Solid State Nucl. Magn. Reson.*, 36(1):1–10, 2009. doi:10.1016/j.ssnmr.2009.06.005. Cited on page 66.

[91] M. Edén, H. Annersten, and A. Zazzi. Pulse-Assisted Homonuclear Dipolar Recoupling of Half-Integer Quadrupolar Spins in Magic-Angle Spinning NMR. *Chem. Phys. Lett.*, 410(1-3):24–30, 2005. doi:10.1016/j.cplett.2005.04.030. Cited on page 70.

[92] M. Edén and L. Frydman. Quadrupolar-Driven Recoupling of Homonuclear Dipolar Interactions in the Nuclear Magnetic Resonance of Rotating Solids. *J. Chem. Phys.*,

114(9):4116–4123, 2001. doi:10.1063/1.1344886. Cited on pages 26, 67, 146, and 157.

[93] M. Edén and L. Frydman. Homonuclear NMR Correlations between Half-Integer Quadrupolar Nuclei Undergoing Magic-Angle Spinning. *J. Phys. Chem. B*, 107(51):14598–14611, 2003. doi:10.1021/jp035794t. Cited on pages 56, 58, 68, 71, 129, 133, 149, and 154.

[94] M. Edén, J. Grinshtein, and L. Frydman. High Resolution 3D Exchange NMR Spectroscopy and the Mapping of Connectivities between Half-Integer Quadrupolar Nuclei. *J. Am. Chem. Soc.*, 124(33):9708–9709, 2002. doi:10.1021/ja020534v. Cited on page 71.

[95] M. Edén and A. Y. H. Lo. Supercycled Symmetry-Based Double-Quantum Dipolar Recoupling of Quadrupolar Spins in MAS NMR: I. Theory. *J. Magn. Reson.*, 200(2):267–279, 2009. doi:10.1016/j.jmr.2009.07.007. Cited on page 72.

[96] M. Edén, D. Zhou, and J. Yu. Improved Double-Quantum NMR Correlation Spectroscopy of Dipolar-Coupled Quadrupolar Spins. *Chem. Phys. Lett.*, 431(4-6):397–403, 2006. doi:10.1016/j.cplett.2006.09.081. Cited on page 72.

[97] A. E. Elalaoui, A. Maillard, and M. D. Fontana. Raman Scattering and Non-Linear Optical Properties in Li2B4O7. *J. Phys.: Condens. Matter*, 17(46):7441–7454, 2005. doi:10.1088/0953-8984/17/46/027. Cited on page 93.

[98] R. R. Ernst. *The Success Story of Fourier Transformation in NMR*, volume 1 of *Encyclopedia of Magnetic Resonance*. Wiley, Chicester, 1996. doi:10.1002/9780470034590.emrhp0051. Cited on page 3.

[99] R. R. Ernst and W. A. Anderson. Application of Fourier Transform Spectroscopy to Magnetic Resonance. *Rev. Sci. Instrum.*, 37(1):93–102, 1966. doi:10.1063/1.1719961. Cited on pages 3 and 51.

[100] R. R. Ernst, G. Bodenhausen, and A. Wokaun. *Principles of Nuclear Magnetic Resonance in One and Two Dimensions*. Clarendon Press, Oxford, 1987. Cited on pages 42, 44, and 80.

[101] G. Facey, D. Gusev, R. H. Morris, S. Macholl, and G. Buntkowsky. 2H MAS NMR of Strongly Dipolar Coupled Deuterium Pairs in Transition Metal Dihydrides: Extracting Dipolar Coupling and Quadrupolar Tensor Orientations from the Lineshape of Spinning Sidebands. *Phys. Chem. Chem. Phys.*, 2(5):935–941, 2000. doi:10.1039/a908942j. Cited on page 67.

[102] T. C. Farrar. Pulsed and Fourier Transform NMR Spectroscopy. *Anal. Chem.*, 42(4):109A–112A, 1970. doi:10.1021/ac60286a022. Cited on page 3.

[103] F. Fayon, G. L. Saout, L. Emsley, and D. Massiot. Through-Bond Phosphorus-Phosphorus Connectivities in Crystalline and Disordered Phosphates by Solid-State NMR. *Chem. Commun.*, 16:1702–1703, 2002. doi:10.1039/b205037b. Cited on page 74.

[104] S. A. Feller, W. J. Dell, and P. J. Bray. 10B NMR Studies of Lithium Borate Glasses. *J. Non-Cryst. Solids*, 51(1):21–30, 1982. doi:10.1016/0022-3093(82)90186-7. Cited on page 91.

[105] G. Ferlat, T. Charpentier, A. P. Seitsonen, A. Takada, M. Lazzeri, L. Cormier, G. Calas, and F. Mauri. Boroxol Rings in Liquid and Vitreous B2O3 from First Principles. *Phys. Rev. Lett.*, 101(6):065504–4, 2008. doi:10.1103/PhysRevLett.101.065504. Cited on page 90.

[106] L. Frydman and J. S. Harwood. Isotropic Spectra of Half-Integer Quadrupolar Spins from Bidimensional Magic-Angle-Spinning NMR. *J. Am. Chem. Soc.*, 117(19):5367–5368, 1995. doi:10.1021/ja00124a023. Cited on page 5.

[107] E. Fukushima and S. B. W. Roeder. *Experimental Pulse NMR: A Nuts and Bolts Approach*. Addison-Wesley, Reading Massachusetts, 1981. Cited on pages 51 and 78.

[108] Z. Gan. Deuterium Polarization Transfer in Rotating Solids and its Application in Structural Investigation. *Mol. Phys.*, 95(6):1143–1152, 1998. doi:10.1080/002689798166161. Cited on page 67.

[109] Z. Gan and H.-T. Kwak. Enhancing MQMAS Sensitivity Using Signals from Multiple Coherence Transfer Pathways. *J. Magn. Reson.*, 168(2):346–351, 2004. doi:10.1016/j.jmr.2004.03.021. Cited on page 64.

[110] Z. Gan, P. Srinivasan, J. R. Quine, S. Steuernagel, and B. Knott. Third-Order Effect in Solid-State NMR of Quadrupolar Nuclei. *Chem. Phys. Lett.*, 367(1-2):163–169, 2003. doi:10.1016/S0009-2614(02)01681-0. Cited on page 30.

[111] Z. H. Gan. Isotropic NMR Spectra of Half-Integer Quadrupolar Nuclei Using Satellite Transitions and Magic-Angle Spinning. *J. Am. Chem. Soc.*, 122(13):3242–3243, 2000. doi:10.1021/ja9939791. Cited on page 6.

[112] S. Ganapathy, S. Schramm, and E. Oldfield. Variable-Angle Sample-Spinning High Resolution NMR of Solids. *J. Chem. Phys.*, 77(9):4360–4365, 1982. doi:10.1063/1.444436. Cited on page 4.

[113] A. Gençten, O. Tezel, and S. Bahçeli. Product Operator Theory for Spin-3/2 Nuclei and Application to 2D *J*-Resolved NMR Spectroscopy. *Chem. Phys. Lett.*, 351(1-2):109–114, 2002. doi:10.1016/S0009-2614(01)01270-2. Cited on page 73.

[114] I. P. Gerothanassis and C. G. Tsanaktsidis. Nuclear Electric Quadrupole Relaxation. *Concepts Magn. Res.*, 8(1):63–74, 1996. doi:10.1002/(SICI)1099-0534(1996)8:1<63::AID-CMR5>3.0.CO;2-N. Cited on pages 44, 45, and 104.

[115] A. A. Goktas, G. F. Neilson, and M. C. Weinberg. Crystallization of Lithium Borate Glasses. *J. Mater. Sci.*, 27(1):24–28, 1992. Cited on page 95.

[116] M. Goldman. Formal Theory of Spin-Lattice Relaxation. *J. Magn. Reson.*, 149(2):160–187, 2001. doi:10.1006/jmre.2000.2239. Cited on page 44.

[117] B. H. Goodreau and J. T. Spencer. Small Heteroborane Cluster Systems. 5. Factors Affecting the 2D 11B–11B (Boron-11) COSY NMR Spectra of Terminal- and Bridge-Substituted Pentaborane Cluster Systems. *Inorg. Chem.*, 31(12):2612–2621, 1992. doi:10.1021/ic00038a056. Cited on page 74.

[118] P. J. Grandinetti. Does Phase Cycling Work for Nuclei Experiencing Strong Quadrupolar Couplings? *Solid State Nucl. Magn. Reson.*, 23(1-2):1–13, 2003. doi:10.1016/S0926-2040(02)00022-X. Cited on page 42.

[119] P. Guerry, M. E. Smith, and S. P. Brown. 31P MAS Refocused INADEQUATE Spin-Echo (REINE) NMR Spectroscopy: Revealing *J* Coupling and Chemical Shift Two-Dimensional Correlations in Disordered Solids. *J. Am. Chem. Soc.*, 131(33):11861–11874, 2009. doi:10.1021/ja902238s. Cited on page 74.

[120] H. S. Gutowsky and D. W. McCall. Nuclear Magnetic Resonance Fine Structure in Liquids. *Phys. Rev.*, 82(5):748, 1951. doi:10.1103/PhysRev.82.748. Cited on page 72.

[121] U. Haeberlen. *Advances in Magnetic Resonance*. Academic Press, New York, 1976. Cited on page 20.

[122] U. Haeberlen and J. S. Waugh. Coherent Averaging Effects in Magnetic Resonance. *Phys. Rev.*, 175(2):453, 1968. doi:10.1103/PhysRev.175.453. Cited on page 3.

[123] E. L. Hahn and D. E. Maxwell. Chemical Shift and Field Independent Frequency Modulation of the Spin Echo Envelope. *Phys. Rev.*, 84(6):1246, 1951. doi:10.1103/PhysRev.84.1246. Cited on page 23.

[124] M. R. Hansen, G. K. H. Madsen, H. J. Jakobsen, and J. Skibsted. Refinement of Borate Structures from B-11 MAS NMR Spectroscopy and Density Functional Theory Calculations of B-11 Electric Field Gradients. *J. Phys. Chem. A*, 109(9):1989–1997, 2005. doi:10.1021/jp045767i. Cited on page 130.

[125] M. R. Hansen, T. Vosegaard, H. J. Jakobsen, and J. Skibsted. B-11 Chemical Shift Anisotropies in Borates from B-11 MAS, MQMAS, and Single-Crystal NMR Spectroscopy. *J. Phys. Chem. A*, 108(4):586–594, 2004. doi:10.1021/jp030939h. Cited on page 99.

[126] R. K. Harris and E. D. Becker. NMR Nomenclature: Nuclear Spin Properties and Conventions for Chemical Shifts—IUPAC Recommendations. *J. Magn. Reson.*, 156(2):323–326, 2002. doi:10.1006/jmre.2002.2554. Cited on page 78.

[127] R. K. Harris and B. E. Mann. *NMR and the Periodic Table*. Academic Press, London, 1978. Cited on pages 17 and 78.

[128] P. Hartmann, C. Jäger, and J. W. Zwanziger. Off-Angle Correlation Spectroscopy Applied to Spin-1/2 and Quadrupolar Nuclei. *Solid State Nucl. Magn. Reson.*, 13(4):245–254, 1999. doi:10.1016/S0926-2040(99)00003-X. Cited on page 69.

[129] S. R. Hartmann and E. L. Hahn. Nuclear Double Resonance in the Rotating Frame. *Phys. Rev.*, 128(5):2042, 1962. doi:10.1103/PhysRev.128.2042. Cited on page 3.

[130] S. Hayashi. Magic-Angle Spinning Nuclear Magnetic Resonance of Half-Integer Quadrupole Nuclei: Effect of Spin-Locking Efficiency on Powder Lineshapes. *Solid State Nucl. Magn. Reson.*, 3(2):93–101, 1994. doi:10.1016/0926-2040(94)90027-2. Cited on page 41.

[131] S. Hayashi and K. Hayamizu. Shift References in High-Resolution Solid-State NMR. *Bull. Chem. Soc. Jpn.*, 7:2429–2430, 1989. doi:10.1246/bcsj.62.2429. Cited on page 78.

[132] P. Hodgkinson. pNMRsim: A General Simulation Program for Large Problems in Solid-State NMR. *http://www.dur.ac.uk/solids.nmr/software/pnmrsim/*, 2009. Cited on pages 84 and 149.

[133] P. Hodgkinson and L. Emsley. Numerical Simulation of Solid-State NMR Experiments. *Prog. Nucl. Magn. Reson. Spectrosc.*, 36(3):201–239, 2000. doi:10.1016/S0079-6565(99)00019-9. Cited on page 10.

[134] P. J. Hore, J. A. Jones, and S. Wimperis. *NMR: The Toolkit*. Oxford University Press, Oxford, 2000. Cited on pages 9 and 42.

[135] D. I. Hoult. The Origins and Present Status of the Radio Wave Controversy in NMR. *Concepts Magn. Res. A*, 34A(4):193–216, 2009. doi:10.1002/cmr.a.20142. Cited on page 49.

[136] D. I. Hoult and B. Bhakar. NMR Signal Reception: Virtual Photons and Coherent Spontaneous Emission. *Concepts Magn. Res.*, 9(5):277–297, 1997. doi:10.1002/(SICI)1099-0534(1997)9:5<277::AID-CMR1>3.0.CO;2-W. Cited on page 49.

[137] B. Hu, J.-P. Amoureux, and J. Trébosc. Indirect Covariance NMR Spectroscopy of through-Bond Homo-Nuclear Correlations for Quadrupolar Nuclei in Solids under High-Resolution. *Solid State Nucl. Magn. Reson.*, 31(4):163–168, 2007. doi:10.1016/j.ssnmr.2007.03.002. Cited on page 76.

[138] C. E. Hughes, M. Carravetta, and M. H. Levitt. Some Conjectures for Cogwheel Phase Cycling. *J. Magn. Reson.*, 167(2):259–265, 2004. doi:10.1016/j.jmr.2004.01.001. Cited on page 43.

[139] I. Hung, A. P. Howes, T. Anupõld, A. Samoson, D. Massiot, M. E. Smith, S. P. Brown, and R. Dupree. Al-27 Double Rotation Two-Dimensional Spin Diffusion NMR: Complete Unambiguous Assignment of Aluminium Sites in 9Al2O3·2B2O3. *Chem. Phys. Lett.*, 432(1-3):152–156, 2006. doi:10.1016/j.cplett.2006.10.085. Cited on page 71.

[140] I. Hung, A. P. Howes, B. G. Parkinson, T. Anupõld, A. Samoson, S. P. Brown, P. F. Harrison, D. Holland, and R. Dupree. Determination of the Bond-Angle Distribution in Vitreous B2O3 by 11B Double Rotation (DOR) NMR Spectroscopy. *J. Solid State Chem.*, 182(9):2402–2408, 2009. doi:10.1016/j.jssc.2009.06.025. Cited on pages 90

and 132.

[141] I. Hung, A.-C. Uldry, J. Becker-Baldus, A. L. Webber, A. Wong, M. E. Smith, S. A. Joyce, J. R. Yates, C. J. Pickard, R. Dupree, and S. P. Brown. Probing Heteronuclear 15N–17O and 13C–17O Connectivities and Proximities by Solid-State NMR Spectroscopy. *J. Am. Chem. Soc.*, 131(5):1820–1834, 2009. doi:10.1021/ja805898d. Cited on pages 73 and 75.

[142] I. Hung, A. Wong, A. P. Howes, T. Anupõld, J. Past, A. Samoson, X. Mo, G. Wu, M. E. Smith, S. P. Brown, and R. Dupree. Determination of NMR Interaction Parameters from Double Rotation NMR. *J. Magn. Reson.*, 188(2):246–259, 2007. doi:10.1016/j.jmr.2007.07.009. Cited on pages 35 and 98.

[143] I. Hung, A. Wong, A. P. Howes, T. Anupõld, A. Samoson, M. E. Smith, D. Holland, S. P. Brown, and R. Dupree. Separation of Isotropic Chemical and Second-Order Quadrupolar Shifts by Multiple-Quantum Double Rotation NMR. *J. Magn. Reson.*, 197(2):229–236, 2009. doi:10.1016/j.jmr.2009.01.005. Cited on page 35.

[144] S. J. Hwang, C. Fernandez, J. P. Amoureux, J. Cho, S. W. Martin, and M. Pruski. Quantitative Study of the Short Range Order in B2O3 and B2S3 by MAS and Two-Dimensional Triple-Quantum MAS 11B NMR. *Solid State Nucl. Magn. Reson.*, 8(2):109–121, 1997. doi:10.1016/S0926-2040(96)01280-5. Cited on page 90.

[145] D. Iuga. Nuclear Magnetic Resonance Studies of Half-Integer Quadrupolar Nuclei. *Ph.D. Thesis, Nijmegan University, The Netherlands*, 2003. Cited on page 39.

[146] D. Iuga, C. Morais, Z. H. Gan, D. R. Neuville, L. Cormier, and D. Massiot. NMR Heteronuclear Correlation between Quadrupolar Nuclei in Solids. *J. Am. Chem. Soc.*, 127(33):11540–11541, 2005. doi:10.1021/ja052452n. Cited on page 73.

[147] D. Iuga, H. Schäfer, R. Verhagen, and A. P. M. Kentgens. Population and Coherence Transfer Induced by Double Frequency Sweeps in Half-Integer Quadrupolar Spin Systems. *J. Magn. Reson.*, 147(2):192–209, 2000. doi:10.1006/jmre.2000.2192. Cited on page 64.

[148] N. Ivchenko, C. E. Hughes, and M. H. Levitt. Multiplex Phase Cycling. *J. Magn. Reson.*, 160(1):52–58, 2003. doi:10.1016/S1090-7807(02)00108-8. Cited on pages 43 and 64.

[149] G. Jaccard, S. Wimperis, and G. Bodenhausen. Multiple-Quantum NMR Spectroscopy of S=3/2 Spins in Isotropic Phase: A New Probe for Multiexponential Relaxation. *J. Chem. Phys.*, 85(11):6282–6293, 1986. doi:10.1063/1.451458. Cited on page 44.

[150] N. E. Jacobsen. *NMR Spectroscopy Explained*. Wiley, Hoboken, 2007. Cited on pages 51, 55, and 78.

[151] J. Jeener, B. H. Meier, P. Bachmann, and R. R. Ernst. Investigation of Exchange Processes by Two-Dimensional NMR Spectroscopy. *J. Chem. Phys.*, 71(11):4546–4553, 1979. Cited on pages 3 and 55.

[152] K. R. Jeffrey and R. L. Armstrong. Nuclear-Quadrupole-Resonance Study of Lattice Dynamics in K2PtCl6. *Phys. Rev.*, 174(2):359, 1968. doi:10.1103/PhysRev.174.359. Cited on pages 44 and 104.

[153] G. E. Jellison and P. J. Bray. A Structural Interpretation of B10 and B11 NMR Spectra in Sodium Borate Glasses. *J. Non-Cryst. Solids*, 29(2):187–206, 1978. doi:10.1016/0022-3093(78)90113-8. Cited on page 91.

[154] G. E. Jellison, S. A. Feller, and P. J. Bray. Re-Examination of Fraction of 4-Coordinated Boron Atoms in Lithium Borate Glass System. *Phys. Chem. Glasses*, 19(3):52–53, 1978. Cited on page 91.

[155] A. Jerschow. From Nuclear Structure to the Quadrupolar NMR Interaction and High-Resolution Spectroscopy. *Prog. Nucl. Magn. Reson. Spectrosc.*, 46(1):63–78, 2005. doi:10.1016/j.pnmrs.2004.12.001. Cited on pages 25, 26, and 27.

[156] A. Jerschow and N. Müller. Efficient Simulation of Coherence Transfer Pathway Selection by Phase Cycling and Pulsed Field Gradients in NMR. *J. Magn. Reson.*, 134(1):17–29, 1998. doi:10.1006/jmre.1998.1491. Cited on page 43.

[157] P. A. V. Johnson, A. C. Wright, and R. N. Sinclair. A Neutron Diffraction Investigation of the Structure of Vitreous Boron Trioxide. *J. Non-Cryst. Solids*, 50(3):281–311, 1982. doi:10.1016/0022-3093(82)90092-8. Cited on page 90.

[158] E. R. Johnston, M. J. Dellwo, and J. Hendrix. Quantitative 2D Exchange Spectroscopy Using Time-Proportional Phase Incrementation. *J. Magn. Reson.*, 66(3):399–409, 1986. doi:10.1016/0022-2364(86)90184-8. Cited on pages 4, 56, and 135.

[159] C. Joo, U. Werner-Zwanziger, and J. W. Zwanziger. Anisotropy-Correlated Spectroscopy of Quadrupolar Nuclei. *Solid State Nucl. Magn. Reson.*, 16(1-2):77–83, 2000. doi:10.1016/S0926-2040(00)00057-6. Cited on page 69.

[160] S. Joyce, J. Yates, C. Pickard, and F. Mauri. A First Principles Theory of Nuclear Magnetic Resonance J-Coupling in Solid-State Systems. *J. Chem. Phys.*, 127(20):204107, 2007. doi:10.1063/1.2801984. Cited on pages 75 and 145.

[161] E. I. Kamitsos and G. D. Chryssikos. Borate Glass Structure by Raman and Infrared Spectroscopies. *J. Mol. Struct.*, 247:1–16, 1991. doi:10.1016/0022-2860(91)87058-P. Cited on pages 90 and 91.

[162] J. Kanellopoulos, D. Freude, and A. Kentgens. A Practical Comparison of MQMAS Techniques. *Solid State Nucl. Magn. Reson.*, 32(4):99–108, 2007. doi:10.1016/j.ssnmr.2007.09.003. Cited on page 64.

[163] H.-M. Kao and C. P. Grey. INEPT Experiments Involving Quadrupolar Nuclei in Solids. *J. Magn. Reson.*, 133(2):313–323, 1998. doi:10.1006/jmre.1998.1455. Cited on page 73.

[164] M. Karplus. Contact Electron-Spin Coupling of Nuclear Magnetic Moments. *J. Chem. Phys.*, 30(1):11–15, 1959. doi:10.1063/1.1729860. Cited on page 24.

[165] M. Karplus. Vicinal Proton Coupling in Nuclear Magnetic Resonance. *J. Am. Chem. Soc.*, 85(18):2870–2871, 1963. doi:10.1021/ja00901a059. Cited on page 24.

[166] W. Keller, W. Haubold, and B. Wrackmeyer. Indirect Nuclear Spin-Spin Coupling in Tetrachlorotetraborane(4) and Halogenated Polyhedral Phospha- and Arsaboranes. *Magn. Reson. Chem.*, 37(8):545–550, 1999. doi:10.1002/(SICI)1097-458X(199908)37:8<545::AID-MRC496>3.0.CO;2-E. Cited on page 74.

[167] A. P. M. Kentgens. A Practical Guide to Solid-State NMR of Half-Integer Quadrupolar Nuclei with Some Applications to Disordered Systems. *Geoderma*, 80(3-4):271–306, 1997. doi:10.1016/S0016-7061(97)00056-6. Cited on page 33.

[168] A. P. M. Kentgens. Off-Resonance Nutation Nuclear Magnetic Resonance Spectroscopy of Half-Integer Quadrupolar Nuclei. *Prog. Nucl. Magn. Reson. Spectrosc.*, 32(2):141–164, 1998. doi:10.1016/S0079-6565(98)00015-6. Cited on page 41.

[169] A. P. M. Kentgens, E. R. H. van Eck, T. G. Ajithkumar, T. Anupõld, J. Past, A. Reinhold, and A. Samoson. New Opportunities for Double Rotation NMR of Half-Integer Quadrupolar Nuclei. *J. Magn. Reson.*, 178(2):212–219, 2006. doi:10.1016/j.jmr.2005.09.014. Cited on page 71.

[170] A. P. M. Kentgens and R. Verhagen. Advantages of Double Frequency Sweeps in Static, MAS and MQMAS NMR of Spin I=3/2 Nuclei. *Chem. Phys. Lett.*, 300(3-4):435–443, 1999. doi:10.1016/S0009-2614(98)01402-X. Cited on page 64.

[171] R. Kerner. A Model for Formation and Structural Properties of Alkali Borate Glasses. *J. Non-Cryst. Solids*, 135(2-3):155–170, 1991. doi:10.1016/0022-3093(91)90416-4. Cited on page 90.

[172] H. Kessemeier and R. E. Norberg. Pulsed Nuclear Magnetic Resonance in Rotating Solids. *Phys. Rev.*, 155(2):321, 1967. doi:10.1103/PhysRev.155.321. Cited on

page 105.

[173] J. Kieffer. Understanding the Anomalous Behaviours of B2O3 Glass. *Phys. Chem. Glasses-Eur. J. Glass Sci. Technol. B*, 50:294–300, 2009. Cited on page 90.

[174] M. Kodama, S. Feller, and M. Affatigato. Thermal and Mechanical Properties of Lithium Borate Glasses in Relation to the Glass Structure. *J. Therm. Anal.*, 57(3):787–796, 1999. doi:10.1023/A:1010133923482. Cited on page 91.

[175] M. Kodama, N. Nakashima, and T. Matsushita. Velocity of Sound in and Elastic Properties of Cs2O-B2O3 Glasses. *Jpn. J. Appl. Phys.*, 32(1):2227–2229, 1993. doi:10.1143/JJAP.32.2227. Cited on pages 90 and 91.

[176] W. L. Konijnendijk and J. M. Stevels. The Structure of Borate Glasses Studied by Raman Scattering. *J. Non-Cryst. Solids*, 18(3):307–331, 1975. doi:10.1016/0022-3093(75)90137-4. Cited on page 91.

[177] J. H. Kristensen, H. Bildsøe, H. J. Jakobsen, and N. C. Nielsen. Application of Lie Algebra to NMR Spectroscopy. *Prog. Nucl. Magn. Reson. Spectrosc.*, 34(1):1–69, 1999. doi:10.1016/S0079-6565(98)00026-0. Cited on pages 8 and 9.

[178] S. Kroeker and J. F. Stebbins. Three-Coordinated Boron-11 Chemical Shifts in Borates. *Inorg. Chem.*, 40(24):6239–6246, 2001. doi:10.1021/ic010305u. Cited on pages 90 and 91.

[179] A. C. Kunwar, G. L. Turner, and E. Oldfield. Solid-State Spin-Echo Fourier Transform NMR of 39K and 67Zn Salts at High Field. *J. Magn. Reson.*, 69(1):124–127, 1986. doi:10.1016/0022-2364(86)90224-6. Cited on page 83.

[180] H.-T. Kwak, P. Srinivasan, J. Quine, D. Massiot, and Z. Gan. Satellite Transition Rotational Resonance of Homonuclear Quadrupolar Spins: Magic-Angle Effect on Spin-Echo Decay and Inversion Recovery. *Chem. Phys. Lett.*, 376(1-2):75–82, 2003. doi:10.1016/S0009-2614(03)00958-8. Cited on pages 70 and 84.

[181] F. H. Larsen, H. J. Jakobsen, P. D. Ellis, and N. C. Nielsen. QCPMG-MAS NMR of Half-Integer Quadrupolar Nuclei. *J. Magn. Reson.*, 131(1):144–147, 1998. doi:10.1006/jmre.1997.1341. Cited on page 49.

[182] R. W. Lee. Hot-Pressed Neodymium-Iron-Boron Magnets. *Appl. Phys. Lett.*, 46(8):790–791, 1985. doi:10.1063/1.95884. Cited on page 88.

[183] S. Lee, W. Richter, S. Vathyam, and W. S. Warren. Quantum Treatment of the Effects of Dipole–Dipole Interactions in Liquid Nuclear Magnetic Resonance. *J. Chem. Phys.*, 105(3):874–900, 1996. doi:10.1063/1.471968. Cited on page 18.

[184] S. K. Lee, M. Deschamps, J. Hiet, D. Massiot, and S. Y. Park. Connectivity and Proximity between Quadrupolar Nuclides in Oxide Glasses: Insights from through-Bond and through-Space Correlations in Solid-State NMR. *J. Phys. Chem. B*, 113(15):5162–5167, 2009. doi:10.1021/jp810667e. Cited on page 73.

[185] F. Lefebvre, J. P. Amoureux, C. Fernandez, and E. G. Derouane. Investigation of Variable Angle Sample Spinning (VASS) NMR of Quadrupolar Nuclei. I. Theory. *J. Chem. Phys.*, 86(11):6070–6076, 1987. doi:10.1063/1.452446. Cited on page 5.

[186] A. Lesage, D. Sakellariou, S. Steuernagel, and L. Emsley. Carbon–Proton Chemical Shift Correlation in Solid-State NMR by through-Bond Multiple-Quantum Spectroscopy. *J. Am. Chem. Soc.*, 120(50):13194–13201, 1998. doi:10.1021/ja983048+. Cited on page 73.

[187] M. H. Levitt. *Spin Dynamics*. Wiley, Chichester, 2001. Cited on pages 18, 23, 25, 44, and 78.

[188] M. H. Levitt. mPackages 3.36 for Mathematica™. *http://www.mhl.soton.ac.uk/public/Main/software/mPackages/*, 2007. Cited on page 93.

[189] M. H. Levitt, P. K. Madhu, and C. E. Hughes. Cogwheel Phase Cycling. *J. Magn. Reson.*, 155(2):300–306, 2002. doi:10.1006/jmre.2002.2520. Cited on page 43.

[190] M. H. Levitt, D. P. Raleigh, F. Creuzet, and R. G. Griffin. Theory and Simulations of Homonuclear Spin Pair Systems in Rotating Solids. *J. Chem. Phys.*, 92(11):6347–6364, 1990. doi:10.1063/1.458314. Cited on pages 150 and 151.

[191] Z. H. Liu, F. Deng, and S. W. Ding. Effects of Pulse Strength, Width, and Sample Spinning Speed on the Spectral Spin Diffusion of Multiquantum Coherences of Spin-3/2 Quadrupolar Nuclei. *J. Chem. Phys.*, 120(2):740–748, 2004. doi:10.1063/1.1630569. Cited on pages 68 and 69.

[192] A. Llor and J. Virlet. Towards High-Resolution NMR of More Nuclei in Solids: Sample Spinning with Time-Dependent Spinner Axis Angle. *Chem. Phys. Lett.*, 152(2-3):248–253, 1988. doi:10.1016/0009-2614(88)87362-7. Cited on page 5.

[193] A. Y. H. Lo and M. Edén. Efficient Symmetry-Based Homonuclear Dipolar Recoupling of Quadrupolar Spins: Double-Quantum NMR Correlations in Amorphous Solids. *Phys. Chem. Chem. Phys.*, 10(44):6635–6644, 2008. doi:10.1039/b808295b. Cited on page 72.

[194] I. J. Lowe. Free Induction Decays of Rotating Solids. *Phys. Rev. Lett.*, 2(7):285, 1959. doi:10.1103/PhysRevLett.2.285. Cited on page 3.

[195] I. J. Lowe and R. E. Norberg. Free-Induction Decays in Solids. *Phys. Rev.*, 107(1):46, 1957. doi:10.1103/PhysRev.107.46. Cited on pages 3 and 51.

[196] A. Lupulescu, S. P. Brown, and H. W. Spiess. Rotor-Encoded Heteronuclear MQ MAS NMR Spectroscopy of Half-Integer Quadrupolar and Spin I=1/2 Nuclei. *J. Magn. Reson.*, 154(1):101–129, 2002. doi:10.1006/jmre.2001.2464. Cited on page 102.

[197] K. J. D. MacKenzie and M. E. Smith. *Multinuclear Solid-State NMR of Inorganic Materials*. Pergamon, Amsterdam, 2001. Cited on pages 11, 33, and 78.

[198] S. Macura and R. R. Ernst. Elucidation of Cross Relaxation in Liquids by Two-Dimensional N.M.R. Spectroscopy. *Mol. Phys.*, 41(1):95–117, 1980. doi:10.1080/00268978000102601. Cited on pages 54, 58, and 133.

[199] S. Macura, Y. Huang, D. Suter, and R. R. Ernst. Two-Dimensional Chemical Exchange and Cross-Relaxation Spectroscopy of Coupled Nuclear Spins. *J. Magn. Reson.*, 43(2):259–281, 1981. doi:10.1016/0022-2364(81)90037-8. Cited on page 55.

[200] P. K. Madhu, A. Goldbourt, L. Frydman, and S. Vega. Sensitivity Enhancement of the MQMAS NMR Experiment by Fast Amplitude Modulation of the Pulses. *Chem. Phys. Lett.*, 307(1-2):41–47, 1999. doi:10.1016/S0009-2614(99)00446-7. Cited on pages 64 and 102.

[201] P. K. Madhu and M. H. Levitt. Signal Enhancement in the Triple-Quantum Magic-Angle Spinning NMR of Spins-3/2 in Solids: The FAM-RIACT-FAM Sequence. *J. Magn. Reson.*, 155(1):150–155, 2002. doi:10.1006/jmre.2002.2508. Cited on page 64.

[202] O. Majérus, L. Cormier, G. Calas, and B. Beuneu. Temperature-Induced Boron Coordination Change in Alkali Borate Glasses and Melts. *Phys. Rev. B*, 67(2):024210, 2003. doi:10.1103/PhysRevB.67.024210. Cited on page 91.

[203] G. Mali. Spin-Locking and Recoupling of Homonuclear Dipolar Interaction between Spin-3/2 Nuclei under Magic-Angle Sample Spinning. *J. Magn. Reson.*, 185(2):318–325, 2007. doi:10.1016/j.jmr.2007.01.008. Cited on page 72.

[204] G. Mali, G. Fink, and F. Taulelle. Double-Quantum Homonuclear Correlation Magic Angle Sample Spinning Nuclear Magnetic Resonance Spectroscopy of Dipolar-Coupled Quadrupolar Nuclei. *J. Chem. Phys.*, 120(6):2835–2845, 2004. doi:10.1063/1.1638741. Cited on page 72.

[205] G. Mali and V. Kaučič. Enhancing Sensitivity or Resolution of Homonuclear Correlation Experiment for Half-Integer Quadrupolar Nuclei. *J. Magn. Reson.*, 171(1):48–56, 2004.

doi:10.1016/j.jmr.2004.08.003. Cited on pages 71 and 72.

[206] G. Mali, V. Kaučič, and F. Taulelle. Measuring Distances between Half-Integer Quadrupolar Nuclei and Detecting Relative Orientations of Quadrupolar and Dipolar Tensors by Double-Quantum Homonuclear Dipolar Recoupling Nuclear Magnetic Resonance Experiments. *J. Chem. Phys.*, 128(20):204503, 2008. doi:10.1063/1.2928809. Cited on page 72.

[207] P. P. Man. Second-Order Quadrupole Effects on Hahn Echoes in Fast-Rotating Solids at the Magic Angle. *Phys. Rev. B*, 55(13):8406, 1997. doi:10.1103/PhysRevB.55.8406. Cited on page 34.

[208] P. P. Man. *Quadrupole Couplings in Nuclear Magnetic Resonance, General*. Encyclopedia of Analytical Chemistry. Wiley, Chicester, 2000. Cited on page 41.

[209] M. M. Maricq and J. S. Waugh. NMR in Rotating Solids. *J. Chem. Phys.*, 70(7):3300–3316, 1979. doi:10.1063/1.437915. Cited on pages 4, 20, 23, 34, and 56.

[210] L. Marinelli and L. Frydman. On the Origin of Spinning Sidebands in MQMAS NMR Experiments. *Chem. Phys. Lett.*, 275(3-4):188–198, 1997. doi:10.1016/S0009-2614(97)00746-X. Cited on page 102.

[211] D. Marion and K. Wüthrich. Application of Phase Sensitive Two-Dimensional Correlated Spectroscopy (COSY) for Measurements of 1H-1H Spin-Spin Coupling Constants in Proteins. *Biochem. Biophys. Res. Commun.*, 113(3):967, 1983. doi:10.1016/0006-291X(83)91093-8. Cited on pages 4 and 53.

[212] L. M. Martinez and C. A. Angell. A Thermodynamic Connection to the Fragility of Glass-Forming Liquids. *Nature*, 410(6829):663–667, 2001. doi:10.1038/35070517. Cited on page 88.

[213] J. I. Mason. *Multinuclear NMR*. Plenum Press, New York, 1987. Cited on pages 74 and 75.

[214] D. Massiot. Sensitivity and Lineshape Improvements of MQ-MAS by Rotor-Synchronized Data Acquisition. *J. Magn. Reson. Ser. A*, 122(2):240–244, 1996. doi:10.1006/jmra.1996.0202. Cited on page 63.

[215] D. Massiot, F. Fayon, B. Alonso, J. Trébosc, and J.-P. Amoureux. Chemical Bonding Differences Evidenced from *J*-Coupling in Solid State NMR Experiments Involving Quadrupolar Nuclei. *J. Magn. Reson.*, 164(1):160–164, 2003. doi:10.1016/S1090-7807(03)00134-4. Cited on page 73.

[216] D. Massiot, F. Fayon, M. Deschamps, S. Cadars, P. Florian, V. Montouillout, N. Pellerin, J. Hiet, A. Rakhmatullin, and C. Bessada. Detection and Use of Small *J* Couplings in Solid State NMR Experiments. *C. R. Chim.*, page doi:10.1016/j.crci.2009.05.001, 2009. doi:10.1016/j.crci.2009.05.001. Cited on page 73.

[217] D. Massiot, F. Fayon, V. Montouillout, N. Pellerin, J. Hiet, C. Roiland, P. Florian, J.-P. Coutures, L. Cormier, and D. R. Neuville. Structure and Dynamics of Oxide Melts and Glasses: A View from Multinuclear and High Temperature NMR. *J. Non-Cryst. Solids*, 354(2-9):249–254, 2008. doi:10.1016/j.jnoncrysol.2007.06.097. Cited on page 73.

[218] M. Massot, C. Julien, and M. Balkanski. Investigation of the Boron-Oxygen Network in Borate Glasses by Infrared Spectroscopy. *Infrared Phys.*, 29(2-4):775–779, 1989. doi:10.1016/0020-0891(89)90124-3. Cited on page 90.

[219] E. Matthias, B. Olsen, D. A. Shirley, J. E. Templeton, and R. M. Steffen. Theory of Nuclear Magnetic Resonance Detected by Nuclear Radiations. *Phys. Rev. A*, 4(4):1626, 1971. doi:10.1103/PhysRevA.4.1626. Cited on page 11.

[220] A. E. McDermott, F. Creuzet, R. G. Griffin, L. E. Zawadzke, Q.-Z. Ye, and C. T. Walsh. Rotational Resonance Determination of the Structure of an Enzyme-Inhibitor Complex: Phosphorylation of an (Aminoalkyl)Phosphinate Inhibitor of D-Alanyl-D-Alanine Ligase by ATP. *Biochemistry*, 29(24):5767–5775, 1990. doi:10.1021/bi00476a018. Cited

on page 59.

[221] A. Medek, J. S. Harwood, and L. Frydman. Multiple-Quantum Magic-Angle Spinning NMR: A New Method for the Study of Quadrupolar Nuclei in Solids. *J. Am. Chem. Soc.*, 117(51):12779–12787, 1995. doi:10.1021/ja00156a015. Cited on pages 6 and 62.

[222] B. N. Meera and J. Ramakrishna. Raman Spectral Studies of Borate Glasses. *J. Non-Cryst. Solids*, 159(1-2):1–21, 1993. doi:10.1016/0022-3093(93)91277-A. Cited on pages 90 and 91.

[223] S. Meiboom and D. Gill. Modified Spin-Echo Method for Measuring Nuclear Relaxation Times. *Rev. Sci. Instrum.*, 29(8):688–691, 1958. doi:10.1063/1.1716296. Cited on page 49.

[224] B. H. Meier. *Polarization Transfer and Spin Diffusion in Solid-State NMR*, volume 18 of *Advances in Magnetic and Optical Resonance*. Academic Press, New York, 1994. Cited on pages 55 and 59.

[225] E. M. Menger and W. S. Veeman. Quadrupole Effects in High-Resolution Phosphorus-31 Solid-State NMR Spectra of Triphenylphosphine Copper(I) Complexes. *J. Magn. Reson.*, 46(2):257–268, 1982. doi:10.1016/0022-2364(82)90141-X. Cited on page 73.

[226] V. K. Michaelis, P. M. Aguiar, and S. Kroeker. Probing Alkali Coordination Environments in Alkali Borate Glasses by Multinuclear Magnetic Resonance. *J. Non-Cryst. Solids*, 353(26):2582–2590, 2007. doi:10.1016/j.jnoncrysol.2007.04.029. Cited on page 91.

[227] Y. Millot and P. P. Man. Procedures for Labeling the High-Resolution Axis of Two-Dimensional MQ-MAS NMR Spectra of Half-Integer Quadrupole Spins. *Solid State Nucl. Magn. Reson.*, 21(1-2):21–43, 2002. doi:10.1006/snmr.2001.0043. Cited on page 63.

[228] M. G. Mortuza, R. Dupree, and D. Holland. Studies of the Effect of Paramagnetic Impurity in the Structure of Sodium Disilicate Glass. *J. Mater. Sci.*, 35(11):2829–2832, 2000. doi:10.1023/A:1004751303503. Cited on page 105.

[229] K. T. Mueller, J. H. Baltisberger, E. W. Wooten, and A. Pines. Isotropic Chemical Shifts and Quadrupolar Parameters for Oxygen-17 Using Dynamic Angle Spinning NMR. *J. Phys. Chem.*, 96(17):7001–7004, 1992. doi:10.1021/j100196a028. Cited on page 97.

[230] K. T. Mueller, B. Q. Sun, G. C. Chingas, J. W. Zwanziger, T. Terao, and A. Pines. Dynamic-Angle Spinning of Quadrupolar Nuclei. *J. Magn. Reson.*, 86(3):470–487, 1990. doi:10.1016/0022-2364(90)90025-5. Cited on page 5.

[231] S. Mukhopadhyay, K. P. Ramesh, R. Kannan, and J. Ramakrishna. Rare-Earth Ion-Assisted Nuclear Spin-Lattice Relaxation in Nd3+-Doped Binary Sodium Borate Glasses: B11 NMR Study. *Phys. Rev. B*, 70(22):224202, 2004. doi:10.1103/PhysRevB.70.224202. Cited on page 104.

[232] S. Mukhopadhyay, K. P. Ramesh, and J. Ramakrishna. 11B NMR Spin-Lattice Relaxation Study in Nd3+-Doped Binary Alkali Borate Glasses: A Possible Method to Look at the Environment of Rare-Earth Sites in Glasses. *Phys. Rev. B*, 72(5):054201, 2005. doi:10.1103/PhysRevB.72.054201. Cited on page 104.

[233] K. Müller. Spin Relaxation in Isolated and Coupled Non-Integer Quadrupolar Nuclei: Theory and Application for I=3/2 Nuclei. *Phys. Chem. Chem. Phys.*, 4(22):5515–5523, 2002. doi:10.1039/b206852d. Cited on page 146.

[234] M. Munowitz. *Coherence and NMR*. Wiley, Chicester, 1988. Cited on pages 22 and 39.

[235] M. Murakami, T. Shimizu, M. Tansho, Y. Takano, S. Ishii, E. A. Ekimov, V. A. Sidorov, and K. Takegoshi. 10B/11B 1D/2D Solid-State High-Resolution NMR Studies on Boron-Doped Diamond. *Diam. Relat. Mat.*, 18(10):1267–1273, 2009. doi:10.1016/j.diamond.2009.05.005. Cited on pages 88 and 133.

[236] M. Murakami, T. Shimizu, M. Tansho, A. Vinu, K. Ariga, T. Mori, and K. Takegoshi. Two-Dimensional 11B–11B Exchange NMR Study in Mesoporous Boron Carbon Nitride at 21.8T. *Solid State Nucl. Magn. Reson.*, 31(4):193–196, 2007. doi:10.1016/j.ssnmr.2007.04.003. Cited on pages 71 and 133.

[237] G. Neyens. Nuclear Magnetic and Quadrupole Moments for Nuclear Structure Research on Exotic Nuclei. *Rep. Prog. Phys.*, 66(4):633–689, 2003. doi:10.1088/0034-4885/66/4/205. Cited on page 8.

[238] M. Nijman, M. Ernst, A. P. M. Kentgens, and B. H. Meier. Rotational-Resonance NMR Experiments in Half-Integer Quadrupolar Spin Systems. *Mol. Phys.*, 98(3):161–178, 2000. doi:10.1080/00268970009483280. Cited on pages 60, 70, 150, and 159.

[239] J. D. Odom, P. D. Ellis, and H. C. Walsh. High-Resolution Boron Nuclear Magnetic Resonance. I. Pentaborane(9). *J. Am. Chem. Soc.*, 93(14):3529–3530, 1971. doi:10.1021/ja00743a040. Cited on page 73.

[240] E. T. Olejniczak, S. Vega, and R. G. Griffin. Multiple Pulse NMR in Rotating Solids. *J. Chem. Phys.*, 81(11):4804–4817, 1984. doi:10.1063/1.447506. Cited on page 83.

[241] J. Ollerenshaw and R. E. D. McClung. Construction of Phase Cycles of Minimum Cycle Length: Makecycle. *J. Magn. Reson.*, 143(2):255–265, 2000. doi:10.1006/jmre.1999.2004. Cited on page 43.

[242] A. J. Painter and M. J. Duer. Double-Quantum-Filtered Nuclear Magnetic Resonance Spectroscopy Applied to Quadrupolar Nuclei in Solids. *J. Chem. Phys.*, 116(2):710–722, 2002. doi:10.1063/1.1425831. Cited on page 72.

[243] G. E. Pake. Nuclear Resonance Absorption in Hydrated Crystals: Fine Structure of the Proton Line. *J. Chem. Phys.*, 16(4):327–336, 1948. doi:10.1063/1.1746878. Cited on page 22.

[244] B. G. Parkinson, D. Holland, M. E. Smith, A. P. Howes, and C. R. Scales. Effect of Minor Additions on Structure and Volatilization Loss in Simulated Nuclear Borosilicate Glasses. *J. Non-Cryst. Solids*, 353(44-46):4076–4083, 2007. doi:10.1016/j.jnoncrysol.2007.06.016. Cited on page 88.

[245] B. G. Parkinson, D. Holland, M. E. Smith, A. P. Howes, and C. R. Scales. The Effect of Oxide Additions on Medium-Range Order Structures in Borosilicate Glasses. *J. Phys.: Condens. Matter*, 19(41):415114, 2007. doi:10.1088/0953-8984/19/41/415114. Cited on page 91.

[246] B. Z. Pevzner, V. P. Klyuev, I. G. Polyakova, and V. F. Borodzyulya. Peculiar Properties of Barium Diborate Polycrystals. *Phys. Chem. Glasses-Eur. J. Glass Sci. Technol. B*, 47:534–537, 2006. Cited on page 102.

[247] D. J. Philp and P. W. Kuchel. A Way of Visualizing NMR Experiments on Quadrupolar Nuclei. *Concepts Magn. Res. A*, 25A(1):40–52, 2005. doi:10.1002/cmr.a.20029. Cited on page 42.

[248] K. J. Pike, R. P. Malde, S. E. Ashbrook, J. McManus, and S. Wimperis. Multiple-Quantum MAS NMR of Quadrupolar Nuclei. Do Five-, Seven- and Nine-Quantum Experiments Yield Higher Resolution Than the Three-Quantum Experiment? *Solid State Nucl. Magn. Reson.*, 16(3):203–215, 2000. doi:10.1016/S0926-2040(00)00081-3. Cited on page 62.

[249] A. Pines, M. G. Gibby, and J. S. Waugh. Proton-Enhanced Nuclear Induction Spectroscopy. A Method for High Resolution NMR of Dilute Spins in Solids. *J. Chem. Phys.*, 56(4):1776–1777, 1972. doi:10.1063/1.1677439. Cited on page 3.

[250] A. Pines, M. G. Gibby, and J. S. Waugh. Proton-Enhanced NMR of Dilute Spins in Solids. *J. Chem. Phys.*, 59(2):569–590, 1973. doi:10.1063/1.1680061. Cited on page 3.

[251] A. Pines, D. J. Ruben, S. Vega, and M. Mehring. New Approach to High-Resolution

Proton NMR in Solids: Deuterium Spin Decoupling by Multiple-Quantum Transitions. *Phys. Rev. Lett.*, 36(2):110, 1976. doi:10.1103/PhysRevLett.36.110. Cited on page 40.

[252] R. V. Pound. Nuclear Electric Quadrupole Interactions in Crystals. *Phys. Rev.*, 79(4):685, 1950. doi:10.1103/PhysRev.79.685. Cited on page 27.

[253] R. V. Pound. *Early Days in NMR*, volume 1 of *Encyclopedia of Magnetic Resonance*. Wiley, Chicester, 1996. doi:10.1002/9780470034590.emrhp0142. Cited on page 2.

[254] S. Prasad, T. M. Clark, T. H. Sefzik, H.-T. Kwak, Z. Gan, and P. J. Grandinetti. Solid-State Multinuclear Magnetic Resonance Investigation of Pyrex®. *J. Non-Cryst. Solids*, 352(26-27):2834–2840, 2006. doi:10.1016/j.jnoncrysol.2006.02.085. Cited on page 87.

[255] E. M. Purcell, H. C. Torrey, and R. V. Pound. Resonance Absorption by Nuclear Magnetic Moments in a Solid. *Phys. Rev.*, 69(1-2):37, 1946. doi:10.1103/PhysRev.69.37. Cited on page 2.

[256] P. Pyykkö. Spectroscopic Nuclear Quadrupole Moments. *Mol. Phys.*, 99(19):1617–1629, 2001. doi:10.1080/00268970110069010. Cited on page 26.

[257] I. I. Rabi. Space Quantization in a Gyrating Magnetic Field. *Phys. Rev.*, 51(8):652, 1937. doi:10.1103/PhysRev.51.652. Cited on page 2.

[258] S. F. Radaev, L. A. Muradyan, L. F. Malakhova, Y. V. Burak, and V. I. Simonov. Atomic Structure and Electron Density of Lithium Tetraborate Li2 B4 O7. *Kristallografiya*, 34:1400–1407, 1989. Cited on page 93.

[259] D. P. Raleigh, M. H. Levitt, and R. G. Griffin. Rotational Resonance in Solid State NMR. *Chem. Phys. Lett.*, 146(1-2):71–76, 1988. doi:10.1016/0009-2614(88)85051-6. Cited on pages 59 and 150.

[260] N. F. Ramsey. Electron Coupled Interactions between Nuclear Spins in Molecules. *Phys. Rev.*, 91(2):303, 1953. doi:10.1103/PhysRev.91.303. Cited on page 23.

[261] N. F. Ramsey and E. M. Purcell. Interactions between Nuclear Spins in Molecules. *Phys. Rev.*, 85(1):143, 1952. doi:10.1103/PhysRev.85.143. Cited on page 72.

[262] D. Reed. The Role of NMR in Boron Chemistry. *Chem. Soc. Rev.*, 22:109–116, 1993. doi:10.1039/CS9932200109. Cited on page 74.

[263] J. S. Rigden. *Rabi's Resonance Method*, volume 1 of *Encyclopedia of Magnetic Resonance*. Wiley, Chicester, 1996. doi:10.1002/9780470034590.emrhp0154. Cited on page 2.

[264] M. E. Rose. *Elementary Theory of Angular Momentum*. Wiley, New York, 1957. Cited on pages 11 and 31.

[265] D. Rovnyak, M. Baldus, G. Wu, N. V. Hud, J. Feigon, and R. G. Griffin. Localization of 23Na+ in a DNA Quadruplex by High-Field Solid-State NMR. *J. Am. Chem. Soc.*, 122(46):11423–11429, 2000. doi:10.1021/ja001022o. Cited on page 69.

[266] M. Rubinstein and H. A. Resing. Nuclear Spin-Lattice Relaxation in Amorphous and Crystalline B2O3. *Phys. Rev. B*, 13(3):959, 1976. doi:10.1103/PhysRevB.13.959. Cited on pages 90, 103, and 104.

[267] P. S. Salmon, R. A. Martin, P. E. Mason, and G. J. Cuello. Topological Versus Chemical Ordering in Network Glasses at Intermediate and Extended Length Scales. *Nature*, 435(7038):75–78, 2005. doi:10.1038/nature03475. Cited on page 90.

[268] A. Samoson and E. Lippmaa. Central Transition NMR Excitation Spectra of Half-Integer Quadrupole Nuclei. *Chem. Phys. Lett.*, 100(3):205–208, 1983. doi:10.1016/0009-2614(83)87276-5. Cited on page 41.

[269] A. Samoson and E. Lippmaa. Synchronized Double-Rotation NMR Spectroscopy. *J.*

Magn. Reson., 84(2):410–416, 1989. doi:10.1016/0022-2364(89)90389-2. Cited on pages 5, 81, and 98.

[270] A. Samoson, E. Lippmaa, and A. Pines. High-Resolution Solid-State NMR Averaging of 2nd-Order Effects by Means of a Double-Rotor. *Mol. Phys.*, 65(4):1013–1018, 1988. doi:10.1080/00268978800101571. Cited on pages 5 and 34.

[271] B. C. Sanctuary, T. K. Halstead, and P. A. Osment. Multipole N.M.R. IV. Dynamics of Single Spins. *Mol. Phys.*, 49(4):753–784, 1983. doi:10.1080/00268978300101531. Cited on page 25.

[272] B. S. R. Sastry and F. A. Hummel. Studies in Lithium Oxide Systems: I, Li2O–Li2O B2O3. *J. Am. Ceram. Soc.*, 41(1):7–17, 1958. doi:10.1111/j.1151-2916.1958.tb13496.x. Cited on pages 92 and 94.

[273] B. S. R. Sastry and F. A. Hummel. Studies in Lithium Oxide Systems: V, Li2O–Li2O B2O3. *J. Am. Ceram. Soc.*, 42(5):216–218, 1959. doi:10.1111/j.1151-2916.1959.tb15456.x. Cited on page 92.

[274] J. Schaefer, E. O. Stejskal, and R. Buchdahl. High-Resolution Carbon-13 Nuclear Magnetic Resonance Study of Some Solid, Glassy Polymers. *Macromolecules*, 8(3):291–296, 1975. doi:10.1021/ma60045a010. Cited on page 3.

[275] S. Sen and J. F. Stebbins. Phase Separation, Clustering, and Fractal Characteristics in Glass: A Magic-Angle-Spinning NMR Spin-Lattice Relaxation Study. *Phys. Rev. B*, 50(2):822, 1994. doi:10.1103/PhysRevB.50.822. Cited on page 104.

[276] S. Sen and J. F. Stebbins. Structural Role of Nd3+ and Al3+ Cations in SiO2 Glass: A 29Si MAS-NMR Spin-Lattice Relaxation, 27Al NMR and EPR Study. *J. Non-Cryst. Solids*, 188(1-2):54–62, 1995. doi:10.1016/0022-3093(95)00099-2. Cited on page 103.

[277] N. Sennova, R. Bubnova, J. Shepelev, S. Filatov, and O. Yakovleva. Li2B4O7 Crystal Structure in Anharmonic Approximation at 20, 200, 400 and 500 °C. *J. Alloy. Compd.*, 428(1-2):290–296, 2007. doi:10.1016/j.jallcom.2006.03.049. Cited on pages 92, 101, and 145.

[278] R. D. Shannon. Revised Effective Ionic Radii and Systematic Studies of Interatomic Distances in Halides and Chalcogenides. *Acta Crystallogr. Sect. A*, 32(5):751–767, 1976. doi:10.1107/S0567739476001551. Cited on page 105.

[279] J. E. Shelby. Thermal Expansion of Alkali Borate Glasses. *J. Am. Ceram. Soc.*, 66(3):225–227, 1983. doi:10.1111/j.1151-2916.1983.tb10023.x. Cited on pages 91 and 92.

[280] J. E. Shelby. *Introduction to Glass Science and Technology*. The Royal Society of Chemistry, Cambridge, 1997. Cited on page 89.

[281] R. Siegel, T. T. Nakashima, and R. E. Wasylishen. Sensitivity Enhancement of NMR Spectra of Half-Integer Quadrupolar Nuclei in the Solid State via Population Transfer. *Concepts Magn. Res. A*, 26A(2):47–61, 2005. doi:10.1002/cmr.a.20037. Cited on page 66.

[282] R. N. Sinclair, R. Haworth, A. C. Wright, B. G. Parkinson, D. Holland, J. W. Taylor, N. M. Vedishcheva, I. G. Polyakova, B. A. Shakhmatkin, S. A. Feller, B. Rijal, and T. Edwards. Neutron Spectroscopic Studies of Caesium Borate Crystals and Glasses. *Phys. Chem. Glasses-Eur. J. Glass Sci. Technol. B*, 47:405–411, 2006. Cited on pages 91, 92, and 93.

[283] C. P. Slichter. *Principles of Magnetic Resonance*. Springer-Verlag, Berlin Heidelberg, 1989. Cited on pages 22, 24, 44, and 84.

[284] O. W. Sørensen, G. W. Eich, M. H. Levitt, G. Bodenhausen, and R. R. Ernst. Product Operator-Formalism for the Description of NMR Pulse Experiments. *Prog. Nucl. Magn. Reson. Spectrosc.*, 16:163–192, 1983. doi:10.1016/0079-6565(84)80005-9. Cited on

pages 4 and 9.

[285] O. W. Sørensen, M. Rance, and R. R. Ernst. Z Filters for Purging Phase- or Multiplet-Distorted Spectra. *J. Magn. Reson.*, 56(3):527–534, 1984. doi:10.1016/0022-2364(84)90317-2. Cited on page 63.

[286] J. K. Srivastava and S. J. Supe. The Thermoluminescence Characterisation of Li2B4O7 Doped with Cu. *J. Phys. D: Appl. Phys.*, 22(10):1537–1543, 1989. doi:10.1088/0022-3727/22/10/020. Cited on page 93.

[287] D. J. States, R. A. Haberkorn, and D. J. Ruben. A Two-Dimensional Nuclear Overhauser Experiment with Pure Absorption Phase in 4 Quadrants. *J. Magn. Reson.*, 48(2):286–292, 1982. Cited on pages 4, 53, 81, and 164.

[288] B. Q. Sun, P. R. Costa, D. Kocisko, J. P. T. Lansbury, and R. G. Griffin. Internuclear Distance Measurements in Solid State Nuclear Magnetic Resonance: Dipolar Recoupling via Rotor Synchronized Spin Locking. *J. Chem. Phys.*, 102(2):702–707, 1995. doi:10.1063/1.469182. Cited on page 133.

[289] D. Suter and R. R. Ernst. Spin Diffusion in Resolved Solid-State NMR Spectra. *Phys. Rev. B*, 32(9):5608, 1985. doi:10.1103/PhysRevB.32.5608. Cited on page 54.

[290] J. Swenson, L. Börjesson, and W. S. Howells. Structure of Borate Glasses from Neutron-Diffraction Experiments. *Phys. Rev. B*, 52(13):9310, 1995. doi:10.1103/PhysRevB.52.9310. Cited on pages 90 and 91.

[291] J. Szeftel and H. Alloul. Nuclear Spin Lattice Relaxation in the Amorphous State: Towards an Understanding. *J. Non-Cryst. Solids*, 29(3):253–281, 1978. doi:10.1016/0022-3093(78)90149-7. Cited on pages 44 and 104.

[292] T. Terao, H. Miura, and A. Saika. Simplification and Assignment of Carbon-13 Spectra by Using *J*-Resolved NMR Spectroscopy in Solids. *J. Am. Chem. Soc.*, 104(19):5228–5229, 2002. doi:10.1021/ja00383a040. Cited on page 73.

[293] A. Tokatlı, A. Gençten, M. Sahin, O. Tezel, and S. Bahçeli. Product Operator Descriptions of INEPT and RINEPT NMR Spectroscopies for ISn (I=1/2, S=3/2) Spin Systems. *J. Magn. Reson.*, 169(1):68–72, 2004. doi:10.1016/j.jmr.2004.04.005. Cited on page 73.

[294] J. Trébosc, J.-P. Amoureux, and Z. Gan. Comparison of High-Resolution Solid-State NMR MQMAS and STMAS Methods for Half-Integer Quadrupolar Nuclei. *Solid State Nucl. Magn. Reson.*, 31(1):1–9, 2007. doi:10.1016/j.ssnmr.2006.09.002. Cited on page 64.

[295] J. T. Urban. Nuclear Magnetic Resonance Studies of Quadrupolar Nuclei and Dipolar Field Effects. *Ph.D. Thesis, University of California, Berkeley*, 2004. Cited on pages 26 and 50.

[296] J. Van Kranendonk. Theory of Quadrupolar Nuclear Spin-Lattice Relaxation. *Physica*, 20(7-12):781–800, 1954. doi:10.1016/S0031-8914(54)80191-1. Cited on pages 44 and 104.

[297] J. H. Van Vleck. The Dipolar Broadening of Magnetic Resonance Lines in Crystals. *Phys. Rev.*, 74(9):1168, 1948. doi:10.1103/PhysRev.74.1168. Cited on page 22.

[298] L. van Wüllen and W. Müller-Warmuth. 11B MAS NMR Spectroscopy for Characterizing the Structure of Glasses. *Solid State Nucl. Magn. Reson.*, 2(5):279–284, 1993. doi:10.1016/0926-2040(93)90009-C. Cited on page 91.

[299] A. J. Vega. MAS NMR Spin Locking of Half-Integer Quadrupolar Nuclei. *J. Magn. Reson.*, 96(1):50–68, 1992. doi:10.1016/0022-2364(92)90287-H. Cited on page 64.

[300] A. J. Vega. *Quadrupolar Nuclei in Solids*, volume 7 of *Encyclopedia of Magnetic Resonance*. Wiley, Chicester, 1996. doi:10.1002/9780470034590.emrstm0431. Cited on pages 40 and 41.

[301] S. Vega. Fictitious Spin 1/2 Operator Formalism for Multiple Quantum NMR. *J. Chem. Phys.*, 68(12):5518–5527, 1978. doi:10.1063/1.435679. Cited on pages 40 and 57.

[302] T. Vosegaard, P. Florian, D. Massiot, and P. J. Grandinetti. Multiple Quantum Magic-Angle Spinning Using Rotary Resonance Excitation. *J. Chem. Phys.*, 114(10):4618–4624, 2001. doi:10.1063/1.1333407. Cited on page 64.

[303] J. D. Walls, K. H. Lim, and A. Pines. Theoretical Studies of the Spin Dynamics of Quadrupolar Nuclei at Rotational Resonance Conditions. *J. Chem. Phys.*, 116(1):79–90, 2002. doi:10.1063/1.1421613. Cited on page 70.

[304] Q. Wang, B. Hu, O. Lafon, J. Trébosc, F. Deng, and J. P. Amoureux. Double-Quantum Homonuclear NMR Correlation Spectroscopy of Quadrupolar Nuclei Subjected to Magic-Angle Spinning and High Magnetic Field. *J. Magn. Reson.*, 200(2):251–260, 2009. doi:10.1016/j.jmr.2009.07.009. Cited on page 72.

[305] T.-J. Wang. Nuclear Electric Hexadecapole Interactions in Solids. *J. Magn. Reson.*, 64(2):194–198, 1985. doi:10.1016/0022-2364(85)90343-9. Cited on page 25.

[306] J. R. H. Wentorf. Synthesis of the Cubic Form of Boron Nitride. *J. Chem. Phys.*, 34(3):809–812, 1961. doi:10.1063/1.1731679. Cited on page 87.

[307] J. Whitaker, E. Ahn, P. Hari, G. A. Williams, P. C. Taylor, and J. C. Facelli. Indirect (J) Coupling of Inequivalent 75As Nuclei in Crystalline and Glassy As2Se3 and As2S3. *J. Chem. Phys.*, 119(16):8519–8525, 2003. doi:10.1063/1.1612920. Cited on page 75.

[308] H. E. White. Pictorial Representations of the Electron Cloud for Hydrogen-Like Atoms. *Phys. Rev.*, 37(11):1416, 1931. doi:10.1103/PhysRev.37.1416. Cited on page 12.

[309] S. Wi and L. Frydman. Residual Dipolar Couplings between Quadrupolar Nuclei in High Resolution Solid State NMR: Description and Observations in the High-Field Limit. *J. Chem. Phys.*, 112(7):3248–3261, 2000. doi:10.1063/1.480498. Cited on pages 56, 67, 71, 75, and 132.

[310] S. Wi, V. Frydman, and L. Frydman. Residual Dipolar Couplings between Quadrupolar Nuclei in Solid State Nuclear Magnetic Resonance at Arbitrary Fields. *J. Chem. Phys.*, 114(19):8511–8519, 2001. doi:10.1063/1.1357440. Cited on page 73.

[311] S. Wi, H. Heise, and A. Pines. Reintroducing Anisotropic Interactions in Magic-Angle-Spinning NMR of Half-Integer Quadrupolar Nuclei: 3D MQMAS. *J. Am. Chem. Soc.*, 124(36):10652–10653, 2002. doi:10.1021/ja027043v. Cited on page 70.

[312] S. Wi, J. W. Logan, D. Sakellariou, J. D. Walls, and A. Pines. Rotary Resonance Recoupling for Half-Integer Quadrupolar Nuclei in Solid-State Nuclear Magnetic Resonance Spectroscopy. *J. Chem. Phys.*, 117(15):7024–7033, 2002. doi:10.1063/1.1506907. Cited on page 70.

[313] J. W. Wiench and M. Pruski. Probing through Bond Connectivities with MQMAS NMR. *Solid State Nucl. Magn. Reson.*, 26(1):51–55, 2004. doi:10.1016/j.ssnmr.2003.10.004. Cited on page 73.

[314] P. T. F. Williamson, A. Verhoeven, M. Ernst, and B. H. Meier. Determination of Internuclear Distances in Uniformly Labeled Molecules by Rotational-Resonance Solid-State NMR. *J. Am. Chem. Soc.*, 125(9):2718–2722, 2003. doi:10.1021/ja028210u. Cited on page 59.

[315] P. T. F. Williamson, A. Verhoeven, K. W. Miller, B. H. Meier, and A. Watts. The Conformation of Acetylcholine at its Target Site in the Membrane-Embedded Nicotinic Acetylcholine Receptor. *Proceedings of the National Academy of Sciences*, 104(46):18031–18036, 2007. doi:10.1073/pnas.0704785104. Cited on page 59.

[316] G. Wingefeld and G. Hoppe. Zur Konstitution Von Ba2WO3F4 Und Ba2MoO3F4. *Z. Anorg. Allg. Chem.*, 518(11):149–160, 1984. doi:10.1002/zaac.19845181115. Cited on page 164.

[317] A. Wong, A. P. Howes, B. Parkinson, T. Anupõld, A. Samoson, D. Holland, and

R. Dupree. High-Resolution 17O Double-Rotation NMR Characterization of Ring and Non-Ring Oxygen in Vitreous B2O3. *Phys. Chem. Chem. Phys.*, 11(32):7061–7068, 2009. doi:10.1039/b906501f. Cited on page 90.

[318] A. C. Wright. Longer Range Order in Single Component Network Glasses? *Phys. Chem. Glasses-Eur. J. Glass Sci. Technol. B*, 49:103–117, 2008. Cited on page 90.

[319] A. C. Wright, J. L. Shaw, R. N. Sinclair, N. M. Vedishcheva, B. A. Shakhmatkin, and C. R. Scales. The Use of Crystallographic Data in Interpreting the Correlation Function for Complex Glasses. *J. Non-Cryst. Solids*, 345–346:24–33, 2004. doi:10.1016/j.jnoncrysol.2004.07.066. Cited on page 91.

[320] A. C. Wright, N. M. Vedishcheva, and B. A. Shakhmatkin. Vitreous Borate Networks Containing Superstructural Units: A Challenge to the Random Network Theory? *J. Non-Cryst. Solids*, 192–193:92–97, 1995. doi:10.1016/0022-3093(95)00432-7. Cited on page 90.

[321] A. C. Wright, N. M. Vedishcheva, and B. A. Shakhmatkin. A Crystallographic Guide to the Structure of Borate Glasses. *Mat. Res. Soc. Symp. Proc.*, 455:381–396, 1997. Cited on pages 90 and 92.

[322] G. Wu, S. Kroeker, R. E. Wasylishen, and R. G. Griffin. Indirect Spin-Spin Coupling in Multiple-Quantum Magic-Angle-Spinning NMR Spectra of Quadrupolar Nuclei. *J. Magn. Reson.*, 124(1):237–239, 1997. doi:10.1006/jmre.1996.1042. Cited on page 73.

[323] G. Wu, D. Rovnyak, and R. G. Griffin. Quantitative Multiple-Quantum Magic-Angle-Spinning NMR Spectroscopy of Quadrupolar Nuclei in Solids. *J. Am. Chem. Soc.*, 118(39):9326–9332, 1996. doi:10.1021/ja9614676. Cited on page 64.

[324] Y. Wu, B. Q. Sun, A. Pines, A. Samoson, and E. Lippmaa. NMR Experiments with a New Double Rotor. *J. Magn. Reson.*, 89(2):297–309, 1990. doi:10.1016/0022-2364(90)90236-3. Cited on pages 5 and 34.

[325] T. Yano, N. Kunimine, S. Shibata, and M. Yamane. Structural Investigation of Sodium Borate Glasses and Melts by Raman Spectroscopy.: I. Quantitative Evaluation of Structural Units. *J. Non-Cryst. Solids*, 321(3):137–146, 2003. doi:10.1016/S0022-3093(03)00158-3. Cited on page 90.

[326] W. H. Zachariasen. The Atomic Arrangement in Glass. *J. Am. Chem. Soc.*, 54(10):3841–3851, 1932. doi:10.1021/ja01349a006. Cited on page 89.

[327] M. Zanger and G. Moyna. Measurement of the Isotopic Ratio of 10B/11B in NaBH4 by 1H NMR. *J. Chem. Educ.*, 82(9):1390–1392, 2005. Cited on page 73.

[328] S. K. Zaremba. Good Lattice Points, Discrepancy, and Numerical Integration . *Ann. Mat. Pura. Appl.*, 73(1):293–317, 1966. doi:10.1007/BF02415091. Cited on page 84.

[329] J. Zhong and P. J. Bray. Change in Boron Coordination in Alkali Borate Glasses, and Mixed Alkali Effects, as Elucidated by NMR. *J. Non-Cryst. Solids*, 111(1):67–76, 1989. doi:10.1016/0022-3093(89)90425-0. Cited on page 91.

[330] V. E. Zorin, S. P. Brown, and P. Hodgkinson. Origins of Linewidth in 1H Magic-Angle Spinning NMR. *J. Chem. Phys.*, 125(14):144508–13, 2006. doi:10.1063/1.2357602. Cited on pages 56, 100, 101, 112, 121, and 147.

[331] V. E. Zorin, M. Ernst, S. P. Brown, and P. Hodgkinson. Insights into Homonuclear Decoupling from Efficient Numerical Simulation: Techniques and Examples. *J. Magn. Reson.*, 192(2):183–196, 2008. doi:10.1016/j.jmr.2008.02.012. Cited on page 86.

[332] J. W. Zwanziger. The NMR Response of Boroxol Rings: A Density Functional Theory Study. *Solid State Nucl. Magn. Reson.*, 27(1-2):5–9, 2005. doi:10.1016/j.ssnmr.2004.08.004. Cited on page 90.